Mechanisms of Enhancement in Lead-Free Piezoceramic Composites

Vom Fachbereich Material- und Geowissenschaften

Der Technischen Universität Darmstadt

Zur Erlangung des akademischen Grades

Eines Doktors der Naturwissenschaft

(Dr. rer. nat.)

Genehmigte Dissertation von

Azatuhi R. Ayrikyan, M.Sc.

Aus Moskau, Russland

Hauptberichterstatter: Prof. Dr. Kyle G. Webber

Nebenberichterstatter: Prof. Dr. Hans-Joachim Kleebe

Tag der Einreichung: 16.5.2018

Tag der mündlichen Prüfung: 28.9.2018

Darmstadt

Darmstadt, Technische Universität Darmstadt
Jahr der Veröffentlichung des Dissertations: 2019
Tag der mündlichen Prüfung: 28.9.2018

We begin by knowing little and believing much, and we sometimes end by inverting the quantities.

Mary Ann Evans, otherwise known as George Eliot, Middlemarch

In honor of my grandfather, Lev Sirotenko, and his father, Mattvei Sirotenko.

Acknowledgements

The completion of this work would not have been possible without the incredible team of scientists I was surrounded by throughout my doctoral studies. I would like to first thank Professor Kyle Webber for giving me the opportunity to pursue a PhD in his newly established research group. Thank you for your guidance and help in coming to Germany, being a researcher at not one, but two major research universities here, and giving me the opportunity to work with such a strong and dynamic research group.

Secondly, I would like to thank Professor Jurgen Rodel for his support and encouragement during my first two years at TU Darmstadt. He provided an incredible model for what a globally minded and international scientific leader should be.

The colleagues with whom I worked, both at TU Darmstadt and in universities around the world, were my motivation and source of strength throughout the challenges intrinsic to scientific research. I am particularly indebted to the many postdoctoral fellows who trained me on cutting edge fabrication and measurement techniques and helped me to understand very complex results. Thank you to Dr. Jurij Koruza, who taught me solid-state synthesis and ceramics processing, and served as a mentor for my first year at TU Darmstadt. A huge thank you to Dr. Neamul Khansur, who taught me everything I know about X-ray diffraction and crystallography, and who provided an enormous amount of assistance in Rietveld refinement of my results. Dr. Leopoldo Molina-Luna and Dr. Michael Durrschnabel were instrumental to the compositional investigations performed by EDS and TEM in this work, and have helped me achieve very novel insights in the field of composite ceramic chemistry. From the same research group, I had invaluable discussions on prior work in this field with Dr. Ljubomira Schmidt, which inspired a large part of the first section of this dissertation. Dr. Till Fromling, from NAW, provided a great deal of insight and guidance in the investigation of dielectric behavior and chemistry, as well as overcoming the challenges of cultural understanding in Germany. I was very fortunate to have the support and interest of Dr. Pedro Braga of TU Darmstadt's chemistry department, which resulted in a very productive collaboration on the use of NMR for detailed analysis of the solid-state chemistry of composites. I would also like to express my gratitude and appreciation for the support, both scientific and personal, from Dr. Alexander Martin and Dr. Barbara Kaeswurm in Erlangen.

The support I received for the completion of this project was on an international level: thanks to Dr. Yoshitaka Ehara, who was a Humboldt fellow with the research group in TU Darmstadt, I was able to collaborate with Professor Shintaro Yasui and Professor Mitsuri Itoh at the Tokyo Institute of Technology. Through their support, we had the

opportunity conduct structural investigations at the micron-scale at the SPring8 Synchrotron in Japan. It was an incredible experience, for which I am very grateful.

I was very fortunate to share an office with a real Heiner my first two years in Darmstadt, and even more fortunate that we moved to Erlangen together. The support of Philipp T. Geiger throughout my time in Germany was invaluable, both scientifically and personally. I am also very grateful to my colleague and friend Dr. Florian Schader, who developed many of the instruments used in this work for ferroelastic testing and was always available for support, both technical and emotional, when there were problems with measurements. He also provided invaluable insight into the final chapter of this thesis, for which I am very grateful. I would also like to acknowledge the help and support of my friend and colleague Dr. Martin Bloemker, who, seeing the crazy hours I kept, would often bring me food and water while I trapped myself in my office. He was kind enough, despite his busy schedule as a laboratory manager at Merck, to exhaustively review my introduction and literature review. It was a privilege to work with and befriend these three brilliant young men.

I would also like to gratefully acknowledge the undergraduate and masters students both at the Technical University of Darmstadt and the Friedrich Alexander University of Erlangen-Nuremberg who I had the privilege of supervising, namely, in chronological order, Young-Mi Kim, Florian Weyland, Sebastian Steiner, Hakimeh Wakily, Ebru Erdem, Stephanie Keller and Andreas Kastner. All of these brilliant young minds made significant contributions to this work, and I am honored to have had the opportunity to work with these budding scientists.

Finally, I would like to acknowledge the many sacrifices my family and loved ones have made to enable me to reach this point in my academic career. My mother and father have been examples for me of how to survive any hardship that comes my way and have given me the strength do to that. My brother and sister have been not just siblings, but the closest of friends, and role models of academic and professional achievement. And my grandmother, who I was lucky as a young woman to have as a model for women pursuing science, and as a support throughout my life.

Preface and Introduction

The aim of this work is to investigate lead-free ferroelectric ceramic/ceramic composites, with the ultimate goal of elucidating the mechanisms of their enhanced electromechanical response. Previous work has shown that a composite comprised of a highly disordered nonpolar ferroelectric matrix material and an ordered polar seed material results in an increased electromechanical response under specific circumstances [1], [2]. The mechanisms used to explain this enhancement have been based on the electrical and mechanical interactions between the seed and matrix during application of an electric field.

It is this author's assertion that the interactions between the seed and matrix during processing also play a significant role in the enhancement observed in lead-free ferroelectric composite systems. The fabrication of ceramic/ceramic composites requires high-temperature sintering of the seed and matrix for formation of densified pellets. As densification during sintering is a diffusion driven process, and the two constituents are not chemically identical, fundamental laws of kinetics dictate that diffusion between the two constituents should occur at the high temperatures required for ceramics processing. In addition, because the densification process is not identical between the two constituents, a difference in the sintering trajectories will result in a nonzero stress state during sintering, which is well established to effect the microstructure [3]–[6]. The structure-property relationships in composites can provide new insight into these mechanisms, but there have been significant challenges in investigating structure at the microscale. To that end, model systems of 2-2 composites were prepared and utilized to investigate these phenomena.

2-2 composites facilitate the investigation of chemical interactions between the two constituents. The influence of chemistry on the electromechanical behavior of ferroelectrics is profound. This work focuses on the perovskite family, with the crystal structure ABO_3. The more chemically inhomogeneous the system, the more complex this perovskite crystal structure is, due to multiple A- and B-site cation occupancies. The ionic radius and oxidation state of the A- and B-site cations have a profound influence on the electromechanical response. In a polycrystalline material, this discussion is further complicated by the formation of chemically inhomogeneous grains, which form a core-shell structure. In fact, the composite structure as a means of improving electromechanical behavior was first proposed based on the idea of emulating the core-shell inhomogeneity observed in certain lead-free piezoceramics [7]. Therefore, the path to improving piezoceramics through the composite approach must include an investigation of the influence of chemical interactions on their electromechanical response. However, probing the chemistry and its impact on crystal structure in 0-3 composites has proven quite challenging. The 2-2 composite structure allows for an investigation of these interactions through readily available laboratory equipment, such as scanning electron microscopes and laboratory-based X-ray diffraction tools.

2-2 composites also allow for a more simplified investigation of the stress state. In 0-3 composites, the difference in thermal strain both during sintering and during cooling in the densified body results in a fairly complex three-dimensional stress state. A 2-2 composite, on the other hand, results in two-dimensional biaxial in-plane stresses. In this work, the stresses generated are treated as uniform throughout each layer, which is an assumption for the ease of discussion and calculation that does not correspond to the reality of stress gradients in the final sintered body. In addition to the influence of stress on microstructure during sintering, the residual stress state in the final sintered body will have an influence on the electromechanical response of the composite. Because many ferroelectrics also have a ferroelastic response, an investigation of the influence of mechanical stress on the crystal structure as well as the dielectric and ferroelectric properties of lead-free ferroelectrics was performed in this work as well. This investigation provides insight on the electromechanical response of composites in which internal stresses are present.

In light of the influences of diffusion and internal stress on electromechanical behavior, the electromechanical response of several 0-3 and 2-2 composite systems are investigated. The influence of co-sintering interactions on the electromechanical behavior of electroceramics plays an important role in the improvement of lead-free material systems for the replacement of current commercially dominant lead-based systems. It is the hope of this author that the results discussed herein will provide insight and inspiration for future investigations in this field, enabling the development of viable lead-free alternatives for piezoelectric ceramics.

Table of Contents

Table of Figures

Table of Abbreviations and Symbols

BA	$BiAlO_3$
BT	$BaTiO_3$
BKT	$Bi_{0.5}K_{0.5}TiO_3$
BNKT	$Bi_{0.5}(Na_{1-x}K_x)_{0.5}TiO_3$
BNKT-BA	$(1-y)Bi_{0.5}(Na_{1-x}K_x)_{0.5}TiO_3-yBiAlO_3$
BNT	$Bi_{0.5}Na_{0.5}TiO_3$
BNT-BT	$(1-x)Bi_{0.5}Na_{0.5}TiO_3-xBaTiO_3$
BNT-BT-KNN	$(1-x-y)Bi_{0.5}Na_{0.5}TiO_3-xBaTiO_3-yK_{0.5}Na_{0.5}NbO_3$
BNT-ST	$(1-x)Bi_{0.5}Na_{0.5}TiO_3-xSrTiO_3$
C	Capacitance
CIP	Cold Isostatic Press
d_{33}^*	Piezoelectric coefficient under large signal applied electric field
d_{33}	Piezoelectric coefficient under small-signal applied electric field
D	Electric Displacement
D_x^*	Diffusivity of element x
DIC	Digital Image Correlation
E	Electric field
E_c	Coercive Electric Field
EDS	Energy Dispersive Spectroscopy
ER	Ergodic Relaxor
ESRF	European Synchrotron Radiation Facility

HRSEM	High Resolution Scanning Electron Microscopy
KNN	$(K_{0.5}Na_{0.5})NbO_3$
LVDT	Linear Variable Displacement Transducer
MPB	Morphotropic Phase Boundary
PFM	Piezoforce Microscopy
NMR	Nuclear Magnetic Resonance
NR	Nonergodic Relaxor
P	Polarization
P_r	Remanent Polarization
PLZT	$Pb_{1-y}La_yZr_xTi_{1-x}O_3$
PMN	$Pb(Mg_{1/3}Nb_{2/3})O_3$
PNN	$Pb(Ni_{1/3}Nb_{2/3})O_3$
PZT	$PbZr_xTi_{(1-x)}O_3$
Q	Charge
ST	$SrTiO_3$
PNR	Polar Nanoregion
RE	Relaxor
SAED	Selected Area Electron Diffraction
SEM	Scanning Electron Microscope
T_d	Depoling Temperature
TEM	Transmission Electron Microscopy
V	Voltage

XRD	X-ray diffraction
Y	Young’s Modulus

Symbols

δ	Dielectric loss angle
ε	Strain
ε_{rem}	Remanent Strain
λ	Wavelength
σ	Mechanical Stress
σ_c	Coercive Stress
ω	Frequency

Page intentionally left blank

1. Theoretical Background

1.1. Ceramics

This work focuses on the fabrication and evaluation of lead-free piezoceramics. Therefore, an introduction to the general material class of ceramics, as well as more detailed information on the development of electroceramics, will be provided in this work to facilitate the reader's journey into this field.

Ceramics are defined as nonmetallic, inorganic compounds. Most ceramics are polycrystalline; however, single crystal ceramics are also under frequent investigation. The atomic scale of properties, such as bonding and crystal structure, as well as the microstructural scale of properties, such as grain size and porosity, are both known to affect the bulk properties of the ceramic. Intrinsic properties are determined by the behavior of the material at the atomic scale. These properties include the melting point, elastic modulus, and coefficient of thermal expansion. Extrinsic properties depend on the microstructure and include behavior such as dielectric permittivity, piezoelectric coefficient, and mechanical strength. The composition inherently determines the crystal structure and, therefore, intrinsic behavior of a ceramic. However, microstructural properties, such as grain size and porosity, can be altered during the ceramic fabrication process. It is often the microstructural properties that predominantly determine the final extrinsic properties relevant to the application of functional or advanced ceramics. The interrelationship between chemical composition, microstructure, and functional properties is depicted in Figure 1.1. Unless otherwise noted, the reference for Section 1.1 is from Ref. [8].

Functional ceramics, often termed advanced ceramics, are the primary subject of this work. Significant emphasis has been placed on functional, or advanced ceramics, in the last 60 years. They differ from traditional ceramics in that they are designed around specific engineering applications. These design parameters involve careful tailoring of the fabrication of the material, from compositional selection to sintering routes, in order to optimize the desired bulk properties. Properties critical to engineering applications are highly dependent on the microstructure, and include dielectric permittivity [9], piezoelectric coefficients [10], mechanical hardness and yield strength [11], and a variety of others.

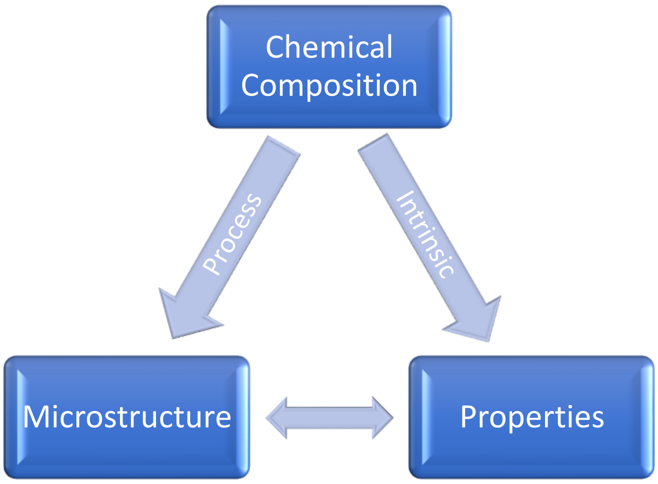

Figure 1.1: Summary of structure-property relationships in ceramics

Several fabrication methods are common to the processing of advanced ceramics. They include chemical vapor deposition, directed metal oxidation, reaction bonding, sol-gel processing, polymer pyrolysis, melt casting, and solid-state synthesis based methods. The latter will be discussed in detail because it was the method used to produce the materials discussed in this thesis.

Powder fabrication is the first step in assuring high quality functional ceramics. It is important to have high purity starting materials and methods that allow accurate measure of stoichiometry of the chemical composition when beginning powder production. A powder is shaped into what is termed a “green body” and then densified by sintering. The densification by sintering is sometimes preceded by a compaction step to assure homogeneous packing of the green body, and, thereby, a final homogeneously sintered ceramic body. As densification is a diffusion driven process, interdiffusion of chemical elements can create chemical inhomogeneities or even new phases during sintering. This is an important point for co-sintered ceramic/ceramic composites. Fabrication of ceramics from an assemblage of finely divided particles can be split into two methods: melt casting and firing of compacted powders. This work focuses on electroceramics produced from the latter, more widely used method.

The first step for producing high quality functional ceramics is the production of high quality powder. In perovskite electroceramics, the calcination route is employed, in which carbonates and oxides of the starting materials are heated to a temperature that induces release of carbons, resulting in a solid-state reaction that forms a solid oxide powder. Prior to calcination, the starting powders are homogenized in size through a comminution step, generally a size reduction by milling. This powder is then shaped and compacted by pressing, and then densified through solid-state sintering. The sample is heated to within 50-75% of its melting point, resulting in a joining together of the particles by necking, wherein the space between the particles is filled and the sintered body is densified. This process is depicted schematically in Figure

1.2. The driving force for sintering is the reduction of free energy at the surface of the consolidated particles. This reduction is achieved by atomic diffusion processes that involve either transport of atoms from the inside of the grains into the pores, termed densification, or rearrangement of the pore surface without a decrease in the pore volume, termed coarsening. Sintering can be seen as a competitive interaction between the processes of coarsening and densification.

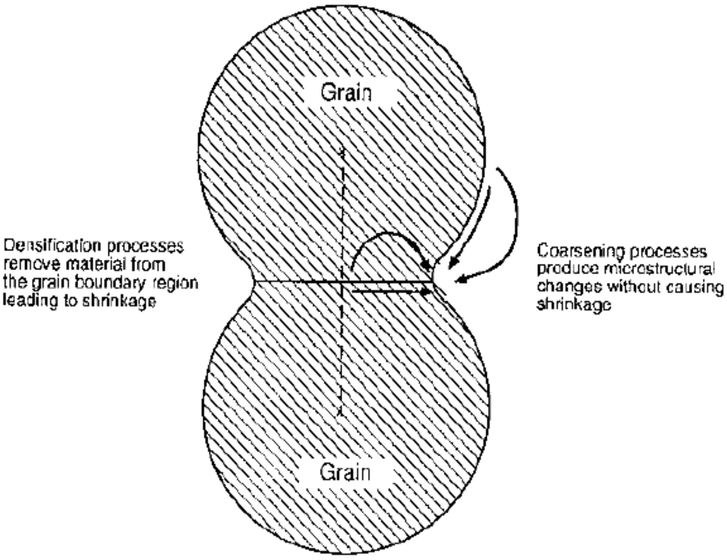

Figure 1.2: Mechanisms of densification and grain growth, from [9]

1.2. Electroceramics

Electroceramics are a subgroup of functional ceramics that are affected by the presence of an electrical field. The source for this discussion is “Electroceramics” by Moulson *et al.* [12], unless otherwise stated. As we approach the subject of ferroelectricity, we would be remised to not mention ferromagnetism, the phenomenon on which the understanding of ferroelectricity is based. One of the earliest examples of an electroceramic is lodestone, or magnetite (Fe_3O_4), which was first observed in the medieval period and considered useful for sorcery. An excellent example of this behavior can be observed not far from Darmstadt, at the Frankenstein castle, where a lodestone has supposedly served as a meeting point for witches for several centuries [13]. In its vicinity, compasses cannot function. However, with the addition of some ingenuity by modern-day engineers, this phenomenon has also been taken advantage of through its application in medicine, such as the Magnetic Resonance Imaging system, as well as water purification methods. An area of functional ceramics perhaps more relevant to the subject of the present dissertation is the use of ceramics for radio applications. This work focuses on the category of electroceramics that exhibit dielectric and ferroelectric behavior, for which a deeper discussion follows below.

1.3. Dielectrics

Dielectrics are a particularly relevant type of functional ceramic for the present study because the materials described in this work exhibit both dielectric and ferroelectric behavior. They are a class of insulators that respond to the presence of an electric field by a locally limited rearrangement of charges. All atoms undergo such a displacement in response to an electrical field due to the differential response of the positively charged nucleus and negatively charged electron cloud, *i.e.*, dipole formation. This electrically induced displacement results in the formation of dipoles, defined as two point charges of equal and opposite value with a certain distance x between them. While the local internal electric field may vary across the sample on the micro and nanometer length scale, over the bulk of a ceramic sample an average polarization can be found when sufficient dipoles are aligned in the same direction, resulting in a charge distribution that can be treated as a capacitance. A summary of the important features of dielectrics and subcategories thereof is provided in Figure 1.3, those subcategories of dielectrics pertaining to this work, *i.e.*, pyroelectrics, piezoelectrics and ferroelectrics, will be discussed in subsequent sections.

1.3.1. Polarization Response in Dielectrics

The discussion below is modified from Ref. [14] and is depicted in graphical form in Figure 1.4. The average electric field E over the volume of interest V is the sum of both external and internal electrical fields e(r) and is defined as

$$E = \frac{1}{V}\int dV\ e(r) \qquad 1.1$$

The macroscopic electric field caused by a uniform polarization is equal to the electric field in vacuum of a surface charge density on the surface of a body. This electrical field is compensated by an internal electrical field called the depolarization field, which is opposed to P, the polarization of the body induced by the applied electrical field. Therefore, the total electrical field on the specimen is the sum of the internal electrical field and the applied electrical field. The relationship between the induced polarization and the applied field depends linearly on the electrical susceptibility χ of the material. This intrinsic property can be temperature and frequency dependent.

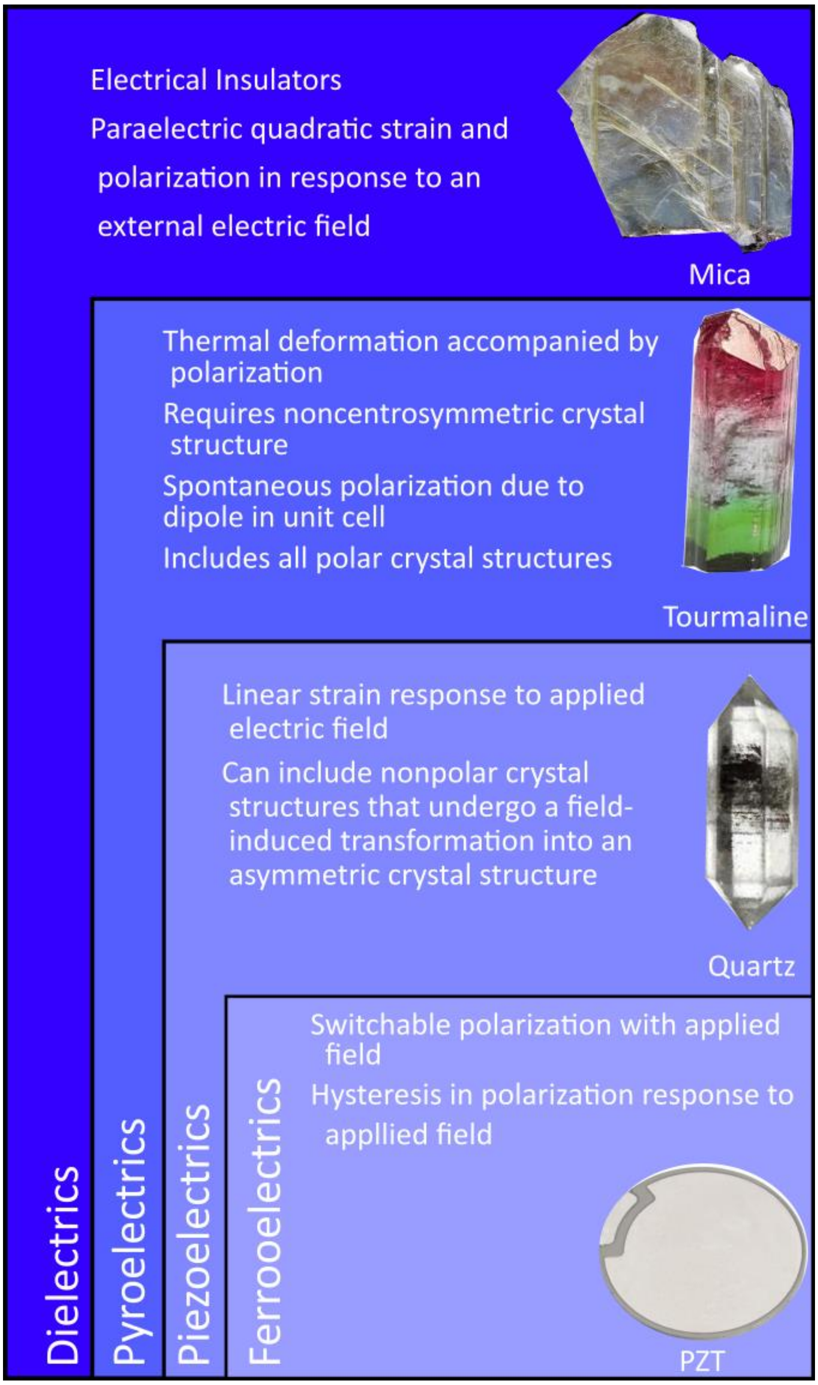

Figure 1.3: Dielectrics and subcategories thereof, including pyroelectrics, piezoelectrics, and ferroelectrics

The value of the local electric field that acts at the site of an atom is significantly different from the value of the macroscopic electrical field. Thus, the local field is not the same as the macroscopic average field E even in a uniform crystal lattice structure. The mechanism of polarization of a material is the formation of local dipoles in response to an electrical field. The polarization is defined as the dipole moment per unit volume, which can be written

$$P = \sum_{0}^{N} r_n q_n \tag{1.2}$$

where r_n is the position vector of the charge q_n, and the summation is from n=1 to n=N, where N is the number of dipole moments. The polarization therefore is greatest when charges are accumulated in a common position r. This accumulation is at its maximum in electrical dipoles. The electrical field generated by these dipoles at a distance can be calculated as

$$E(r) = \frac{3(P * r)r - r^2 P}{4\pi\epsilon_0 r^5} \tag{1.3}$$

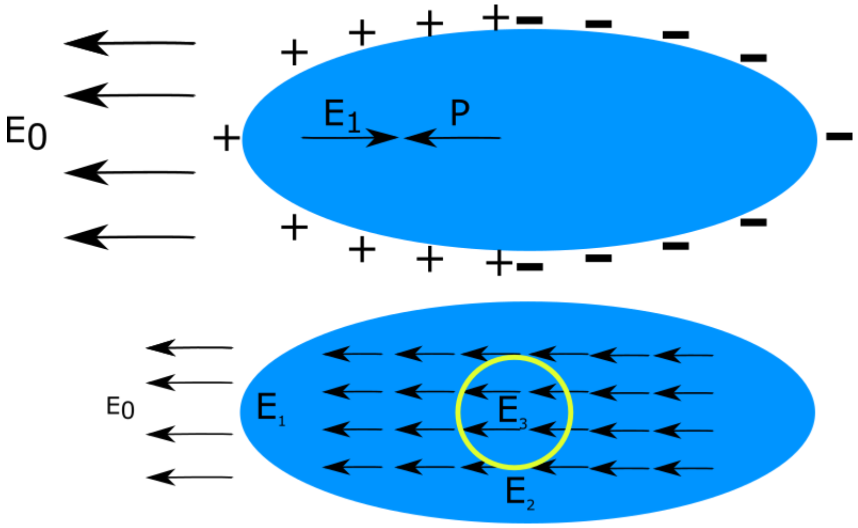

Figure 1.4: Polarization response to an applied electric field through the formation of internal fields, modified from [14]

As shown in Figure 1.4, the internal electrical field on an atom in the bulk material is the sum of the external applied field and the fields generated by the dipole moments formed from the applied electrical field surrounding that atom. This is calculated using a mathematical simplification that separates the dipoles generated by the applied field into three groups: the electrical field called the depolarization field from fixed charges on the surface of the body, neighboring dipoles lying within an imaginary sphere called the Lorenz cavity field and dipoles on the surface of the Lorenz cavity.

The Lorentz field due to the polarization charges on the surface of the Lorentz sphere can be calculated in terms of the polarization due to the applied electrical field. It is opposite the depolarization field.

$$E_{Lorentz1} = \frac{1}{3\epsilon_0} P \tag{1.4}$$

The Lorentz field due to dipoles within the Lorentz cavity depends on the crystal structure of the material. For a cubic system, the local field on a lattice site within the Lorentz sphere can be calculated using the Lorentz relation:

$$E_{local} = E + \frac{1}{3\epsilon_0} P \tag{1.5}$$

This relation states that the total electrical field acting on an atom in a cubic site is the macroscopic field E plus the field from the polarization of other atoms in the specimen. This is because the field within the sphere for a cubic system is zero when all the atoms are replaced by point dipoles parallel to each other.

Energy losses in real materials must also be considered in determining the polarization response of dielectrics. There will always be a lag between the applied electric field and the polarization response through the displacement D, which can be represented mathematically as

$$E = E_0 \, cos(\omega t) \qquad 1.6$$

$$D = D_0 \, cos(\omega t - \delta) \qquad 1.7$$

where δ represents the loss angle and ω represents the frequency. In the presence of dielectric losses, the permittivity becomes complex and can be represented as

$$\varepsilon = \varepsilon' - i\varepsilon'' \qquad 1.8$$

where ε' and ε'' represents the real and imaginary components of the permittivity, respectively. The loss angle can then be calculated as

$$\delta = tan^{-1}\left({}^{\varepsilon'}/_{\varepsilon''}\right) \qquad 1.9$$

However, loss tangent is generally reported without calculating the loss angle. The inverse of the loss tangent is called the quality factor, and is an important figure of merit in the use of dielectrics for radio frequency applications. Measurement of permittivity is performed by applying very low electric fields and determining the slope of the polarization to electric field, which is the value of the permittivity.

1.3.2. Equivalent Circuit Model of Dielectrics

Dielectrics are often treated as idealized capacitors with a zero resistance. This idealization, however, is rarely sufficient to describe the behavior of these materials. Therefore, it is convenient to incorporate their resistivity values into an equivalent circuit model. In so doing, the losses can also be accounted for. Such an equivalent circuit is shown in Figure 1.5.

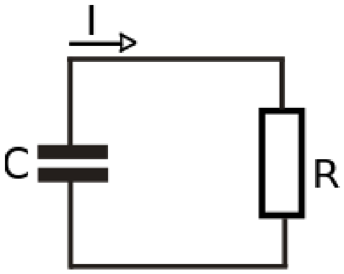

Figure 1.5: Equivalent circuit for dielectric materials

The resistance can be treated as

$$R = \frac{tan\,\delta}{\omega C} \tag{1.1}$$

and represents the dielectric loss that occurs as a result of the lag between the applied electric field and the resulting polarization. However, C is also dependent on the frequency. Capacitance can be mathematically defined as:

$$C = \frac{\varepsilon A}{h} \tag{1.2}$$

A being the sample area and h being the sample height. The relative permittivity is the ratio between the permittivity of the material and the permittivity of air, making this value is unitless. The permittivity is defined as

$$\varepsilon = \varepsilon_0(1 + \chi) \tag{1.3}$$

where ε_0 defines the permittivity of free space and χ is the electric susceptibility of the material. Permittivity is measured through the equivalent circuit model of a capacitor, where the charge across the capacitor and the geometry enable a determination of the permittivity, using the equation above.

1.3.3. Frequency Dependence of Dielectric Response

The bulk dielectric properties can be described in terms of an electric flux, or electric displacement D in response to an applied electric field, E, which induces a polarization, P, which can be further described mathematically by:

$$D = 4\pi P + E = \varepsilon E \tag{1.4}$$

where ε is the dielectric constant. In an anisotropic material, ε and therefore D must be treated as tensors. Considering the atomic level response to electric field, it becomes apparent that the bulk polarization response is a summation of the response of individual atoms in a crystal lattice to the applied field. In a single crystal, the effects are relatively straightforward to model. However, in bulk polycrystalline ceramics, the relationship between atomic level displacement and the bulk response is complicated by inhomogeneities within and between individual grains.

The net polarization of a dielectric includes contributions from several mechanisms. Electrical and ionic polarization contributions arise from the crystal lattice of the material, and are therefore termed intrinsic contributions. Domain wall, orientation and space-charge polarizations are extrinsic contributions to the total polarization. Each contribution responds to external electric fields on different time scales and, as a consequence, different frequency regimes, as shown in Figure 1.6.

Electronic polarization occurs in all dielectrics, and is based on the displacement of the negatively charged electron shell against the positively charged core. The electronic polarizability is generally temperature independent, and proportional to the volume of the electron shell. Therefore larger atoms have a larger electronic polarizability. The resonance of electronic polarization is in the petahertz frequency range.

Orientation polarization is a consequence of the alignment of permanent dipoles. An external electric field can generate a preferred orientation of the dipoles, which is disrupted by thermal energy. In ceramics, the frequency range for orientation polarization is in the 10^{-3} – 10^{6} Hz range.

Ionic polarization occurs in ionic crystals as a consequence of the displacement of positive and negative sublattices under an applied electric field above the megahertz range. The charge distribution arising from ionic and atomic displacement contributes to the charge from dipole displacement, and, therefore, increase the total charge measured across the sample. Therefore, measurements of permittivity are usually performed over a limited frequency range of 10^{4} Hz to limit the electrical interactions to ionic and electronic polarization.

At frequencies in the 10^{-3} Hz range, the influence of space-charge polarization due to Maxwell-Wagner interactions can be detected. Such interactions occur at the interface of two materials with different charge carrier relaxation times, and are usually related to chemical inhomogeneities [15]. Space-charge polarization can be distinguished from orientation polarization in that it is not temperature-dependent, whereas the dielectric response of orientation dipoles reduce with temperature.

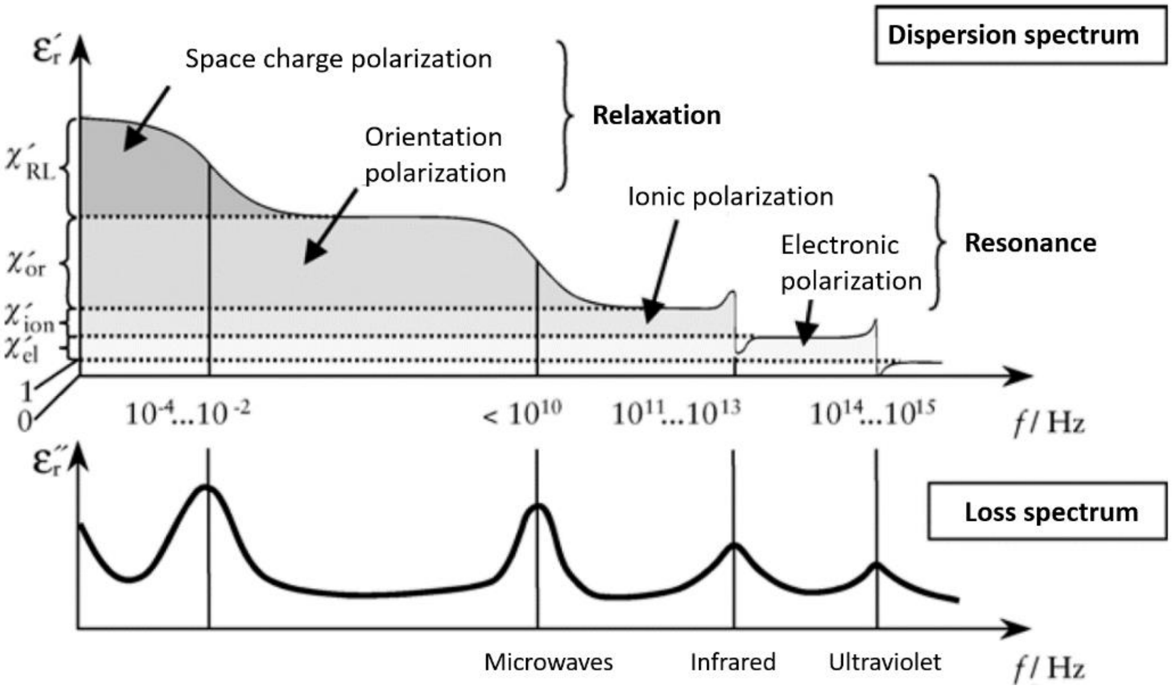

Figure 1.6: Dependence of dielectric response on frequency, with top panel showing permittivity and bottom panel showing dielectric loss, from [16]

The discussion below considers a largely simplified system in which the electric response is considered only in the range of a few unit cells of a dielectrically susceptible crystal lattice.

1.4. Crystallinity of Electroceramics

An asymmetric crystal structure is necessary for the formation of spontaneous polarization observed in piezoelectric materials. Of the 32 point groups describing all crystalline systems, 11 are centrosymmetric and, therefore, cannot be piezoelectric. All 21 other point groups do not have an inversion center and can therefore be piezoelectric, with the exception of the group 432 [16]. Of these 21 points groups, there are ten polar groups with a unique polar axis that can exhibit spontaneous polarization and are, therefore, ferroelectric. The precise point groups belonging to each category are outlined in Table 1.

For this work, the crystal structure utilized is predominantly perovskite, which at high symmetry is cubic but at lower symmetries transforms to an orthorhombic, rhombohedral, or tetragonal crystal structure. The prototypical perovskite unit cell structure is described by the expression ABO_3, possessing a center B-site cation, 8 corner A-site cations, and 6 face centered oxygen anions, and is shown schematically in Figure 1.7.

Table 1: Crystallographic point groups classification categorized by point groups with relationship to piezoelectric and ferroelectric behavior, modified from [17]. An asterisk is placed over the 432 point group to highlight that despite it being a non-centrosymmetric crystal structure, it is not piezoelectric

Crystal Class	Centro-symmetric point groups (not piezoelectric)*		Non-centrosymmetric point groups (piezoelectric)				
			Polar (ferroelectric)		Non-polar		
Cubic	$m\bar{3}$	$m\bar{3}m$	none		432*	$\bar{3}m$	23
Tetragonal	4 or m	4 or mmm	4	4mm	$\bar{4}$	$\bar{4}2m$	22
Orthorhombic	mmm		mm2		222		
Hexagonal	6 or m	6 or mmm	6	6mm	$\bar{6}$	$\bar{6}2m$	622
Trigonal	$\bar{3}$	$\bar{3}m$	3	3m	32		
Monoclinic	2 or m		2	m	None		
Triclinic	$\bar{1}$		1		None		

For a cubic lattice in the perovskite ABO_3 structure, the lattice constant a can be calculated as:

$$a = \sqrt{2}(r_A + r_O) = 2(r_B + r_O) \qquad 1.16$$

where r_A is the ionic radius of the A-site cation and r_B is the ionic radius of the B-site cation. Generally, this is calculated as the stoichiometric proportions added when mixing the chemicals randomly dispersed in a given material. Changes in lattice site occupancy can also change the level of symmetry in the crystal, which is reflected in a reduced Goldschmidt tolerance factor, expressed in the equation below:

$$t = \frac{r_A + r_O}{\sqrt{2(r_B + r_O)}} \qquad 1.10$$

A lower t value means a lower level of symmetry. A t value of 1 represents cubic symmetry, $0.71 < t < 0.9$ represents a tetragonal symmetry, and $t < 0.71$ is an orthorhombic or rhombohedral symmetry [18].

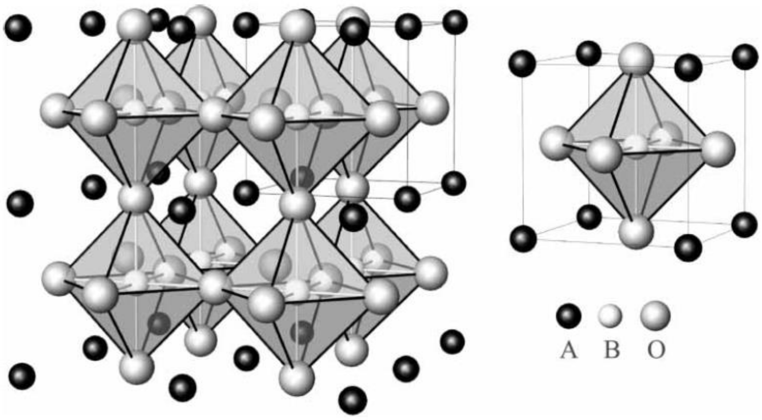

Figure 1.7: The ideal cubic perovskite structure. Large open circles denote the oxygen atoms, smaller open and solid circles denote the metal cations with A and B sites, respectively, from [19]

1.5. Pyroelectricity

Pyroelectrics are dielectrics in which the spatial charge distribution is affected by temperature. The first historic evidence of pyroelectricity was found in tourmaline, in which it was observed that a charge was created on opposite faces of the crystal during heating or cooling [20]. In a crystal system that possesses a unique polar axis, a permanent electric dipole is formed, which is equivalent to a spontaneous polarization, accompanied by a corresponding spontaneous strain. Spontaneous polarization can be defined as the centers of positive and negative charges being in different positions within the unit cell in the absence of any external field, resulting in a permanent dipole [21]. The bulk strain and polarization in pyroelectrics is the result of electrostriction, or the shift of charged ions in the lattice. Electrostrictive strain is characterized by a quadratic relationship with the applied field, as shown in the equation below, in non-tensor form:

$$S = dE + ME^2 \qquad 1.11$$

It should be noted that electrostriction occurs in all dielectric materials. In contrast, piezoelectric materials exhibit a linear response to an applied electric field, and is limited to materials with a unique polar axis.

1.6. Piezoelectricity

Piezoelectricity is defined as an electrical polarization produced by mechanical strain, the polarization response being proportional to the strain and changing sign with it. This phenomenon was first described by the Curie brothers in quartz through the observation that by applying mechanical stress to crystals that were formerly known to have a pyroelectric response, an electrical charge could be measured across the crystal [20]. They asserted, for the first time, that this behavior depends on an asymmetry in the crystal structure. The piezoelectric properties of a material can be described by the direct piezoelectric effect, wherein an applied mechanical stress results in a change in polarization

$$D_i = d_{ijk}\sigma_{jk} \tag{1.12}$$

where D is the electric displacement, and σ is the applied mechanical stress. It is a linear and reversible property, as shown in the equation below, describing the converse or indirect piezoelectric response:

$$S_{ij} = d_{kij}E_k \tag{1.13}$$

1.7. Ferroelectricity

1.7.1. Ferroelectric Domain Formation

If the dipole moment of the unit cell, (*i.e.*, spontaneous polarization), of a pyroelectric crystal can switch between at least two different orientations, the material is considered ferroelectric. Ferroelectric behavior was first observed in Rochelle Salt (sodium potassium tartrate tetrahydrate ($NaKC_4O_6.4H_2O$)) by J. Valasek in 1920 [22]. This behavior contrasts with that of a simple dielectric in that a long-range order of dipoles is formed due to the spontaneous polarization throughout the material and enhances the response to an applied external field. This long-range order results in a domain structure, which comprises regions with unit cells of equal spontaneous polarization, *i.e.*, dipoles, aligned in a single direction. To prevent energetically unfavorable surface charge accumulation, domains of opposite polarization direction are aligned next to each other, divided by a domain wall. A single grain can, therefore, have domains of different polarization, with clearly observable domain boundaries, termed domain walls. Domain walls have a width of a few unit cells, over which the polarization is gradually changed from domain to domain, resulting in an internal strain. The formation of domains with antiparallel polarizations is a mechanism of reducing the fringing electric field, as shown in Figure 1.8. This results in a mixed orientation consisting of a combination of the polarization directions, shown in the bottom of Figure 1.8. The angle between the polarization directions of domains depends on the crystal symmetry of the material. For a material with a tetragonal crystal structure, domains may be oriented 90° or 180° to each other. In a ferroelectric with extant domains, the application of a field first induces expansion of domains oriented parallel to the field, resulting in an increased net polarization aligned with the electric field. Beyond a threshold field, termed the coercive field (E_c), domain wall motion begins, meaning that domains aligned antiparallel to the field begin to switch polarization direction.

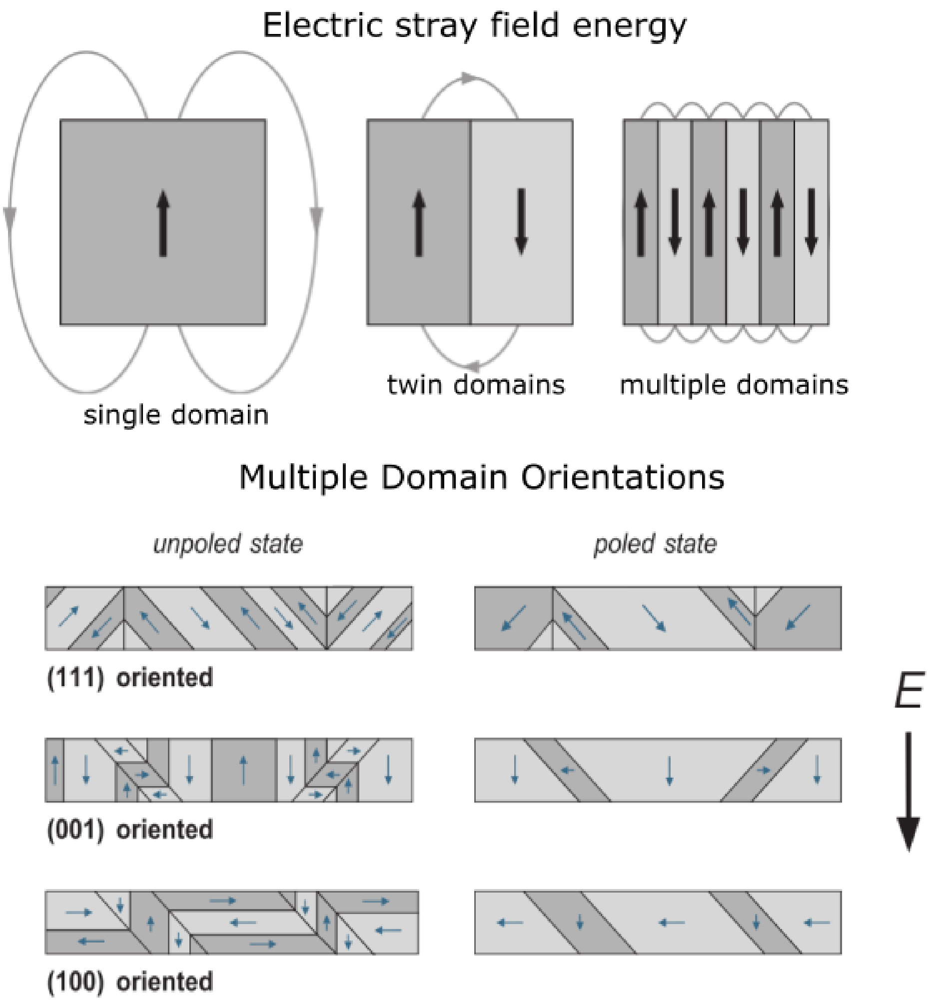

Figure 1.8: Depiction of optimized domain configuration mechanisms and influence of poling on polycrystalline ceramic domain orientation, modified from [21]

1.7.2. Ferroelectric Hysteresis

Ferroelectrics can also be distinguished from dielectrics by the hysteresis in the permittivity as a function of applied electric field, whereas a non-ferroelectric dielectric will not have such a hysteresis [16]. This phenomenon, first observed in Rochelle salts, is shown in Figure 1.9. Polarization can be calculated as a function of applied electric field using the equation below:

$$P = \epsilon_0 \chi E \qquad 1.14$$

where χ is the electric susceptibility of the material, and ε_0 is the permittivity of air. The measurable bulk polarization in ferroelectrics, as well as the hysteresis in its dielectric response, is associated with domain alignment parallel to the applied electric field.

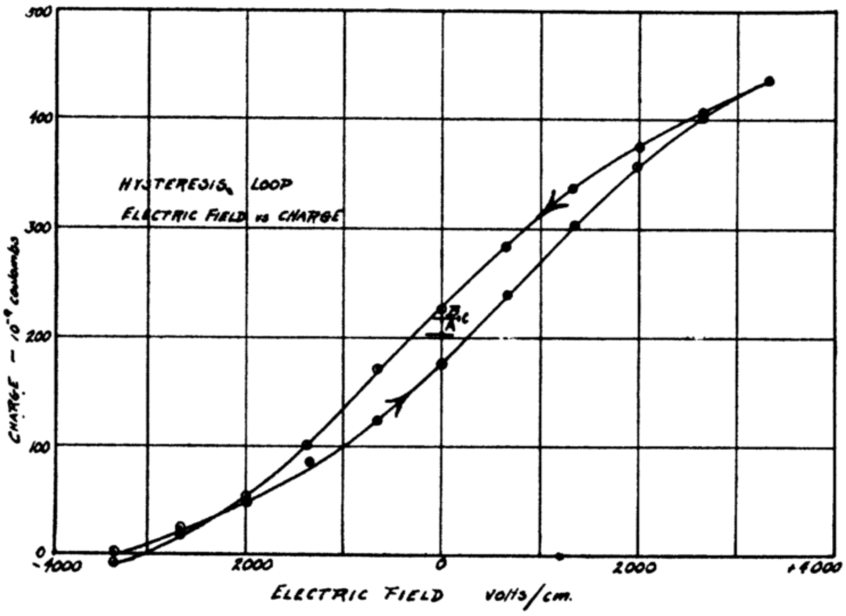

Figure 1.9: Dielectric charge as a function of electric field in Rochelle Salt, from [22]

The reorientation of domains results not only in a change in the bulk polarization of a ferroelectric, but also a mechanical strain. The electromechanical response of ferroelectrics is the result of two mechanisms that contribute to the electric-field-induced strain: an intrinsic and extrinsic contribution. The intrinsic contribution arises from lattice distortion as a result of the migration of the B-site cation, increasing the proximity of A and B-site cations and thereby increasing the repulsion between them. The extrinsic contribution is the result of non-180° domain wall motion, as 180° domain wall motion does not result in any measurable mechanical deformation.

The growth and orientation of domains under applied electric field is shown in Figure 1.10. In the unpoled state, denoted point (A) in Figure 1.10, a net zero polarization and strain will be observed in the material due to the randomness of the domain orientation. Upon application of an electric field, equal to or greater than the coercive field E_c, an eventual saturation of polarization is achieved, resulting in a coalescence of domains and strong favorability of the direction of domain orientation aligned with the applied field, as shown at point B in Figure 1.10. The strain and polarization response achieves a maximum positive value at this position as well. Upon removal of the field, as shown at point C in Figure 1.10, the domains are no longer completely uniformly aligned, but some domains remain oriented parallel to the previously applied field. This results in a measurable remanence in the strain and polarization. As the field is reduced to negative values, domains begin to switch to an orientation antiparallel to that shown in point B of Figure 1.10, but again with a strong favorability of domain orientation direction along the negative applied field. This in turn results in a maximum negative strain and polarization, as shown with point D of Figure 1.10. Upon increasing the electric field back up to a total zero field, some domains once again retain an orientation parallel to the last negative applied field, and this domain configuration is antiparallel to that of C.

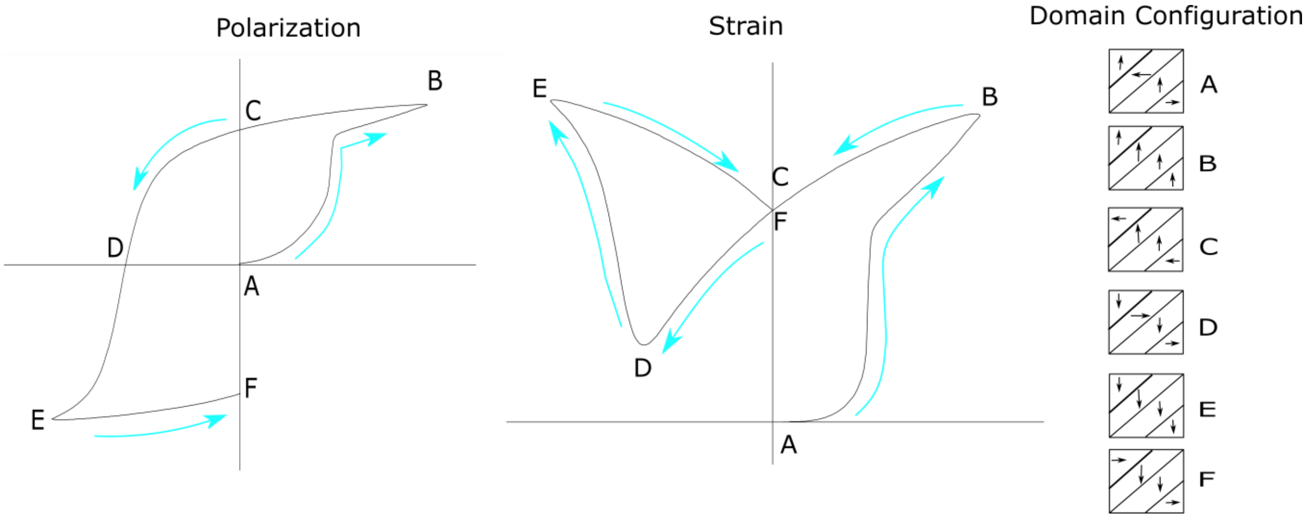

Figure 1.10: Schematic of polarization and strain response to applied electric field, with associated domain configurations (A): random orientation of unpoled polycrystalline ceramic (B) Domain growth along positive applied electric field (C) Remanent strain and polarization due to aligned domains remaining after removal of applied field (D) back-switching to random orientation of domains resulting in net zero polarization and a negative strain response (E) Domain growth along the negative applied electric field (F) Remanent strain and polarization due to remaining domains aligned along negative field direction after removal of field

An important parameter in the analysis of ferroelectric materials for electromechanical applications is the usable strain. It is defined as the difference between the remanent strain (at point C) and maximum strain under a positive electric field (at point B). This value is further used to define d_{33}^*, the large signal piezoelectric coefficient, which is the ratio of the usable strain to the maximum applied electric field.

1.7.3. Ferroelectric Temperature Dependence

Ferroelectrics are further characterized by their permittivity response as a function of temperature, which follows a so-called Curie-Weiss behavior

$$\varepsilon_r = \frac{C}{T - T_c} \qquad 1.15$$

where C is a material-dependent constant, T is the temperature, and T_c is the Curie-Weiss temperature.

Nonlinearities in permittivity as a function of temperature are often associated with changes in the crystal structure, as shown in Figure 1.11. These nonlinearities are associated with phase transitions in the crystal structure upon heating, which past the Curie-Weiss temperature results in a cubic, nonferroelectric lattice.

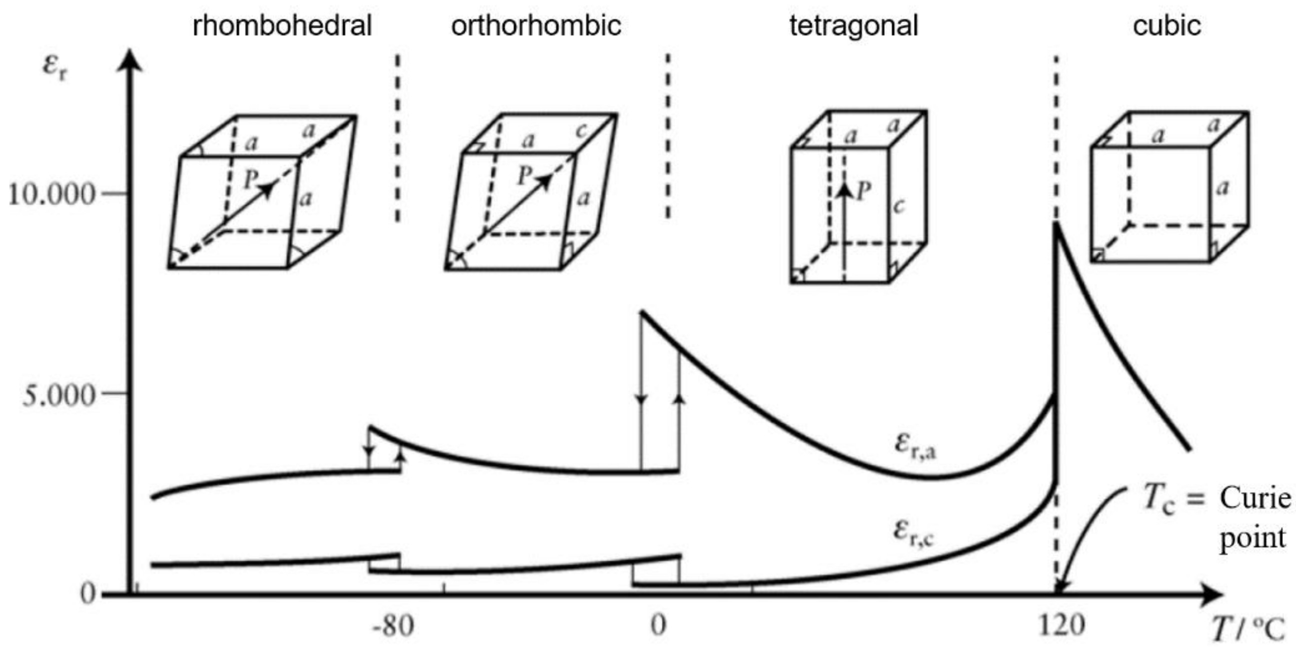

Figure 1.11: Temperature-dependent dielectric behavior as it relates to crystallographic phase transitions, modified from [16]

1.8. Relaxors

Relaxor ferroelectrics have a perovskite structure of ABO_3 as is the case with other ferroelectric materials [23]. However, the structure is considered complex due to disorder in the arrangement of different cations on crystallographically equivalent sites. As a result, complex ferroelectrics display some distortion of the perovskite structure, through a variety of mechanisms including octahedral tiliting and formation of lower-symmetry variants such as the tetragonal and rhombohedral crystal structure. This also implies that the bond length in a relaxor is random, which has further implications for its response to temperature and electric field. At a specific composition, termed the morphotropic phase boundary, or MPB, a peak in the dielectric and ferroelectric response can often be observed [24], [25]. The MPB composition also corresponds to the composition at which a mixed crystalline phase can be observed [26], [27].

In addition to lattice distortion, disorder in the crystal structure gives rise to random fields, due to the random positioning of A- or B-site cations. This can result in a highly polarizable cubic matrix in which dipole moments are embedded. When coupled, such dipole moments form a region of local polarization, and, due to their length-scale, are termed polar nanoregions (PNRs).

In terms of bulk dielectric behavior, relaxors are characterized by a distinctive permittivity curve which has a broad temperature-dependent peak indicating a diffuse phase transition, and high frequency dispersion of the temperature-dependent permittivity at temperatures below the phase transition temperature, as opposed to the behavior of ferroelectrics that have a sharp drop in polarization [28].

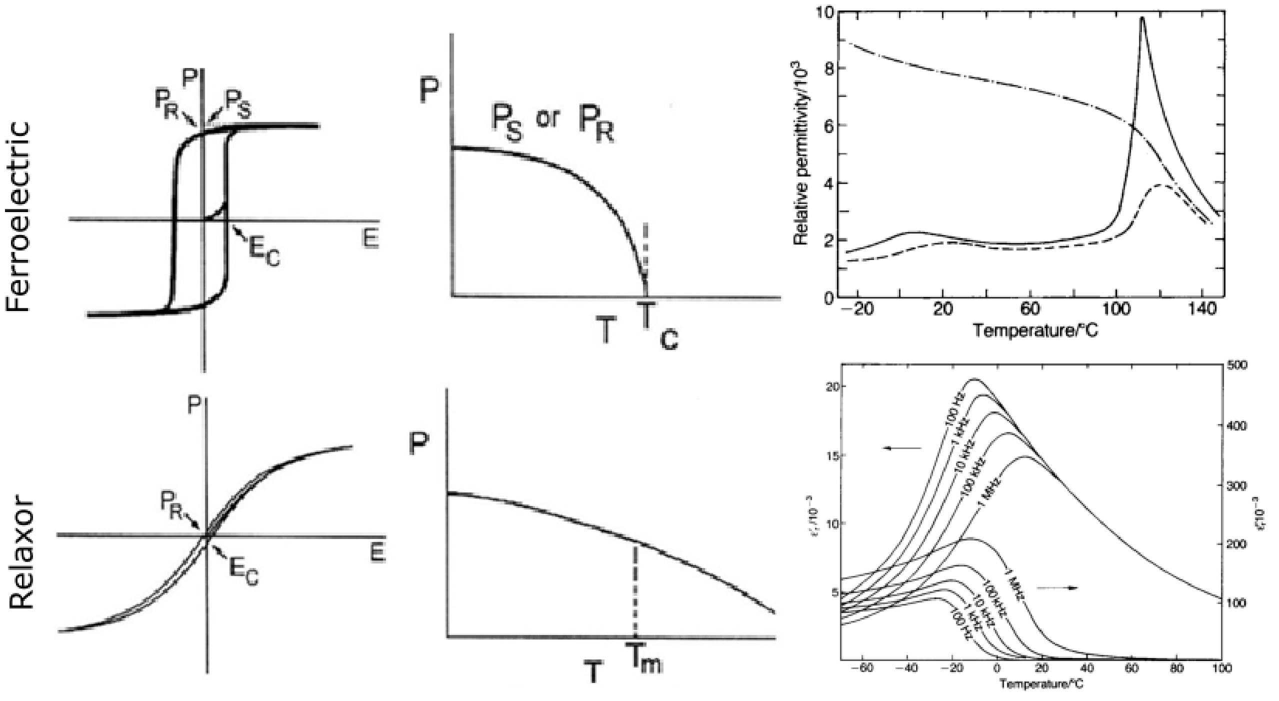

Figure 1.12: Comparison of the dielectric and ferroelectric behavior between classic ferroelectrics and relaxors, from left to right, a narrow polarization loop as compared to ferroelectrics, a broad temperature-dependent transition of the polarization state in relaxors as compared to a sharp one at T_c in ferroelectrics, and temperature-dependent permittivity, modified from [12]

In the simplest case, there are several equivalent orientations of the dipole in a dielectric [19]. Where there is no dipole-dipole interaction, this results in a single relaxation time. With increasing disorder in the lattice, an increase in the distribution of the relaxation time can be observed through measurement of dielectric permittivity as a function of frequency.

The correlation length of dipoles is inversely proportional to temperature. Consequently, polar nanoregions can be observed at high temperatures, whereas with decreasing temperature, these polar nanoregions coalesce into microscopic domains of aligned polarization orientation [29]. Upon further decrease of temperature, the domains permeate the sample and a long-range ferroelectric order is established in the sample. The reverse is also true: upon increasing temperature, the long-range ferroelectric order can be disrupted. The temperature at which a long-range ferroelectric order is disrupted is termed the depoling temperature, or T_d. This temperature is generally defined as the temperature at which the piezoelectric coefficient is reduced to half of its original value [30]. Instead of a Curie temperature above which no domains can be observed, a transition from noncentro-symmetric to cubic phase occurs over a broad temperature range. The temperature at which dipoles reduce their mobility and begin to form PNRs is termed the Burns temperature, T_B, [31], [32], as shown in Figure 1.13.

Several models have been used to explain this behavior. The first model was that of a smeared phase transition in which a superposition of multiple critical phase transitions with slightly different phase transition temperatures, due to the chemical disorder of the perovskite structure [33]. PNRs were first discussed in relaxor materials as an explanation for optical birefringence at low temperature by Burns and Scott, in whose name the temperature at which PNR behavior becomes significant, was named [32]. The explanation of PNRs for the dependence of optical refractive index on temperature was based on the fact that the deviation of the refractive index from a linear behavior is proportional to the square of the local spontaneous polarization, averaged over a suitable length and time scale. The higher the deviation from linear behavior, the larger the local spontaneous polarization. It is important to note that the transition described here is not a structural one in terms of crystallography, but rather a change in the order of the sample from long-range to short-range. A glassy transition model based on dipolar glass proposes a freezing temperature at which PNRs become less mobile [31]. Finally, the random field model proposes a real temperature-induced phase transition from the paraelectric to the ferroelectric phase and introduces a long-range order between PNRs [34]. Depending on the properties being measured, (electrical, mechanical, or optical), the temperature at which the dissolution of PNRs, T_B, can be observed varies significantly. Therefore, T_B is not considered a phase transition temperature.

Many relaxors undergo a phase change to long-range ferroelectric order upon application of an electric field. The mechanism by which this occurs is still under investigation, but it is established that PNRs align and grow parallel to the direction of an applied electric field. Under a sufficiently high field, the PNRs coalesce into aligned domains [35].

1.8.1. Ergodic and Nonergodic Relaxors

Relaxors can be classified into two categories based on statistical physics, which divides systems into ergodic (ER) and non-ergodic (NR) behaviors. An ergodic system is one in which the temporal and spatial average is equal to zero, and consequently a nonergodic system can be described as one in which the temporal and spatial average is nonzero. ER systems in solid-state physics were first described in magnetic spin glasses, where a strong correlation between chemical disorder and ergodicity was observed [36]. The ergodicity of the strain and polarization response to an applied electric field is apparent in the absence of a remanent strain and polarization upon removal of the field. Increasing complexity of the perovskite through multiple occupancies of A-site and B-site cations has been shown to increase the chemical disorder of the system, and result in an ergodic strain and polarization response to an applied electric field. Those ergodic relaxors used in this study are described in greater detail in the literature review.

The ER and NR state of a relaxor are strongly temperature-dependent, and the same material may be in a NR state at low temperatures and an ER state at higher temperatures. This is shown schematically in Figure 1.13. Above $T_{B,}$ the permittivity follows a Curie-Weiss behavior. Below T_B, a transformation to an ergodic relaxor phase takes place, whose primary mechanism is the development of randomly orientated and freely rotating PNRs. An ergodic relaxor phase is characterized by a reversal to the initial state of lowest free energy after removal an external field. Cooling further below T_B results in an increase in the size and number of PNRs, which also begin to slow down. Canonical relaxors, shown in Figure 1.13 (a), are characterized by a freezing temperature T_f at which the PNRs become frozen into an irreversible or nonergodic state. The dielectric behavior between the temperature of maximum permittivity (T_m) and T_f is characterized by a high degree of frequency dispersion in the temperature dependence dielectric constant. The dielectric peak is typically of the same order of magnitude as the Curie point in ordinary ferroelectrics but differs from them in that it is highly diffuse and its temperature is strongly frequency dependent.

A schematic of the formation of PNRs as a function of temperature in NR and ER relaxors is shown in Figure 1.14, based on impedance spectroscopy data [38] and *in-situ* transmission electron microscopy (TEM) [39] of NR and ER relaxors. In an NR relaxor, PNRs undergo a NR to ER transition at T_f. From T_f to T_m, low temperature PNRs dominate the material. The main contribution to the permittivity arises from relaxation of LT-PNRs. Above T_m, the PNRs transform to high temperature PNRs with a tetragonal symmetry. Further increasing the temperature results in only PNRs of tetragonal symmetry. In an ER relaxor, on the other hand, the T_f shifts to much lower temperatures, resulting in a broader temperature range in which the ER phase is present. The phase transition from LT-PNRs to HT-PNRs contributes less to the permittivity in ER relaxors because the overall density of PNRs is reduced. PNRs are destabilized and the transition from an ER phase to the paraelectric phase, (*i.e.,* T_B), occurs at a lower temperature than in the NR relaxor.

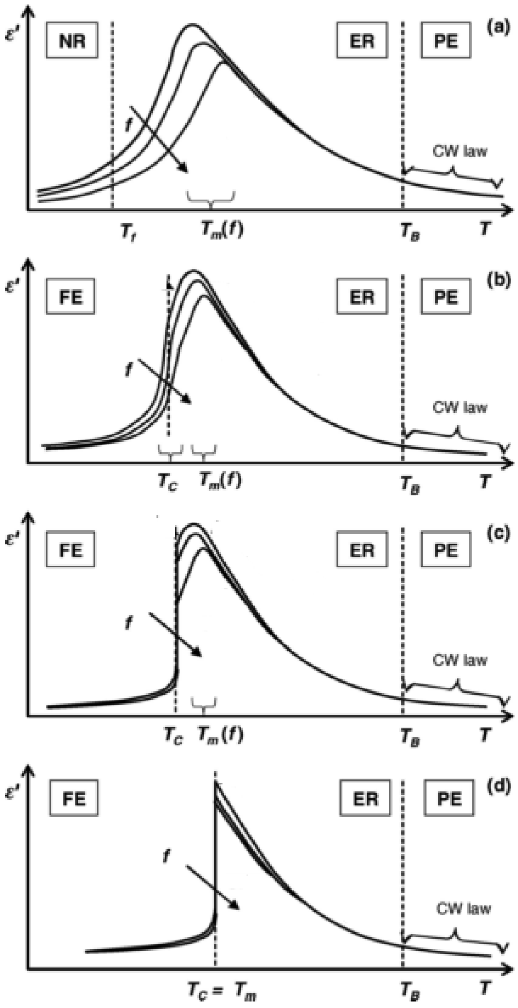

Figure 1.13: Temperature evolution of dielectric and structural properties in relaxor materials (a) canonical relaxor (b) diffuse relaor to ferroelectric phase transition at $T_C<T_m$ (c) crystal with sharp relaxor-to-ferroelectric transition at $T_C<T_{ma}$ (d) crystal with sharp relaxor-to-ferroelectric transition at $T_C=T_m$. The temperature dependence of the dielectric constant at different frequencies is shown, and the temperature intervals governed by the Curie-Weiss law. PE indicates a paraelectric phase, NR indicates a nonergodic relaxor, ER is an ergodic relaxor and FE is a ferroelectric phase, modified from [37]

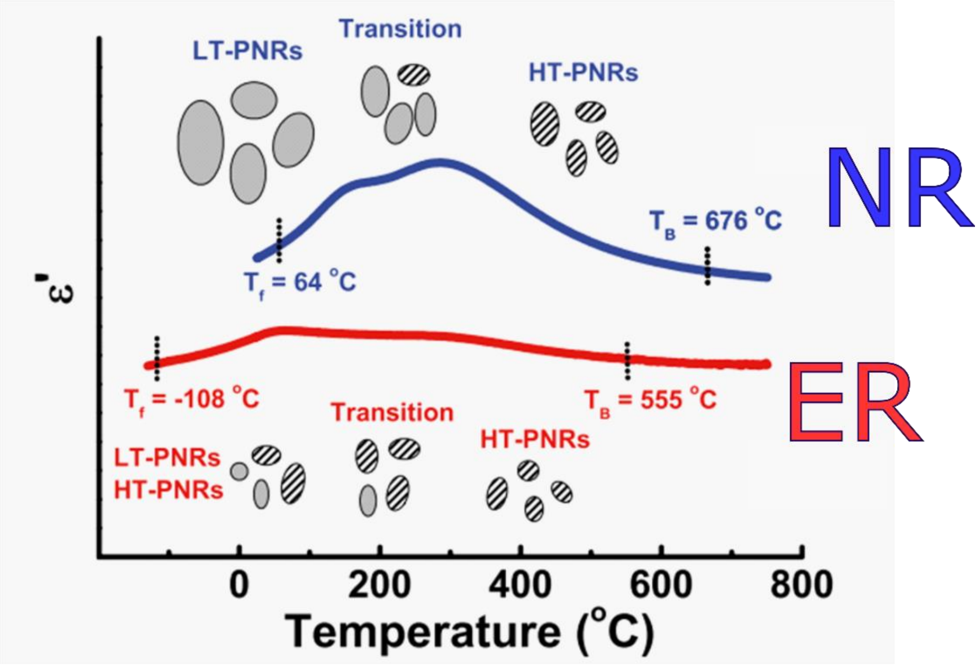

Figure 1.14: Schematic of thermal evolution of PNRs in ergodic and nonergodic relaxors and their contributions to the dielectric constant, modified from [38]

1.9. Ferroelasticity

A material is ferroelastic if it has two or more stable and energetically equivalent orientation states that can be switched back and forth through the application of a mechanical stress [40], [41]. Ferroelasticity was first recognized by Aizu, who described it as analogous to ferroelectricity due to the hysteresis of its response to mechanical stress, where mechanical stress and strain in a ferroelastic correspond to electric field and polarization in a ferroelectric [42]. In the ferroelastic case, the spontaneous polarization that is reoriented results in a measurable change in mechanical strain, whereas in the ferroelectric case, as discussed above, the reorientation of the spontaneous polarization with applied electric field results in a measurable polarization as well as a strain. Ferroelasticity is often coupled with other phenomenon, such as ferroelectricity [43]. This interrelationship is important to bear in mind when considering the interaction of ferroelectric materials with residual stresses, such as composites [44].

One of the first full hysteresis loops in terms of a stress-strain curve demonstrating ferroelasticity was in $Pb_3(PO_4)_2$ [45]. This was attributed to the displacement of Pb in response to mechanical stress, as shown in Figure 1.15. This experiment was able to show a full hysteresis loop can be observed because both tensile and compressive stresses could be successfully applied on the material. Most ceramics, however, can only be measured under a compressive stress, and therefore result in measurements resembling those shown in Figure 1.16.

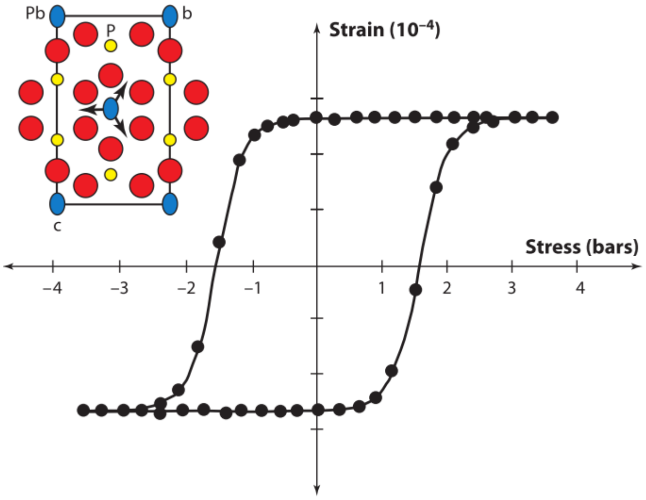

Figure 1.15: Mechanical hysteresis in $Pb_3(PO_4)_2$ *with applied uniaxial stress, one of the first recorded measurements of ferroelastic behavior [41]*

Mechanical stress can also induce domain alignment, as shown in Figure 1.16. The initial strain state is 0, which corresponds to a random orientation of domains. As the stress is increased on the sample, from Figure 1.16 A to B, the domains begin to reorient and those domains aligned perpendicular to the direction of stress grow preferentially. At the maximum stress, point B in Figure 1.16, the domains are aligned in one direction, which often corresponds to a maximum strain. In poled samples, *i.e.*, those in which a domain formation has been induced, a measurable change in polarization can also be observed during application of mechanical stress, indicative of domain switching. The stress-strain relationship is nonlinear and hysteretic, and therefore not a purely elastic deformation. From B to C in Figure 1.16, the stress is reduced and results in some domain reorientation. However, some domains remain oriented parallel to the applied stress, accompanied by an observable remanence in the strain after removal of the field.

There are several characteristic parameters of the ferroelastic response: maximum strain, hysteresis, remanent strain and back-switching. The parameters of maximum strain and remanent strain are found at points B and C of Figure 1.16 respectively. Hysteresis is defined as the area enclosed by the stress-strain curve, and is representative of a nonlinear stress-induced state change. This state change in relaxors is interpreted to be the growth and alignment of PNRs along the direction of the applied field, up to a coercive stress where domains are formed [47]. Back-switching provides an indication of internal stresses that counter the applied mechanical compressive stress, and is calculated by the formula below:

$$\%\ of\ Back - switching = \left(1 - {}^{\varepsilon_{rem}}/_{\varepsilon_{ideal}}\right) \times 100\% \qquad (1.16)$$

The ideal remanent strain is determined by projecting a tangent line from the top of the curve to the x-axis. The x-axis intercept of this tangent line is considered the ideal remanent strain under the condition of no back-switching. The difference between the ideal and actual remanent strain is generally attributed to domain orientation reversal due to electrical and mechanical fields that overcome the applied compressive stress, thereby "back-switching" some domains to their original configuration during unloading [46].

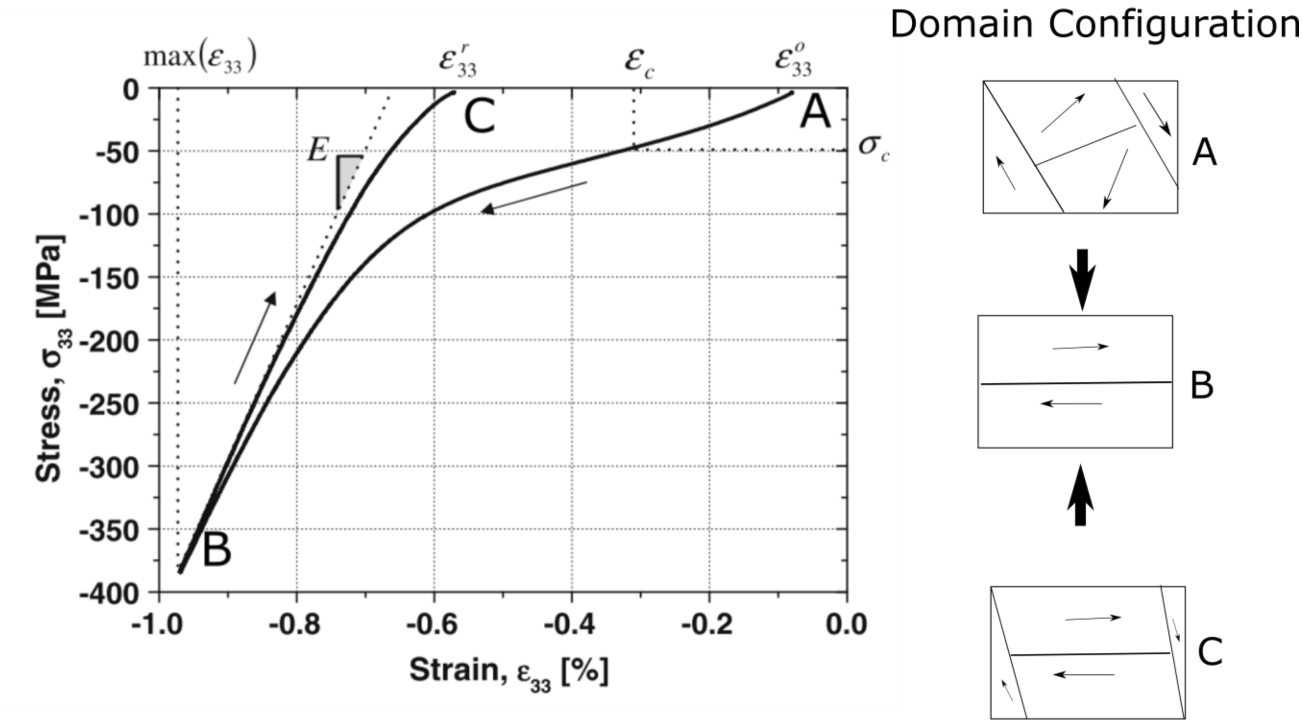

Figure 1.16: Domain orientation under applied stress, depicting the ferroelastic behavior of PZT, modified from [46].

2. Literature Review

Having addressed the fundamental physics governing the phenomenology of ferroelectrics and piezoelectrics that arise as a result of ferroelectricity, it is now important to understand the path by which novel materials have developed. This chapter will provide an overview of the lead-based materials used currently used for piezoelectric applications in engineering, followed by an in-depth examination of $Bi_{0.5}N_{0.5}TiO_4$ (BNT)-based piezoceramics that have been proposed as lead-free alternatives.

2.1. Lead-Based Ferroelectrics

Lead zirconate titanate ($Pb(Zr,Ti)O_3$, PZT) is the predominant material used for the majority of piezoelectric applications. PZT has a perovskite crystal structure with Ti on the B-site and Pb and Zr on the A-sites. It was first reported as a solid-state solution in 1952, and as a useful piezotransducer in 1954 [48]. It supplanted $BaTiO_3$ (BT) as a ferroelectric because of its piezoelectric coefficient of 600 pC/N [49] (a significantly higher value than BT's 190 pC/N) [50], higher Curie temperature of 350 °C as compared to 130 °C in BT, (enabling greater thermal stability), and ease of synthesis due to lower sintering temperatures and flexibility of the formation of solid-state solutions with other compounds [49].

The properties of PZT were shown to be highly tunable through the addition of isovalent and aliovalent dopants. Aliovalent dopants can be further divided into donors and acceptors. Dopants are termed donors when they result in vacancies in the A or B site, due to the excess positive charge that is balanced by the vacancy formation. In order to balance the excess positive charge, a decrease in oxygen vacancy concentration also occurs in donor dopants. Acceptor dopants, which are more negatively charged than the original element, result in the formation of oxygen vacancies to maintain charge neutrality. An example of a donor dopant is the addition of lanthanum to PZT, resulting in a relaxor with a cubic structure at room temperature, undergoing a field-induced ferroelectric state upon application of an external electric field. PLZT has a reduced coercive field, increased dielectric constant, and mechanical compliance, as well as the interesting optical property of transparency [51]. This phenomenon is not common to ceramics, and was discovered in the late 1960s. Relative to $BaTiO_3$, it has a much higher piezoelectric coupling factor k_p of 0.72 as compared to 0.35 [52].

$Pb(Mg_{1/3}Nb_{2/3})O_3$ (PMN) was the first relaxor discovered in the 1960s in its single crystal form, and developed as a polycrystalline ceramic in the 1980s [33]. Its relaxor nature was attributed to the fact that the Mn and Nb cations both occupy the B-site in a disordered manner, resulting in frequency dispersion due to varying sizes of dipoles formed in the presence of random electric fields. It is often used as a solid-state solution with lead titanate (PT, $PbTiO_3$) in order to increase the thermal stability of the relaxor phase [37] . PMN can be transformed into a ferroelectric through the application of an electric field, as well as by the addition of PT. Giant ferroelectric and dielectric responses have been observed at the morphotropic phase boundary between the rhombohedral and tetragonal phases of PMN-PT, which occurs at 45% PT [53]. In addition, there is a critical electric field at which the properties of PMN-PT are enhanced and the energy required to undergo the phase transition is reduced, as evidenced by the reduction of latent heat during relaxation. PMN's dielectric behavior is considered analogous to that of a spin-glass with polarization fluctuations, attributed to polarization rotations between [111] variants of the rhombohedral crystal structure [54]. These fluctuations require a certain activation energy and influence the dipole-dipole interactions that lead to the formation of PNRs. The frequency dependence of the temperature at which maximum permittivity is observed is explained by the fact that higher frequencies are not able to switch the larger clusters, which means that the activation energy is higher and this energy barrier is overcome through higher kinetic energy available at higher temperatures.

2.2. Lead-Free Ferroelectrics

Lead-free ferroelectric materials were developed in response to legislation limiting the use of lead in electronic applications in primarily the European Union and Asia [55]. Several alternatives have been investigated, including solid-state solutions of $Bi_{0.5}Na_{0.5}TiO_3$ (BNT), $BaTiO_3$ (BT), and $K_xNa_{1-x}NbO_3$ (KNN), [49], [56]–[58]. This section will detail the development of these materials and their unique properties as singular materials and as solid-state solutions with each other. A summary of the large signal electromechanical response of the three materials listed above is shown in Figure 2.1.

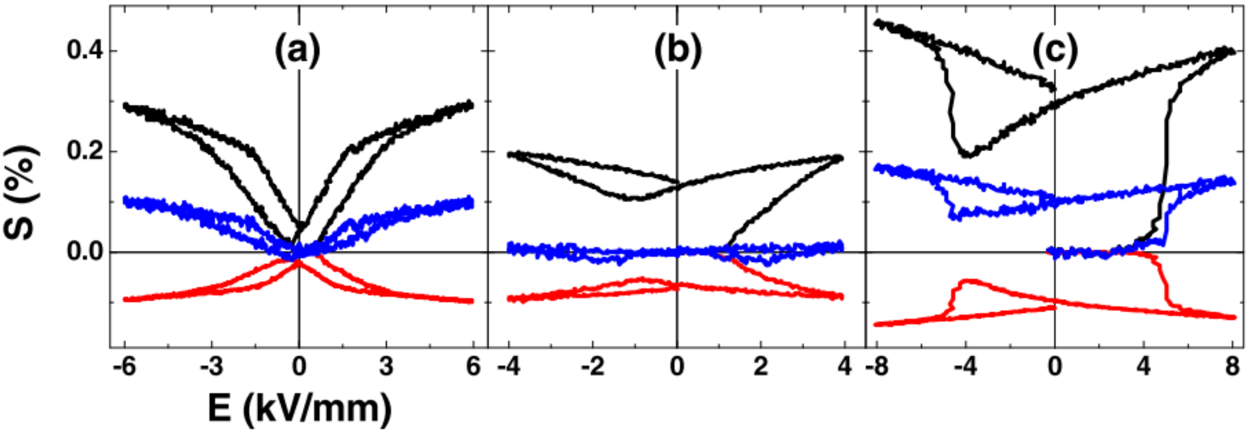

Figure 2.1: Electric-field-induced strains of (a) BT, (b) KNN, and (c) BNT with the associated volume change, measured during bipolar poling cycle at 50 mHz. Black represents the longitudinal strain, red represents the transverse strain and blue represents the total volume change determined from the transverse and longitudinal strains. Note that the maximum electric field applied for BNT is larger at 8 kV/mm than that of BT or KNN [59].

One of the first examples of tailoring of chemical composition for the enhancement of electrical behavior in functional ceramics is the development of BT as a dielectric capacitor. This was achieved simultaneously in the Soviet Union by Goldman and Wul, in Japan by Ogawa and Waku and in the United States by Wainer and Thielke [60]. It was observed that with the addition of barium, the crystal structure of titanate is modified to a perovskite. Rzhanov *et al.* state that the dielectric permittivity of modified titanates is increased in comparison to pure titanate due to the compositionally driven crystallographic phase transition from a centro-symmetric crystal structures to a perovskite crystal [61]. The dielectric permittivity was also shown to increase with an increased ionic radius of the rare-earth metal inclusions. However, the permittivity of BT is an order of magnitude larger than other titanates, such as calcium titanate and strontium titanate, which also have perovskite structures. Wul proposed that this sharp increase was because BT was the only perovskite in which the distance between the Ti and oxygen was greater than the sum of their radii. BT also displayed a characteristic temperature dependence of its permittivity and a significant hysteresis in its dielectric behavior, leading to its implementation as a ferroelectric. Rzhanov observed that the presence of impurities in the starting powders resulted in a perovskite structure, and the synthesis of BT from chemically pure starting components rendered the final material non-ferroelectric [61]. XRD results indicated that the undoped BT was rhombohedral in crystal structure, while carefully controlled doping with 2 mol % aluminum or 5 mol % strontium resulted in a tetragonal crystal structure. The latter two compositions also showed a significantly higher dielectric constant, as compared to the undoped BT. The conclusion of this work was that BT when produced from technical raw powder, without absolute purity, includes naturally occurring dopants and is therefore always perovskite and ferroelectric. This was also the first hint of a complex perovskite structure, in which the lattice sites were not homogeneously occupied by the same element, as the low amounts of dopants (or impurities) made a homogeneous distribution thereof unlikely.

The dielectric and ferroelectric properties of BT are strongly temperature-dependent. To better understand the underlying physical mechanism, Megaw proved the existence of a first order phase transition with temperature, by performing temperature-dependent X-ray diffraction. These transitions had previously been predicted by the Landau-Devonshire-Ginzburg thermodynamic model of ferroelectric phenomena. Megaw proposed that the high dielectric permittivity observed at the Curie temperature of 110 °C was due to the coexistence of low symmetry crystallographic phases, resulting in strain due to lattice mismatch, which enhanced the dipole formation of BT crystals [62].

Further work on titanates led to the discovery of BNT by Smolenskii *et al.* in 1960 [33]. BNT was initially proposed to have a rhombohedral crystal structure. However, significant asymmetry has been observed in its crystal structure pointing to an asymmetry in bond length between Bi-O and Na-O, indicating that Bi^{3+} is heavily under-bonded in the average rhombohedral structure. This suggests a monoclinic crystal structure [63]. Transmission electron microscopy (TEM) investigations of BNT by Dorcet and Trolliard revealed two types of ferroelectric domains characterized by interface boundaries due to differences in tilt angle [64]. This investigation also revealed tetragonal platelets embedded within an *R*3*c* structure, which impede the relaxation process. The tetragonal platelets, due to their nanometer dimensions, may be connected to the formation of polar nanoregions in relaxors. This structure is in contrast to that of PMN, in which no such octahedral tilting has been observed. Further investigations of the temperature-dependent behavior of BNT by *in-situ* TEM revealed that with increasing temperature the antiphase octahedral tilting of the rhombohedral phase reduced, eventually giving rise to the in-phase octahedral tilt position typical of a tetragonal phase.

A solid solution of BNT and BT, known as BNT-BT, was first developed by Takenaka *et al.*, and demonstrated superior piezoelectric properties ascribed to a rhombohedral to tetragonal phase transition when the composition is between 6 and 7 mol% BT [65]. BNT is rhombohedral at room temperature, whereas a solid solution with BT results in the presence of a tetragonal phase. A key feature in its electromechanical response is its high remanent polarization of approximately 30 μC/cm^2 and remanent strain of 0.15% (depending on frequency), upon removal of an applied field higher than the coercive field. This remanence has been observed both under mechanical stress and electrical fields and has been attributed to an irreversible field-induced phase transition from pseudocubic to tetragonal symmetry. Pure BNT also has a very high coercive field of 7.3 kV/mm, and the addition of BT has been shown to reduce it [65], [66]. In the compositional range between approximately 5 and 8 mol% BT, a morphotropic phase boundary has been observed with transmission electron microscopy by Ma *et al.* [67]. At these compositions, certain piezoelectric and ferroelectric properties were optimized, such as a lower coercive field and higher piezoelectric coefficient d_{33}. In this region, unpoled NBT-BT appears pseudocubic in XRD studies by Daniels *et al.* [68] with a lack of domain structure when observed through TEM by Ma *et al.* [69]. Above 8 mol% BT content there is an increase in peak splitting at the (200) reflection, indicative of an increased tetragonal phase with increasing BT content, [70], [71] which has been confirmed by Xu *et al*. [72]. This also corresponds to the formation of a visible domain structures. A temperature and composition phase diagram summarizing these structure-property relationships in BNT-BT is shown in Figure 2.2.

The structure of BNT-BT depends not only on composition but also temperature. The rhombohedral/tetragonal morphotropic phase boundary occurs at a lower BT content with elevated temperature, and above 110 °C begins to show “antiferroelectric” behavior. A maximum in its piezoelectric properties such as d_{33} and d_{33}^* can also be observed at this composition and temperature range.

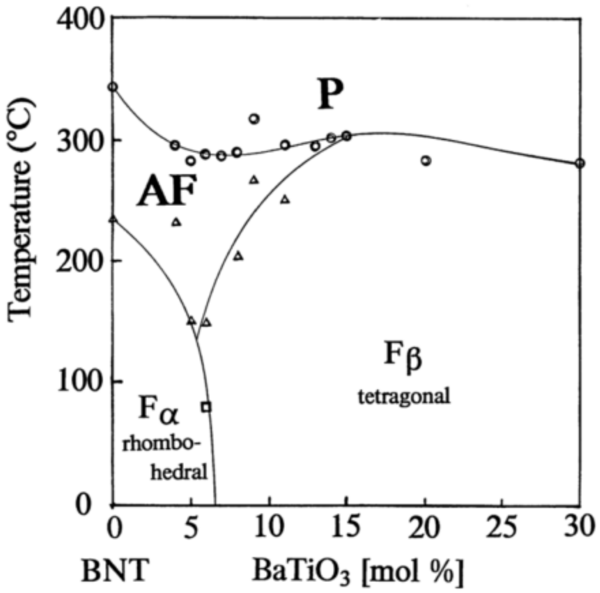

Figure 2.2: Phase diagram of BNT-BT as a function of composition and temperature, from [65].

Evidence of BNT-BT compositions near the MPB undergoing an electric field-induced transition from a pseudo cubic to a tetragonal symmetry has been obtained using *in-situ* X-ray diffraction. Unlike the electric field-induced electromechanical response in PZT materials, which has been attributed to ferroelectric domain switching processes [73], [74], the lead-free BNT-BT system exhibits a relaxor-to-ferroelectric (RE-FE) transition through the application of electrical [75] and mechanical fields [76]. These transitions can result in large remanent strain and polarization values, which have been attributed to the coalescence of the local polar nanoregions into a long-range ferroelectric order [77]. Daniels *et al.* showed with electric field-dependent synchrotron that the electric-field-induced phase transition in polycrystalline NBT-7BT is caused by a distortion of the pseudocubic structure, followed by a pseudocubic→tetragonal transition [78]. Similarly, Ma *et al*. showed using *in-situ* TEM that there is a partial, but irreversible, transformation of *P*4*bm* relaxor nanodomains to *P*4*mm* ferroelectric lamellar domains as the electric field is loaded from 0 → 2.5 kV/mm in unpoled NBT-7BT [79]. Upon further increase of the electric field, the RE phase completely vanishes and a new *P*4*mm* → *R*3*c* (FE-FE) transition can be observed. Analogously, Schader *et al*. observed a similar RE-FE transition upon the application of a compressive stress; *in-situ* stress-dependent synchrotron measurements revealed a pseudocubic to mixed rhombohedral-tetragonal structure transition [76]. Groszewicz *et al.* observed, through NMR investigations, that there is a coexistence of a cubic and polar phase in unpoled MPB NBT-BT, supporting the description of polar nanoregions embedded in a cubic nonpolar matrix [80]. Upon application of an electric field, the cubic matrix becomes polarized and adopts the local structure of nearby PNRs, resulting in a ferroelectric response to electric field.

BNT has also been adjusted chemically through the substitution of potassium as an A-site cation, $Bi_{0.5}(Na_{1-x}K_x)_{0.5}TiO_3$ (BNKT). This composition can be considered a binary solid-state solution of BNT and BKT, and was first discovered by Elkechai *et al.* in 1996 [81]. It was observed that an optimum in ferroelectric properties occurred at 0.78BNT-0.22BKT. At room temperature, as discussed above, BNT is rhombohedral, whereas BKT is tetragonal [82], with larger lattice parameters. Predictably, BNKT can be divided into two phases, a rhombohedral phase on the sodium-rich side and a tetragonal phase on the potassium-rich side. Because K has a slightly larger ionic radius (1.64 Å in K as compared to 1.39 Å in Na) [83], the lattice parameters increase with increasing BKT content. This increase leads to the formation of a tetragonal crystal structure [84]. Two compositions below the MPB were found to have rhombohedral structure, while the MPB composition of BNKT22 showed a tetragonal crystal structure. Although all three compositions showed a similar macroscopic strain response, there were significant differences in the microscopic origin of the strain. Under applied electric field the rhombohedral compositions undergo a lattice strain and domain switching without a phase transformation, whereas the MPB composition shows, in addition to intrinsic lattice strain and domain switching, an electric-field-induced phase transition from tetragonal to mixed-phase rhombohedral and tetragonal symmetries. More recent work by Khansur *et al.* has also shown the electric field dependence of crystal structure in this material system [85].

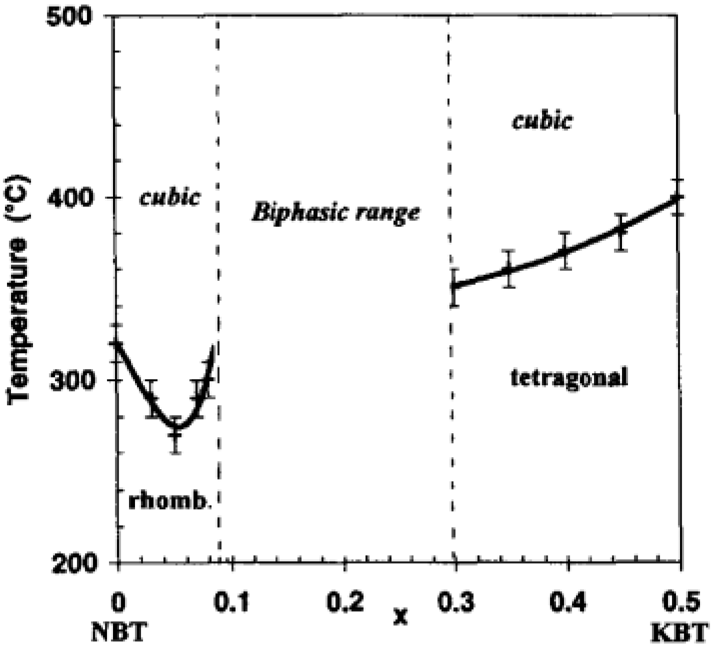

Figure 2.3: Phase diagram of BNKT as a function of composition and temperature [81].

The three compositions studied by Khansur *et al.* [85] fall under the biphasic range of the phase diagram developed by Elkechai *et al.* [81], shown in Figure 2.3. It appears that they undergo an electric field dependant transition from tetragonal to rhombohedral. TEM investigations of BNKT under applied electric field have also revealed mechanisms of the evolution of electromehanical response in this system [86]. Quadrant-like domains with submicron length polar lamellar subdomains as substructures were revealed by TEM in this system. However, no subdomain heirarchical structures have been observed in pure BNT, indicating that this structure depends on the effect of BKT on the crystal structure and domain formation. These structures have been labelled polar nanotwins, and consist of small polar lamellar sub-domains stacked along the (001) plane, with a rhombohedral (*R3c*) phase. These subdomains self-assemble into a quandrant oriented along the (110) plane corresponding to the tetragonal *P*4*bm* phase. As shown in Figure 2.4, selected area electron diffraction (SAED) reveals a dominance of the *R*3*c* phase by the high intensity of the integral (oee) and (oeo) peaks, however the superlattice reflections of the *R*3*c* phase are also detectable (highlighted with yellow circles). The fine lamellar polar domains consist of many nanometer scale oxygen tilt nonpolar domains in which the *P*4*bm* and *R*3*c* phases coexist. Increasing BKT content resulted in an increase in the size of the subdomains, corresponding to an evolution of the polar nanoregions from an average *R*3*c* phase to a *P*4*bm* phase. Further investigations of BNKT as a function of potassium concentration were performed by Levin *et al.* in which a clear MPB was observed at 0.2BKT content [26].

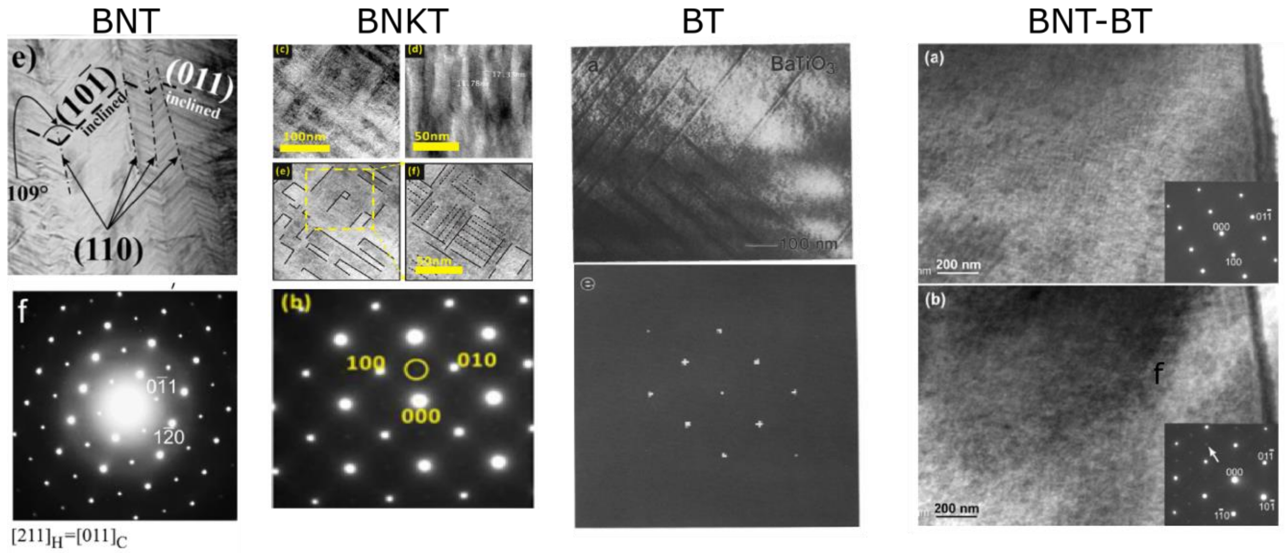

R3C , with tetragonal 001 oriented platelets coexistence of contrasting octahedral tilt systems

Subdomain heirarchical structures comprised of polar nanotwins with tetragonal structure but surrounded by a rhombohedral domain

90° domain walls and a tetragonal domain structure

Relaxor nanodomains with a mix of tetragonal and rhombohedral symmetries, converts to domains with tetragonal crystal structure upon application of electric field

Figure 2.4: TEM and SAED of relaxor ferroelectrics and the relevant structural information derived thereof, in BNT [87], BNKT [88], BT [89], and BNT-BT [69]

Another family of lead-free ferroelectrics that has shown significant promise in replacing PZT is based on potassium sodium niobate ($(K_xNa_{1-x})NbO_3$), (KNN). KNN was first discovered by Egerton and Dillon in 1959 [90] for use in ultrasonic delay lines. This system is orthorhombic at room temperature, and undergoes an orthorhombic to tetragonal phase transition above 200 °C [91], [92]. Above 400 °C, KNN becomes cubic and displays paraelectric behavior [91], [93]. On cooling from room temperature, KNN undergoes an orthorhombic to rhombohedral phase transition [94]. Dopants and modifications to synthesis routes have resulted in significant enhancement of its ferroelectric and electromechanical properties [95]. For instance, template growth of KNN doped with Li and Sb has resulted in a large and small signal piezoelectric constant, as well as temperature stability, comparable to that of PZT [96].

2.2.1. BNT-BT-KNN

BNT-BT and KNN were combined into a ternary solid-state solution by Zhang *et al.* to form BNT-BT-KNN [97]. The objective was to substitute a small portion of the rhombohedral BNT with orthorhombic KNN, thereby inducing a chemical disorder that would increase the ergodicity of the system. In so doing, remanent strain and polarization would be reduced, thereby increasing the usable strain. In addition to being useful as an actuator material, it was found that the addition of KNN to BNT-BT resulted in a temperature stable permittivity up to 300 °C, rendering it suitable for use as a high-temperature dielectric [98]. It was also observed that varying the BT content in BNT-BT-KNN changed both the microstructure and the electromechanical response. By way of example, a comparison of BNT-5BT-2KNN and BNT-7BT-2KNN shows that the higher BT content results in a d_{33}^{*} value of 469 pm/V versus 269 pm/V [99]. To better investigate the effect of KNN content on the structure and field-induced phase transitions, Daniels *et al.* used a stoichiometrically graded sample that contained compositions across the ternary phase diagram of BNT-BT and BNT-BT-KNN [78]. These investigations revealed that the addition of KNN results in a reduced lattice parameter, easily attributed to the smaller ionic radius of K^+ and Na^+ relative to Ba^{2+}, all of which occupy the A-site in the perovskite unit cell. Furthermore, with increasing KNN content, the electric-field-induced pseudocubic to tetragonal phase transition occurs at higher electric fields. TEM investigations of BNT-BT-KNN by Kleebe and Schmidt showed a core-shell structure in the grains, with a primarily tetragonal phase in the core and a mixed rhombohedral and tetragonal phase in the shell, as shown in Figure 2.6 [100]. Upon application of an electric field, lamellar domain formation is observed [101]. The rhombohedral domains were hypothesized to act as nucleation sites for electric-field-induced phase transformations to the ferroelectric state. PFM investigations revealed that increasing KNN content in BNT-BT disrupted electric field-induced long-range order, as shown in Figure 2.5.

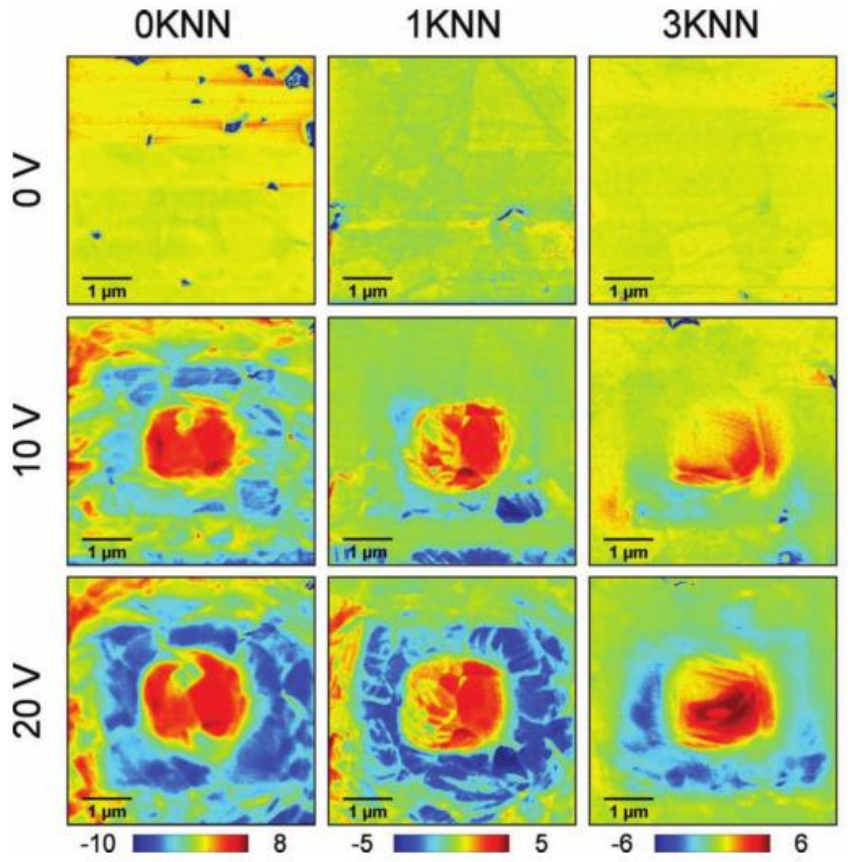

Figure 2.5: PFM investigations of field-induced polarization response in BNT-BT and BNT-BT-KNN [96]

2.2.2. BNT-ST

A binary solid-state solution of BNT and strontium titanate ($SrTiO_3$, ST) was first synthesized in 1974 by Sakata and Masuda [102], who investigated the addition of ST to BNT as a means of reducing the phase transition temperature. A morphotropic phase boundary between a rhombohedral ferroelectric and a pseudocubic or tetragonal phase with paraelectric behavior was observed in the range of 26-28 at. % ST [103]. This system has also shown ergodicity in its electromechanical response. In the MPB composition of 25 at. % ST, it undergoes a relaxor-to-ferroelectric phase transition at 3 kV/mm [104]. BNT-ST also exhibits a core-shell structure, both chemically and structurally (see Figure 2.6). The core is comprised of a strontium-depleted tetragonal phase, whereas the shell is a strontium rich rhombohedral phase [105]. This chemical and structural disorder is believed to contribute to its ergodicity, as *in-situ* TEM investigations have revealed that in the virgin unpoled state, domain contrast can be observed in the core, whereas the shell has a homogeneous contrast [105]. Upon application of an electrical field, the domain walls within the core reoriented, but no core growth was observed. Instead, the contrast in the shell became heterogeneous, but no clear domain patterns could be observed. In the SAED pattern, the intensity of the ½ *ooe* superstructure reflections reduced upon application of the field, in both the core and the shell, rendering a structural comparison between the two components challenging. The d_{33}^{*} increases with increasing ST content up to 28 at. % [103], [106].

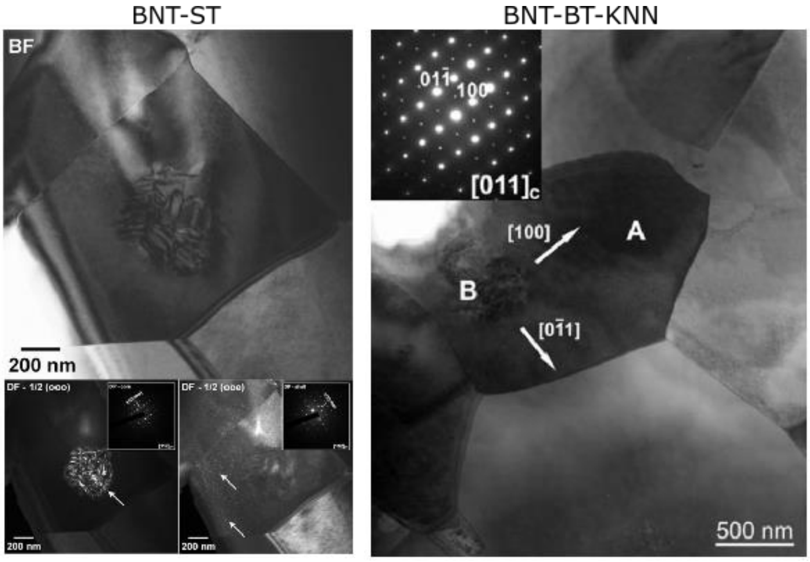

Figure 2.6: BNT-ST and BNT-BT-KNN core-shell structure, from [105] and [100] respectively

2.2.3. BNKT-BA

A binary solution of $BiAlO_3$ (BA) and BNKT has also been demonstrated to be an ergodic relaxor. The additional BA phase was first produced in a ferroelectric form by Zylberberg *et al*. [107]. A solid solution with the composition (1-x)$Bi_{0.5}(Na_{0.75}K_{0.25})TiO_3$–x$BiAlO_3$ was first reported by Ullah *et al*. [108]. Narrow polarization hysteresis loops indicated that the addition of BA significantly disrupts the ferroelectric order of the BNKT ceramics, resulting in an enhancement of the unipolar strain and a reduction of the remanent strain. For x=0.025, a composition close to the tetragonal-pseudocubic phase boundary, a large electric-field-induced strain of 0.29% and a large signal piezoelectric coefficient d_{33}^{*} of 484 pm/V were observed, suggesting that the (1-x)$Bi_{0.5}(Na_{0.75}K_{0.25})TiO_3$–x$BiAlO_3$ is a promising candidate for lead-free actuator systems. The electromechanical properties of this binary solid solution are shown to be highly dependent on composition: increasing the potassium concentration also disrupted the ferroelectric order, resulting in increased ergodicity [109]. The same work showed that changes to composition also affected the grain size and crystal symmetry, with increasing K content resulting in higher amounts of high symmetry tetragonal phase and a reduced, more rectangular grain morphology. The structure and electromechanical properties of BNKT-BA are also profoundly affected by the BA content: increasing BA content showed a shift of the XRD pattern to lower angles, indicating a higher unit cell volume, as well as a slight increase in grain size and a higher proportion of sharp rectangular edges of grains [110]. Diffuse phase transitions at T_d and T_m became more pronounced with increasing BA content as well. The ferroelectric properties also varied significantly as a function of BA content, with the remanent polarization initially increasing when up to 2 mol % of BA was added to BNKT-

BA, above which the remanent polarization fell to nearly zero. Further work showed that a high (>5 mol %) BA content results in an ergodicity in the strain hysteresis loops as well [108].

2.3. Ferroelectric Composites

Although existing BNT-based materials have shown promising electromechanical behavior, they typically require large electrical fields, up to 8kV/mm, and display significant hysteresis during actuation, which can lead to self-heating and possible component failure [97], [111]. In addition, due to the nature of the large strain response, the electromechanical properties are temperature-dependent, showing a maximum in the vicinity of the ferroelectric-relaxor transition temperature ($T_{F\text{-}R}$). Therefore, a number of recent studies have addressed these points; in particular ceramic-ceramic composite structures have been implemented to decrease the required external poling field [1], [7], [112].

A brief introduction to composite theory is necessary prior to discussion of ceramic/ceramic composites studied here. Composites have a variety of structures, whose nomenclature was established by Newnham in 1986 [113]. The nomenclature for different composite structures is based on the dimensions of self-connectedness between the components of each phase. Each phase in a composite can be self-connected in zero, one, two or three dimensions. In a diphasic, (two phase) composite, there are ten connectivity patterns used to describe the tensor properties of diphasic composites: 0-0, 1-0, 2-0, 3-0, 1-1, 2-1, 3-1, 2-2, 2-3, and 3-3. A figure depicting these connectivity patterns according to Newnham is shown in Figure 2.7. Processing considerations determine which composite structures are used with greater regularity. 0-3 composites are produced easily by tumble mixing, whereas 2-2 composites can be easily produced by laminating films manufactured with tape casting. These are produced either with alternating layers of metallic electrodes and ceramics or alternating layers of ceramics of different compositions, known as multi-composition multilayer systems [114]. A good example of this structure is the multilayer ceramic capacitor, for which the method of tape casting was developed [115]. Howatt *et al*. were the first to produce multilayer ceramic capacitors through tape casting [116], using this method to produce a multilayer TiO_2 ceramic capacitor.

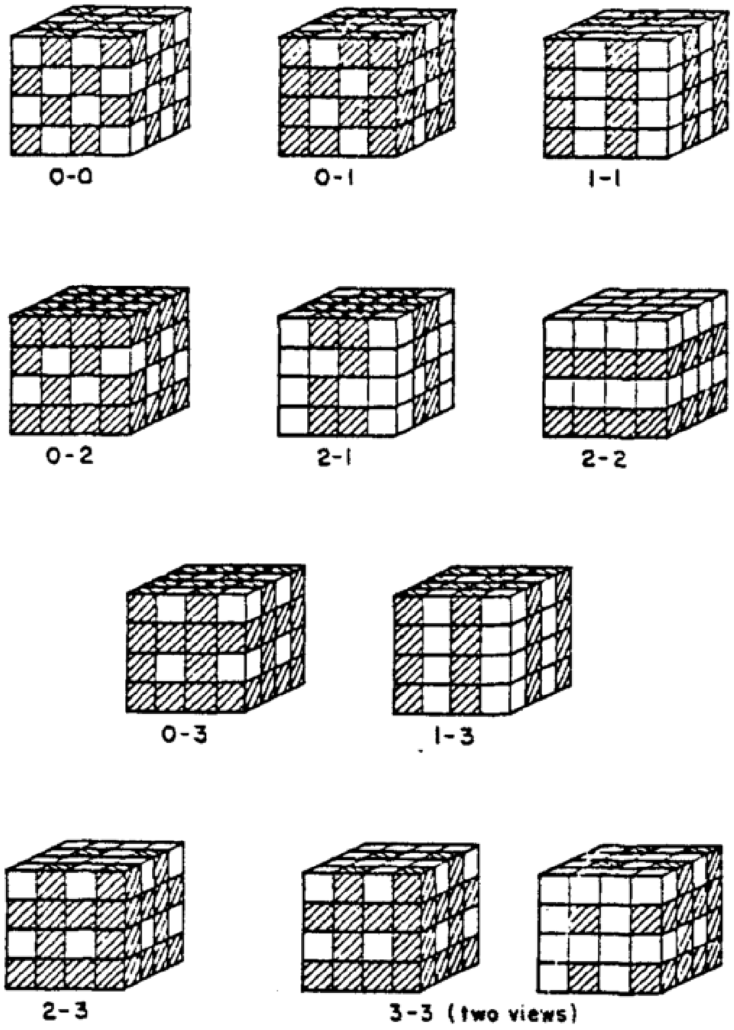

Figure 2.7: Composite structures and nomenclature from [117]

Composite formation results in a change of properties, which are either a sum property or a product property. A sum property is based on the rule of mixtures, for example, where the combination of materials with different Young's moduli result in a final material system with a Young's modulus that is the average of its components. The rule of mixtures approximation is the simplest method of predicting composite behavior. It is described mathematically in the equation below, X being the value of the property being determined, *e.g.*, permittivity, maximum strain or polarization, or remanence:

$$X_t = V_f^s \times X_s + V_f^M \times X_M \tag{2.1}$$

where the total composite property value is determined by the products of the volume fraction of each component ($V_f^{Component}$) and that component's property value (X). A product property is more complex, and has been defined as a result of force interaction between phases of a system, such as a magnetostrictive strain in one component resulting in an internal electric field in a piezoelectric component. It utilizes different properties in the two phases of a composite to produce a third property through the interaction of two phases. In some cases, a product property is found in a composite that is entirely absent in composite constituents. This was observed, for instance, in composites of piezoelectric PZT and magnestrotictive Ni-ferrite, resulting in a magnetoelectric material [118].

Effective medium approximations can be used to predict the properties of composites based on the proportion of the constituents and their properties and provide insight into the product properties of composites. The Bruggeman model is one such approximation, used for describing inclusions within a matrix, and can account for inclusions of varying shapes, from spherical to elliptical [119]. The Maxwell-Gartner approximation is used for composites in which the inclusions are physically separated at a minimum distance from each other and is, therefore, more appropriate for composites with a low volume fraction of inclusions [120] [121].

A simple rule of mixtures approximation was used to formulate the predicted value in this work because the assumptions of the effective medium approximations are violated in the 2-2 composite, which, as stated above, is based on inclusions having a 0-3 connectivity. This approximation assumes no interaction between the ferroelectric seed inclusions, contrary to the Bruggeman and Maxwell-Gartner approximations.

Recent advances in thin film fabrication have opened new avenues for producing piezoelectric and ferroelectric materials. Thin film deposition techniques such as physical vapor deposition, pulsed laser deposition, chemical vapor deposition, and molecular beam epitaxy have enabled the fabrication of films approaching the nanoscale. This has opened new sets of questions about the influence of internal stresses on ferroelectric and piezoelectric phenomena, particularly at the nano and microscale. Although this is not the primary focus of this work, a brief outline of recent advances in the field of ferroelectric thin film composites is warranted, as it provides insight into the phenomena affecting 2-2 ceramic/ceramic composites.

Nath *et al.* produced multilayer thin films of $BaSrTiO_3$ with three distinct compositional layers by metal organic solution deposition, including three post-deposition annealing steps at 750 °C [122]. The average piezoresponse of the multilayer sample exceeded a homogeneous sample by up to 50%. Such an improvement was predicted by Ban *et al.* in this system and was attributed to the presence of internal stresses from variation of the lattice parameter within the compositionally graded sample [123]. The distribution of polarization across the multilayer was modeled using the equation below:

$$A\frac{d^2P}{dz^2} = \bar{\alpha}P + \bar{\beta}P^3 + \gamma P^5 \tag{2.1}$$

where A, $\bar{\alpha}$ and $\bar{\beta}$ are position and composition dependent expansion coefficients. In the case where a thermal or mechanical gradient is applied across a compositionally homogeneous sample, a similar model is used wherein the expansion coefficients are determined in a slightly different manner. The three different methods of obtaining the polarization gradient and their influence on the net polarization as a function of position are shown in Figure 2.8.

In addition, thin films of single compositions have shown significant changes in dielectric and ferroelectric behavior. For instance, ST was shown to be a ferroelectric at room temperature when deposited as a thin film, despite the fact that as a ceramic it is cubic and predominantly isotropic [125], [126]. Thin films of BT showed an increase of the Curie temperature by 500 °C relative to BT single crystals, which was attributed in large part to the biaxial stresses generated during thin film fabrication [127].

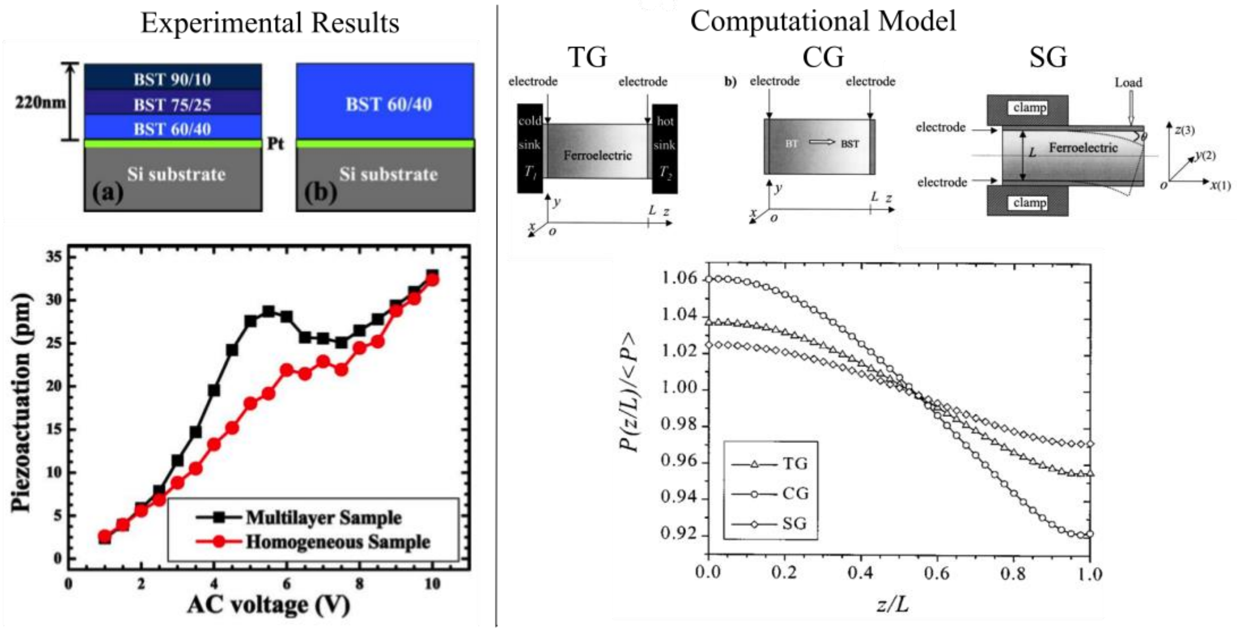

Figure 2.8: BaSrTiO₃ multilayer thin films and the enhanced piezoresponse thereof demonstrated experimentally in [124], accompanied by computational models of thermally graded (TG), compositionally graded (CG) and strain-graded (SG) thin films, in which the graded polarization response is highest for CG thin films, modified from [123]

Thin films have many interesting features, however there are disadvantages to their industrial application, specifically in the complexity and expense of the fabrication methods listed above. Therefore, ceramic ferroelectrics are currently the primary commercial material used in most piezoelectric applications. As was mentioned in the introduction to this work, ceramic fabrication has prehistoric origins and the techniques for producing high quality electroceramics are well established.

Lead-based composite systems have a long history in the field of piezoelectrics. The co-fired multilayer stack actuator is a key element of commercial piezoelectric actuators. It consists of thin piezoelectric disks between 0.1 and 0.5 mm in thickness bonded together and sandwiched between electrodes [128]. PMN in particular became a broadly used piezoelectric component of stack actuators instead of PZT because of its higher strains and lower hysteresis [129]. Most stack actuators were produced through tape-casting, with an internal Pt barrier electrode to prevent interactions during sintering, as shown in Figure 2.9.

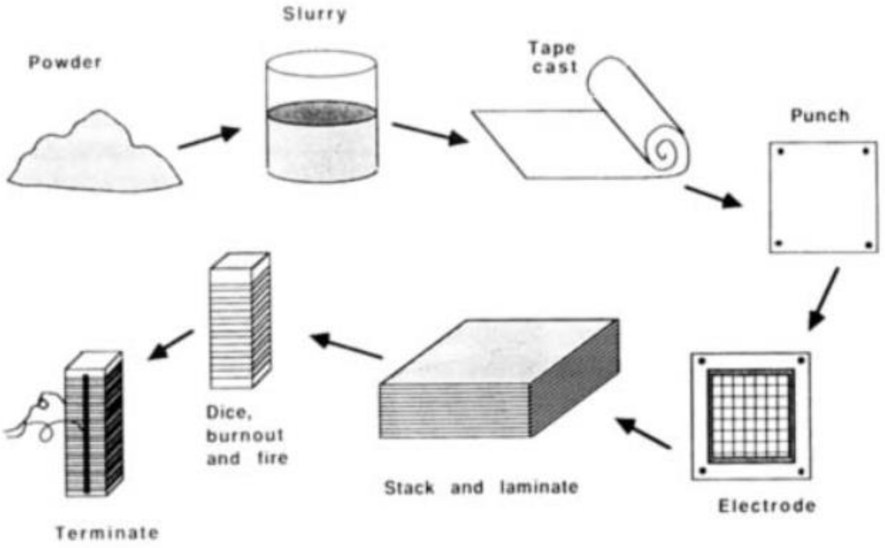

Figure 2.9: Flow chart for stack actuator fabrication from lead-based materials, taken from [129]

Shrout *et al.* produced a 2-2 composite comprised of different compositions of PMN-PT to increase the thermal stability of the elastic properties, enabling a broader temperature range for resonator applications [130]. The dielectric permittivity of the composite was significantly lower than the pure PMN and 0.8PMN-0.2PT, which results in a lower maximum permittivity and an increased thermal stability. From 0 to 80 °C, the composites showed a stable mechanical quality factor and resonant frequency, as compared to the pure constituent, PMN. However, PMN-PT showed had a slightly larger temperature stability region up to 100 °C.

The focus of this work is ceramic/ceramic composites, inspired by investigations of lead-free BNT-based ferroelectric mixed ceramic-ceramic composites with 0-3 connectivity [113]. These systems comprise ferroelectric “seeds” embedded in a nonpolar matrix material [7]. The matrix material was an ergodic relaxor that displayed a large unipolar strain with a corresponding large coercive field and low remanence, whereas the seed was a nonergodic relaxor that showed a large remanence and lower unipolar strain. This approach was based on the premise that the seed would act as a nucleation point for the polar order in the ergodic relaxor matrix material. In the aforementioned studies, it was found that lead-free

0-3 ceramic-ceramic composites showed retention of the large strain found in the matrix material and a decrease of the coercive field. The electromechanical response of the BNKT-BA/BNT and BNT-BT-KNN/BNT-BT 0-3 composite systems is shown in Figure 2.10, in which enhancement relative to the pure matrix can be observed.

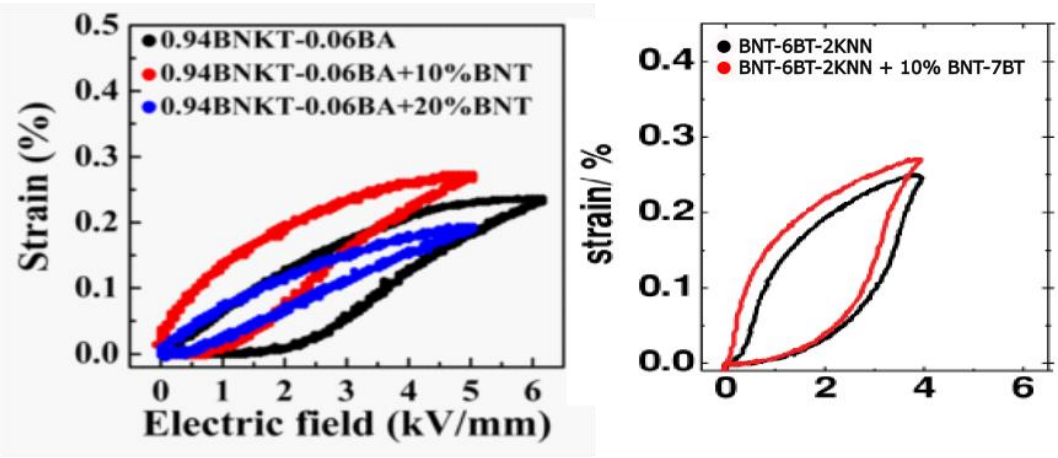

Figure 2.10: Enhancement of unipolar strain and reduction of coercive field in BNKT-BA/BNT composites [2] and enhancement at low fields observed in BNT-BT-KNN/BNT-BT composites [1]

From *in-situ* XRD measurements it has been proposed that the addition of a polar seed induces a small volume fraction of the surrounding matrix to undergo an irreversible electric-field-induced phase transformation from a pseudocubic phase to a mixed tetragonal and rhombohedral phase with an accompanying increase in the lattice strain of the mixed composite relative to that of the pure ergodic matrix [131]. A mechanism for the observed increase in strain is proposed: the seed material irreversibly transforms from a relaxor to a ferroelectric under applied field, serving as a nucleation point that allows the ferroelectric domains to further propagate into the surrounding relaxor matrix at a reduced external field level [131]. The mechanism responsible for the observed macroscopic response has been described by polarization and strain coupling between the seed and matrix [132]. These interactions can be described as a product property as explained above.

Polarization coupling is based on an equivalent circuit model of the composite system comprised of two nonlinear hysteretic capacitors in series (CIS), with differing capacitance values between the ergodic matrix and the nonergodic seed. The equivalent circuit and its influence on the distribution of electric fields and polarization response are depicted in Figure 2.11. Because capacitors in series must have an equal charge on each capacitor, the charge on the ergodic matrix increases, resulting in an inhomogeneous distribution of electric fields inside the composite. This facilitates the nucleation of domains through the coalescence of polar nanoregions [1]. Higher local fields in this composite system were confirmed through piezoforce microscopy by Gobeljic *et al.* [133].

Figure 2.11: Schematic of the equivalent circuit used for the polarization coupling model. The 0-3 and 2-2 composites are both represented by an equivalent circuit of two nonlinear capacitors (seed and matrix) connected in series.

The effective capacitance of the total composite can be calculated using the capacitor in series model with the equation below:

$$C_{eff} = \frac{Q}{|\Delta V|} = \frac{A\varepsilon_0}{\left(\frac{h_{RE}}{\varepsilon_{RE}} + \frac{h_{FE}}{\varepsilon_{FE}}\right)} \tag{2.2}$$

where Q represents the total charge, ΔV is the voltage potential drop across the total composite, A is the surface area, ε_0 is the permittivity of free space, and ε and h represent the dielectric constant and layer thickness, respectively; subscripts RE and FE denote either the relaxor or ferroelectric layer. The CIS model assumes a difference in charge distribution across the two components due to their difference in permittivity. Since the polarization across the capacitors must be equal, the external applied field is distributed between both components, of different permittivities, which results in different local electric fields on each component. The component with lower dielectric permittivity will have a larger local electric field, particularly relative to the applied field. This larger local field was used to explain the increased strain observed in the composite system relative to the pure matrix.

Some doubt has been cast on the appropriateness of the CIS model for ferroelectric multilayers. Sun *et al.* showed a large discrepancy between the predicted permittivity and the experimental values in ferroelectric/ferroelectric bilayers, and attributed this difference to the complexity of interactions between each layer, where domain formation and electrostatic interaction contribute to the total polarization of the system [134]. Their work showed that a dielectric bilayer could be modeled using the CIS description, but bilayers comprising ferroelectrics were described better by an electrostatically coupled model, given by the equation below:

$$\varepsilon_{eff} = A\varepsilon_0 \left[\frac{1}{\varepsilon_0}\left(\frac{h_{RE}}{h}\frac{dP_{RE}}{dE} + \frac{h_{FE}}{h}\frac{dP_{FE}}{dE}\right)\right], \tag{2.3}$$

where P is the polarization normal to the interlayer interface in layer i and therefore *dP/dE* is the first derivative of the polarization with respect to the internal electric field in the layer. This model was most appropriate in cases where the magnitude of the difference in spontaneous polarization between the two layers was large. However, in some cases a surface charge at the interface occurred because of the large difference in polarization, effectively screening the influence of the polarization of the other component and resulted in a decoupling of the layers. In those cases, the CIS model could accurately predict the effective permittivity of the bilayer system.

Detailed experimental investigations of the mechanism of polarization coupling in 2-2 composites have been performed by Grigoriev *et al.* in PZT bilayers, revealing that interface charges play an important role in polarization switching dynamics, supporting the conclusions made by Sun *et al.* about electrostatic interactions [135]. Dausch *et al.* measured the large signal polarization response of bilayers composed of antiferroelectric and ferroelectric PZT thin films and compared them with the predictions of the CIS model [136]. The thin films were produced by a dip coating and rapid thermal treatment, thereby limiting the chemical interaction between the layers as compared to ceramic/ceramic composites [137]. They also found large discrepancies between the experimental values and the CIS model, and attributed those differences to the absence of the electrode-dielectric interface in the composite system, just as in the electrostatically coupled multilayer described by Sun *et al.*

Damjanovic *et al.* demonstrated that bilayer ferroelectrics have a more complex response than the CIS model predicts [138]. They showed a frequency dependence of the dielectric and ferroelectric behavior of the composite, even when the pure end members have no such frequency dependence. This behavior was termed Maxwell-Wagner piezoelectric relaxation, and was shown to occur not only in bilayer structures but also in heterogeneous ferroelectric ceramics with anisotropic grains, demonstrating that a 2-2 composite system can provide insight into the interactions between components in 0-3 composites as well. The physical basis for this phenomenon is described in the equation below:

$$d_{tot}^{"} = \frac{\omega\tau(\tau_2-\tau_1)(d_2-d_1)\upsilon_1\upsilon_2\sigma_1\sigma_2}{(1+\omega^2\tau^2)(\upsilon_1\sigma_2+\sigma_1\upsilon_2)(\upsilon_1\tau_1\sigma_2+\sigma_1\tau_2\upsilon_2)}, \qquad (2.4)$$

where the total piezoelectric coefficient of the system, $\mathrm{d}_{\mathrm{tot}}^{"}$, is shown to be dependent on frequency ω, the difference between the piezoelectric constants of the two end members d_1 and d_2, the difference in the relaxation times of the two end members τ_1 and τ_2, and the volume fraction of each component, υ_1 and υ_2. It is clear from the equation above that the piezoelectric coefficient of the bilayer system is frequency dependent, even when the coefficients d_1 and d_2 are not.

Nevertheless, due to its simplicity, the CIS model has remained the predominant method by which the ferroelectric and piezoelectric behavior of composite systems is modeled. The CIS model was used to model the behavior of BNT-BT-KNN/BNT-BT 0-3 composites by Groh et al. [1]. This model was able to accurately predict the poling and depoling fields as a function of seed content. However, the d_{33}^{*} values proved more challenging to predict with the CIS model. The simulation at an applied field of 4 kV/mm gave significantly lower values than the experimental results, but did show an increase in the d_{33}^{*} at 10% seed content, paralleling the experimental results. The simulation overlapped nicely with the experimental results under an applied field of 6 kV/mm. These results are reproduced in Figure 2.12.

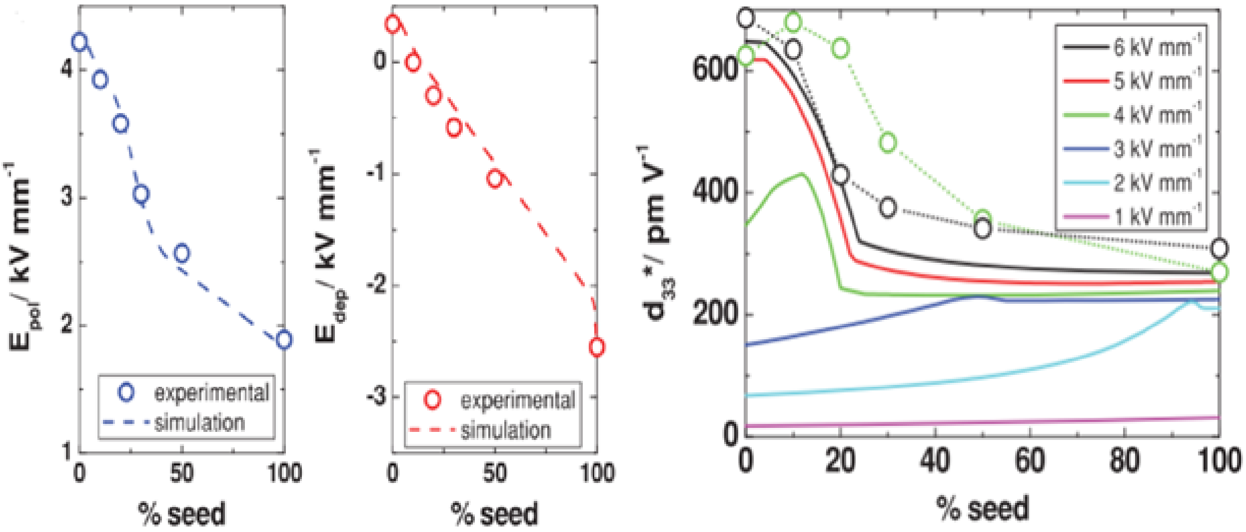

Figure 2.12: E_{pol}, E_{dep} and d_{33}^{*} as a function of seed content from experimental data and CIS simulations in BNT-BT-KNN/BNT-BT composites, from [1]: Epol, Edep and d_33^* as a function of seed content from experimental data and CIS simulations in BNT-BT-KNN/BNT-BNT composites, from [1]

Strain coupling is another interaction between components of a composite that is neglected in the equivalent circuit model. As a mechanism of enhancement, it is based on the fact that the two components of the composite have different radial piezoelectric coefficients, therefore the component with the higher piezoelectric coefficient will induce a strain in the component with the lower coefficient, resulting in a higher strain response under the same electric field [139]. The strain coupling model considers two possible contributions to the strain: the difference in the piezoelectric coefficient during application of an electric field, and the difference in remanent strain states after poling. The remanent strain in the nonergodic relaxor will affect the surrounding ergodic matrix, giving rise to internal stresses after the first application of an electric field. The remanent strain in the polar seed phase was found to result in internal stresses after electrical poling, using the equations below [132]:

$$\sigma_{RE} = \varepsilon_{remnant}^{FE}[\frac{1}{Y_{RE}} + \frac{1}{Y_{FE}}\left(\frac{{}^{n}RE\,{}^{h}RE}{{}^{n}FE\,{}^{h}FE}\right)(1+\varepsilon_{r}^{FE})]^{-1} \tag{2.5}$$

$$\sigma_{FE} = -\sigma_{RE}\left(\frac{{}^{n}RE\,{}^{h}RE}{{}^{n}FE\,{}^{h}FE}\right) \tag{2.6}$$

where Y is the elastic modulus, n is the number of layers, h is the thickness of each layer and ε_r^{FE} is the lateral remanent strain in the polar seed. This calculation revealed that the polar seed phase was in tension and the ergodic relaxor matrix phase was in compression after electrical poling. Therefore, the composite structure results in a contribution to the total strain as a consequence of the different remanent states of each constituent. In addition, the difference in d_{31}^* contraction between the two components during electrical loading will contribute to internal stresses. Both strain and polarization coupling enhancement mechanisms were evaluated by Zhang *et al*. through the formation of multilayer serial and parallel connected composites [132]. Zhang *et al.*'s work revealed an enhanced d_{33}^* for both polarization coupled and strain coupled 2-2 composites at 30% seed content under an applied field of 4 kV/mm with a frequency of 50 mHz. The same composition, 30% seed content, was found to have an optimal d_{33}^* in the 0-3 composite. As a result, it was concluded that the enhancement observed in 0-3 composites arises from a combination of polarization and strain coupling between the seed and matrix phase. This work also revealed the microscopic relaxation of domain formation after poling by PFM, where the relaxation of the ergodic relaxor was strongly influenced by the presence of the polar seed.

Enhancement due to composite structures is not limited to 0-3 composites, as 2-2 layered composites have also been used to optimize ferroelectric, piezoelectric, and dielectric properties [132]. The multilayer approach has also been used to tailor the large field electrical constitutive behavior of ferroelectrics; for example in 2-2 composites of PZT and PLZT it was observed that the coercive field and remanence could be lowered while increasing saturation polarization by optimizing the end member content [137]. While initial investigations of 2-2 composites were centered on the bulk macroscopic dielectric, ferroelectric, and piezoelectric behavior [114], recent investigations have emphasized the effects of co-firing in these systems and residual stresses due to differences in shrinkage [44], [140], [141].

Interdiffusion is a factor in the synthesis of composites that to date has not been exhaustively investigated in ferroelectric composite systems. There is a large body of evidence for the occurrence of interdiffusion during sintering in a variety of ceramic materials. These effects include interdiffusion from electrodes into the ceramic [142]–[144], as well as interdiffusion between constituents in ceramic/ceramic composites. Interdiffusion between PZT and lead nickel niobate (PNN) multilayers has been demonstrated through electron probe microbeam analysis [145]. In BNT-based materials, interdiffusion between the metallic electrode and ceramic have also been observed [144]. This phenomenon was attributed to the high concentration of A-site vacancies in BNT due to the volatility of bismuth. In some systems, diffusion could not be immediately concluded; for example TEM investigations of BNT-BT-KNN based composites have shown at least two different types of grains in a composite system, which was attributed to the presence of chemically distinct seed and matrix grains, Figure 2.13 [1]. PFM investigations of the same composite system have stated that intermixing of the constituents, especially close to grain boundaries, cannot be excluded due to evidence that the "ergodic grains" measured in this study exhibited broader hysteresis loops than those of pure ergodic relaxor materials, indicating that the ergodic grains were altered by the nonergodic grains through nanometer sized-inclusions distributed in the surrounding "ergodic relaxor" matrix [146]. However, an exhaustive quantitative investigation of chemical composition across multiple grains has proven challenging due to the submicron length scale at which diffusion occurs [147].

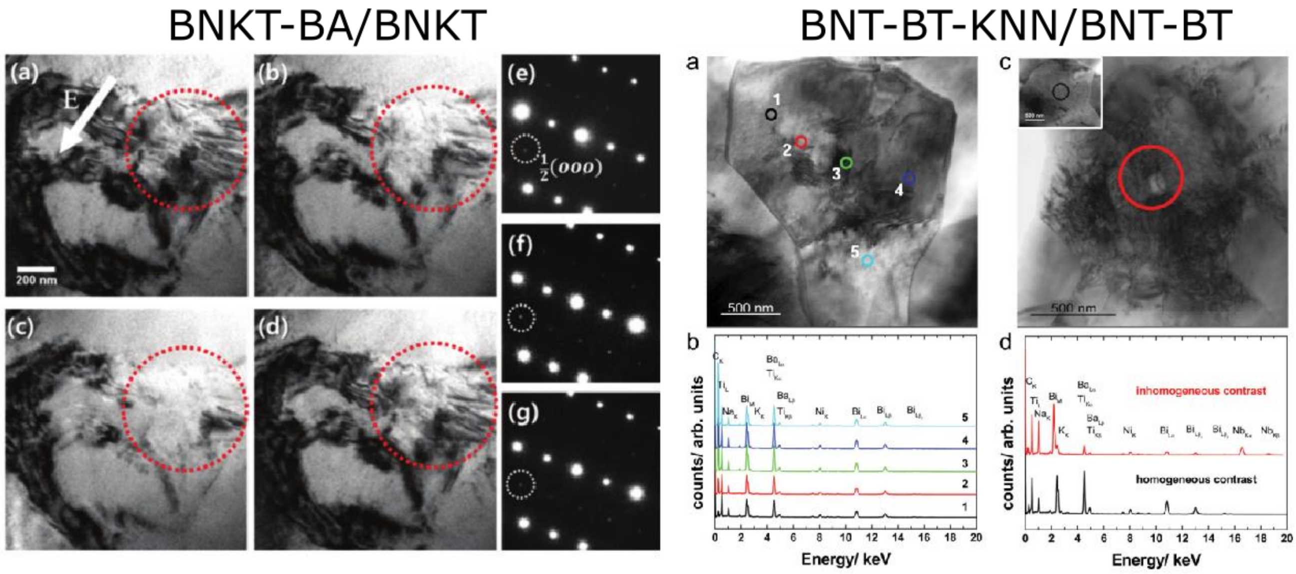

Figure 2.13: TEM and EDS investigations of composite materials, BNKT-BA/BNKT[136] and BNT-BT-KNN/BNT-BT [101]

TEM investigations of BNKT-BA/BNKT composites, on the other hand, have shown the influence of the composite structure on the final crystalline phase, but did not include corollary measurements of composition in the same grains analyzed using SAED [148], also shown in Figure 2.13. Those investigations, however, revealed that under an applied electric field, a charge accumulation occurs at the phase boundary between BNKT and BNKT-BA due to the difference in permittivity between the two materials. An investigation of interdiffusion in BNKT-BA/BNT composites was performed through a sintering study, in which it was shown that an increased sintering time of 36 h results in a reduced coercive field of 0.98 kV/mm, from 1.4 kV/mm at a 4 h sintering time, and an increase in the d_{33}^{*} to 1000 pm/V [149], which was attributed to the enlarged grain size of BNT as well as K^{+} and Al^{3+} doping in the BNT grains. Further investigations on enhancement mechanisms in BNKT-BA based composites were performed by changing the structure from a 0-3 to a 2-2 structure, and it was observed that the coercive field was higher in the 0-3 composites than in the 2-2 composites, as was the total bipolar strain [150].

Mechanical stress arising from co-sintering is also an important factor in the behavior of ferroelectric composites, as it can have a dramatic influence on the microstructure during processing, as well as an impact on domain switching due to residual stresses in the final sintered body [1], [112]. It is well established that co-sintering of ceramic composites can influence the microstructure [151]. Co-sintered structures have been investigated for internal stresses due to differences in shrinkage rate [152], but the precise effects of co-sintering on ferroelectric properties of lead-free composites has to date not been elucidated. There is an increasingly large body of evidence for stress-induced structural phase transitions in single crystal and polycrystalline ferroelectrics [131], [132], making the presence of such stresses an important consideration in the optimization of lead-free ceramic composites. In addition, recent work has also demonstrated that an external mechanical stress can induce a transition from the relaxor state to a metastable long-range ferroelectric order state, [29] analogous to the well-known electrical case [92]. The presence of internal stresses in laminate structures is well established and has been observed in metals [153], polymers [154], and ceramics, in which it is often attributed to a difference in sintering rates [151]. For instance, the size and orientation of grains have been shown to depend on the internal stress fields caused by differences in thermal expansion and sintering trajectories [155], [3]. Understanding and manipulating these stresses, primarily through changes in the substrate, has enabled improvements in the properties of piezoelectrics, both in lead-based piezoceramics, such as PZT films for ultrasound applications [156], and lead-free ferroelectrics, such as dielectric permittivity in $BaTiO_3$ multilayer composites [157].

A summary of the significant piezoelectric and ferroelectric properties for actuator applications is provided in Table 2, enabling a comparison of recent lead-free piezoceramics with the commercially dominant PZT. As can be observed from this table, the composite system has provided one of the most viable alternatives to PZT because of its reduced coercive field and increased d_{33}^* value. Understanding the mechanisms by which this enhancement occurs enables the development of new lead-free material systems, not only through changes in composition but also through tailoring of fabrication methods to take advantage of interactions during sintering, such as the aforementioned influence of internal stresses and interdiffusion

By changing the composite structure from a mixed (0-3) composite to a multilayer (2-2) composite, an investigation of the interactions between the seed and matrix phase in lead-free ceramics is achieved. As will be discussed in great detail in the chapters that follow, 2-2 composites further facilitate the investigation of interactions between the seed and matrix material by providing a macroscale, two-dimensional, experimental model of these interactions.

*Table 2:Summary of large signal piezoelectric response of BNT-based ferroelectrics in comparison to PZT, *BNT Td depends strongly on stoichiometry [158]**for BNT-BT-3KNN rather than BNT-BT-2KNN, ***for BNT-25ST rather than BNT-28ST*

	Ec (kV/mm)	d_{33}^* (pm/V)	ε_r (poled, RT)	Phase transition temperature (Td/Tc/Tf) (°C)
PZT [49]	1.5	600	8000	Tc: 330 - 420 °C depending on composition [157]
BNT [49]	7.3	500 [59]	780	Td: 187 °C-300 °C* [159], [160]
BNKT [108]	2.55	212	1030 [161]	Tc: 292 °C [162] Td: 233 °C [163]
BNT-6BT [59]	2.3	280	1600	Tc: 288 °C [164] Td: 110 °C [165]
BNT-6BT-2KNN [166]	3.59	560	2000	Tf : 48 °C**
BNKT-6BA [2]	3.2	440	1550	Tf : 20 °C* [167]
BNT-28ST [102]	2.33	600	1600	110 °C [168]***
Composite: BNKT-BA/20% BNKT [167]	1.3	780 [2]	1483	Td : >120 °C
Composite: BNKT-BA/20% BNT [149]	0.8	750	1333 [2]	n/a
Composite: BNT-BT-2KNN/10%BNT-BT [147]	1	680	2000	T_d : 125 °C [169]***

3. Experimental Methods

3.1. Powder and Sample Preparation

BNT-7BT, the primary seed powder utilized, was produced using the following powders with >99% purity from Alfa Aesar, (Karlsruhe, Germany): Bi_2O_3, $BaCO_3$, $NaCO_3$, TiO_2. BNKT-6BA was produced using Alfa Aesar powder of the following purity and composition: Bi_2O_3, K_2CO_3, $NaCO_3$, TiO_2, and Al_2O_3. BNT-6BT-3KNN powder was produced using the following powders with a purity >99% Bi_2O_3, $BaCO_3$, K_2CO_3, $NaCO_3$, Nb_2O_5, TiO_2, all from Alfa Aesar.

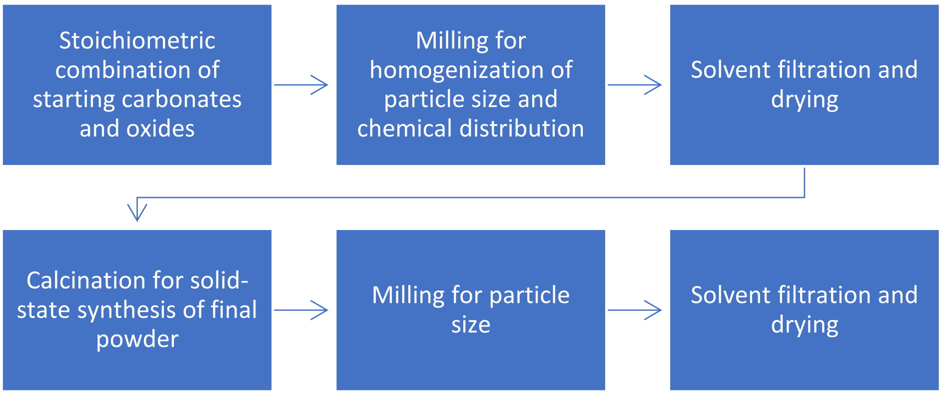

Figure 3.1: Flow diagram of solid-state powder synthesis

The powder processing procedure is summarized in Figure 3.1 and described in more detail below. The raw powders were ball milled for 24 h in ethanol at 120 rpm in a nylon milling vial with 5 mm diameter yttrium stabilized zirconia milling balls, in order to homogenize the distribution of chemical constituents prior to solid-state synthesis. The milling was performed in a planetary mill, (Pulversiette 5, Fritsch GmbH, Idar-Oberstein, Germany). They were then dried for 48 h in a drying oven at 100 °C (Memmert GmbH + Co. KG, Schwabach, Germany). After drying, they were pestled with an agate mortar and pestle, and then calcined in a two-step calcination process in alumina crucibles (Gieß-Technische-Sonderkeramik GmbH & Co. KG, Düsseldorf, Germany). The calcination was performed with a heating rate of 5 °C/min, a holding time of 2 h at 700 °C, a further heating at 5 °C/min to 800 °C, which was held for 3 h, followed by cooling at an uncontrolled rate to room temperature. After calcination, the calcined powder was ball milled for 20 min to produce larger powder of 2 µm, and 24 h to produce powder of 1 µm. They were then dried for 48 h in a drying oven at 100 °C. After drying, they were pestled with an agate mortar and pestle.

Figure 3.2: Flow chart of sample preparation

As shown in Figure 3.1, pure end members were produced with the compositions described above, and characterized for electromechanical properties and phase purity by XRD. A perovskite phase is expected to be identified in phase pure calcinated materials. The XRD was performed in a diffractometer (Bruker D8 Advance, Bruker, Billerica, USA) using Cu-K radiation with a wavelength of 1.5425 Å. The data was collected in the range of 10° to 90° with a step size of 0.02° and a measuring time of 5 s at each step. Sintered discs were annealed at 400 °C prior to the measurement to prevent mechanical stresses from affecting the XRD results. Phase purity was evaluated both in powders and sintered bodies. The measurements were performed by Jean-Christophe Jaude, TU Darmstadt.

Powders with no secondary phases in XRD were then tested for desired electromechanical behavior. The matrix powder was selected based on ergodicity, meaning its remanent strain must be below 5% of the total strain. The matrix powder BNT-6BT-3KNN must also have a maximum strain of at least 0.2 % at 4 kV/mm. The seed powder was selected for quality based on its correspondence to literature values in unipolar strain and polarization.

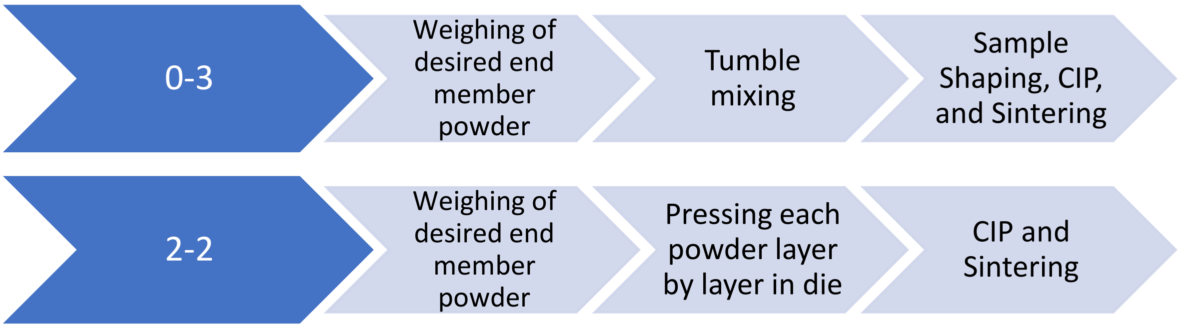

Figure 3.3: Processing of composite samples

For the production of 0-3 composites, the matrix and seed powder were mixed together by rolling the mixed powders on a rolling bank for 30 min. Following the mixing procedure, the samples were shaped into disks by hand pressing in a uniaxial press with a 10 mm diameter in the green body. For large signal electromechanical properties, approximately

0.3 g of powder was used. For large signal ferroelastic measurements under applied stress, and dielectric small signal properties under applied stress, samples were pressed with approximately 1.8 g of powder. This is summarized in Figure 3.3.

For the production of 2-2 composites, the matrix was shaped into a disk by introduction into a uniaxial press with a 10 mm diameter. The powder was pressed by hand for 5 s, the press removed from the die, and the seed powder was introduced into the die. The powder was again pressed by hand for 5 s, the press was removed from the die, and then the final layer of matrix powder was introduced. The final pressing step, by hand was held for 10 s. Care was taken between each pressing step to clean the press with silicon oil to avoid cross contamination of seed and matrix between designated layers.

The shaped green bodies were then placed inside a latex sheath, evacuated from gas, and pressed isostatically in oil using a cold isostatic press (KIP 100E, Paul-Otto Weber GmbH, Remshalden, Germany) at 300 MPa for 90 s. After pressing, the samples were sintered for 2 or 3 h at 1100 °C in sacrificial powder. Care was taken to assure that the sacrificial powder was the same as the matrix powder. They were subsequently ground to a plane parallel surface using a 15 um grinding wheel. The final grinding step was performed by Michael Heyse of TU Darmstadt.

3.1.1. Density

Density of ground samples was measured using the Archimedes method. In this method, open pores of a complex geometry are filled with water by leaving individual samples in distilled water while under vacuum. The sample is first weighed dry ($M_{d)}$, then weighed after fluid impregnation into the pores, (M_i) and then weighed while immersed in water (M_w). The density is calculated with the following equation:

$$p = p_{H_2O} \times \frac{M_d}{M_i - M_w} \qquad 3.1$$

p_{H_2O} is the density of water as a function of temperature. The relative density is then calculated as the ratio of the measured density by the Archimedes method to the theoretical density. The theoretical density is the density of the material with 0% porosity, determined from the stoichiometric formula by atomic weight of its constituents, and divided by the volume determined from the lattice constants by XRD.

3.2. Electrical Characterization

3.2.1. Strain and Polarization as a Function of Electric Field and Frequency

Three different pieces of equipment were used for the measurement of large signal electromechanical behavior. For samples of dimensions greater than 2 mm, and room temperature measurements, a modified Sawyer-Tower circuit was used. This method was used primarily for samples larger than 2 mm, and their reference measurements. Alternatively, for samples below 2 mm measured at 4 kV/mm, a commercially available system was used (aixPES system, AixACCT Systems GmbH, Aachen, Germany). For determination of local strain during application of large fields, in collaboration with Dr. Di Chen and Professor Mark Kamlah of Kalrsuhe Institute of Technology, a digital image correlation system was used. All large signal measurements are performed with the sample immersed in silicone oil. Each measurement method is described in more detail below.

Room Temperature Characterization

Strain and polarization measurements as a function of applied electrical field were performed on a modified Sawyer-Tower circuit. An electrical field with a triangular signal is applied through a LabView program to a voltage source (20/20C, TREK, Inc., New York, USA). The sample was in series with a capacitor of known capacitance, hereon referred to as C_{ref}. The voltage drop V across the reference capacitor with capacitance C is proportional to the polarization charge Q, based on the equation

$$Q = V \cdot C \tag{3.2}$$

Capacitors in series have equal charge. By measuring the voltage across the reference capacitor, with a known capacitance, the charge across the reference capacitor and, therefore, the sample in series to it can be measured. The polarization is simply the charge divided by the area of the sample, or P=Q/A. Therefore, a determination of the polarization as a function of applied electrical field is possible throughout electrical cycling by constantly gathering data points for the voltage across the reference capacitor. Care must be taken to assure that the reference capacitor's capacitance is an order of magnitude higher than that of the measured sample, otherwise the voltage drop across the capacitor can be too large and result in sample breakdown [16].

Simultaneous measurement of strain as a function of applied field takes place through a laser displacement sensor (D63, Philtec, Inc., Annapolis, USA). The sample is held in place with a contact, which is displaced upon a change in dimension of the sample. The optical sensor is comprised of a light-emitting glass fiber optic which shines a laser directly onto the highly reflective metal surface on top of the upper contact point. A displacement of the sample is thereby detected in the fiber optic by a change in light intensity induced by the displacement of the upper contact relative to the laser source.

Temperature-Dependent Characterization

Temperature-dependent strain measurements were performed in a commercially available system from Aixacct, (aixPES system, Aixacct Systems GmbH, Aachen, Germany), with a limitation of 10 kV available, making it only usable for samples below 2 mm when a desired field of 6 kV/mm was applied. Displacement is determined through a built-in single-beam laser interferometer using a single beam laser interferometer (Polytec OFV-5000 Vibrometer Controller), while polarization is determined through the virtual ground method. The heating rate for increases in temperature is approximately 1 °C/min, with 10 min of equilibration time provided for the temperature to stabilize prior to measurement. Frequencies from 50 mHz to 1 Hz were used during applications of electric fields up to 6 kV/mm. Details of the frequency, field and temperature are provided with each measurement result collected from this device.

Digital Image Correlation (DIC)

Samples for digital image correlation measurements under applied electric field were prepared from pure end member samples and layered structures synthesized as described above. After sintering, the samples were ground to rectangular shapes from cylindrical samples. The base of the samples was 5 x 5 mm and the height was 6 mm. One face of the sample was covered with speckles for displacement tracking. Artificial speckles were sprayed onto the observation surfaces by means of an air brush (AT-Airbrush Pistole Kit, AT-AK-02, Agora-Tec, Germany) instead of the natural textures on the surfaces.

A schematic of the measurement setup is shown in Figure 3.4. A linear variable displacement transducer (LVDT) sensor (Type W1T3, HBM, Darmstadt, Germany) was used to measure the bulk displacement of the sample, and a digital camera (PL-B782F, Pixelink, Ottawa, Canada) was used to record the local displacement of markers along the surface of the sample. An oil bath was used to prevent arcing from the sample. An electric field with a loading rate of 0.016 kV/mm s^{-1} (0.01 Hz) was supplied by a bipolar high-voltage power supply (HCB 15-30000, F.u.G., Rosenheim, Germany). A total of 3 bipolar cycles was applied on the sample. A lens with 2X magnification (MVO-TML telecentric measuring lens, Edmund Optics Inc., Germany) was used to provide a high image resolution of 1.75 µm/pixel. 2 images per second were generated using the digital camera during the application of the electric field. The experiment was controlled and the data were acquired by a computer running LabView 2009. After the experiment, Matlab R2011b was used to analyze the images saved to a hard disc. These measurements were performed by Dr. Di Chen and Professor Mark Kamlah of the Karlsruhe Institute of Technology.

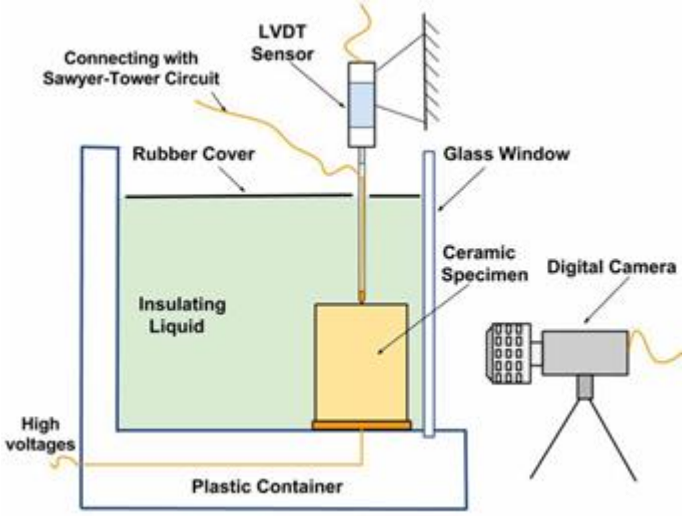

Figure 3.4: Schematic of DIC measurement setup with applied electric field, from [170]

3.2.2. Small Signal Dielectric Response Measurements

The small signal dielectric permittivity and loss were measured as a function of temperature at frequencies from 10^2 Hz to 10^6 Hz from room temperature to 450 °C with a heating rate of 2 °C/min in a Nabertherm LE4/11/R6 furnace equipped with a custom-made spring clamped sample holder and contacted with external platinum electrodes. The samples were poled at an electric field of 2 kV/min for 5 min at 150 °C and then cooled under the same field to room temperature. The capacitance of the sample was determined using an LCR impedance analyzer (HP4192A, Hewlett-Packard Co., Palo Alto, USA). The relative permittivity was calculated using the equation:

$$\varepsilon_r = \frac{Cd}{\varepsilon_0 A} \qquad 3.3$$

A denoting the sample area and *d* the sample thickness, whereas *C* is the capacitance measured by the LCR meter.

3.3. Mechanical Characterization

3.3.1. Large Signal Stress-Dependent Measurements

Stress-dependent large signal (strain and polarization) and small signal (permittivity) properties were measured on a mechanical load frame (Zwick Z030) outfitted with a modified Sawyer-Tower circuit. This setup included heating elements capable of reaching 600 °C. The permittivity small signal behavior was measured through a custom built LabView program developed by Dr. Florian Schader, while the large signal properties were measured with a commercially available

Zwick software that accompanies the device. Low temperature stress-dependent measurements were performed on the Instron load frame (5967, Instron GmbH, Darmstadt, Germany), in which associated commercial software was used for measurement recording and signal application. Strain was measured through a calibrated LVDT. Applied stress was controlled through the load frame.

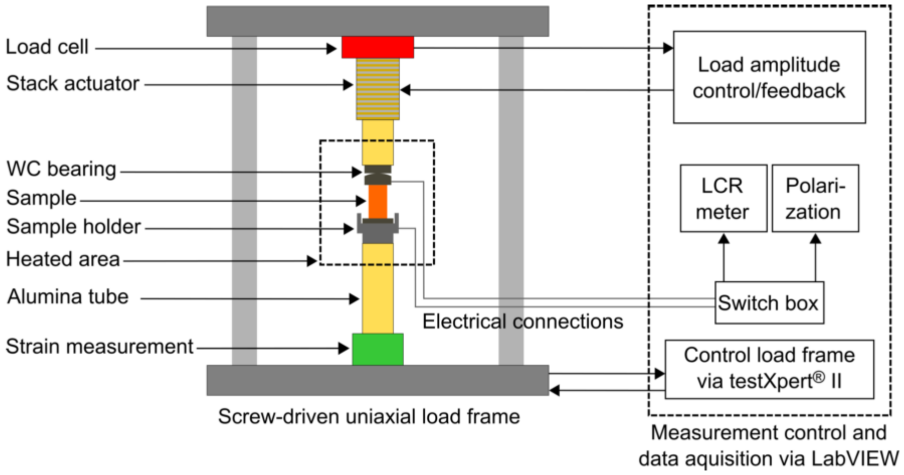

Figure 3.5: Schematic of load frame used for stress-dependent measurements, taken from [171]:

3.3.2. Vickers Indentation

Vickers indentation was performed on the bulk end members as well as the individual layers of the composite structure. During testing, a weight of 2 kg was used with a loading time of 10 s. A total of 5 indents for each sample were used to determine repeatability. Prior to Vickers indentation, samples were vertically sectioned and polished to a 1 µm surface finish. Samples were annealed to 400 °C for 30 min prior to testing, meaning that all samples were in the virgin state during indentation. An additional experiment was performed on a mechanically textured sample. Prior to indentation, the sample was applied with a uniaxial compressive stress of –500 MPa (loading/unloading rate of –4 MPa/s). Immediately after mechanical loading, three Vickers indents were applied. For all indentation experiments, the subsequent crack lengths were measured using optical microscopy (Olympus BX51 light microscope, Tokyo, Japan).

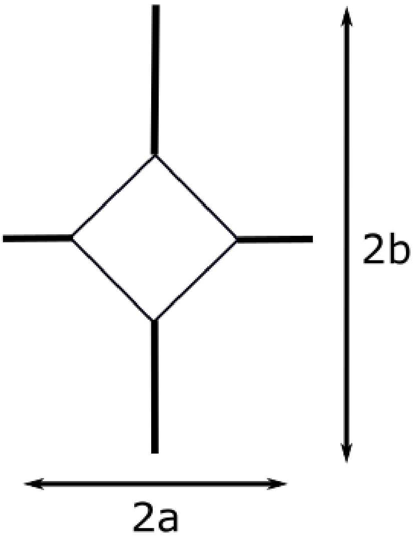

Figure 3.6: Schematic of crack length analysis from Vickers indentation, with 2a being the length of the horizental crack and 2b being the length of the vertical crack

3.3.3. Nanoindentation

Nanoindentation measurements were performed with the assistance of Olena Prach at the Technical University of Darmstadt. These measurements were performed on an MTS3 NanoIndenter® XP with a three-sided diamond Berkovich indenter tip having a nominal centerline-to-face angle of 65.27° at room temperature, with an indentation force of 45 mN and target depth of 5000 nm. All samples investigated by nanoindentation were first polished with diamond paste of 1 µm coarseness.

For 2-2 composites, the sample cross-section perpendicular to the seed/matrix interface was prepared in this manner by first cutting the sample in half with a diamond wire saw, imbedding the sample in an epoxy resin, and then polishing. Indents were made along the cross section in a grid every 50 µm along the samples height, and in a row with 50 µm spacing between each indent in the row. The area in which indents were taken was aligned with the area in which EDS compositional analysis was performed, detailed below.

3.4. Microstructural Characterization

3.4.1. SEM Sample Preparation and Measurements

2-2 samples were prepared for microstructural investigation by vertical sectioning using a diamond wire saw, followed by polishing to a 0.25 µm surface finish on the vertically cut face. They were thermally etched at 1100 °C for 5 min and sputtered with a thin layer of gold for imaging by scanning electron microscopy. For Energy Dispersive Spectroscopy (EDS) investigations, the samples were sputtered with a thin layer of carbon. SEM images of the 2-2 cross-section as well as compositional analysis through the thickness were performed using a SEM (XL 30 FEG; Philips, Eindhoven, the Netherlands). EDS measurements to determine composition were performed on polished samples using a high-resolution SEM (JSM-7600 FEG; JEOL, Tokyo, Japan) also equipped with an EDS detector (Silicon Drift Detector (SSD), 80 mm^2; Oxford Instruments plc, Oxfordshire, UK). The EDS line scan in the high-resolution scanning electron microscopy (HRSEM) was performed with a dwell time of 3 ms, over ten points across the interface region for each line using a beam energy of 8 kV. 50 such lines were collected with a distance of 50 µm between each line.

Grain size was characterized using the freeware ImageJ (National Institute of Health version 1.48). The grain size was analyzed from a series of SEM images across the 2-2 samples at a magnification of 50000x and an accelerating voltage of 20 kV. Each image contained approximately 150 grains. The grain size was determined through the following method: each grain was outlined by hand with a drawing tool and measured with a built-in script for the grain area, which was then back-calculated into a grain diameter.

3.4.2. Light Microscopy

Light microscopy images (DM2500, Leica, Wetzlar, Germany) were taken of the samples at a magnification of 50x, every 100 µm. Analysis of pore size and porosity were obtained with a stack script written and implemented in ImageJ, wherein the images were converted to binary pictures and the dark areas were analyzed for size and percent coverage of the image.

3.4.3. Transmission Electron Microscopy

TEM images were taken using a JEOL 2100F (JEOL Ltd., Tokyo, Japan). Compositional analysis of TEM samples was performed by EDS analysis using with an accelerating voltage of 200 keV. These measurements were performed with Dr. Michael Durrschnaebel and Dr. Leopoldo Molina-Luna. The samples were ground to a thickness of about 100 µm and polished using diamond paste. They were then sliced into samples of 3 mm diameter by ultrasonic disc cutting (Model 601, Gatan Inc., Pleasanton, USA) and dimpled in the center to 10 µm thickness. The final thickness of the sample was reduced to below 3 µm by argon milling (Rapid Etching System 010, Bal-tec AG, Balzers, Liechtenstein). For EDS measurements, the samples were sputter-coated with carbon (MED 010, Bal-tec AG, Balzers, Liechtenstein) to prevent charging under the electron beam. Sample preparation was performed by the author.

3.4.4. Nuclear Magnetic Resonance

The coordination number of aluminum in BNKT-BA composites was analyzed using nuclear magnetic resonance spectroscopy (NMR). This work was performed with Dr. Pedro B. Groszewicz of the Chemistry Department at TU

Darmstadt. Solid-state NMR spectra were acquired with a Bruker Avance III spectrometer with a carrier frequency of 156.37 MHz for ^{27}Al and 158.75 for ^{23}Na. Composite pellets were ground to powders, which were then mixed with boron nitride (1:2 volume) to facilitate spinning, and samples were spun under MAS conditions at a spinning frequency of 13 kHz in 4 mm ZrO_2 rotors.

For ^{27}Al MAS NMR experiments, a single-pulse sequence with a pulse length of 2.0 μs and a dwell time of 0.4 μs ensured appropriate excitation and recording of the complete spectrum. A total number of 40960 scans were accumulated, with a recycle delay of 500 ms in between scans. No significant difference was observed for longer recycle delays. ^{23}Na MAS NMR experiments followed a similar protocol, adjusted for the different nucleus.

Two-dimensional ^{27}Al 3QMAS (or MQMAS) NMR spectra were acquired with a Z-filter pulse sequence, [121] with excitation, conversion and Z-filter pulse durations of 4.3 μs, 1.5 μs and 11.0 μs, respectively. The Z-filter delay was 20 μs long, and 64 t1 increments were recorded in a rotor-synchronized fashion, with a recycle delay of 1.0 s, and 3072 scans for each increment. The chemical shift scale was referenced to a 1 M $AlCl_3$ aqueous solution (0 ppm).

3.4.5. Raman Spectroscopy

Raman spectra were measured using a LabRAM HR high resolution microscope with a 633 nm wavelength laser and a 50X objective (Horiba Jobin Yvon, model HR 800, Villeneuve-d'Ascq, France). This measurement was performed on freely sintered BNT-25ST and BNT-7BT polished to a 1 µm surface finish and on the cross-section of a BNT-25ST/BNT-7BT 2-2 bilayer composite, with one spectra collected in each layer.

3.4.6. X-ray Diffraction

In-Situ Stress-dependent XRD

In-situ stress-dependent experiments were carried out at the ID15 beam line of the European Synchrotron Radiation Facility (ESRF). A monochromatic beam of 72.72 keV was used, with a wavelength of 0.17049 Å. A custom-made compact load frame capable of applying compressive stresses up to 10 kN was used to compress the sample during measurement. The compressive load was applied by a piezoelectric actuator (P-235.80, PI Ceramic GmbH, Lederhose, Germany), controlled by an applied field generated by a high-power voltage amplifier (E-481.00, PI Ceramic GmbH). A function generator was used to create a triangular voltage input signal for the amplifier with a maximum voltage of 5 V and frequency of 625 µHz. The maximum possible stress applied on the sample was -593 MPa. The sample was machined to a diameter of 1 mm and a height of 2 mm to retain an aspect ratio of 2:1. Diffraction images were collected in transmission geometry using a Pixium 4700 flat panel area detector at a rate of 2 Hz during the application of the triangular loading profile. Data analysis was performed using the Rietveld refinement method. This method was used to determine the crystal structure as a function of applied stress in BNT-7BT and BNT-BT-KNN. This work was performed with Dr. John Daniels of the University of New South Wales, and Dr. Neamul Hayet Khansur, currently at the Friedrich-Alexander University in Erlangen-Nuremberg.

Micro-X Ray Diffraction

Micro-XRD was performed with a Rigaku SmartLab X-Ray Diffractometer, using a collimator of 300 µm to measure a narrow portion of the composite. The scan was performed over the sample cross-section, a total of 2400 µm with a 150 µm interval between each scan, with a speed of 1 °/min using a wavelength of 1.5418 Å from a Cu Kα source. An XRD pattern was collected every 100 µm using a beam collimator that results in a beam size of 300µm. The size of the beam results in an overlap of the measurement region from the preceding and subsequent measurement position. A total of nine patterns were collected. Diffraction patterns from 20-70° were measured. This work was performed in collaboration with Professor Shintaro Yasui of the Tokyo Institute of Technology.

Further micro-XRD measurements were performed at BL15 in the SPring8 Synchrotron source in Japan, at which a higher spatial and angular resolution were available. A double-crystal monochromator with a liquid-nitrogen cooling system is used for monochromatization of synchrotron beams to a beam size of 100 µm. The beam wavelength was 1 Å. PDMS lenses further focus the beam to a width of 11 µm and a height of 7 µm. For 2-2 composites of BNT-BT-KNN/BNT-BT, the aforementioned beam size was used, with a new diffraction pattern acquired every 20 µm. 80 measurements were performed along the sample for each reflection. For 2-2 composites of BNKT-6BA/BNT-7BT, a beam size of 50 µm in height and 200 µm in length was collected every 100 µm. More details of the sample setup are provided with the associated results. The (111) and (200) reflections were measured with a data collection time of 4 min. All samples were performed along the cross-section of 2-2 composites, under ambient conditions. These measurements were performed in collaboration with and through the assistance of Professor Shintaro Yasui.

4. Investigations of Ceramic/Ceramic Composite Chemical Composition, Correlated Crystal Structure and the Influence of Processing

4.1. Introduction

As discussed in the introduction, in the burgeoning field of ceramic/ceramic composites, the investigation of structure-property relationships has yielded a variety of important insights into the role of chemical composition, crystal structure, and microstructure on the piezoelectric and ferroelectric response. In this chapter, taking inspiration from the structural investigations discussed in the literature review, [148], [149], [172], the chemical composition and its influence on crystal structure were investigated in 2-2 and, where possible, 0-3 composites. Due to the challenges of detecting chemical differences between BNT-6BT-3KNN and BNT-7BT, only the crystal structure across 2-2 composites is reported for that system. BNKT-BA/BNT-7BT composites were used as a model system to investigate the degree of interdiffusion between seed and matrix and its influence on the crystal structure within the composite. Given that the A-site is occupied by a combination of Bi^{3+}, Na^{+}, Ba^{2+} and K^{+}, and the B-site is occupied by a combination of Ti and either Al^{4+} or Nb^{5+} depending on the matrix material used, the lattice constants depend on the proportion of elements found on each site.

Evidence of interdiffusion and its influence on crystal structure is shown in both 0-3 and 2-2 composites of BNKT-6BA/BNT-7BT through EDS-TEM and SAADP of the former and EDS-SEM and local micro-XRD measurements of the latter. An investigation of the local atomic scale environment of Al was performed through NMR to further clarify the influence of interdiffusion on the lattice of BNKT-6BA/BNT-7BT composites.

Having demonstrated that interdiffusion does indeed occur in composites, an investigation of the influence of sintering parameters on composition and crystal structure was undertaken. 2-2 composites of BNKT-6BA/BNT-7BT were sintered for 2 h, 6h, 12 h, and 24 h, and their chemical composition along the sample cross-section was evaluated by SEM-EDS. The composition was compared to the crystal structure determined by micro-XRD, where a more homogeneous composition and structure became apparent with increasing sintering time.

4.2. XRD of Sintered Constituents

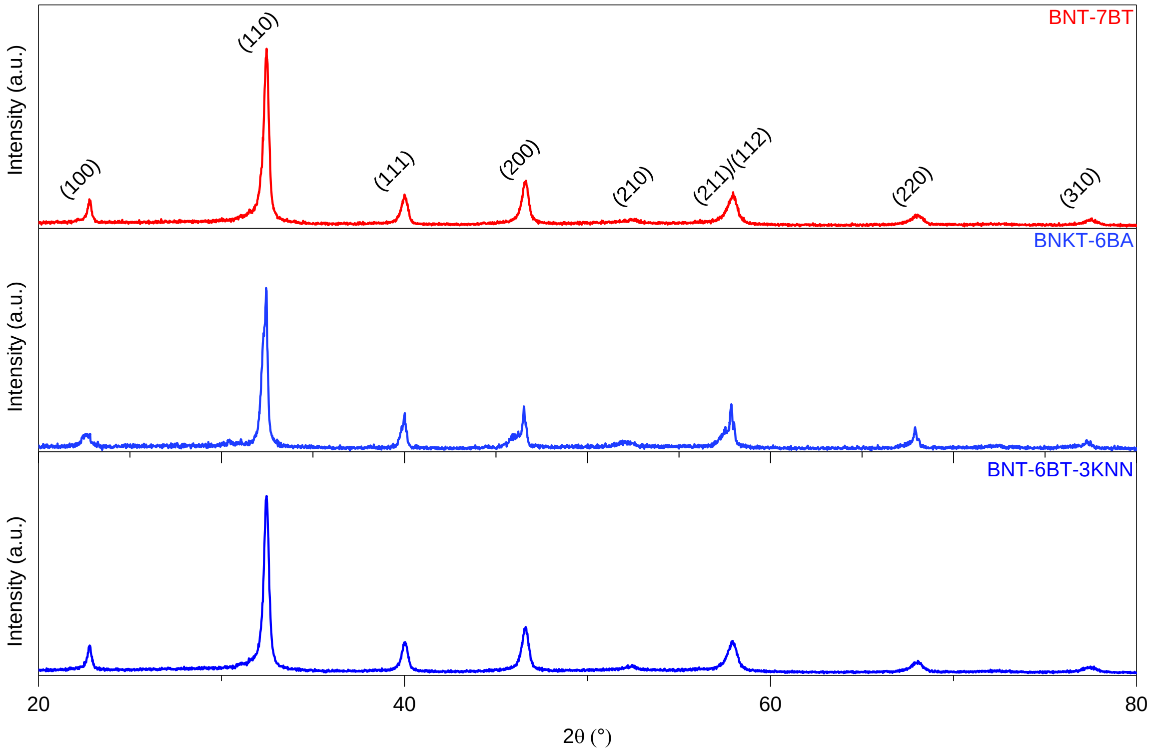

Figure 4.1: XRD patterns of BNT-7BT seed, BNKT-6BA and BNT-6BT-3KNN as matrix, from 20 to 80°

All of the materials used in this work show a perovskite structure in their final freely sintered state. No peaks indicative of a secondary phase are apparent in the diffraction patterns shown in Figure 4.1. The BNT-7BT and BNT-BT-3KNN diffraction patterns are nearly identical and appear pseudo cubic. The BNKT-6BA diffraction pattern shows a shoulder in the (200)/(002) peak indicative of a tetragonal phase, similar to previously published diffraction patterns for this material [108]. The BNT-BT-KNN and BNT-7BT diffraction pattern corresponds well to previously published data on the same material system [173].

4.3. BNT-6BT-3KNN/BNT-7BT Composites

4.3.1. Crystal Structure of BNT-BT-3KNN/10% BNT-7BT 2-2 composite

To better distinguish the influence of the composite system on crystal structure, micro-XRD was used to evaluate the local crystal structure of composites. The measurements were performed both on a laboratory-based Rigaku SmartLab XRD system at TYIT and at BL15 of the SPring8 synchrotron source in Aio, Japan by the author and Professor Shintaro Yasui. Details of this measurement are provided in the Experimental Methods section.

The diffraction patterns as taken across the full measurement spectrum from the 2θ range of 20 to 90° every 300 µm across the cross-section surface for the 10% 2-2 composite is shown in Figure 4.2 The middle region is the seed BNT-

7BT region and the top and bottom regions are BNT-6BT-3KNN, as co-sintered. The diffraction pattern of the matrix region in the composite has broader (111), (200), and (220) peaks relative to the freely sintered BNT-BT-KNN, with shoulders either to the right or left of the peak, indicative of a peak splitting. This is particularly pronounced in the (200) peak. Comparing the seed region of the composite to the pure BNT-7BT diffraction pattern, the (111) and (200) reflections are split in the composite and singlets in the freely sintered constituent.

Refinement of the diffraction patterns shown in Figure 4.2 (a) provides an understanding of the crystal structure as a function of position. Generally, pseudocubic reflections are considered a superposition of the reflections of the tetragonal and rhombohedral phases, which means that the average crystal structure is cubic within the resolution limit of the x-ray diffraction instrument used. In other words, local scale deviation can not be identified using conventional powder x-ray diffraction method [26]. Splitting of a pseudocubic peak enables, through Rietveld refinement, the evaluation of relative phase fractions between the tetragonal and rhombohedral phase. From Figure 4.2(b), it can immediately be observed that the seed region has a higher tetragonal phase fraction than the matrix regions. The ratio of the rhombohedral to tetragonal phase fraction is not uniform throughout the matrix region. In the matrix region to the left of the seed region, *i.e.,* from 300 to 1000 µm, the rhombohedral phase fraction increases. Throughout the sample, it remains a much lower proportion relative to the tetragonal phase.

The change in the lattice parameters of the tetragonal and rhombohedral phases as a function of position are shown in separate panels of Figure 4.2 (c) and (d) respectively. It can also be observed that the lattice parameters of the seed and matrix regions are not uniform. The value for c_{p4bm} is highest in the seed region, with a value of 3.945 Å. A similarly large c_{p4bm} can be observed at the interface between the seed and matrix regions. The a_{p4bm} lattice parameter is more uniform through the composite. For comparison, freely sintered BNT-BT-KNN has a c_{p4bm} of 3.94 Å and BNT-7BT has a c_{p4bm} of 3.91 Å. Therefore, the lattice parameters of the seed region increase in the composite structure relative to the pure seed.

For the rhombohedral parameters, the average difference for both a and c parameters between the two matrix regions is 0.05 Å. The cause of the difference in rhombohedral lattice parameters in the two matrix layers is not immediately clear, but may be due to a difference in stresses during sintering. The presence of stress during sintering is possibly influenced by the setup and sample orientation, where one matrix layer faced the bottom of the crucible, with traces of sacrificial powder, while the other was exposed to sacrificial powder and air. A clear increase in a_{r3c} can be observed from the first matrix region to the seed region, the lattice parameters at the interface region, (from 900-1200 µm) being 0.02 Å larger than the first 300 µm of the matrix region. Previous work by Khansur *et al.* did not observe any difference in lattice parameter between pure BNT-BT-KNN, BNT-BT, and the 0-3 mixed composites thereof [131]. Both 0-3 and 2-2 systems undergo chemical diffusion from one constituent to another. Therefore, it is hypothesized that the most likely difference in lattice parameter in the 2-2 composites is a result of the particularities of this structure, such as in-plane biaxial stresses, which will be discussed in more detail in the following chapters.

In Figure 4.3, a comparison is made between the freely sintered constituents and the respective region of the 10% 2-2 composite. For the BNT-7BT region, the (200) and (211) reflections are much broader, indicative of peak splitting, relative to the freely sintered constituent. In the BNT-BT-KNN region at the edge of the sample, from 100-300 µm, a splitting of the (200) reflection can also be observed, whereas in the freely sintered material it is a singlet indicative of pseudocubic reflections. There is also a slight shift to lower angles in the (110), (111) and (211) peak, indicating an increase in the lattice parameter.

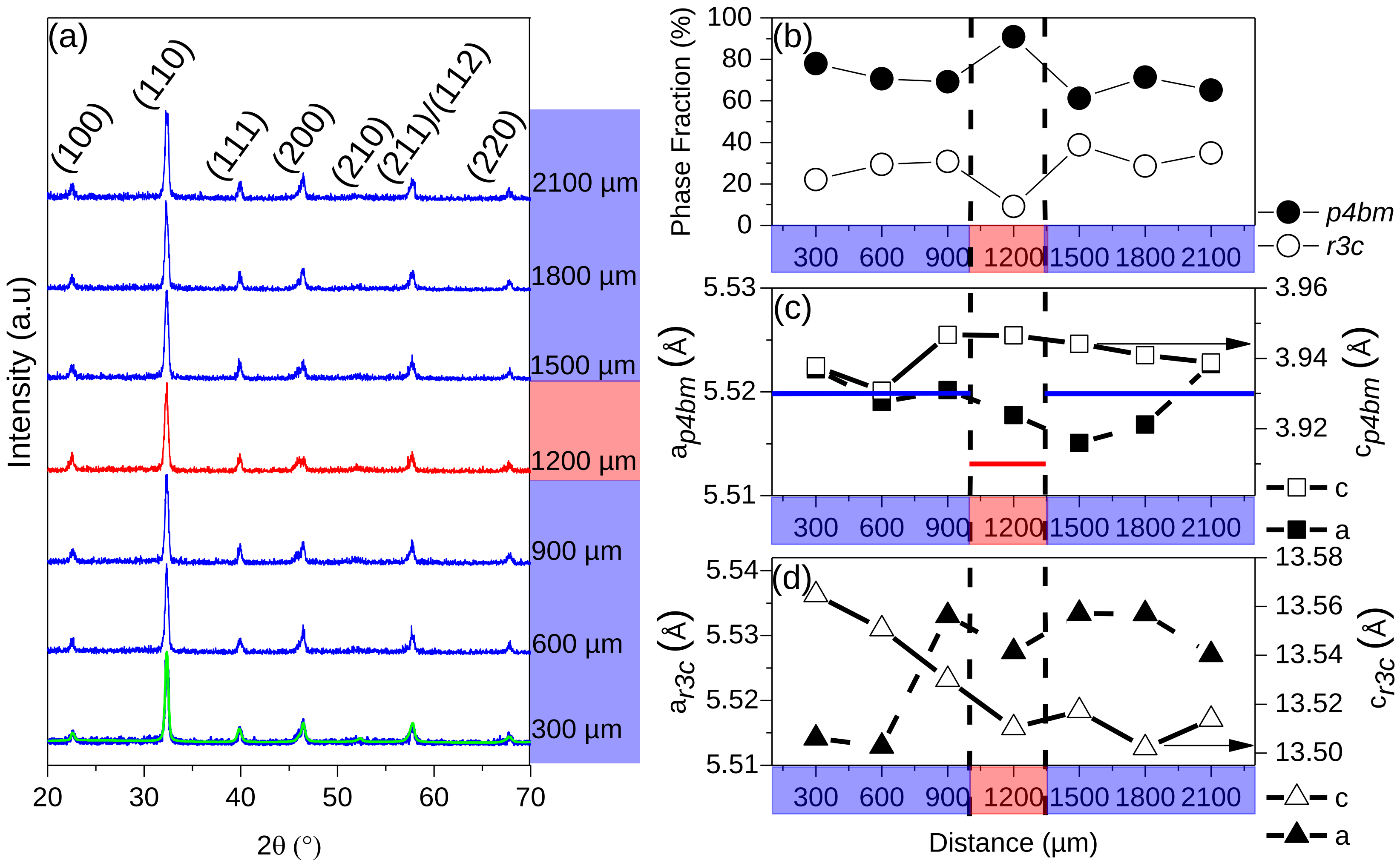

Figure 4.2: Micro-XRD of BNT-BT-KNN/BNT-BT 10% 2-2 composite with spot size resolution of 300 µm, full spectrum from 20° to 70°. The calculated diffraction pattern for the position at 300 µm is shown in green as an overlay on the experimental diffraction pattern as an example of refined structural data used to determine the crystal structure. (b) Phase fraction and lattice parameters of (c) p4bm and (d) r3c phase as a function of position. The a lattice parameter is displayed using the left axis and the c lattice parameter is displayed using the right axis, as indicated by the arrows. The boundaries of the seed and matrix areas are depicted by the red and blue rectangles along the x-axis, as well as dashed lines at the interface.

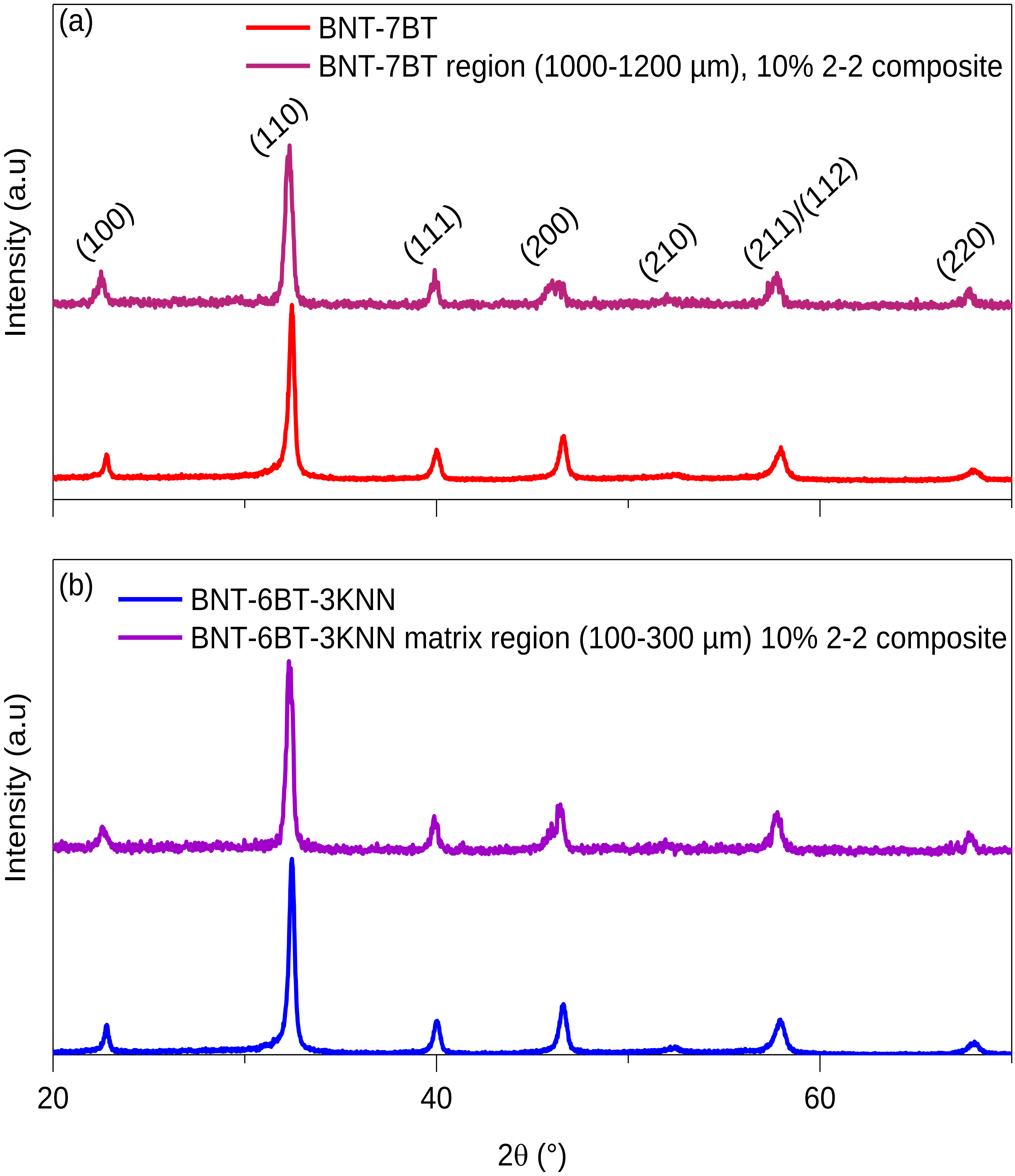

Figure 4.3: Comparison of XRD of (a) BNT-7BT and (b) BNT-BT-KNN freely sintered and in the 10% 2-2 composite thereof, from 20 to 70°

Based on the data obtained from the low-resolution laboratory XRD measurements, the (111) and (200) reflections were selected for further investigation by high-resolution XRD at the SPring8 Synchrotron source. Figure 4.4 depicts the (111) and (200) reflections of a 10% 2-2 composite of BNT-BT-KNN/BNT-BT across the sample, wherein the peak intensity is shown with a color map. The data collection began 0.3 mm from the top edge of the sample, and covered 1.6 mm of the sample, thereby encompassing both the seed/matrix interfaces. The spot size for each measurement was 10 µm x 10 µm, and was collected every 20 µm. These XRD patterns were analyzed in more detail in Figure 4.5 and Figure 4.6.

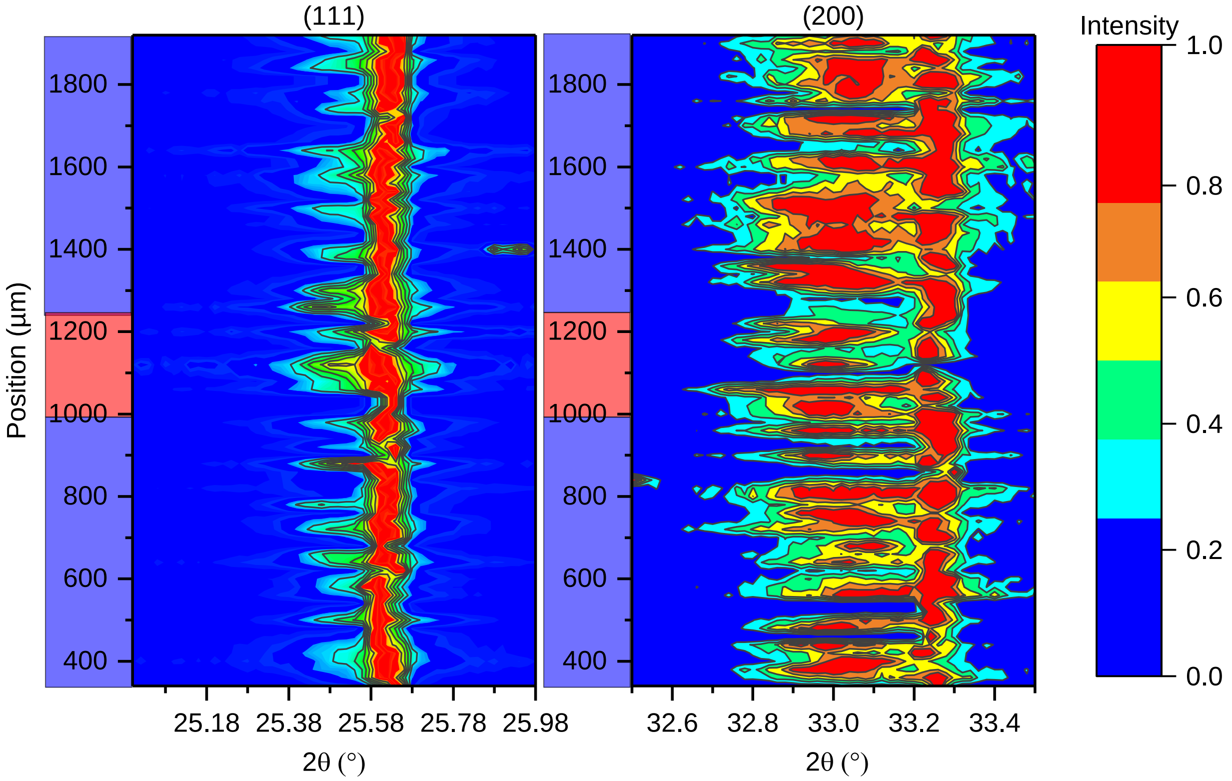

Figure 4.4: Dependence of diffraction profiles on position in BNT-6BT-3KNN/BNT-7BT 10% 2-2 composite at the (111) and (200) reflections, the red region from 990 - 1220 µm indicating the seed and the blue regions from 330 -990 and 1220 -1920 µm indicating the matrix components of the composite

In the seed region, at 1100 µm a shoulder at lower angles is apparent in both the (111) and (200) reflections. A similar diffraction pattern occurs at 1120 µm, precisely the center of the sample, with the shoulder of the (111) reflection increasing in intensity. The splitting of (111) and (200) peaks at 1120 µm points to the presence of a mixed rhombohedral/tetragonal phase. However, the diffraction pattern within the seed region is inhomogeneous. At 1140 µm, (111) reflection is broad and asymmetric in intensity, while the (200) reflection has shifted to a lower angle, with only a small shoulder visible for higher angles. This points to a predominantly rhombohedral phase at 1140 µm, whereas the broad (200) reflection at 1100 and 1120 µm can be interpreted as a superposition of the three reflections expected at this position for an orthorhombic phase. The low angle shoulder seen in the (111) peak at 1100 and 1120 µm further supports this hypothesis.

The XRD patterns of the matrix region are also inhomogeneous. For instance, there is a large difference in diffraction patterns at 500 and 520 µm: *e.g.*, the (200) reflection at 500 µm has a broad shoulder at lower angles, which at 520 µm is reduced in intensity by over 50%. The reduced splitting of the (200) peak at 520 µm points to the reduced presence of the tetragonal phase and a more predominant rhombohedral phase.

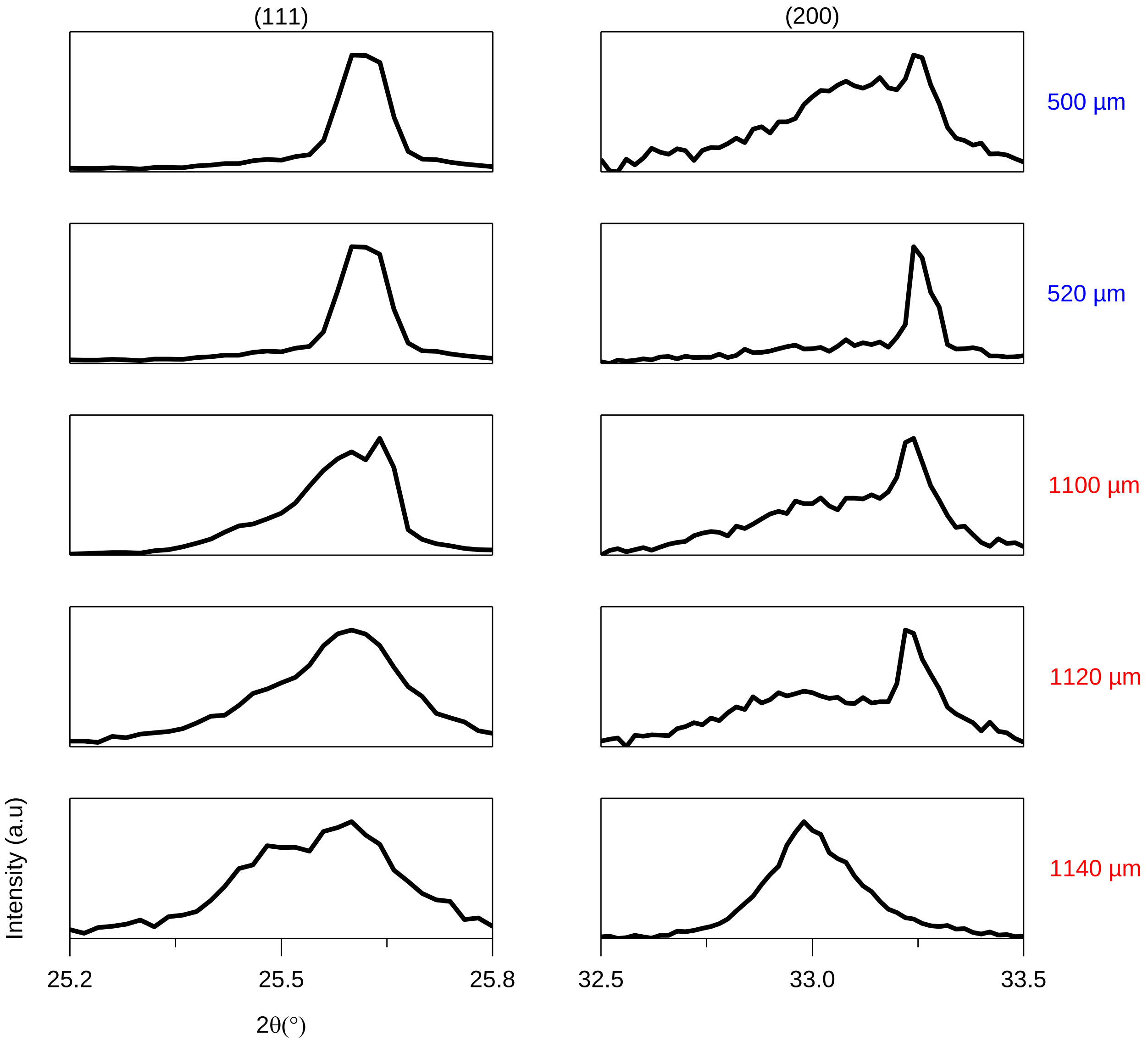

Figure 4.5: Normalized intensity of (111) and (200) reflections of 10% BNT-BT-KNN/BNT-7BT 2-2 composite in diffraction patterns of the matrix region at 500 and 520 µm, and the seed region at 1100, 1120 and 1140 µm of the 10% 2-2 BNT-BT-KNN/BNT-BT composite

In Figure 4.6, XRD reflections at the seed/matrix interface are shown, from 900 to 1040 µm, allowing a more detailed examination of the influence of co-sintering on the crystal structure of the composite. At 900 µm, the (111) reflection is broad, and this continues to be the case until 1020 µm, where a single (111) reflection dominates the diffraction pattern at both 1020 µm and 1040 µm. However, significant beak broadening can be observed in the (111) reflection at

980 µm. The (111) reflection at 1000 µm has a small shoulder at a lower angle and a predominant peak at a higher angle. In general, the FWHM of the (111) reflection narrows as the interface region is approached, and a shift to higher angles can be observed, the former indicative of a higher long-range order and the latter indicating a reduced lattice constant as the seed region is approached. The (200) reflection is generally much broader than the (111) reflection, particularly in the region of 900 to 940 µm. A tetragonal structure has 2 peaks in the (200) reflection, while an orthorhombic structure has 3, and the rhombohedral phase has 1. Therefore, this region can be interpreted as having a mixed phase composition, including an orthorhombic phase. There is a large peak at higher angles, and a broad reflection at lower angles. The larger peak observed at higher angles may therefore be a superposition of the higher angle orthorhombic and tetragonal reflections. The shoulder at lower angles diminish in intensity at 940 µm, but reappear at 960 µm and increase in intensity up to 1040 µm, where the lower angle peak has a higher intensity than the higher angle peak. The reduction in intensity of the peaks at lower angles implies a reduction of the orthorhombic phases at 940 µm. At 1020 and 1040 µm, the increased intensity of the lower angle (200) reflections imply a more dominant tetragonal phase. Changes in the FWHM can also be an indication of a change in microstrain and/or crystallite size. Both of these phenomena will be discussed in Chapter 5. Several areas of discontinuity can also be observed, which are apparent in both the normalized and unnormalized intensity values. These may be attributed to inhomogeneities in the composition and crystal structure of the composite at a smaller length scale than can be discerned continuously with the beam size used in this investigation.

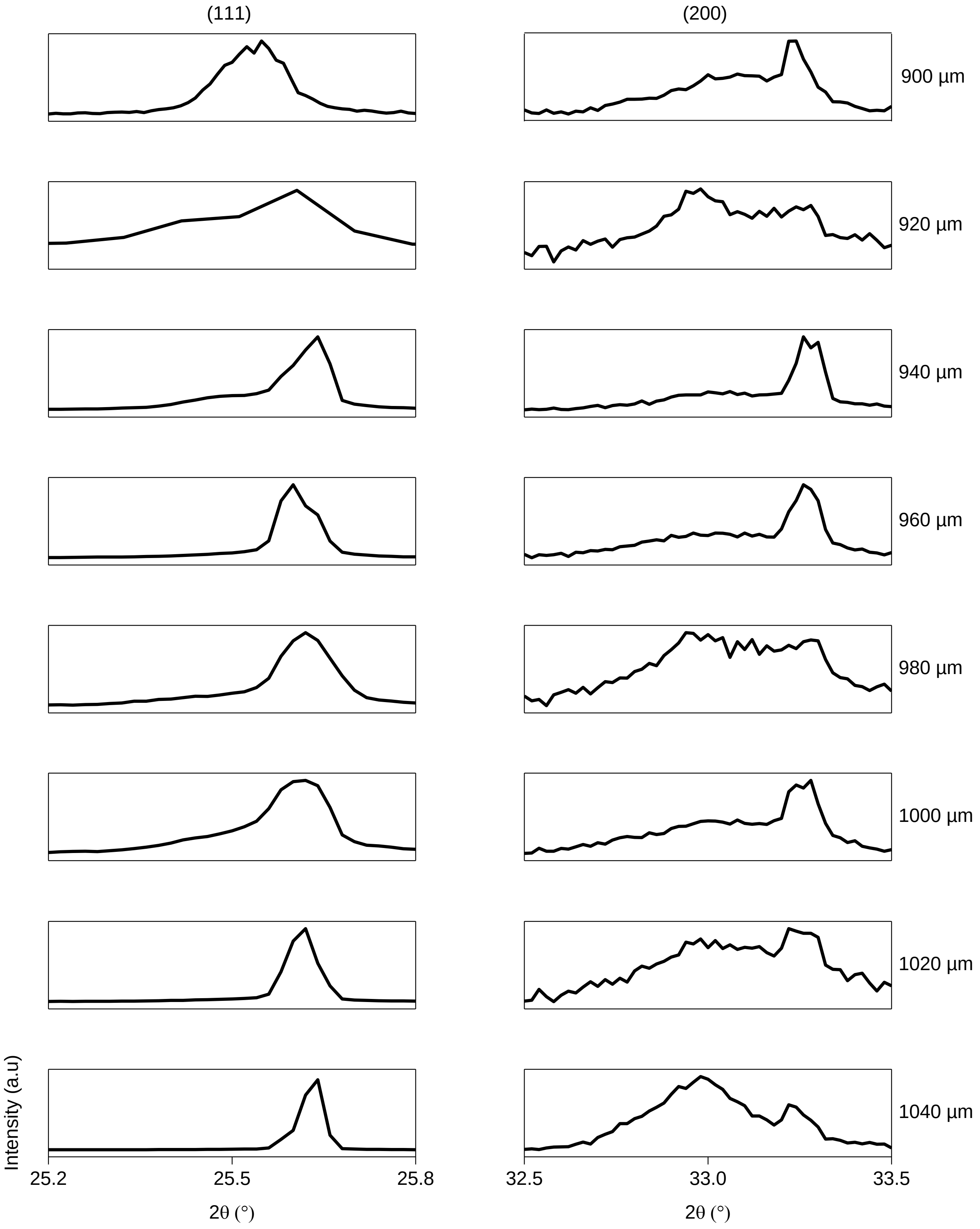

Figure 4.6: Normalized intensity of (111) and (200) reflections of 10% BNT-BT-KNN/BNT-7BT 2-2 composite analysis in the interface region of 900-1040 µm of the 10% 2-2 BNT-BT-KNN/BNT-BT composite

4.3.2. Crystal Structure of BNT-BT-3KNN/20% BNT-7BT 2-2 composite

Further investigations of the crystal structure in the BNT-BT-KNN/BNT-BT 2-2 composite system were performed by examining a 20% BNT-BT sample. The diffraction patterns across the full spectrum from 20° to 90° collected every 300 µm are shown in Figure 4.7. In comparison to the diffraction pattern of the pure BNT-6BT-3KNN, in the matrix region the (111), (200), and (220) reflections are broader and have shoulders either to the right or left of the primary peak, indicative of peak splitting. This is particularly pronounced in the (200) reflection, similar to observations in the 10% BNT-BT composite (see Figure 4.3).

In Figure 4.7(a), the XRD patterns across the sample for the full spectrum from 20° to 90° are shown. Comparing the seed region of the composite to the pure BNT-7BT diffraction pattern, the (111) and (200) reflections are split in the composite and singlets in the freely sintered constituent. The two diffraction patterns in the seed region are not identical: the (110) reflection at 900 µm has a lower shoulder at higher angles, whereas at 1200 µm a double (110) peak can be observed. In addition, the (200) reflection at 900 µm slopes downward to the left of the peak, while at 1200 µm the reflection is broad and uniform.

A comparison between the freely sintered constituent and its respective component of the 2-2 composite is shown in Figure 4.8. As in the 10% composite, a peak splitting of the (200) reflection can be observed in the BNT-7BT region, whereas in the freely sintered BNT-7BT the (200) reflection is a singlet indicative of pseudocubic reflections. Furthermore, all peaks shift an average 0.4° to lower angles relative to the freely sintered constituent can also be observed for all peaks, indicative of an increased lattice constant.

In the BNT-BT-KNN matrix region, the (111), (200), and (210) reflections all have split peaks, whereas the freely sintered matrix material has single peaks at these reflections. Such peak splitting appears to point to an increased rhombohedral phase in the composite matrix relative to the freely sintered constituent. Unfortunately, the noise associated with micro-XRD at this length scale makes it difficult to thoroughly ascertain the crystal structure. The (111) reflection must also be split for a rhombohedral phase to be present in the composite, and this reflection is not clear enough to make such an assertion. However, as will be shown in the next pages, high resolution XRD patterns obtained for the (111) and (200) reflection at the SPring8 Synchrotron point to a more complex, inhomogeneous crystal structure, with some regions showing clear peak splitting in the matrix phase that support the presence of a rhombohedral phase therein, and others showing a single (111) peak and a broad (200) peak indicative of an orthorhombic phase.

From the refinements performed on the structure shown in Figure 4.7 (b)-(d), it is clear that in the seed region, the amount of tetragonal phase increases and the amount of rhombohedral phase decreases. This shift is less pronounced than in the 10% composite, where an increase in 30% of the tetragonal phase was observed between the matrix to the seed, whereas in the 20% composite the increase in tetragonal phase is 20%. The lattice parameters of the tetragonal phase are noticeably larger in the seed region than in the matrix region, with an increase of 0.02 Å in the average value of the *c* and *a* lattice parameters. The *c* lattice parameters of the rhombohedral phase are smaller in the seed region than in the matrix region, dropping by 0.06 Å but increasing more gradually to the right of the seed layer. The *a* lattice parameter of the matrix increased gradually from 300 to 900 µm, but a sharp jump occurs at 1500 µm, where the second seed/matrix interface region is located.

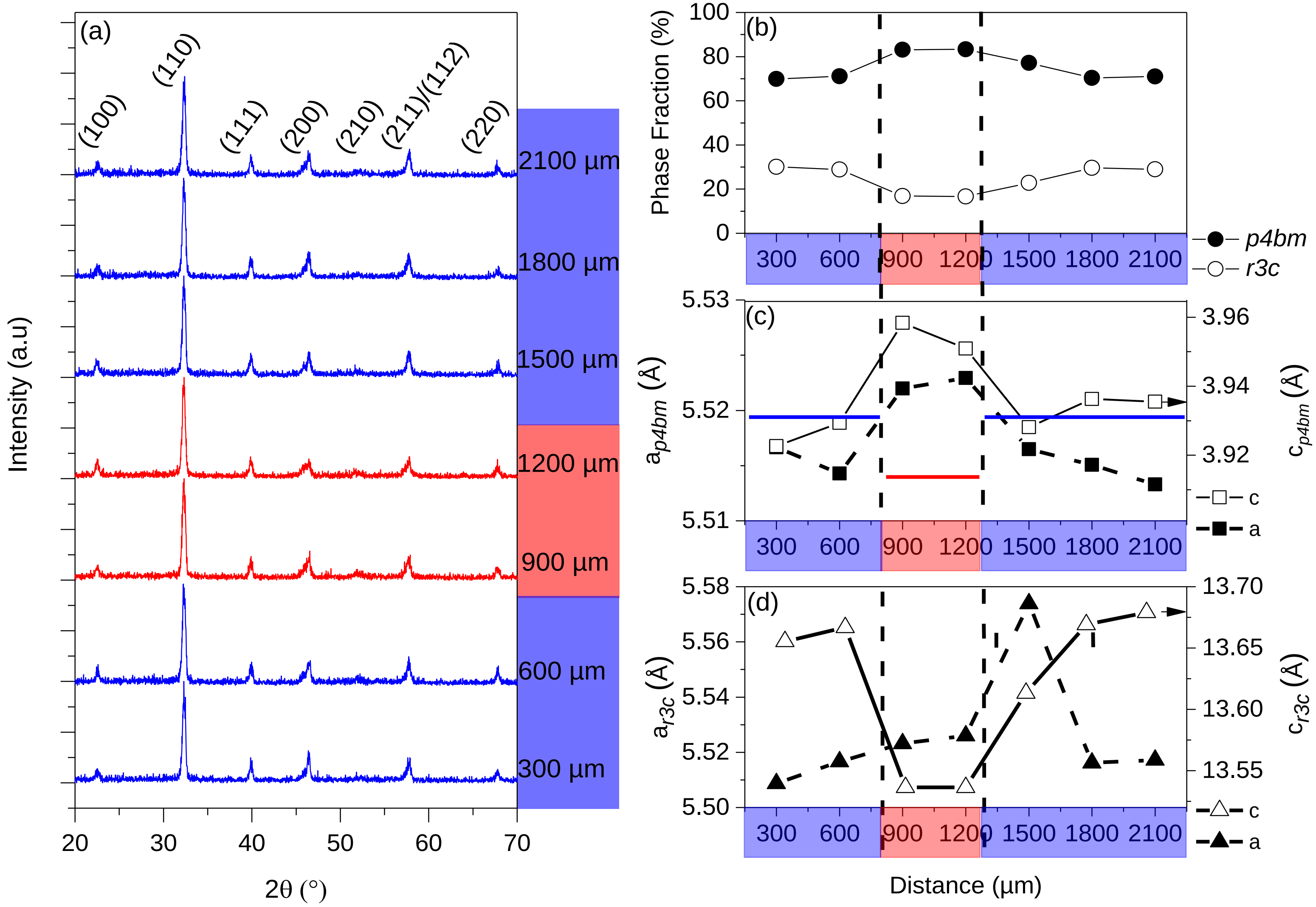

Figure 4.7: (a) Micro-XRD of BNT-B T-KNN/BNT-BT 20% 2-2 composite with spot size resolution of 300 µm, full spectrum from 20° to 70°. (b) Phase fraction and lattice parameters of the (c) p4bm and (d) r3c phases are shown on the right. The a lattice parameter is displayed using the left axis with closed squares and the c lattice parameter is displayed using the right axis using open squares, as indicated by the arrows. The boundaries of the seed and matrix areas are depicted by the red and blue rectangles along the x-axis, as well as dashed lines at the interface.

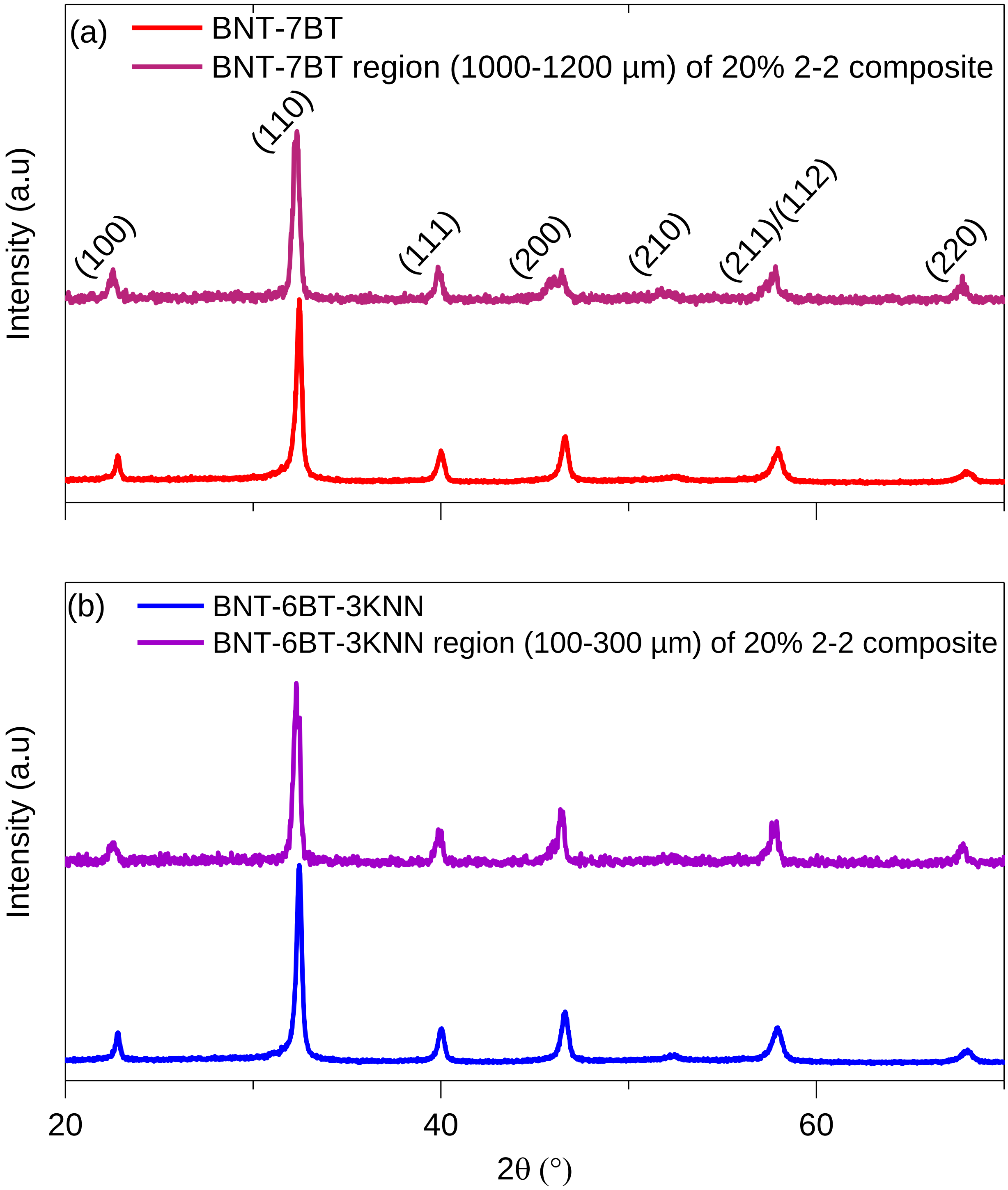

Figure 4.8: Comparison of XRD of (a) BNT-7BT and (b) BNT-6BT-3KNN freely sintered and in the 20% 2-2 composite thereof, from 20° to 70°

To obtain more detailed diffraction data, the (111) and (200) peaks were evaluated at BL15 of the SPring8 synchrotron source. The results of that investigation are shown in Figure 4.9. The measurement parameters were identical to those described for the 10% composite of this system.

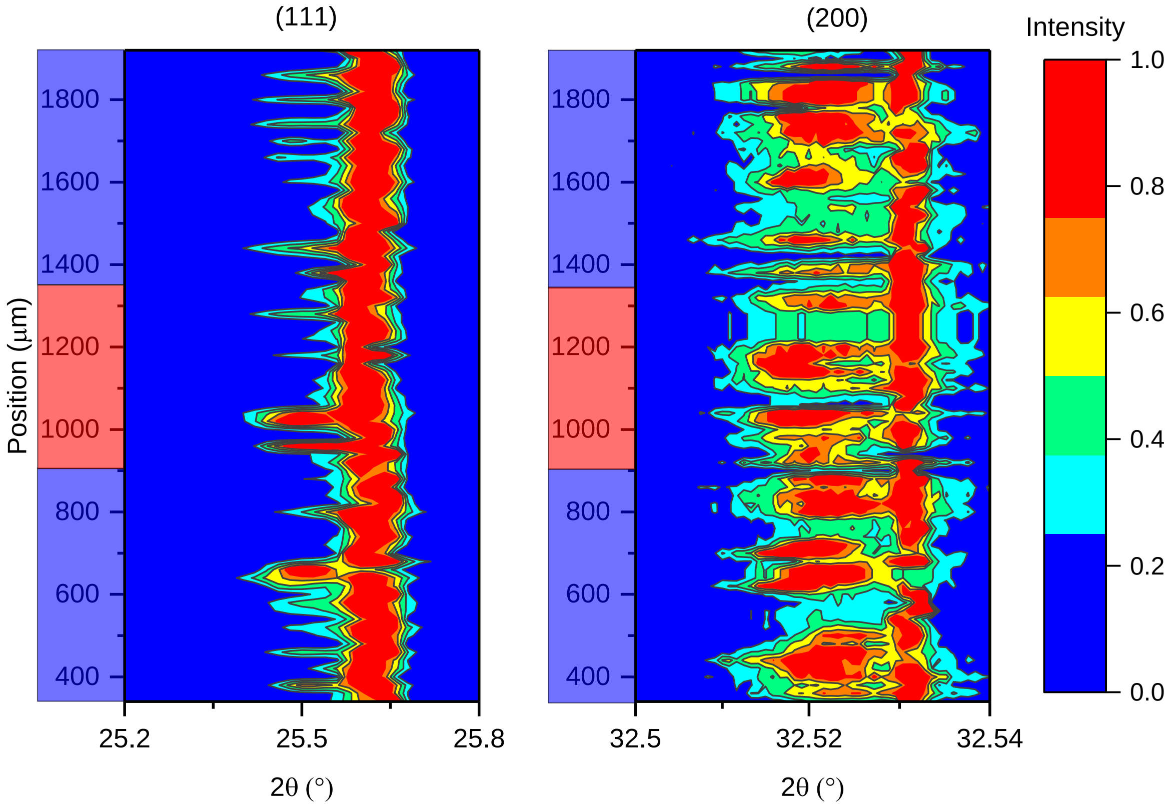

Figure 4.9: Normalized intensity of (111) and (200) reflections of 10% BNT-BT-KNN/BNT-7BT 2-2 composite in diffraction patterns of the matrix region at 500 and 520 µm, and the seed region at 1100, 1120 and 1140 µm of the 10% 2-2 BNT-BT-KNN/BNT-BT composite

In the majority of the matrix region, a single peak in the (111) reflection and a split (200) peak can be observed, characteristic of a tetragonal phase. There are, however, several areas in the bottom matrix region that shows (111) peak splitting, *e.g.*, at 340 µm, 420 µm, and 600 - 660 µm. In those regions of the matrix phase that have a split (111) reflection, a mixed tetragonal and rhombohedral crystal structure can be assigned. The top matrix region differs in its diffraction pattern from the bottom matrix region. The inhomogeneity of crystal structure observed in the matrix phase may be attributed to a number of factors, including interdiffusion as well as inhomogeneity of internal stress distribution. In the regions of 780-880 µm and 1620-1820 µm, there are several areas of the sample where a triple peak can be observed in the (200) reflection. A strong (111) peak broadening can also be observed at the same positions. Such a diffraction pattern may be indicative of either a mixture of rhombohedral and tetragonal phases, or rhombohedral, tetragonal and orthorhombic phases. The bottom matrix region shows a significant shift of the (111) peak to lower angles and broadening of the (200) peak in two positions, from 420 – 500 µm and 620 – 740 µm.

To examine the interface region more closely, several diffraction patterns in the matrix region and seed/matrix interface region are shown in Figure 4.10. At 560 µm, the (111) reflection has a shoulder at lower angles, and the (200) reflection has a sharp peak at 33.3° and a broad low angle shoulder. The broadness of the (200) reflection may be attributed to an orthorhombic phase, in which the (111) peak also shifts to a lower angle, possibly associated with the shoulder observed at lower angles [174]. Therefore, at 560 µm it can be hypothesized that there is a mixed composition of orthorhombic and rhombohedral phases. The presence of a tetragonal phase cannot be excluded, however, because such a phase would result in a split (200) reflection that overlaps with the orthorhombic (200) reflection. As the interface is approached, the lower angle (200) reflections increase in intensity, possibly indicative of a more predominant orthorhombic fraction. A shift of the (111) and (200) peaks to lower angles can be observed at 960 µm, close to the seed/matrix interface. Such a shift to lower angles is indicative of a higher lattice constant. In addition, the (200) reflection at 960 µm has a pronounced sharp peak at 33.24° and a broad diffuse peak at lower angles This diffraction pattern may also be attributed to the presence of an orthorhombic phase. In Figure 4.7, the large-scale 300 um region examined from 600-900 um showed a similar splitting of the (200) peak, indicating that the average diffraction pattern for this region corresponds to the one observed using high resolution micro-XRD. In addition, the broad (100) and (110) peaks in this region, as shown in Figure 4.7, further point to a mixed tetragonal and rhombohedral phase. However, orthorhombic crystal structures can also result in such a diffraction pattern, and a definitive statement on the absence thereof can therefore not be made.

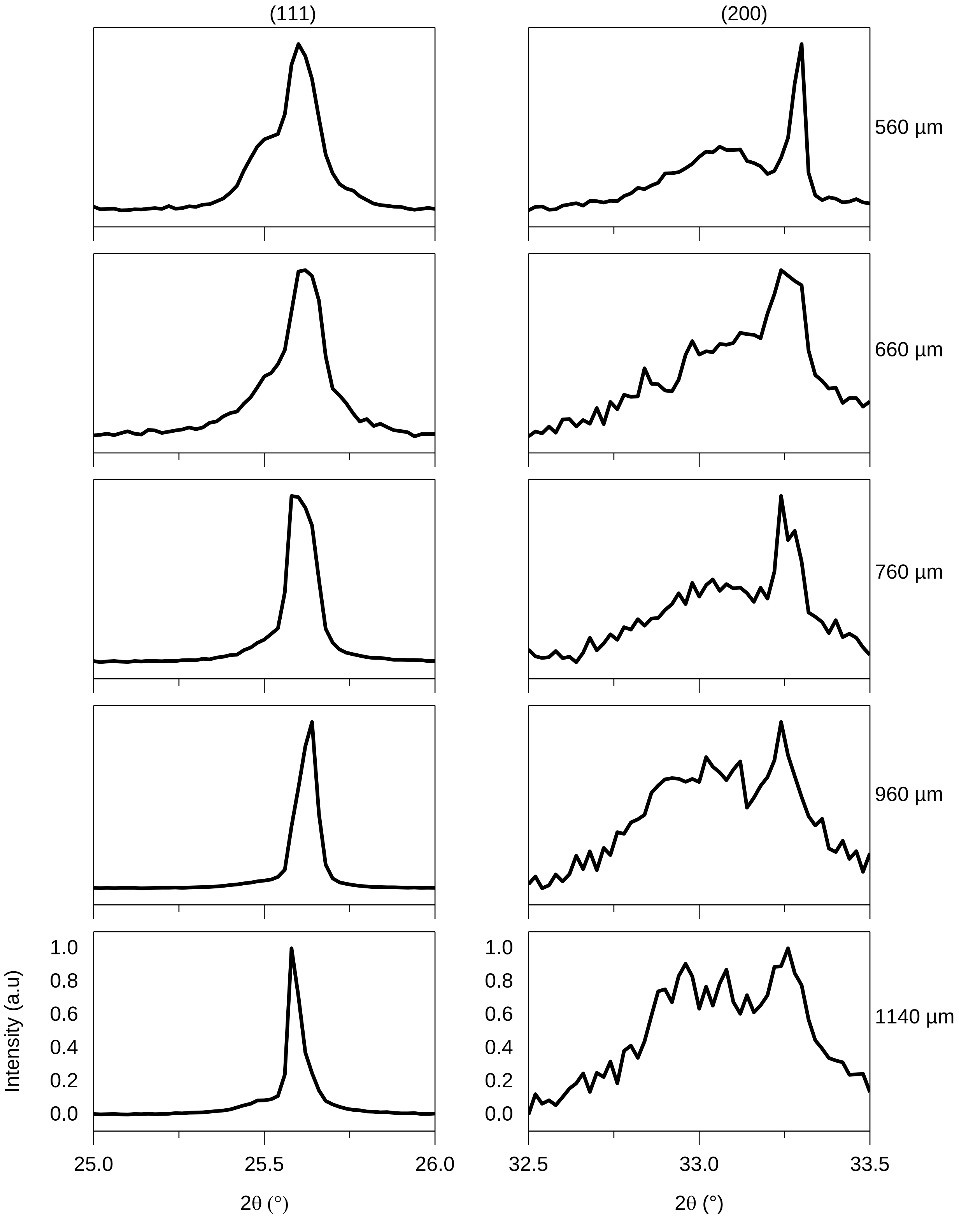

Figure 4.10: Normalized intensity of (111) and (200) reflections of 20% BNT-BT-KNN/BNT-7BT 2-2 composite from the bottom matrix region at 560, 660, 760, 960 and 1140 µm, with the deconvoluted peaks shown with a thin black line and the cumulative peak fit shown with a dotted orange line

Evidence of an orthorhombic phase evolving from co-sintering was found in 0-3 composites of BNT-BT-KNN/BNT-BT by Schmitt *et al.* Because these results were not published, they are reproduced for reference in Figure 4.11. This orthorhombic fraction was not previously observed in freely sintered BNT-BT-KNN or BNT-BT and can be attributed to a high concentration of $KNaNbO_3$, which is known to have an orthorhombic phase at 25 °C [94]. It is, therefore, likely that in the 2-2 composite, an accumulation of the KNN phase at the interface similarly results in the presence of an orthorhombic phase.

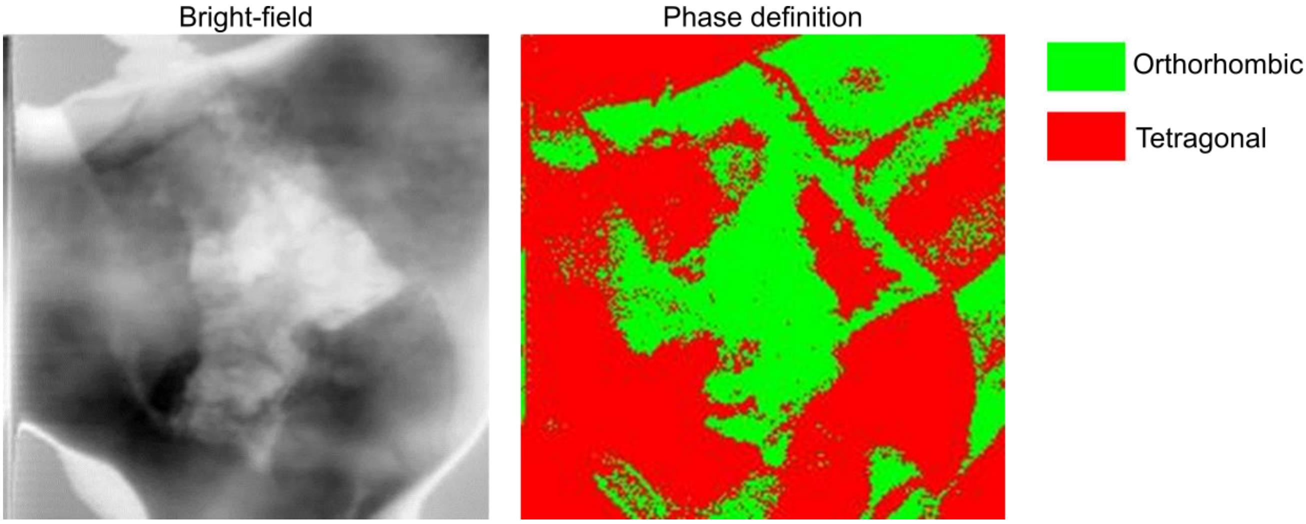

Figure 4.11: TEM Bright-field image and associated phase definition of BNT-6BT-2KNN/10%BNT-6BT 0-3 composite, obtained by ASTAR automated phase and orientation mapping. TEM results obtained by Dr. Ljubomira Schmitt, samples prepared by Dr. Claudia Groh in 2014, used with permission

A direct comparison of lattice parameters in the freely sintered end members and equivalent component of the composite is shown in Table 3. The *a* lattice constant in the composite for both the seed and matrix is significantly larger than the freely sintered sample. The *c* lattice constant, on the other hand, increases for BNT-7BT relative to the freely sintered constituent. In the matrix region, however, only a slight increase is observed in the 10% composite. With 20% seed, a decrease in the *c* lattice constant occurs in the matrix. However, the *c* lattice constant is inhomogeneous throughout the matrix region.

Previous work has shown that the (111) and (200) reflections appear to be singlets in bulk powder diffraction in pure BNT-BT-KNN and BNT-BT. This makes it challenging to distinguish the two constituents structurally because the bulk reflections provide a picture of the average local structure, which appears to be pseudocubic in both materials. The most notable difference observed between the two is a slight reduction of the *a* lattice parameter in BNT-BT-KNN [78]. However, the B-site in BNT-BT-KNN is shared between Ti (0.605 Å) and Nb (0.69 Å), resulting in an increased c_{p4bm} lattice parameter in BNT-BT-KNN as compared to BNT-BT [78].

Table 3: Tetragonal Lattice parameters of BNT-7BT and BNT-6BT-3KNN, freely sintered and in 2-2 composite

	BNT-6BT-3KNN (free)	*BNT-6BT-3KNN (10% composite)*	*BNT-6BT-3KNN (20%composite)*	*BNT-7BT (free)*	*BNT-7BT (10% composite)*	*BNT-7BT (20% composite)*
a (Å)	*3.886*	*5.522*	*5.512*	*3.90*	*5.5177*	*5.522*
c (Å)	*3.930*	*3.938*	*3.922*	*3.91*	*3.9465*	*3.951*

One possible explanation for the changes in lattice parameter observed in the composites is chemical interdiffusion. The gradient in niobium and potassium content, albeit small, could result in migration of those species from the matrix into the seed region. Niobium, whose ionic radius is 0.785^{+} 4^{+}[175], has a slightly larger ionic radius than the B-site cation of Ti^{4+} in BNT-BT, which could result in an increased lattice constant. Similarly, a reduction in the K content of the matrix region could result in a reduced lattice constant, as was observed in this work. Previous work in BNKT-BA has shown that increased K content results in an increase in the lattice parameter, or a shift of the peaks to lower angles [109]. The Ba content has also been shown to influence the crystal structure of BNT-BT-KNN, where the splitting of the (200) reflection and the *c/a* ratio showed a strong dependence on Ba content [176].

A further explanation for changes in the lattice constant could be the presence of internal stresses: a tensile stress would result in expansion of the *c* and *a* lattice parameters, and a compressive stress would result in a decrease of the lattice parameters. A more in-depth discussion of internal stresses due to co-sintering will follow in Chapter 5.

The formation of an orthorhombic phase due to diffusion of K and Nb from the matrix into the seed cannot be ruled out. The single peak (111) reflections and very broad (200) reflections that can be deconvoluted into multiple peaks at the interface regions correspond well to the reflections of an orthorhombic phase. The complete picture of crystal structures formed as a consequence of the composite is quite complex. It can be stated, however, that there is evidence of both lattice strain and possible new phases formed in the composite.

4.4. BNKT-6BA/BNT-7BT Composites

Investigating chemical composition across the BNT-6BT-3KNN/BNT-7BT composites has proven very challenging due to the small chemical gradient between the seed and matrix phases, which are at the detection limit of standard EDS devices. Therefore, a model composite system was proposed with a higher chemical gradient between the seed and matrix.

The system BNKT-6BA/BNT-7BT, where BNKT-6BA is the ER matrix, and BNT-BT is the NR seed, was used because it enables tracking of Al and K into the seed region and Ba into the matrix region. The matrix contains 11.5 mol% K and 6 mol% Al, resulting in a higher gradient of the diffusing elements than in the BNT-6BT-3KNN system described above.

4.4.1. Chemical Composition and Crystal Structure in 0-3 BNKT-6BA/BNT-7BT Composites

Initial investigations of the influence of co-sintering were performed in 0-3 composites of BNKT-6BA/BNT-7BT using TEM and SAED to obtain information on the crystal structure at the granular length scale. These measurements were performed and analyzed by Dr. Leopoldo Molina-Luna and Dr. Michael Durrschnabel.

The high angle annular dark field scanning transmission electron microscope (STEM HAADF) image of a 50% 0-3 composite of BNKT-6BA/BNT-7BT is shown in Figure 4.12, along with the associated EDS spectra collected at 5 positions from the image. Highlighted in red are the Al contents at position 2 and 4, which are both pores. The Al content in these pores is at least 2 times higher than the Al content collected at other spectra. It is interesting to note that the K content at these positions is also higher, however at point 5 the K spectra is also higher. Therefore, it can be assumed that at position 3, a grain that was originally the matrix material is located, and at position 1, a grain that was originally BNT-7BT is located. From this image, it can be concluded that the presence of pores has an effect on the distribution of Al and K in the composites, serving as sinks for diffusing species and possibly forming new chemical phases within the composite.

Figure 4.13 shows the TEM bright field images and diffraction patterns of two grains from the 50% 0-3 composite sample. These diffraction patterns provide an understanding of the change in lattice constants and crystalline phase due to interdiffusion between the seed and matrix. An analysis of the cubic reflections gives an *a* lattice constant of 3.9136 Å for both grains, while bulk XRD of pure BNKT-6BA and pure BNT-7BT give a value of 3.90, revealing a slight enlargement of the lattice constant. However, this difference in values falls within the order of the measurement error of reciprocal lattice space lengths from TEM diffraction.

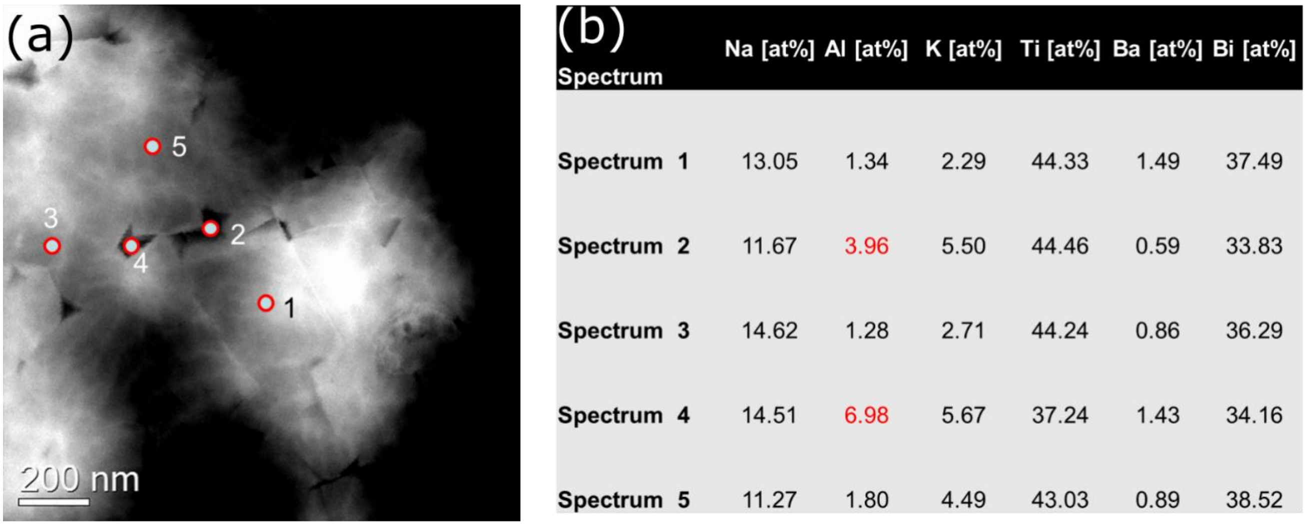

Spectrum	Na [at%]	Al [at%]	K [at%]	Ti [at%]	Ba [at%]	Bi [at%]
Spectrum 1	13.05	1.34	2.29	44.33	1.49	37.49
Spectrum 2	11.67	3.96	5.50	44.46	0.59	33.83
Spectrum 3	14.62	1.28	2.71	44.24	0.86	36.29
Spectrum 4	14.51	6.98	5.67	37.24	1.43	34.16
Spectrum 5	11.27	1.80	4.49	43.03	0.89	38.52

Figure 4.12: (a) STEM-HAADF of BNKT-6BA/BNT-7BT 50% 0-3 composite (b) Table of Na, Al, K, Ti, Ba and Bi content at 5 points in the sample

Kim *et al.* have previously shown that BNKT-BA is characterized by superlattice spots in selected area diffraction patterns (SADP) indexed as ½ (eoo), which are generated from the in-phase octahedral tilt symmetry of the *P*4*bm* tetragonal space group [148]. In the same work, the presence of ½ (ooo) superlattice spots, (characteristic of a rhombohedral phase), was observed in BNKT-BA composites upon the addition of ferroelectric BNKT as a seed material. For the seed phase in this work, BNT-BT has previously been shown to have both ½ (ooo) and ½ (ooe) reflections, indicative of a mixed tetragonal and rhombohedral phase [177]. Therefore, the presence of rhombohedral reflections in the grains of the 0-3 composite shown in Figure 4.13 can be attributed to the presence of BNT-7BT in the composite.

An analysis of the rhombohedral reflections for both grains shows a significant difference in crystal structure, with grain 1 having *a* lattice constant of 1.14 Å and *a* lattice angle of 105˚, and grain 2 having *a* lattice constant of 1.21 Å and *a* lattice angle of 52˚. These lattice angle values suggest that the rhombohedral phase experiences high distortion from the cubic 90˚ angle in both grains. Pure BNT-BT should be predominantly tetragonal with a 90 ˚ angle, as was observed by Schmitt *et al.* in BNT-6BT [177]. Previous work on BNKT-BA has demonstrated a reduced distortion of the rhombohedral structure relative to BNKT [108]. Therefore, the high degree of rhombohedral distortion observed here can be attributed to the influence of the composite system on the crystal structure.

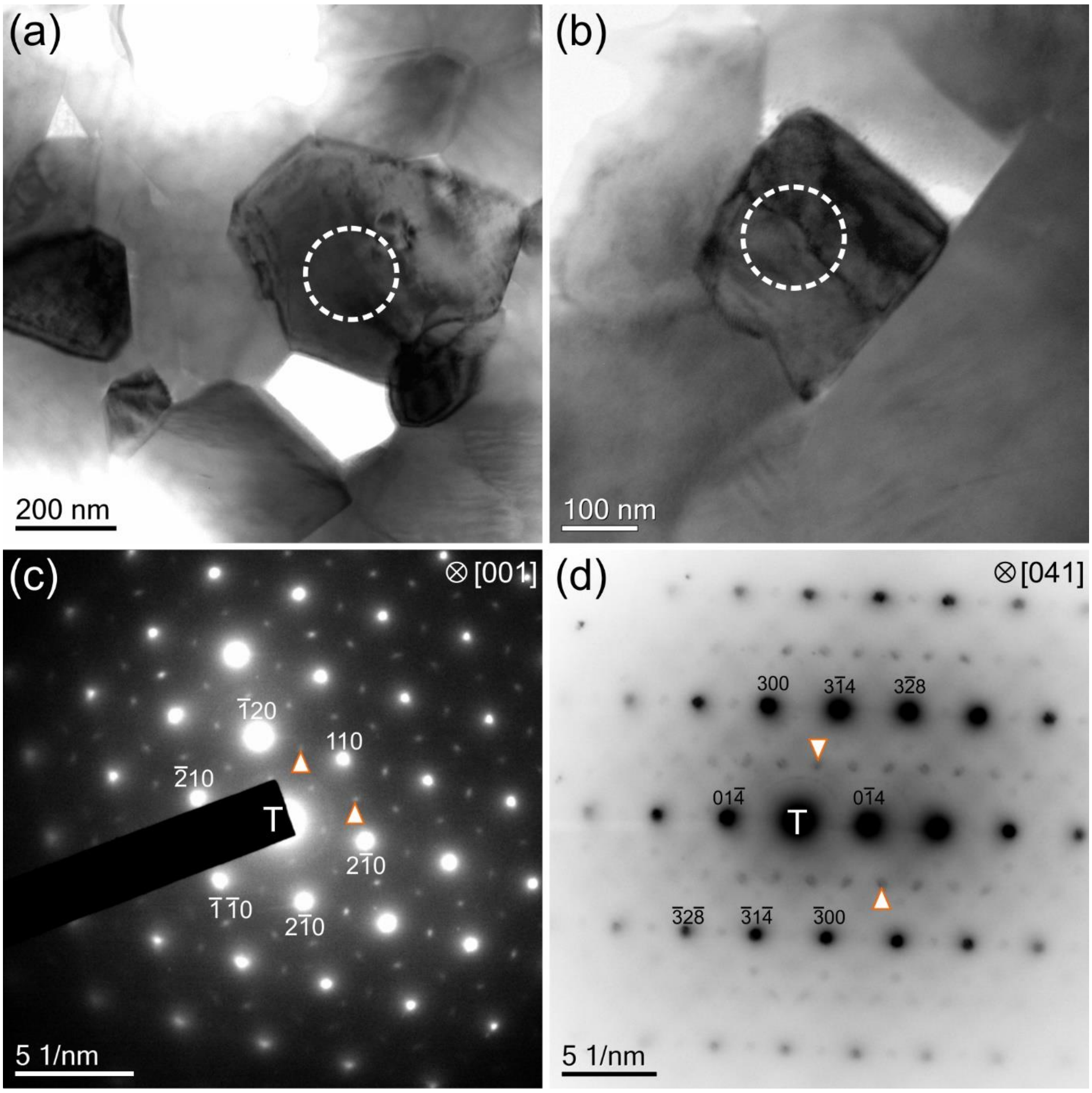

Figure 4.13: TEM bright-field images of BNKT-6BA/BNTBNT-7BT 50% composite. (a) Grain 1 (b) Grain 2 (c) SAED pattern for Grain 1 (d) SAED pattern for Grain 2 with arrows indicating ½ (ooo) reflections

4.4.2. Interdiffusion in 2-2 BNKT-6BA/BNT-7BT Composites as a Function of Composition

To facilitate the investigation of interdiffusion, EDS of 2-2 composites was performed, as shown in Figure 4.14**,** specifically tracking the diffusion of Ba, K and Al between the matrix and seed layers. These measurements were performed and analyzed with the assistance of Dr. Leopoldo Molina-Luna and Dr. Michael Dürrschnabel. The use of SEM further enabled larger scan areas, making it easier to observe an average chemical interaction, whereas TEM investigations present much larger challenges to obtaining a statistical overview of the sample, as only a few grains can be investigated at a time. The nominal value of Al, 6 at. %, in the matrix is shown with a blue line across the top, and the approximate seed region is shown with a green rectangle in each graph, while the Ba content of the pure BNT-7BT seed is 7 at. %, the maximum of each graph. The Ba, Al and K concentrations were measured by collecting spectra in 10 points along a line parallel to the interface between seed and matrix and calculating the mean value and standard deviation for each line. A total of 50 lines with a spacing of 50 µm were collected starting 50 µm from the top sample edge (at left in the figure). These results show that components of the matrix material diffuse throughout the seed material, as the presence of Al and K can be detected throughout the seed region.

According to the theory of kinetics of materials, an error function can be fit to the composition across the 2-2 composite:

$$c(x) = \frac{c_0}{2}\left[erf\left(\frac{x + x_{01}}{4\sqrt{Dt}}\right) - erf\left(\frac{x - x_{02}}{4\sqrt{Dt}}\right)\right] \tag{4.1}$$

where c_0 is the initial concentration of the element, x_{01} and x_{02} are the positions at which $c(x) = c_0$, and D is the diffusivity of the element [178]. Using the experimental values, the diffusivity for a given sintering time can can be determined, *i.e.* $D^* = Dt$. This equation functions as a model for diffusion where, for ease of calculation, constant diffusivity is assumed. This is clearly a simplification of the actual behavior of the chemical composition within the composite, as diffusivity is also strongly dependent on concentration, which changes with time as more diffusion takes place. However, this model suffices to provide insight into a relative measure of the difference in diffusivity between Al and K.

This analysis determined that the diffusivity of Al increased with increasing seed content, as shown in Figure 4(f). The diffusivity of Al is nearly identical (within the error measurement) in the 30, 40, and 50% compositions of the 2-2 composites. On the other hand, the diffusivity of K has a nonlinear relationship with seed content. The highest diffusivity, 210,349 µm^2, is observed in the 10% seed sample, and drops an order of magnitude to 20,729 µm^2 at 20% seed. However, due to the noise in the 10% EDS signal, the fit of the error function for this sample is questionable. An increase in the K diffusivity can be observed with increasing seed content from 20 to 40% seed, but at 50% seed the diffusivity decreases to 30,904 µm^2. The diffusivity of K is an order of magnitude higher than the diffusivity of Al.

Based on the strong fit to the error function of diffusivity, it can be assumed that diffusion of Al and K occurred through the bulk of the grain and not along grain boundaries. Further evidence of bulk diffusion requires more detailed TEM investigations due to the difficulties of resolving chemical composition by EDS-SEM in small grains (0.3-0.5 µm). Previous work in composites with BNKT-BA as an ergodic relaxor matrix with the use of BNKT-1.5BA was previously described by Lee *et al.* [2] and Jeong *et al.* [150]. Differing from the aforementioned works, in the present study a seed with $BaTiO_3$ was used, and the presence of Ba was observed in the BNKT-BA matrix layer, which was not in the original matrix member.

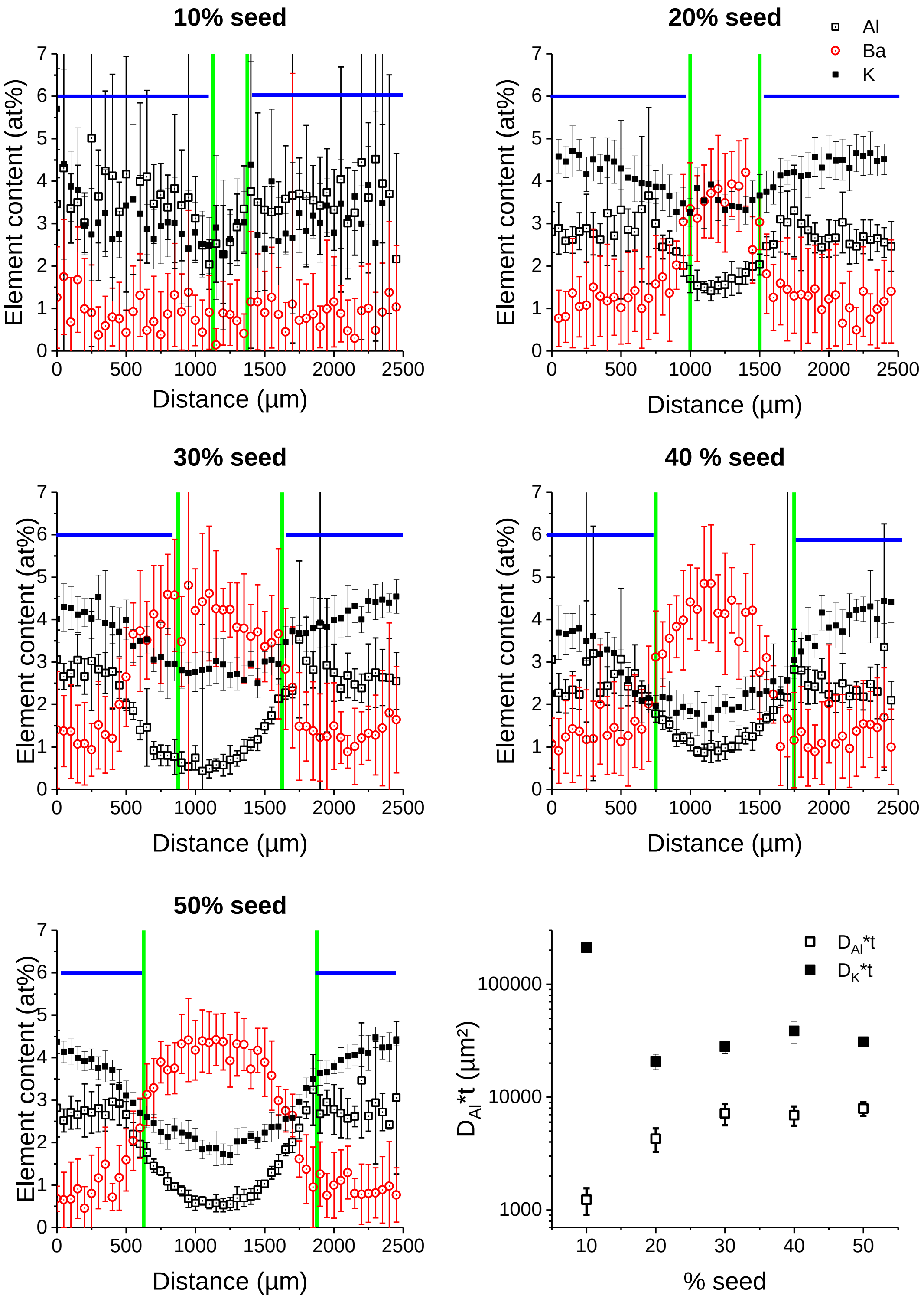

Figure 4.14: Distribution of Al, K and Ba through the thickness of 2-2 composites with (a) 10% (b) 20% (c) 30% (d) 40% and (e) 50% seed content, as measured with EDS. The diffusivity constant of Al and K as a function of seed content is presented in (f) with a logarithmic scale on the Y axis. The nominal value of Al content is shown with a blue line across the top, and the nominal seed region is shown with a green rectangle in graphs (a) – (e), the nominal value of Ba content is 7% and the nominal value of K is 11%.

4.4.3. Crystal Structure of 2-2 BNKT-6BA/BNT-7BT Composites

Micro-XRD was also utilized in this composite system to better understand the influence of co-sintering on the crystal structure. With the availability of compositional data presented in Figure 4.14, the correlation between composition and structure can be investigated with greater ease in the BNKT-BA/BNT-7BT system than the BNT-BT-KNN/BNT-BT system. The diffraction patterns collected across a 30% BNT-7BT 2-2 composite are shown in Figure 4.16, as well as the crystal structure determined through Rietveld refinement. The *c* and *a* lattice parameters for each position in the composite are shown, as well as the lattice distortion, which enables a comparison between the crystal structure of the freely sintered constituents and the composite. To further facilitate comparison of diffraction patterns between the freely sintered constituent and the composite, they are displayed together in Figure 4.15.

The change in lattice parameters is shown in Figure 4.16 (b), based on a tetragonal structure used for Rietveld refinement, further tabulated in Table 4. Only a slight increase in the lattice constants of BNKT-6BA relative to the freely sintered constituent can be observed, particularly in the *c* lattice parameter value at 300, 600, 900, and 1200 µm. The *a* lattice parameter of BNKT-6BA is 3.93 Å, whereas in the composite system it ranges from 3.94 to 3.95 Å. The *c* lattice parameter of BNKT-6BA is 3.90 Å, and only a slight deviation in the composite BNKT-BA region can be observed, with an increase to 3.91 Å. Similarly, the *a* lattice parameter of BNT-7BT is 3.91 Å, which does not vary significantly from the value observed for the composite BNT-7BT region, although a nonuniform *a* lattice parameter is apparent in this region. However, a larger difference between freely sintered BNT-7BT (3.89 Å) and the composite component can be observed in the *c* lattice parameter of BNT-7BT (3.97 Å). In terms of diffraction patterns, the (200) reflection of the matrix phase transforms from a narrow peak at 46.5° with a slight shoulder at lower angles in the freely sintered constituent to a broader peak ranging from 45.5-47.0° in the composite. A similar phenomenon occurs in the (211) and (220) reflections. Such peak broadening can be indicative of an increased complexity of lattice site occupation that results in a larger variety of lattice parameters, observed as a broader set of angles over which the reflection of X-rays by the crystal planes can be detected.

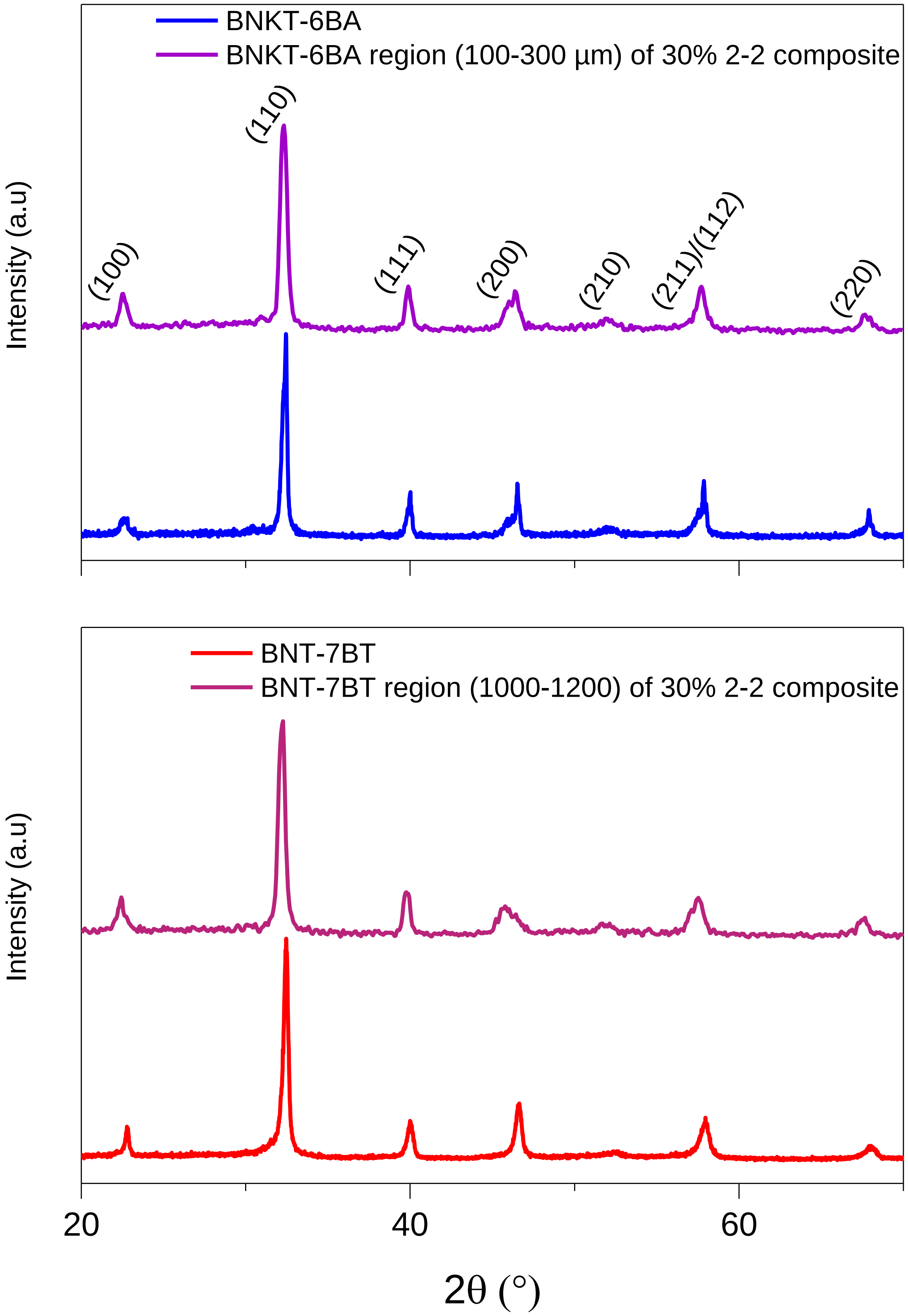

Figure 4.15: Comparison of XRD patterns of freely sintered BNKT-6BA and BNT-7BT and inside the 30% 2-2 composite at 100-200 µm and 1000-1200 µm respectively, collected from 20°-70°

To understand the variation in lattice parameter from the freely sintered constituents from the composites, the influence of interdiffusion should be taken into account. In BNT-7BT, the A-site cations are Bi^{3+}, Na^{+}, and Ba^{2+}, and the B-site cation is Ti^{4+}. In BNKT-BA, the A-site cations with 12-fold oxygen coordination are Bi^{3+}, Na^{+}, and K^{+}, and the B-site cations with octahedral oxygen coordination are Al^{3+} and Ti^{4+}. As K^{+} (1.64 Å [83]) and Al^{3+} (1.41 Å as extrapolated from [83]), in 12-fold coordination, differ in size from the A-site cation Ba^{2+} (1.75 Å) and the B-site cation Ti^{4+} (0.605 Å [83]), it is expected that the diffusion of these elements into the BNT-7BT region will also affect the crystal structure of that component. A reduced lattice constant is expected when the A-site of BNT-7BT is partially occupied by smaller A-site cations. Therefore, a shift to higher angles would occur if Al^{3+} diffuses into the A-site of BNT-BT. Consideration should also be taken of the charges of the A-site substitutions as a result of interdiffusion. Ba has a 2+ valence, which is likely replaced by a K^{+} ion with 1+ valence. Although the two elements have very similar sizes, the lower charge of the K^{+} could result in charge compensation to retain charge neutrality through the formation of oxygen vacancies. Because oxygen acts as a shield from cation repulsion between A and B-site cations, an oxygen vacancy would reduce this shielding and cation repulsion would increase, resultantly expanding the lattice. Oxygen vacancies causing cation repulsion and lattice expansion has previously been shown in yttria stabilized zirconia by Kushima and Yildiz [179]. Lattice strain due to oxygen vacancy formation is well-documented in a number of ceramic materials, generally on the order of 0.1% lattice strain [180]. In the BNKT-6BA region where Ba^{2+} has diffused, it is expected to occupy the A-site, resulting in a larger lattice constant, as observed by the shift of all peaks to lower angles.

The influence of Al interdiffusion on crystal structure is difficult to discern from Rietveld refinement analysis. Al is unlikely to be positioned in the A-site, due to the large difference in both ionic radius and charge between Al and Ba or Bi. However, the likelihood that it substitutes Ti in the B-site is also low, because there is no concentration gradient to drive Ti^{4+} diffusion from the seed into the matrix, creating a B-site vacancy. The position of Al in this composite system was analyzed by NMR and will be discussed in further detail in the next section of this text.

Table 4: Tetragonal Lattice parameters of BNT-7BT and BNKT-6BA, freely sintered and in 2-2 composite

	BNKT-6BA (free)	BNKT-6BA (composite)	BNT-7BT (free)	BNT-7BT (composite)
a (Å)	3.93	3.95	3.91	3.89
c (Å)	3.90	3.91	3.89	3.97

Mechanical compression can also result in a change in lattice constant of the pseudocubic phase in BNT-7BT up to a critical stress, beyond which a transformation to long-range ferroelectrics order has been observed [76]. In nonergodic relaxors, such as BNT-7BT, the transformation results in a remanent strain, which corresponds to apparent changes in the crystal structure as observed by XRD. Specifically, the (222) peak shifts to lower 2θ angles below a coercive stress, indicating an increasing lattice spacing, while above that stress an irreversible phase transition from *R*3*c* to *P*4*mm* occurs [76]. Under compressive stresses alone, the BNT-7BT lattice parameters should reduce, and would result in a shift to higher angles under XRD. These observations provide evidence of the fact that the change in lattice spacing cannot be purely attributed to the stress state of the material. An in-depth analysis of the stress states in the 2-2 composites is presented in the next chapter.

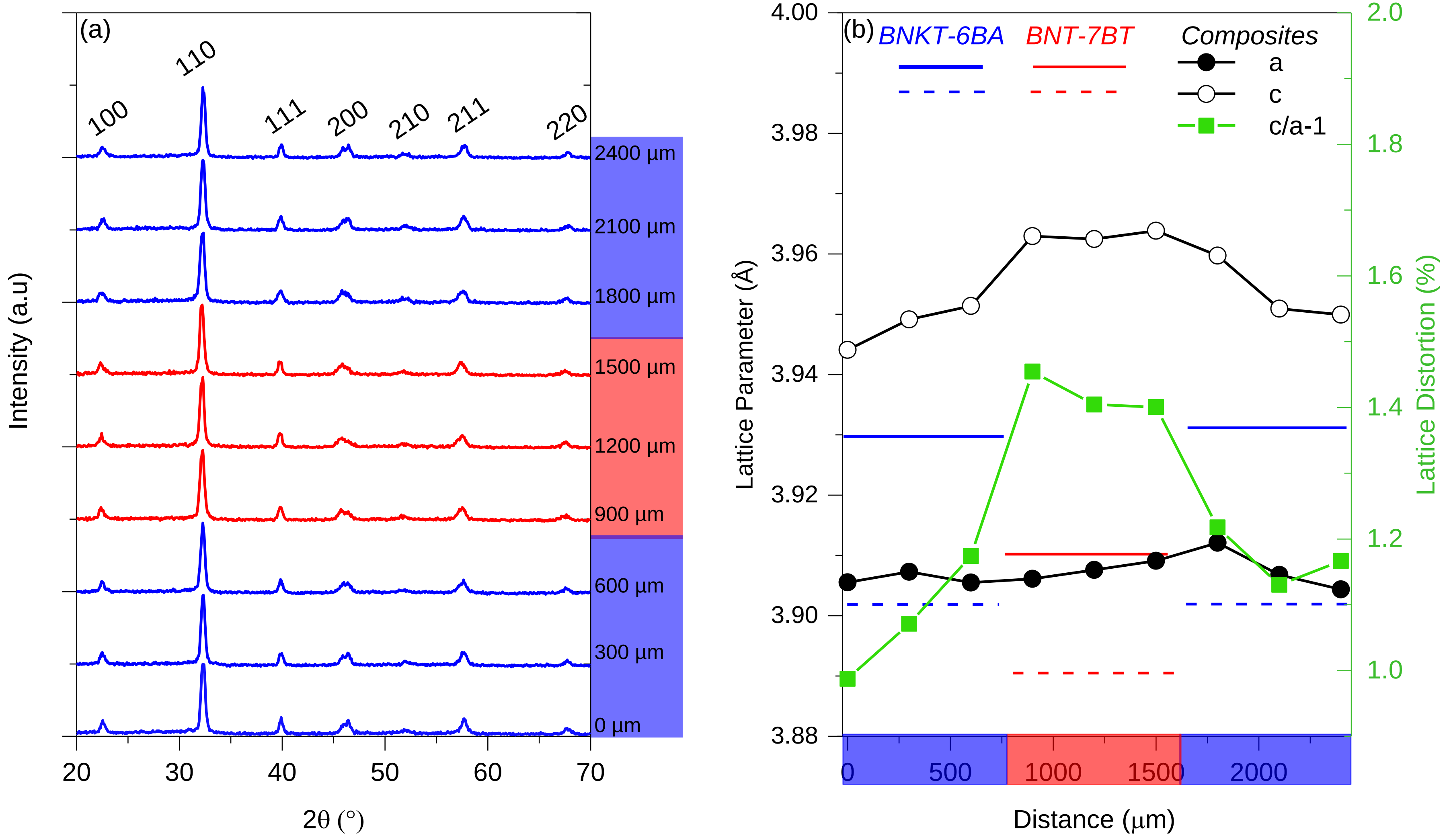

Figure 4.16: The collected diffraction patterns from 20-70° through the thickness of a 50% BNKT-6BA/BNT-7BT composite are shown in (a), while (b) shows the calculated c and a lattice parameters and lattice distortion through the thickness of the sample. The blue lines, solid and dashed, respectively represent the a and c lattice parameters of freely sintered BNKT- 6BA, and the red lines, solid and dashed respectively represent the a and c lattice parameters of freely sintered BNT-7BT.

4.4.4. NMR Investigations of Al in BNKT-6BA/BNT-7BT Composites

To better understand the influence of interdiffusion on the crystal structure, NMR spectroscopy enables an investigation of the coordination number of aluminum in the BNKT-BA/BNT-7BT composite system. This technique has been previously used for structural investigations of BNT-BT by tracking the spectra of quadrupolar perturbed ^{23}Na NMR as a function of BT content, revealing that octahedral tilting was suppressed in BNT-BT with increasing BT content, [80], [181]. Octahedral tilting disorder was correlated to a higher chemical disorder and a stronger relaxor state as compared to the ferroelectric state. All NMR measurements reported in Section 4.4.4 were the work of Dr. Pedro Braga Groszewicz of TU Darmstadt's Department of Chemistry.

In this work, NMR was used to investigate the influence of the composite structure on the coordination of Na and Al. BNKT-6BA, BNT-7BT, and the 2-2 composites comprising 10, 20, 30, 40 and 50% BNT-7BT were examined. For this investigation, the entire 2-2 composite sample was crushed and measured, therefore no local measurements in the seed or matrix region are possible and all data presented in this section represent the NMR response for the entire sample. In Figure 4.17 (a), the NMR spectra of Na is shown for all the pure matrix material BNKT-6BA and the 10, 20, 30, 40 and 50% 2-2 composites. No significant difference in the NMR spectra of Na could be observed in this work, therefore, a more detailed investigation of the NMR spectra of Al was pursued.

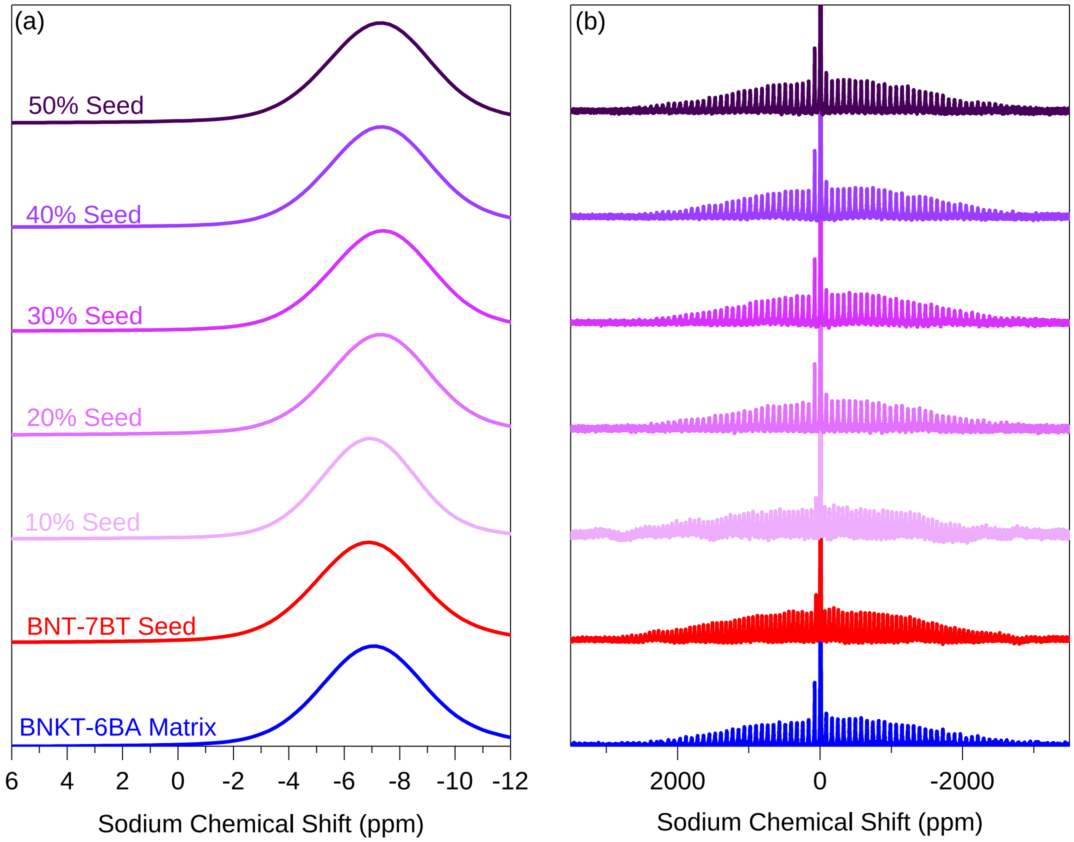

Figure 4.17: ^{23}Na MAS NMR spectra of five 2-2 composite samples with varying seed content, followed by BNT-7BT (seed) and BNKT-6BA (matrix). (a) zoomed in at the central transition, (b) zoomed out to show the spinning sidebands envelope of the satellite transitions

Pure BNKT-BA was analyzed and contrasted to the NMR spectra of Al in composites in Figure 4.18. A major component is observed at 9 ppm, (associated with AlO_6, or B-site coordinated Al), as well as a small signal close to 65 ppm, (associated with AlO_4,). Because there is no site at which a cation can be tetrahedrally coordinating in a perovskite, the AlO_4 signal is ascribed to a secondary phase. A similar NMR signal was observed in $Bi_2Al_4O_9$, for which the signal at 65 ppm was ascribed to tetrahedrally coordinated Al [182]. Therefore, the signal observed at the same position in this work may be ascribed to a secondary phase of $Bi_2Al_4O_9$. However, this signal may also be associated with an Al-associated oxygen vacancy defect dipole. A-site Al has a chemical shift in the negative range [183], which was not observed for the materials studied. Therefore, it can be concluded that Al does not occupy the A-site in BNKT-6BA or the composites thereof. The relative ratio of AlO_6 and AlO_4 components can be determined by normalizing the spectra intensity with respect to the peak at 9 ppm, which corresponds to the AlO_6 component. This major peak remains at the same position and exhibits the same shape for all samples investigated. One can observe that the relative intensity of the signal attributed to AlO_4 sites decreases as a consequence of composite formation as shown in Figure 4.18 (b), in which the 50% seed composite shows a lower intensity of the peak at 65 ppm as compared to the pure matrix. This lower intensity points to either a diminishing quantity of the secondary phase, or a reduction in the quantity of oxygen vacancies in the BNKT-BA region. From these results, it can be speculated that Al occupies both the B-site and a small amount of secondary phase in the pure matrix material. In the composites, with increasing seed content the amount of aluminum with the 65 ppm signal decreases, indicating that the secondary phase containing Al may be the primary source of Al diffusing from the matrix into the seed.

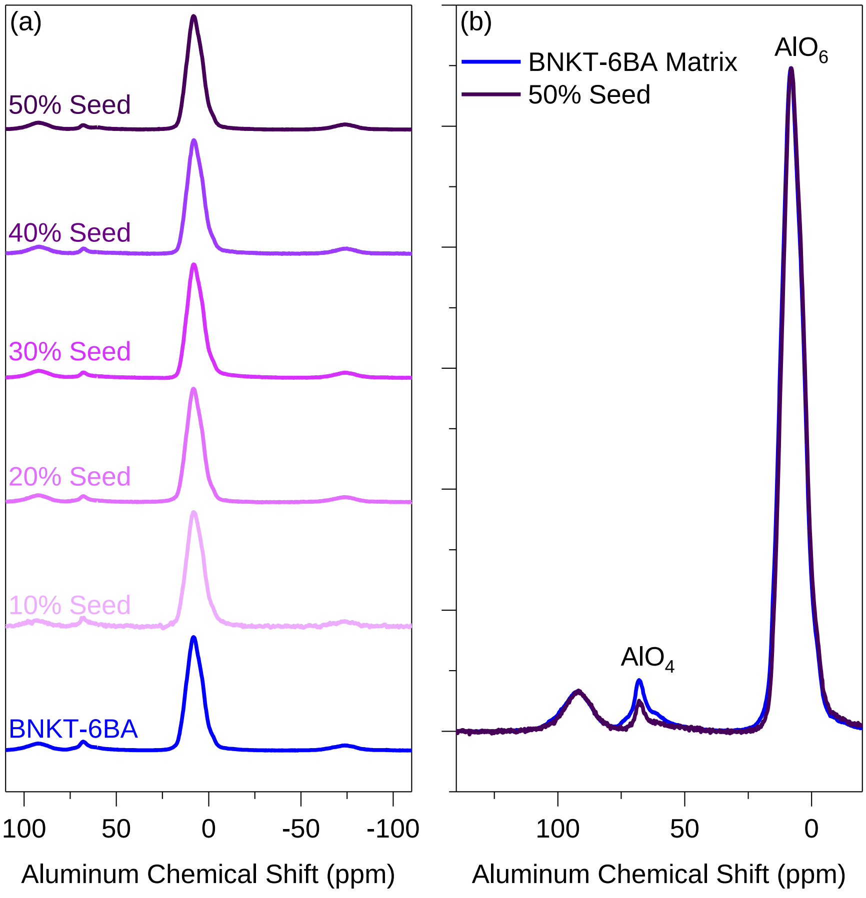

Figure 4.18: (a) Central transition of ^{27}*Al MAS NMR spectrum (MAS 13 kHz – field 14.1 T). B-site Al, or Hexa-(*AlO_6*) and A-site tetra-coordinated (*AlO_4*) regions from -100 to 100 ppm. (b) The* ^{27}*Al MAS NMR spectrum of the BNKT-6BA matrix and the 50% composite, highlighting the 65 ppm and 9 ppm signals*

In pure BNKT-6BA, the AlO_4 corresponds to 6 % of the total aluminum content as shown in Figure 4.19 (a), whereas it corresponds to 3% of the aluminum content in the composite sample with 50% seed. The decrease of the relative intensity of the AlO_4 with respect to the AlO_6 signal occurs in a gradual manner with increasing seed content, as shown in Figure 4.19 (a). A secondary peak at 60 ppm can also be observed, which is normalized to the peak intensity at 65 ppm in Figure 4.19 (b). It can be observed that this shoulder increases in intensity with increasing seed content. Because it is associated with a tetrahedrally coordinated Al, it is not possible for this Al signal to be attributed to an Al occupancy in the perovskite, and instead appears to be a formation of an aluminate as a secondary phase that differs from the original secondary phase found in the matrix material. It is possible that this new secondary phase corresponds to the accumulation of Bi, Al, and K in the pores as observed in Figure 4.12.

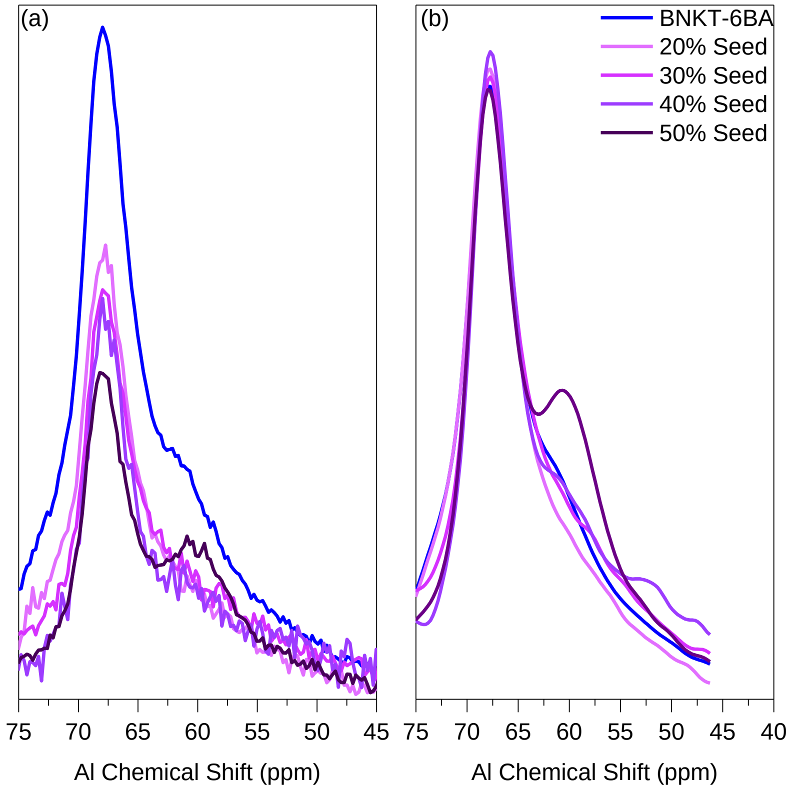

Figure 4.19: ^{27}Al MAS NMR spectrum (MAS 13 kHz – field 14.1 T). (a) AlO_4 signal normalized to AlO_6 signal at 8.5ppm (b) AlO_4 signal intensity normalized to signal at 68 ppm

A closer look at the 9 ppm signal reveals an asymmetric shape with the presence of shoulders (Figure 4.20(a)). These features may correspond to the presence of different Al sites with overlapping signals in this region. As the signals attributed to Al in $Bi_2Al_4O_9$ [182] and Al with AlO_5 coordination in $MgSiO_3$ [183] have been reported to occur in this region, it is important to analyze it with an NMR technique that offers a better resolution than simple 1D MAS NMR. Hence, four selected samples were analyzed with two-dimensional 3QMAS NMR, a method capable of resolving signals with different C_Q parameters, (*i.e.*, magnitudes of quadrupolar moments in response to an external magnetic field) (Figure 4.20 (a)). These spectra clearly show the presence of two signals in this region. The more intense signal ($Al^6{}_1$), located at 9 ppm, is marked by a pronounced distribution of chemical shift (CS) values, as observed from its stretched shape along the CS diagonal line. The second signal ($Al^6{}_2$) is present as a shoulder in the lower part of the 2D contour plots. Its maximum is located at 11 ppm in the MAS dimension, as a result of which it cannot be resolved from the $Al^6{}_1$ in the 1D MAS NMR spectrum. Aided by the 3QMAS experiment, the isotropic value of the chemical shift is determined ($Al^6{}_2$ δ_{ISO} = 17 ppm).

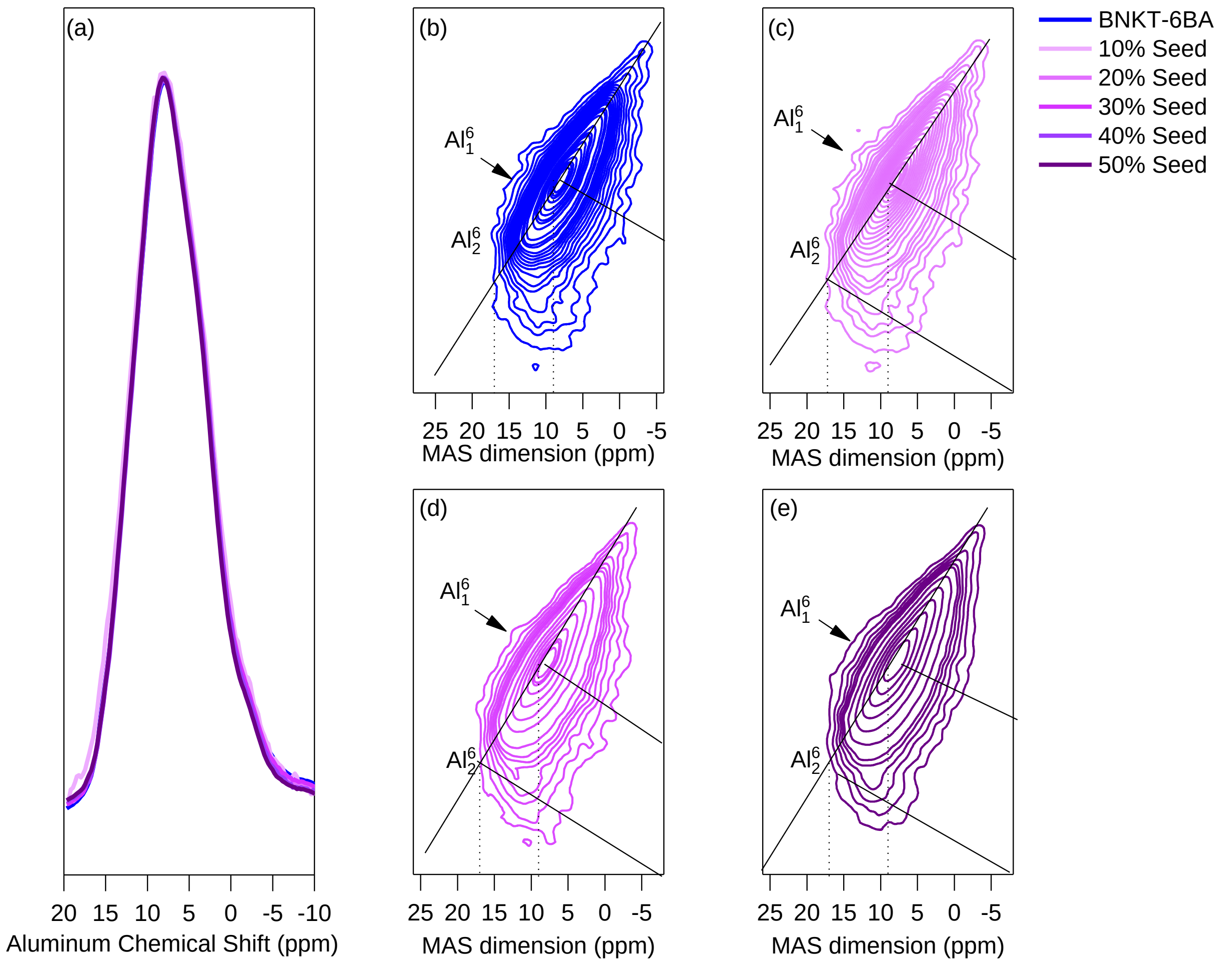

Figure 4.20: Hexa-coordinated (AlO6) region of 27Al NMR spectra. (a): Central transition of 27Al MAS NMR spectrum (MAS 13 kHz – field 14.1 T) (b)-(e) 27Al 3QMAS NMR spectra of selected samples. Both Al61 and Al6¬2 are present in all four spectra. (b) BNKT-6BA (c) BNKT-6BA/20% BNT-7BT (d) BNKT-6BA/30% BNT-7BT (e) BNKT-6BA/ 50% BNT-7BT

The Al^6_1 site presents a distribution of isometric chemical shift values δ_{IISO} and quadrupolar coupling magnitudes C_Q. This may be an effect of mixed occupancy of the B-site by Al and Ti. In BNKT, the perovskite structure exhibits a network of corner-shared octahedra occupied by Ti. In a six-coordinated environment, Ti^{4+} (0.65 Å) has a larger ionic radius than Al^{3+} (0.54 Å). Therefore, the B-site of this titanate is too large to properly accommodate Al ions, as a consequence of which it could be statistically distributed between positions lying close to the center of the octahedra.

An alternative explanation for the marked distribution of NMR parameters related to the local structure of the Al^6_1 site is based on the influence of the next-nearest neighbor on the size and shape of the oxygen octahedra. Their dimension should be the consequence of a distribution of sizes due to the shared occupancy of the A-site in BNKT. A similar effect was attributed to the distribution of local environments observed in $^{47,49}Ti$ NMR spectra of the closely related BNT-xBT perovskites, where the A-site is occupied by Ba, Na and Bi [184]. The interdiffusion of Ba and K between seed and matrix increases the variety of cation arrangements surrounding Al in the B-site and could result in an increased distribution of local structures as reflected by the distribution of NMR parameters for the Al^6_1 site.

An additional octahedral site, the Al^6_2 site, is revealed only by employing ^{27}Al 3QMAS NMR spectra, as its signal severely overlaps with that of the main Al^6_1 component. There are several possible sources for this signal: unreacted aluminum oxide precursor, based on its isotropic value of chemical shift ($\delta_{ISO} = 17$ ppm), AlO_5 sites associated with oxygen vacancies, or two distinct Al sites similar to observations of $LaSrAlO_4$ [185].

Each of the possibilities listed above are examined in more detail. Corundum, or unreacted Al_2O_3 is reported to have a chemical shift of 16 ppm and a C_Q of 2.4 MHz, with an asymmetry parameter $\eta=0$ [186]. The line shape extracted from the 3QMAS spectra in the present material indicates a C_Q of 4.5 MHz with $\eta \approx 1$ for the Al^6_2 site. The larger quadrupolar coupling constant and asymmetry parameter observed for this site makes it incompatible with the assignment to corundum. Another possibility is the presence of secondary phase $Bi_2Al_4O_9$, whose NMR spectra has a peak at 58 and 12 ppm. Because the secondary peak may also be associated with an Al-oxygen vacancy defects, 3QMAS cannot distinguish between the two possible sources of this signal: the oxygen vacancy defect dipole or the secondary phase of $Bi_2Al_4O_9$.

Combining the structural evidence from XRD measurements and the results of NMR, a clearer picture of the position of Al in BNKT-BA/BNT-7BT composites emerges. The *c* lattice parameter increases significantly in both the matrix and seed phases of the composites, as shown in Figure 4.16.. In $BiAlO_3$, Al must have a charge of 3+ to retain charge neutrality in a perovskite structure, which is identical to the charge of Ti in a perovskite structure. However, the substitution of K^+ into the A-site of BNT-BT as a replacement of diffusing Ba^{2+}results in a lower total positive charge in the unit cell, which necessitates a compensating oxygen vacancy. NMR data has shown that the composite structure reduces the amount of initial AlO_4 secondary phase. However, Al is unlikely to substitute the B-site occupied by Ti. An Al-occupied B-site means a smaller B-site cation than a Ti-occupied B-site, which would result in a smaller *c* lattice parameter.

3QMAS NMR revealed a chemical shift in the 9ppm signal that can be attributed to a defect consisting of an octahedrally coordinated aluminum (AlO6) with an associated oxygen vacancy. This value of chemical shift was observed in all composites, indicating the presence of this defect no matter the seed content. In Table 4, it was shown that the c lattice parameter of BNKT-6BA was 3.90 in the freely sintered matrix and 3.95 in the composite, whereas BNT-7BT increased from 3.89 in the freely sintered sample to 3.97 in the composite. Because the associated Al-$V_O^{\cdot\cdot}$ defect exists in the freely sintered matrix material, no change due to its presence will be observed in the matrix phase of the composite. However, diffusion of Al and K into BNT-7BT generates a K-$V_O^{\cdot\cdot}$ defect dipole that increases the c lattice parameter, due to cation repulsion as discussed above. Such a change in the lattice occupancy will also affect the nearest neighbors of Al in the B-site, and its associated NMR signal at 9ppm, as was shown in Figure 4.20.

From the above discussion, a comparison can be made between the lattice of the freely sintered constituent in Figure 4.21(c) and its respective component of the composite in Figure 4.21(d). BNT-7BT, when co-sintered with BNKT-BA, develops a more complex perovskite structure. Initially it is a perovskite with a mixed A-site occupancy by Bi, Na and Ba, and a B-site occupancy of Ti as shown in Figure 4.21(a). In the composite, some of the BNT-BT region is likely to take on the composition shown in Figure 4.21(b), in which the A-site is also occupied by K and the B-site now has a mixed occupancy by Al and Ti.

Previous reports on $BiAlO_4$ have shown that the perovskite structure consists of B-site Al and A-site Bi [187]. However, in this work, NMR investigations have revealed that when combined with BNKT as a binary solid solution, Al occupies the B-site of the perovskite structure in pure BNKT-BA. As no reduction of octahedrally coordinated Al was observed by NMR, it appears that Al in the B-site remains stable, and is therefore still shown as a mixed occupancy of Al and Ti. Limited work is available on the structure of BNKT-BA beyond TEM measurements determining that it is a predominantly tetragonal structure in the unpoled state [188]. As a result, our investigations with NMR provide insight into the chemical structure of the perovskite lattice, as well as the formation of secondary phases in the composite structure. Given that K has a much higher diffusivity than Al, it appears that it is able to penetrate the lattice and enter the A-site of BNT-BT. On the other hand, due to its lower diffusivity, Al diffuses primarily from the secondary phase of $Bi_2Al_4O_9$ in the matrix into a new secondary phase formed at the pores of the seed/matrix interface, and does not appear to affect the lattice structure of BNT-7BT.

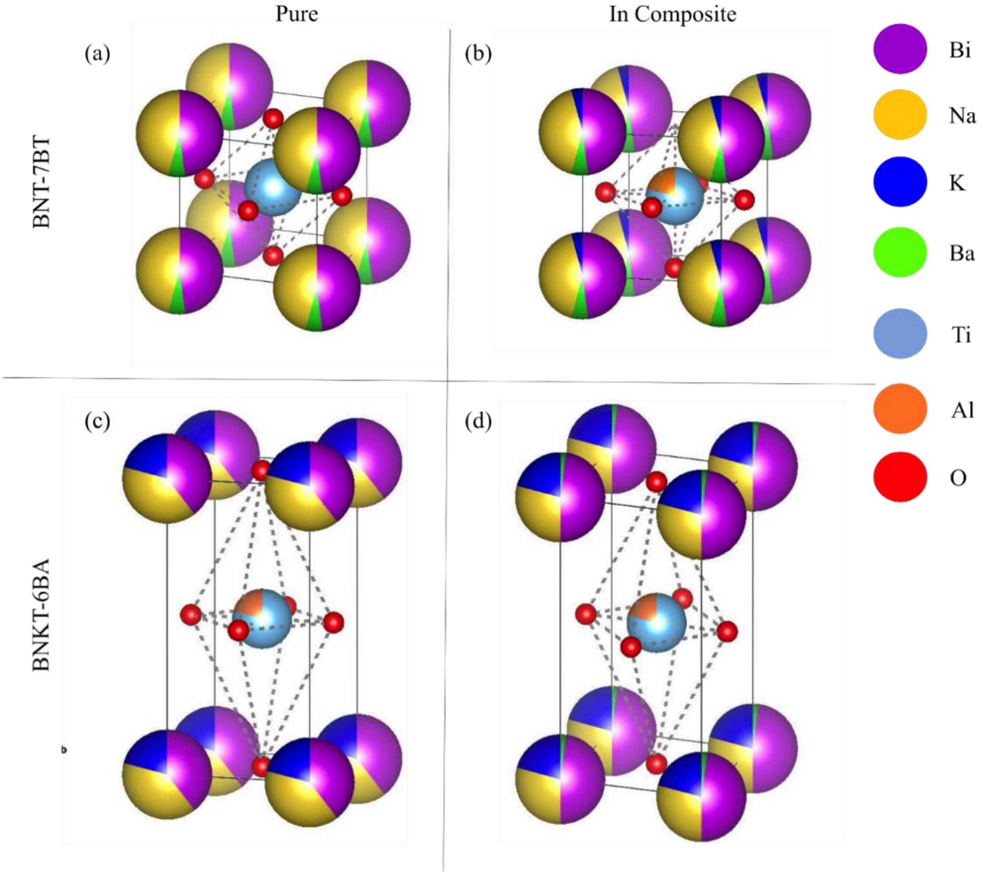

Figure 4.21: (a) Proposed original tetragonal structure of BNT-7BT pure seed (b) Proposed final structure of seed region after interdiffusion, with Al^{4+} ion as interstitial in BNT-7BT lattice, Ti in the B-site and Bi, Na, and Ba in the A-site, as well as diffused K in the A-site with A and B-site occupancy by Al based on NMR results (c) Proposed original tetragonal structure of BNKT-6BA pure matrix (d) Proposed final structure of matrix region after interdiffusion with Ba^{2+} in A-site

4.4.5. Interdiffusion in BNKT-6BA/BNT-7BT 2-2 Composites as a Function of Sintering Time

Having demonstrated that interdiffusion occurs during sintering and influences the crystal structure, it is clear that this interaction can be manipulated by changing the sintering parameters. The variables during sintering that are controlled during sample fabrication include composition, temperature and time. In this work, the influence of sintering time was investigated in more detail by sintering 2-2 composites of 70% BNKT-6BA/ 30% BNT-7BT for 2 h, 6 h, 12 h and 24 h, and examining the chemical composition and crystal structure in these composites. The distribution of Al, K and Ba were tracked through the samples by SEM EDS, and the relative chemical content is shown as the intensity of the signals at 1.44 eV (Al Kα), 3.312 (K Kα) and 4.465 eV (Ba Lα) normalized along the evaluated length of the sample. Only the interface region from 300 µm to 1800 µm was investigated by EDS. The quantities reported at each position are an average of 10 EDS spot scans performed 50 µm apart in a line parallel to the interface. The error bars represent the standard deviation within those 10 scans. This study provided insight into the influence of sintering time on the chemical composition of the 2-2 composite structure, the results of which are shown in Figure 4.22.

A comparison between the 2 h and 6 h sample reveals that the increase in Ba begins at 1000 µm in the 2 h sintered sample and at 900 µm in the 6 h sintered sample. In addition, the Ba content is more uniform throughout the 6 h sample as compared to the 2 h sample. Because the initial dimensions of the seed and matrix phase were identical in both samples before sintering, this difference in composition as a function of position can be attributed to an increased penetration of Ba into the matrix region. At 12 h sintering time, the maximum Ba content occurs at 1700 µm, and a sharp reduction can be observed at 1600 µm, followed by an increase at 1500 µm and a gradient in Ba content from 1500 to 1100 µm. In the 24 h sample, there is no significant difference in Ba content between the nominal seed and matrix regions, with maximum intensities occurring at 800 µm, 1300 µm, and 1600 µm. The Ba content therefore appears to homogenize only after 24 h of sintering.

The diffusion from the matrix into the seed can be observed by tracking the K and Al content. The K content drops at 1200 µm in the 2 h sample, and at 1000 µm in the 6 h sample. In the 6 h sample a maximum of the K content can be observed at 1300 µm, which means that the nominally pure seed region has reduced in dimension due to an increased diffusion of elements from the matrix region. In the 12 and 24 h samples, the K content is constant throughout the investigated region. As was shown in Figure 4.14, the diffusivity of K is an order of magnitude higher than the diffusivity of Al. Therefore, increased sintering time is likely to result in complete diffusion of the K content from the matrix layers into the seed region, with a uniform distribution of the K content throughout the composite. At 12 h, the K intensity is uniform throughout the region investigated, whereas a gradient in the Al intensity can be observed from 1200 to 1700 µm. After 24 h of sintering, a gradient in Al content begins at 800 µm and extends to 1200 µm. From 1400 to 1700 µm no gradient in Al content can be observed, indicating that it has become uniform within the seed region.

It is interesting to note that with increasing sintering time, the standard deviation in the K and Al content at each position reduces significantly. This means that the chemical composition is not homogeneous parallel to the interface at lower sintering times, but becomes more uniform with increasing sintering time not only between the seed and matrix region, but also within the matrix region itself. This is not surprising, as diffusion is a three-dimensional process, and increased diffusion is likely to result in increased homogeneity across the volume of the sample. However, Ba differs slightly from the time-dependent behavior of K and Al, in that the standard deviation of Ba content increases from 2 h to 6 h sintering time. With further increases in sintering time, the standard deviation of Ba decreases in a manner that parallels the K and Al content. One possible explanation for this is that at 2 h of sintering, Ba has not had time to diffuse deep into the matrix region. Because, as stated above, diffusion is a three-dimensional process, the Ba content remains uniform at lower sintering times. This implies that Ba has a lower diffusivity than K and Al. Because the largest possible concentration gradient lies between a pore and a grain, it is also possible that increased sintering time enables diffusion parallel to the interface into pores. This would explain the inhomogeneous distribution of Ba in the 6 h sample, in which Ba is able to diffuse into pores as well as into the matrix region. However, with further sintering time, the composition within pores and grains is likely to become more homogeneous.

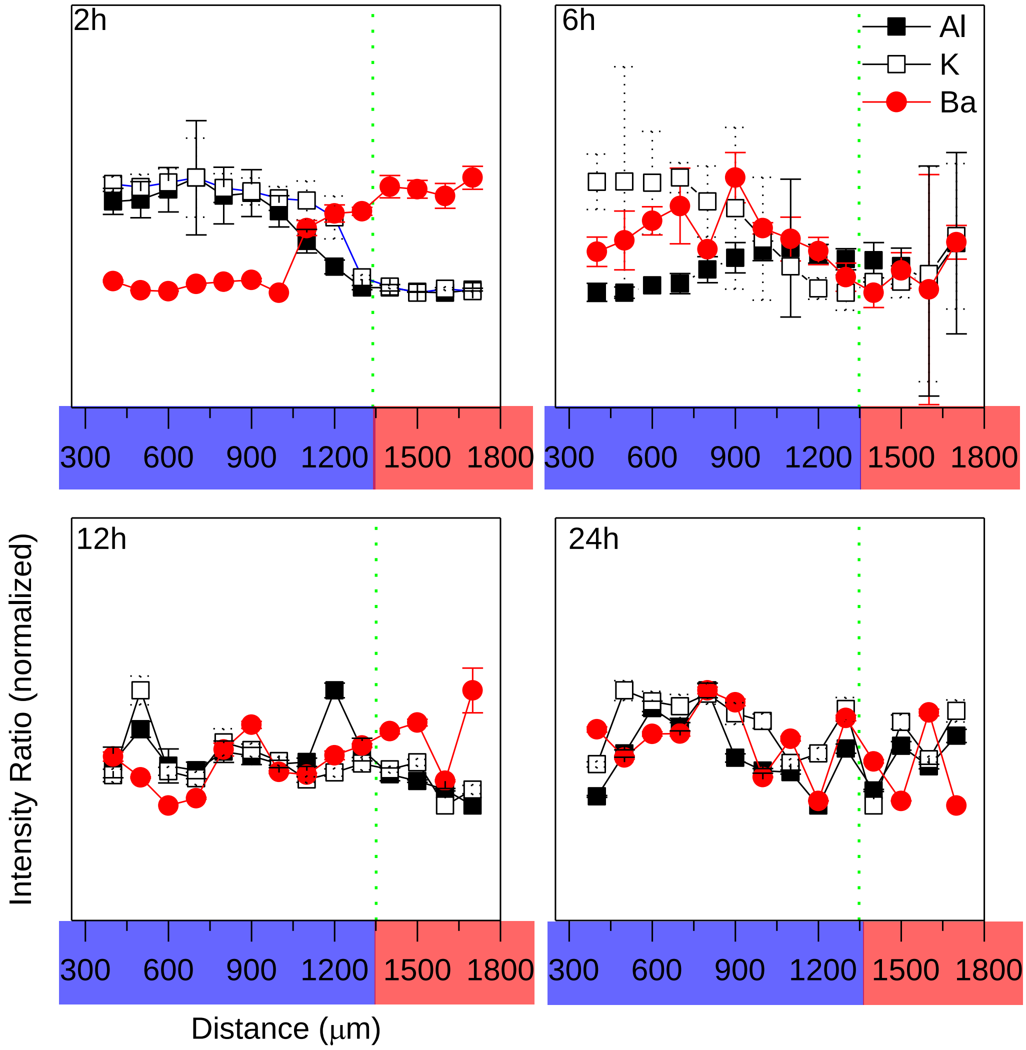

Figure 4.22: Al (black squares), K (open squares) and Ba (red circles) content shown as normalized intensity of EDS signals in BNKT–BA/ 50% BNT-7BT 2-2 composites as a function of position in samples sintered for 2 h, 6 h, 12 h, and 24 h. The dashed green line represents the interface between the seed and matrix before sintering, and the blue and red squares over the x-axis represent the seed and matrix region before sintering. The error bars for the K content are shown as dotted lines to distinguish from the Al content error, which is shown with a solid black line.

From these results. it can be stated that with higher sintering time, the Ba content is depleted from the seed region as it diffuses into the matrix region. These results indicate that control of diffusion by sintering time can enable a tailoring of chemical composition across the composite. The influence thereof on electromechanical properties will be discussed in depth in Chapter 6.

4.4.6. Crystal Structure of BNKT-6BA/BNT-7BT Composites as a Function of Sintering Time

The investigation of chemical composition can be correlated to crystal structure through micro-XRD examination of the samples as a function of position. Local micro-XRD measurement with a spatial resolution of 300 µm was used to determine the full range diffraction pattern from 20 to 70° every 100 µm across the full sample. This was followed by a high resolution XRD investigation of the (111) and (200) reflections across the seed/matrix interface.

In Figure 4.23, it can be discerned that the (200) reflection has increased peak splitting with increasing sintering time, particularly in the seed region. Surprisingly, even after 24 h of sintering, the crystal structure is not homogeneous through the sample. This may be due to other factors influencing crystal structure such as internal stresses. In particular, intergranular stresses will are likely to increase with lower grain size and it is expected that a longer sintering time will result in increased grain size. In the 24 h sample, the (200) reflection has a FWHM of 1° throughout the sample, whereas at 2 h the FWHM ranges from 0.5° to 1°. This peak broadening with sintering time is indicative of a tetragonal phase, characterized by a split (200) peak and a single (111) reflection. Corroboration of a tetragonal phase should be found in splitting of the (100), (110) and (211) peaks, as well as a single peak in the (111) reflection. The (111) reflection is clearly singular, however it is difficult to distinguish peak splitting in the (100) reflection beyond a slight increase in FWHM from 1.3 ° at 2 h to 1.7° (2θ) at 24 h. The (110) reflection clearly has peak splitting at 1600 µm and 800 µm, which is the interface region, further supporting the presence of an expanded region of tetragonal phase with increased sintering time.

In Figure 4.24 (a), the lattice parameters are shown as determined from Rietveld refinement of the diffraction patterns shown in Figure 4.23. The *a* lattice parameter of freely sintered BNT-7BT is 3.883 Å, shown as a solid red line, and the *c* lattice parameter thereof is 3.889 Å, shown as a red dashed line. The lattice parameters for the composite at each sintering time are shown separately as a function of position. From 2 h to 12 h, the increase in sintering time results in a decreased lattice constant throughout the composite. At 24 h sintering time, an increase in the *a* and *c* lattice parameters is apparent. The influence of sintering time on lattice parameters in this work is, however, complex and nonlinear. Figure 4.24 (b) and (c) shows the lattice parameters of the seed at 700 µm and matrix regions at 300 µm, respectively as a function of sintering time. In the seed region, the *a* lattice parameter decreases with increasing sintering time. This may be attributed to increasing substitution of Ba with K, as discussed above. An increase in the *c* lattice parameter of the seed region is observed from 3.89 Å at 2 h to 3.96 Å at 6 h sintering time. However, with increasing sintering time to 12 h the *c* lattice parameter falls to 3.895 Å, and remains at that value in the 24 h sintered sample.

At 2 h sintering time, the *a* lattice parameter of the seed region is higher than the pure seed. With higher sintering times, however, a drop of the *a* lattice parameter to below that of the pure seed can be observed. Increased cation repulsion is expected if K replaces Ba, as a consequence of the formation of oxygen vacancies, thereby increasing the *a* lattice parameter. However, the reduced *a* lattice parameter cannot be explained by cation repulsion, but may be caused by internal stresses, which will be examined in more detail in Chapter 5.

In Figure 4.24 (c), the lattice parameters of the matrix region are shown and compared to the *a* and *c* lattice parameters of the pure freely sintered BNKT-BA, which are shown in the blue dashed and solid lines respectively. It is clear that the *a* lattice parameter of the BNKT-BA region in the composite is well below that of the freely sintered matrix, (3.9 Å), no matter the sintering time. The *c* lattice parameter of the composite is below that of the freely sintered matrix material at 2 and 12 h. When sintered for 6 and 24 h, however, the *c* lattice parameter of BNKT-BA is higher than the freely sintered constituent.

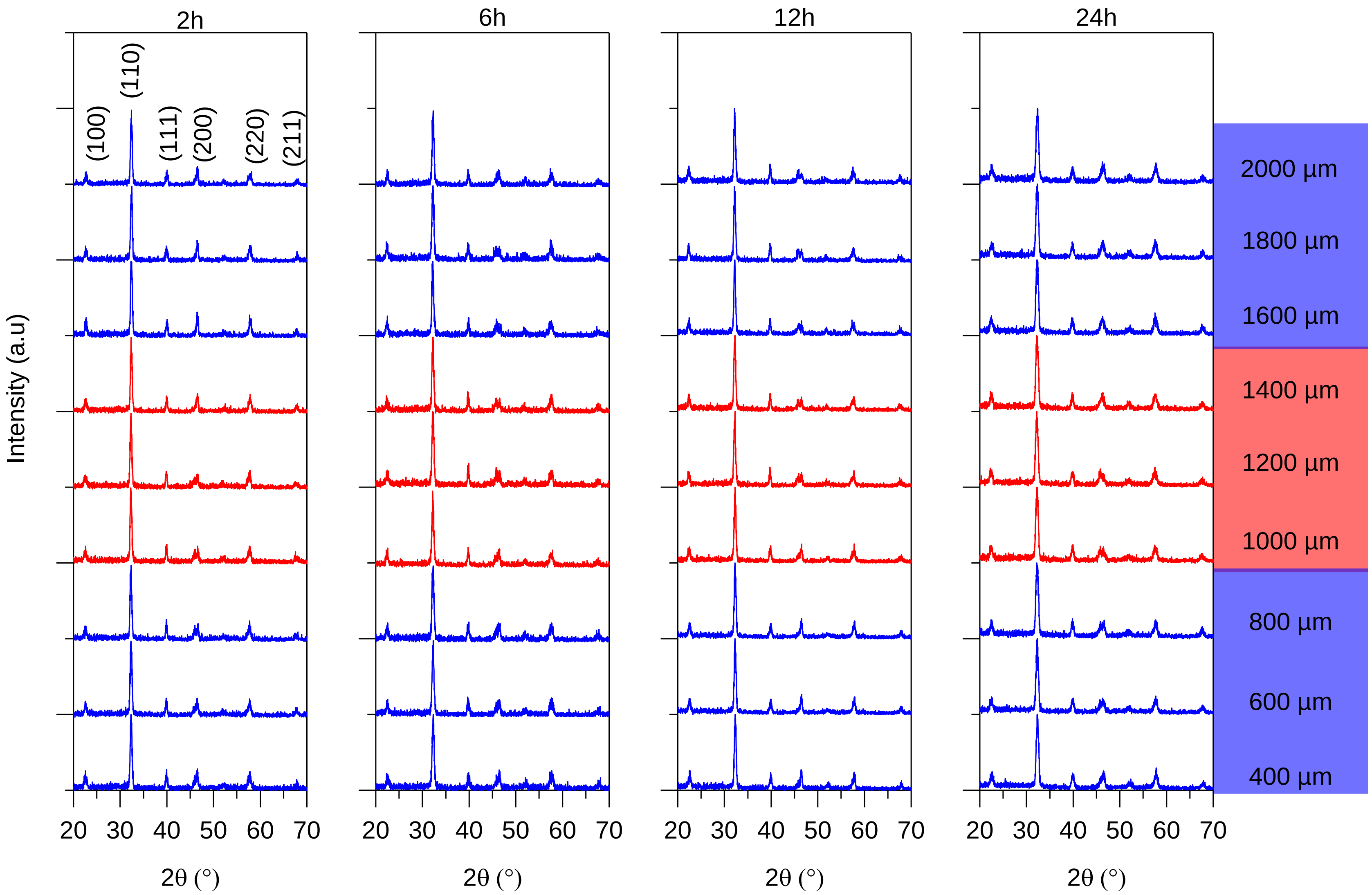

Figure 4.23: Diffraction patterns across 2-2 composites of BNKT-BA/BNT-7BT at different sintering times (2 h, 6 h, 12 h, 24 h) over the full spectrum of 20-70°

In the matrix, the presence of Ba^{2+} as an A-site substitution for K is not expected to increase the lattice constant of the matrix region due to the similarity in ionic radii between K^+ and Ba^{2+}. It is important to bear in mind that the lattice parameters are affected by a number of factors in addition to diffusion, including grain growth, porosity, and residual stresses. All of these factors are also affected by an increased sintering time. In $Ba(Zn_{1/3}Ta_{2/3})O_3$ it was shown that sintering time and temperature influence the order of the Zn and Ta B-site cation, thereby affecting the XRD reflection profiles [189]. Simultaneously, a strong influence of sintering conditions on grain size was also observed. It is well known that as a ceramic increases in grain size, the surface to volume ratio of an individual grain decreases [190]. The resultant internal stress may compress the lattice, resulting in reduced lattice parameters. Uchino *et al.* showed that particle size has a pronounced effect on the tetragonality, or *c/a* ratio, of BT [191]. Frey *et al.* further investigated the influence of microstructure on crystalline phases in BT in sintered ceramics, and showed that with increasing grain size from 0.035 to 0.1 µm, room-temperature XRD profiles and Raman spectra exhibited a transition from a cubic to a tetragonal phase [192]. The influence of grain size on lattice parameters has also been observed in more complex perovskites, such as calcium bismuth niobate ($CaBi_2Nb_2O_9$, CBN), in which the *a* and *c* lattice parameters increased with increasing grain size [193]. The grain size was controlled by sintering parameters such as heating rate, holding time and holding temperature. In terms of internal stress, the presence thereof in laminate structures is well-established and will be discussed in detail in Chapter 5, as well as its potential influence on crystal structure.

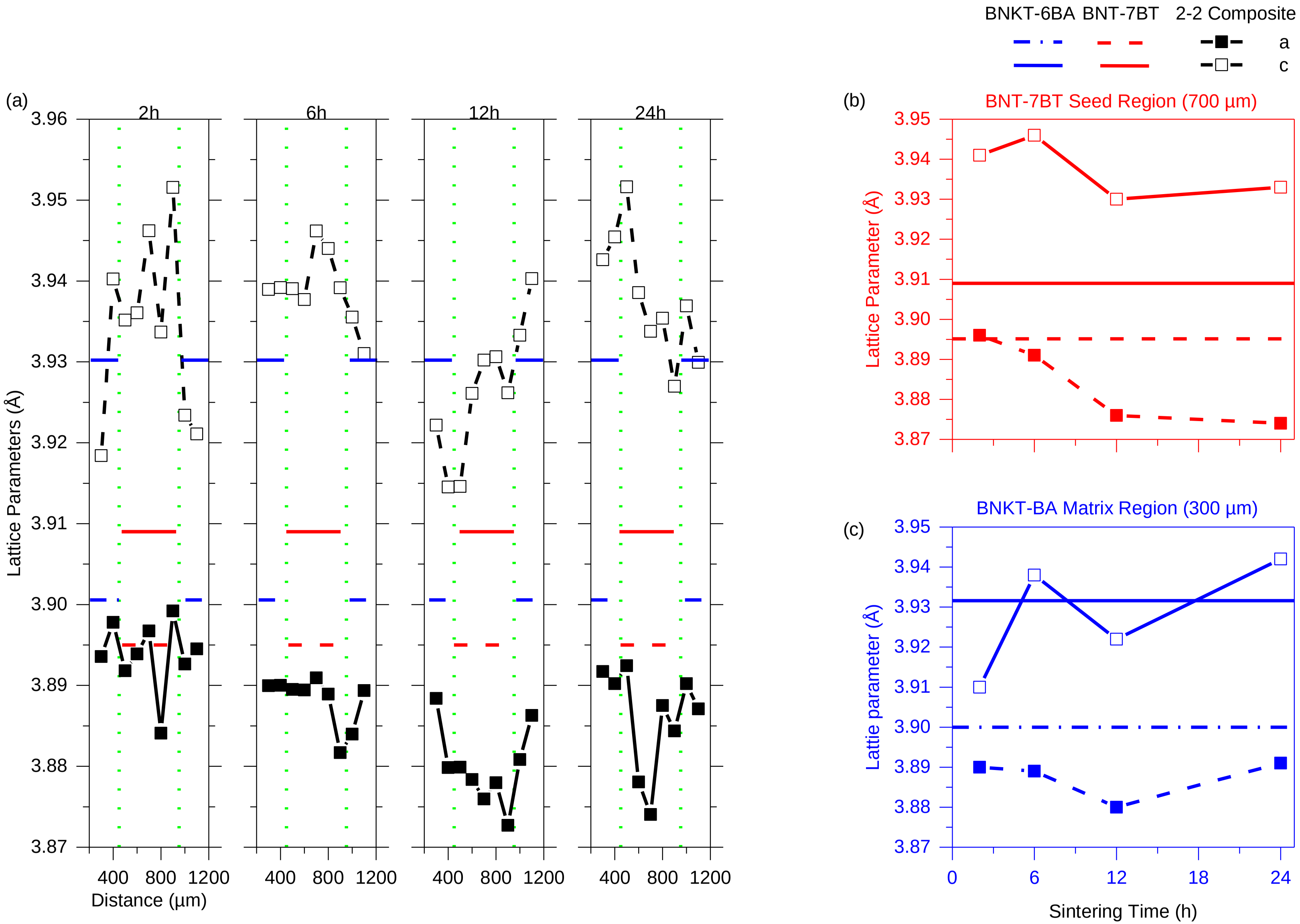

Figure 4.24: Lattice parameters of 2-2 BNKT-BA/BNT-7BT composites sintered at 2 h, 6 h, 12 h and 24 h as determined by Rietveld refinement as a function of position, and second panel where the lattice parameters are shown as a function of sintering time for the BNT-7BT seed region at 700 µm and for the BNKT-6BA matrix region at 300 µm, with the a and c lattice parameters of the pure constituent shown in a dashed and solid line respectively

A more detailed examination of the (111) and (200) reflections for the 2 h, 6 h and 24 h sintered samples at the seed/matrix interface was performed with high-resolution micro-XRD at SPring8, shown in Figure 4.25. In the 2 h sample, the (111) reflection exhibits several changes as a function of position and sintering time, including peak angle position and extent of peak splitting. A slight shoulder in the (111) reflection accompanied by a single (200) reflection as observed over most of the 2 h sample is indicative of a rhombohedral symmetry in the matrix region of the composite. In the seed region, from 1250 to 1350 µm, the (111) peak shifts from 25.62° to 25.56°. In the same region, the (200) reflection is a single peak at 1150 µm and 1200 µm, but a shoulder begins to emerge at 1300 µm, and a clear peak splitting can be observed 1400 µm into the sample.

The crystal structure should be discussed in light of the chemical composition data presented in Figure 4.22. In the 2 h sample, from 1100 to 1400 µm, the (111) peak shifts gradually to a lower angle, and the (200) reflection decreases in FWHM. This region corresponds to the region shown in Figure 4.22 for the 2 h sample in which an interdiffusion region where a gradient of the Ba, K and Al content was apparent. Shifts to a lower lattice constant indicate an increase in lattice parameters, likely due to the diffusion of Ba into the matrix and substituting the smaller K^+ ion in the A-site.

Comparing the position of the (111) peak maximum as a function of position, in both the 2 h and 6 h sample, a shift to lower angles can be observed. At 1150 µm, the (111) peak position is 25.653°, and at 1600 µm, it has shifted to 25.56°. This corresponds to the change in chemical content over the same region, shows a gradient in Al, Ba and K content from 900 to 1700 µm, (see Figure 4.22). Splitting of the (200) reflection occurs throughout the sample, whereas in the 2 h sample the splitting begins at 1400 µm. Increased sintering time results in increased peak splitting of the (200) reflection as well, indicating the presence of a mixed tetragonal/rhombohedral phase in the matrix region of the composite.

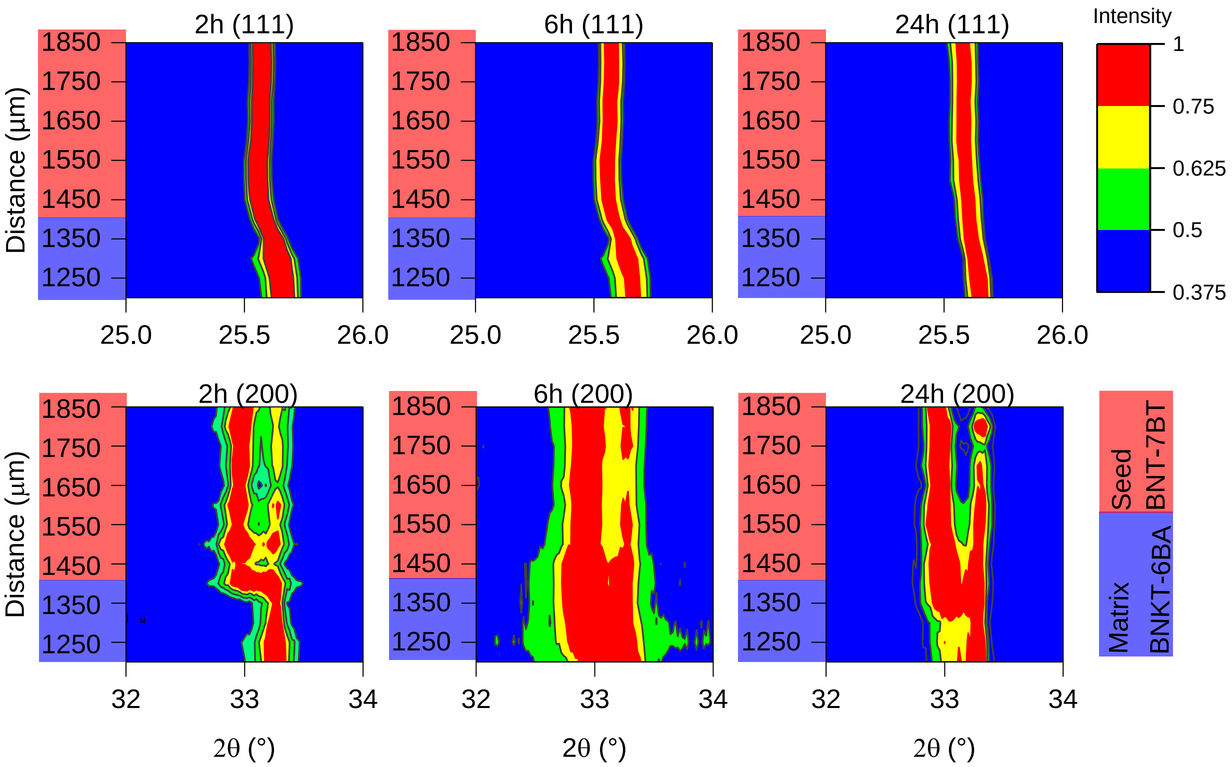

Figure 4.25: (111) and (200) reflections across the seed /matrix interface in BNKT-6BA/BNT-7BT 30% 2-2 composite, the red region from 450 – 650 µm indicating the seed and the blue regions from 0-350 µm indicating the matrix components of the composite. Each reflection was collected using a beam size of 50 µm x 200 µm, every 50 µm along the length of the sample, parallel to the interface. Only one interface was examined.

In the 24 h sample, a shoulder in the (111) reflection is apparent in the seed region from 1150-1300 µm, closer to the nominal seed/matrix interface than in the 2 and 6 h samples. In addition, the (111) peak maximum shifts from 25.64° at 1150 µm to 25.6° at 1200 µm. This shift is much smaller than the one observed in the 2 h sample. Therefore, a longer sintering time results in a more homogeneous distribution of lattice parameters, corroborating the conclusions drawn from Figure 4.24. Peak splitting of the (200) reflection occurs throughout the 24 h sample, similar to the 6 h sample. However, there is a notable difference in the (200) reflections of the 6 h and 24 h samples: in the 6 h sample, the lower angle peak has higher intensity than the higher angle peak, and this is reversed in the 24 h sample at 1150 µm and 1200 µm. Nevertheless, throughout the 24 h sample, a tetragonal crystal structure is predominant. The difference in relative intensities of the peaks in the (200) reflection may have a few different causes. A higher intensity at lower angles, as seen in the 6 h sample, may be due to a higher presence of the rhombohedral phase, whose (200) reflection occurs at an angle between the (200) and (002) reflections of the tetragonal phase. On the other hand, the 24 h sample shows a higher relative intensity in the higher angles of the (200) reflection. This may be due to a higher relative proportion of the tetragonal phase with a reduced lattice constant relative to the 2 h and 6 h samples. However, as shown in Figure 4.24, the refinement did not reveal lower lattice parameters after 24 h of sintering.

As a general observation, the FWHM of the (111) reflection decreases from 0.16 at 2 h to 0.11 at 24 h in the seed region at both 1150 and 1200 µm. Sintering time does not seem to affect the peak position of the (111) reflection significantly, as all peaks fall within 0.02° of each other. The reduction of the FWHM with sintering time implies a reduced dispersion of lattice constants, meaning that the lattice structure becomes more uniform with increasing sintering time [174]. An increase in the uniformity of chemical composition results in an increase in the long-range chemical order of a system. Such a long-range order can be detected by XRD through a reduction in the FWHM. When the long-range order of a relaxor is disrupted, it becomes ergodic. Therefore, it appears that increased sintering time will increase the long-range order of the composite, and as a consequence, its ferroelectric response will become nonergodic. Further evidence thereof is shown in Chapter 6.

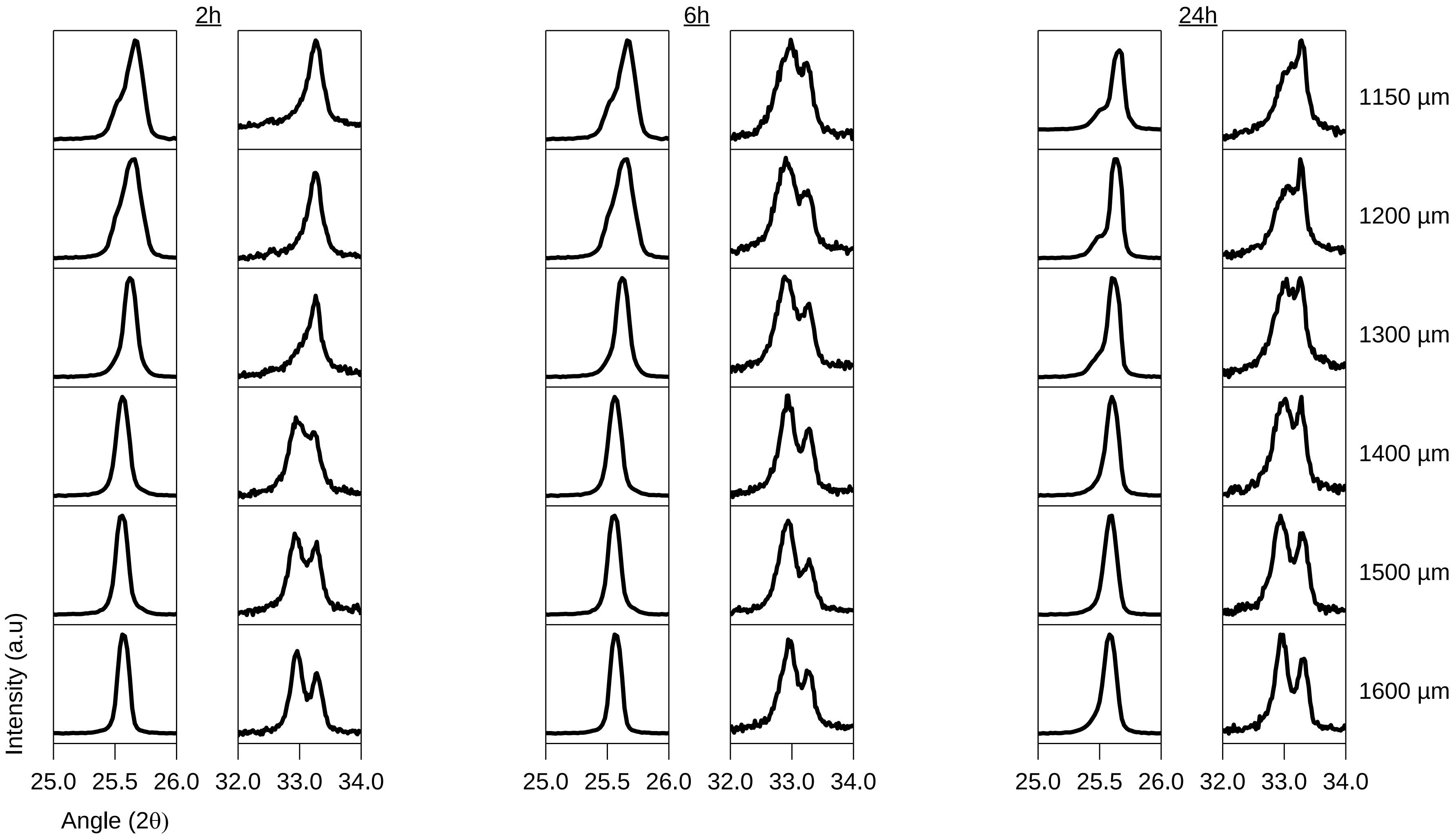

Figure 4.26: Normalized intensity of (111) and (200) peaks from 150 to 500 µm in 2-2 BNKT-BA/BNT-BT composites sintered for 2 h, 6 h, and 24 h

4.5. Summary

In this chapter, the influence of co-sintering on chemical composition and crystal structure in lead-free ferroelectric composite systems was presented. Two composite systems were investigated: BNT-6BT-3KNN/BNT-7BT and BNKT-6BA/BNT-7BT. The former was selected because of previous work showing that it has an electromechanical response comparable to PZT. The influence of co-sintering on crystal structure was investigated by micro-XRD, which revealed changes in diffraction patterns that are indicative of the formation of an orthorhombic phase at the interface of the seed and matrix, possibly due to diffusion of K and Nb.

However, investigations of chemical interaction are limited by the challenges of measuring interdiffusion under very low concentration gradients. Therefore, the BNKT-6BA/BNT-7BT system was used as a model system in which a larger concentration gradient enabled the investigation of both chemical composition and crystal structure as a function of composition and sintering parameters. This investigation revealed significant nonuniformity in the structure found in 0-3 composites. A more exhaustive investigation of chemical and structural changes was performed in 2-2 composites. Interdiffusion of Al, K, and Ba were shown between the seed and matrix layers. The diffusivity of these species was highly dependent on the seed content. The interdiffusion was shown to correspond to changes in crystal structure and lattice parameter. These interactions were further investigated through a sintering study in the same system, which revealed that sintering time had a profound effect on both composition and structure, with increasing sintering time resulting in increased long-range chemical order.

5. Internal Stresses in 2-2 Composites and Influences on Microstructure and Electromechanical Behavior

5.1. Introduction

The previous chapter provided evidence for the influence of co-sintering on chemical and crystal structure in lead-free composite systems. However, interactions between composite constituents are not limited to interdiffusion. The inherent differences in sintering behavior, thermal expansion coefficients and electromechanical properties of the composite constituents are bound to result in internal stresses, and an understanding thereof is essential to the tailoring of composite systems for optimization of piezoelectric response. To that end, 2-2 composites were utilized as an experimental model of the distribution of stress in this work. 0-3 composites are influenced by a stress state with far greater complexity than the 2-2 system in which in-plane axial stresses predominate. Therefore, for this work, the investigation of the influence of stress is limited to 2-2 composites.

The contributions to internal stress investigated in this chapter are the following:

Residual Stresses from Differences in Sintering Shrinkage

Dilatometry measurements of calcined powder were performed, and the shrinkage during sintering is compared in order to determine the stress experienced by each component of the composite during processing. To date, the effects of co-sintering on ferroelectric composites have not been exhaustively investigated, despite the large body of evidence indicating significant internal stresses in laminate structures [44], [141], [151], [194]. Stresses during sintering are also known to affect the microstructure of ceramics [3], [195], [196], and resultant changes in porosity and grain size have been shown to affect the electromechanical response of, *e.g.*, PZT, [156]. Therefore, the effect of the determined stresses on microstructure in 2-2 composites of BNT-based ferroelectrics is evaluated through SEM and light microscopy image analysis. The standard definition of sintering stress is the ratio of particle surface tension to average particle radius, used to describe densification processes in ceramics. In this work, the term sintering stress is instead used to discuss the residual stresses that arise during co-sintering, specifically during densification of composite components with differing sintering trajectories.

Thermal Stresses due to Differences in Coefficients of Thermal Expansion (CTE) in the Sintered Bodies

The differences in CTE will result in residual stresses in the sintered body prior to application of external fields. Mechanical stress can induce ferroelastic switching when it exceeds the coercive stress of the material, as shown in BNT-BT [197], [198]. This will affect the piezoelectric response of the material as well. A determination of the internal stress due to differences in CTE is presented. Evidence of internal stresses due to CTE is shown through the analysis of crack propagation induced through Vickers indentation.

Crystal Structure

To elucidate the atomistic mechanisms behind the influence of mechanical stress, an *in-situ* XRD investigation during application of compressive stress was performed in which the crystal structure of BNT-BT-KNN and BNT-BT are investigated. This data is compared to the diffraction patterns obtained by local micro-XRD in the 2-2 composites as described in Chapter 1.

Influence of Stress on Mechanical Properties

The influence of mechanical stress on elastic properties has been observed in soft PZT during uniaxial load and unloading, which revealed a nonlinear increase and decrease of the elastic modulus, similar to the course of the ferroelastic stress-strain curve [42]. In this work, the influence of applied mechanical stress on the elastic modulus is examined for BNT-7BT and compared to the mechanical properties of BNT-7BT in a 2-2 composite structure obtained through a nanoindentation study. The changes in mechanical properties of the composite relative to the freely sintered constituents are considered in light of mechanical stresses, changes in microstructure, and changes in composition. However, it is important to note that the external applied stress in most investigations is uniaxial, whereas the residual stress state in the 2-2 composites is in-plane biaxial, rendering direct comparison of the effect of mechanical stress challenging.

Mechanical Stresses due to Differences in Field-Induced Strain Mechanisms such as Piezoelectric Response and Relaxor-to-Ferroelectric Transitions

Under an applied field, a difference in the large signal transverse piezoelectric coefficient d_{31}^{*} will result in stresses parallel to the applied field in-plane with the interface in 2-2 composites. These stresses are calculated, and considered in light of strain mapping attained from tracking displacement at the micrometer scale with the help of digital image correlation during applied electric fields in 2-2 composites.

The first part of this chapter discusses the formation of residual stresses as a consequence of the processing of ceramic/ceramic composites in the final sintered body. It is well established that such residual stresses can have as much of an influence on the electromechanical behavior as externally applied stresses [199]–[201]. Therefore, the effect of external applied mechanical stress was evaluated for the properties listed below.

Dielectric and Ferroelectric Response of the Pure Constituents

The dielectric response as a function of stress at 25 °C is shown for BNT-BT-KNN, and BNT-7BT. The polarization response of BNT-BT-KNN, BNKT-6BA, and BNT-7BT are evaluated as a function of applied compressive stress.

5.2. Methodology: Calculation of Internal Stresses

In this chapter, a computational model developed by Chartier *et al.* is used to determine the internal stresses in 2-2 composites [141]. Unless otherwise noted, the reference for the next few paragraphs is this work. This model was developed in order to calculate the stress due to differences in CTE in layered ceramics, but can be applied to the determination of stress states resulting from differences in elongation in response to a variety of stimuli. The first point in a laminate's history at which such internal stresses are present is at the initiation of densification during sintering. If one of the components has densified prior to the other, it begins to act as a dense substrate during grain nucleation and growth of the second component [151]. The equation used for determining stress in the seed σ_S and matrix σ_M in a three-layer laminate structure as used in this study and is given below:

$$\sigma_S(T) = \frac{Y_S Y_M (\varepsilon_S(T) - \varepsilon_M(T))}{(1-v)} \frac{\frac{h_s}{h_M}}{2Y_S \frac{h_s}{h_M} + Y_M} \qquad (5.1)$$

$$\sigma_M(T) = -2\frac{\sigma_S\,(T)}{h_s/_{h_M}} \qquad (5.2)$$

where $Y_s\,(BNT-7BT) = 100\;GPa$ [202], $Y_m\,(BNKT-6BA) = 128\;GPa$ [203], $Y_m(BNT-6BT-3KNN) = 115\;GPa$ [202], v is the Poisson ratio (0.33), (in this work as an approximation for most ceramic materials), $\varepsilon_S, \varepsilon_M$ are the thermal strains in the seed and matrix material at a specified temperature T, and h_S and h_M are the height of the seed and matrix layer, respectively. Because the density of the powders is similar, the weight ratio is treated as equivalent to the height ratio for these calculations. From the above equation, it is clear that the stress states are highly dependent on the proportion of matrix to seed material. It is important to note that this model assumes no interdiffusion between the layers during sintering, which was clearly shown to occur in Chapter 4 for the BNKT-BA/BNT-7BT composite.

5.3. Thermal Strains

As discussed above, the determination of stress in the material requires the measurement of strain caused by differences in either thermal or piezoelectric expansion. A description of how these strains are determined follows below. The first stress state to be discussed is the stress during sintering due to differences in shrinkage of calcined powder. This stress has an influence on the microstructure formed during sintering. The second stress state is due to the difference in

CTE of the sintered bodies as they cool from the sintering temperature to room temperature. These stresses are present before the application of an electric field, and can affect the piezoelectric and dielectric behavior of the composite.

5.3.1. Residual Stresses during Sintering

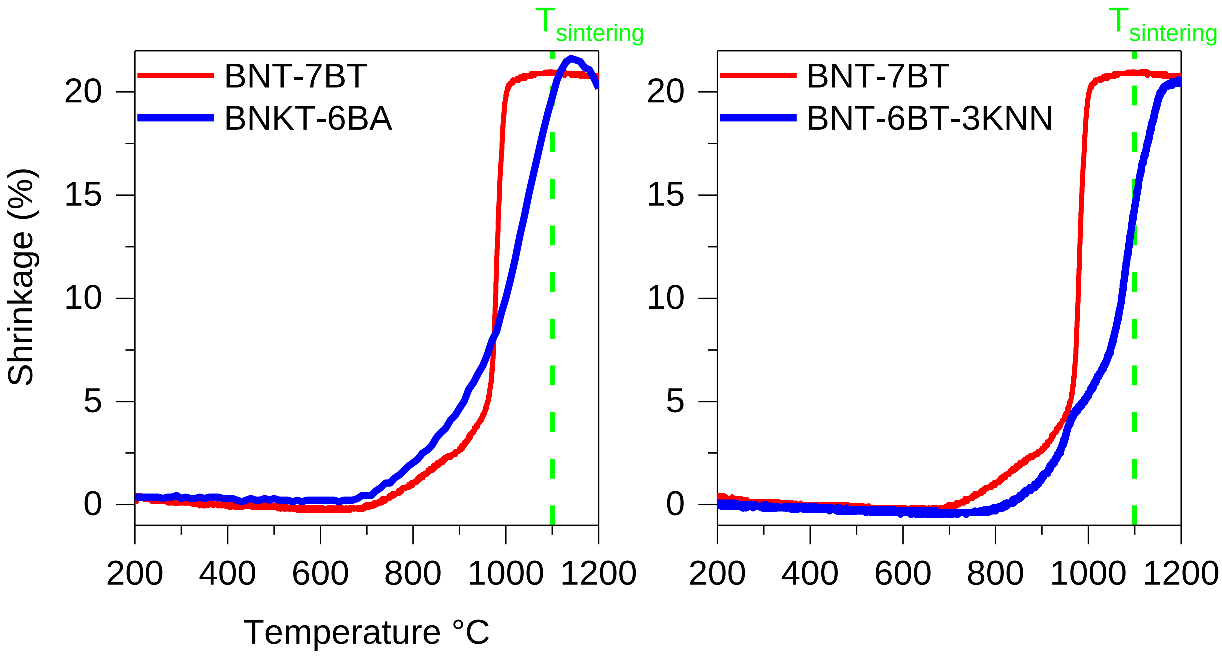

Figure 5.1: Sintering trajectories of BNKT-6BA/BNT-7BT and BNT-6BT-3KNN/BNT-7BT composite system pure end member powder from 200 to 1100 °C at a constant heating rate of 5 °C/min

The sintering trajectories for BNT-7BT and BNKT-6BA powder are shown in Figure 5.1. At 1100 °C, the sintering temperature used in this study, a much larger strain difference is observed between BNT-7BT and in the BNT-BT-KNN than the same material with BNKT-6BA. From 200 °C to 950 °C, the shrinkage of BNKT-6BA is higher than that of BNT-7BT. This may in part be attributed to the high diffusivity of K and Al, as was shown in Figure 4.14. However, because neither component will have reached a densified state in that temperature range, the difference in shrinkage will not result in significant internal stresses during sintering. On the other hand, the increased density of both component above 1000 °C means that the component with a lower shrinkage rate (BNKT-6BA) can be treated as a rigid substrate that induces a constraint on the sintering of the component with the higher shrinkage rate (BNT-7BT).

A schematic of the development of stresses due to differences in sintering shrinkage is shown in Figure 5.2. Before sintering, pressed layers of all starting powders are identical in dimension. At the sintering temperature, shrinkage of the matrix components, BNKT-6BA and BNT-6BT-3KNN, is lower than the shrinkage of the seed layer, BNT-7BT. Because the final cylinder is nearly uniform in diameter, the stress states in the matrix and seed layers of the two composite systems during sintering will differ significantly. The seed layer, in order to accommodate the lower shrinkage of the matrix layer, will experience tensile stresses. The matrix layer, in order to accommodate the relatively higher shrinkage of the seed layer, will experience compressive stresses.

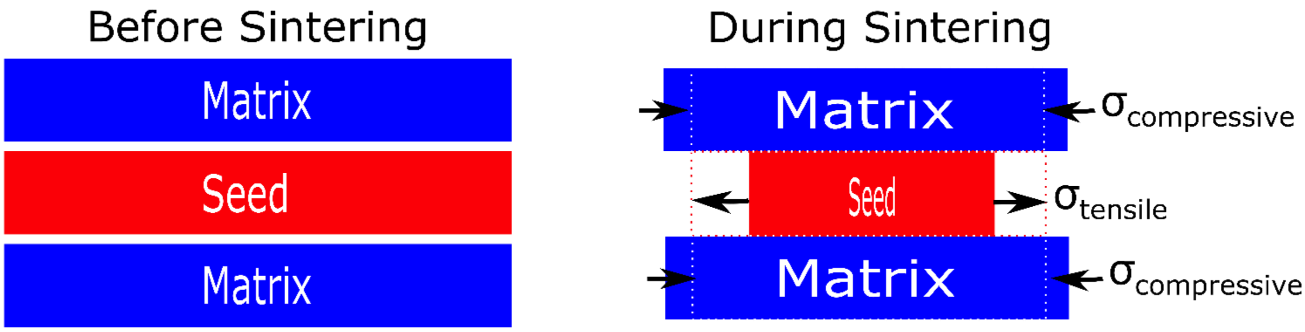

Figure 5.2: Schematic of internal stresses during sintering due to differences in shrinkage between seed and matrix layers. A dashed line represented the sample dimensions upon completion of sintering, where the matrix and seed layers are equal in diameter but with different residual stress states

The sintering stress is calculated at each seed content using Equation 2.1, where the difference in strain at the sintering temperature of 1100 °C is used as the $(\varepsilon_S - \varepsilon_M)\Delta T$ variable. As shown in Figure 5.3, the stress state in BNT-BT-KNN composites is four times higher than the BNKT-BA composites, because of the larger difference in shrinkage between BNT-BT-KNN and BNT-7BT. This is likely to have an impact on 0-3 composites as well. The compressive stress acting on the matrix material appears to increase with increasing seed content, whereas the tensile stress on the seed material decreases with increasing seed content. These stresses have a significant impact on the microstructure and can be optimized to tailor the microstructure by adjusting the temperature at which the sintering is held. Effects on the microstructure include changes in density, grain size, pore size and porosity. These have been shown to change as a consequence of applied mechanical stress during sintering, termed hot forging, [5], [204], as well as through stresses during constrained sintering of a ceramic on a dense substrate [140], [205]–[207]. Previous work on constrained sintering has shown stresses of 140 MPa in BKT films with a thickness of 80 µm sintered on a rigid alumina substrates, as determined from shifts in the XRD reflections [201]. However, such calculations only provide information on residual stresses, and not the stresses extant during sintering. *In-situ* measurements of stress during constrained sintering of Gd-doped ceria have revealed tensile stresses up to 250 MPa [208]. One investigation on the constrained sintering of alumina thick films showed residual tensile stresses of up to 450 MPa [3]. The fact that the stresses calculated in this system are in the GPa range may be due to the assumption of a rigid substrate during sintering. However, as neither component has fully densified, the stresses are likely to be lower than those determined from the Chartier model. These results can nevertheless be used to understand the influence of such stresses on the microstructure of the composites. In addition, these calculations reveal that changing the sintering temperature and volume fraction of seed influences the stress state. This information can be used to manipulate the microstructure, as will be discussed in further detail shortly.

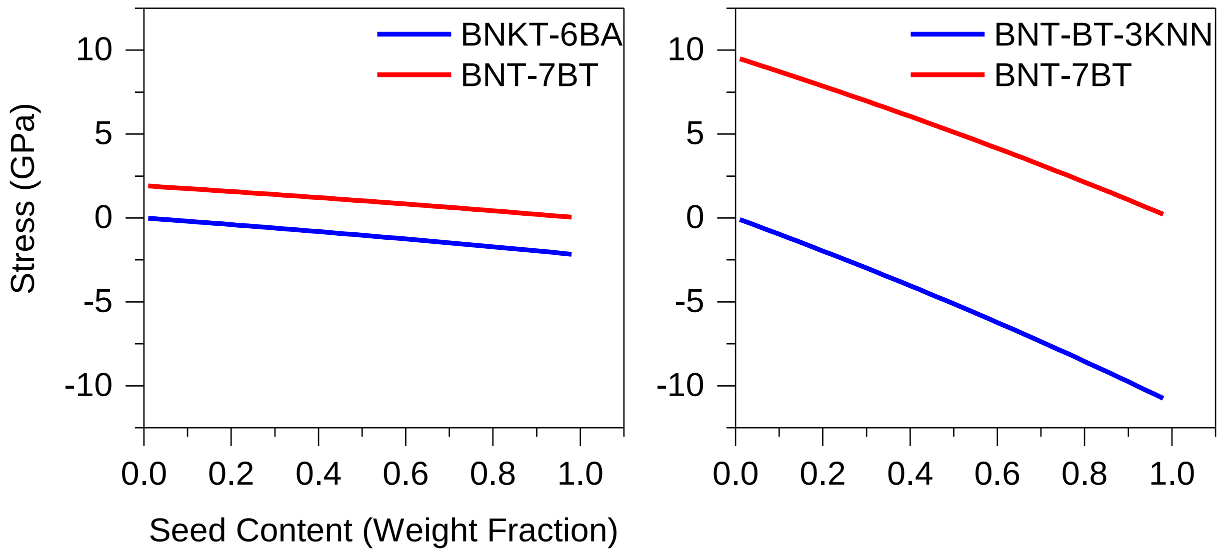

Figure 5.3: Internal stresses at sintering temperature in BNKT-BA/BNT-7BT composites and BNT-BT-KNN/BNT-7BT composites, as a function of seed content.

In Figure 5.4, the sintering stress in the matrix and seed layers of the composite as a function of temperature for the BNKT-BA and BNT-BT-KNN 2-2 composite systems is shown, as calculated with the Chartier model, using the difference in shrinkage between the two components as the thermal strain component of the equation. An optimal sintering temperature can be selected based on the data shown in this figure. Only temperatures above 900 °C are shown because below that temperature the degree of shrinkage is not sufficient for a fully densified ceramic of at least 90% relative density. If the intention is to reduce internal stresses during sintering and not change the microstructure as a consequence thereof, the optimal sintering temperature should have a zero-stress state. This can be found in BNKT-BA composites at 970 °C, 1115 °C and 1187 °C. The temperature range between 1117 °C and 1187 °C has the lowest stress during sintering, *i.e.*, below 1 GPa both in tension and compression. It is also possible to reverse the stress state during sintering by selecting a temperature where the seed is under compression and the matrix is under tension. This occurs between 900 and 975 °C, where the compressive stress would be -3 GPa in the seed and the tensile stress is 1.3 GPa in the matrix. Between 1120 and 1190 °C, the same stress state occurs, with the seed in compression and the matrix in tension, this time at a lower stress of -0.72 GPa and 0.3 GPa respectively, which should result in a reduced change in microstructure relative to the freely sintered end members.

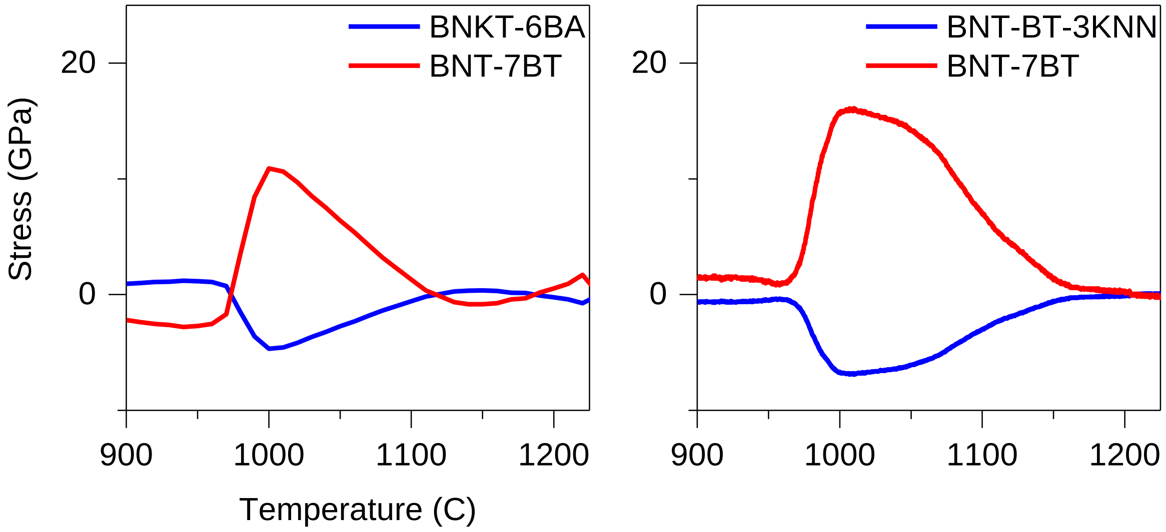

Figure 5.4: Sintering stresses as a function of temperature in each component of a 2-2 composite with 30% seed content, with a BNKT-6BA/BNT-7BT composite shown on the left and a BNT-6BT-3KNN composite shown on the right, with the assumption of constant elastic modulus, Poisson ratio and layer dimensions in this temperature range

In the BNT-BT-KNN system, a minimum stress state occurs at 1210 °C. Between 960 and 1150 °C, the internal stress of the matrix phase is above 2 GPa, and reaches 16 GPa at 1100 °C. It is likely that if the 2-2 composites were sintered in the latter temperature range a delamination would occur due to tensile stresses. This information is useful for selection of the sintering temperature, and can also be used to adjust the microstructure, namely porosity and grain size, without the application of external pressure during sintering.

5.3.2. Influence of Sintering Stress on Microstructure: BNKT-6BA/BNT-7BT 2-2 Composites

Evidence of the influence of the aforementioned stress on the microstructure was obtained in the BNKT-6BA/BNT-7BT 2-2 composite system through an analysis of the granular and pore microstructure across the sample. The stresses formed due to differences in shrinkage rate are relaxed through mechanisms such as grain boundary diffusion, which in turn changes the microstructure of the composite relative to freely sintered end members [140], [208].

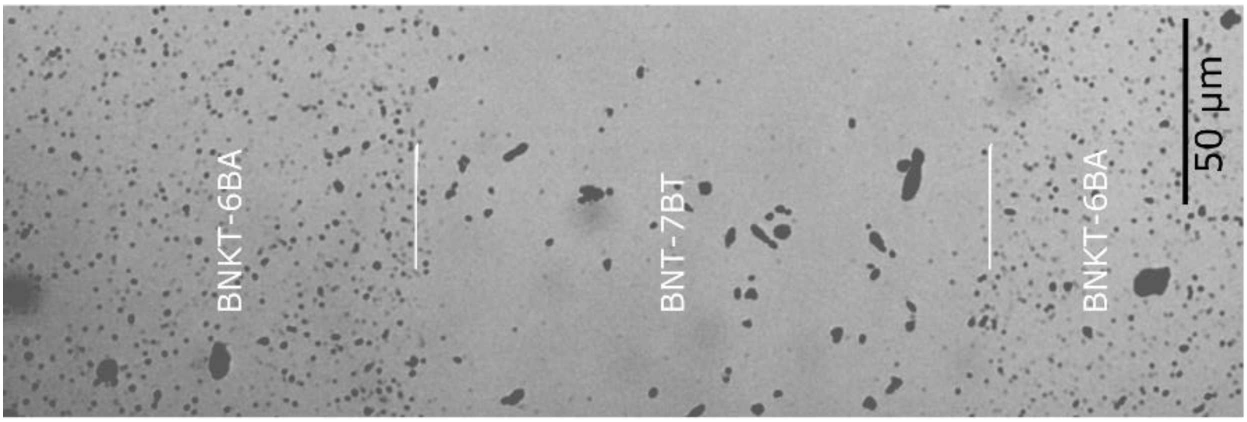

Figure 5.5: Light microscope image of 2-2 composite of BNKT-6BA/10% BNT-7BT, with a white line indicating the interface between the two constituents, sintered for 2 h at 1100 °C

In Figure 5, a light microscope image of a 2-2 composite is shown, as a representative image of the difference in the porosity across the sample. It can be observed that the matrix BNKT-6BA regions have a high number of pores, and that the pore size is on the order of 1 µm. On the other hand, in the seed BNT-7BT region, the pores are between 3 and 10 µm in diameter, and display a decreased circularity. The total porosity in this region is also substantially lower than in the matrix region.

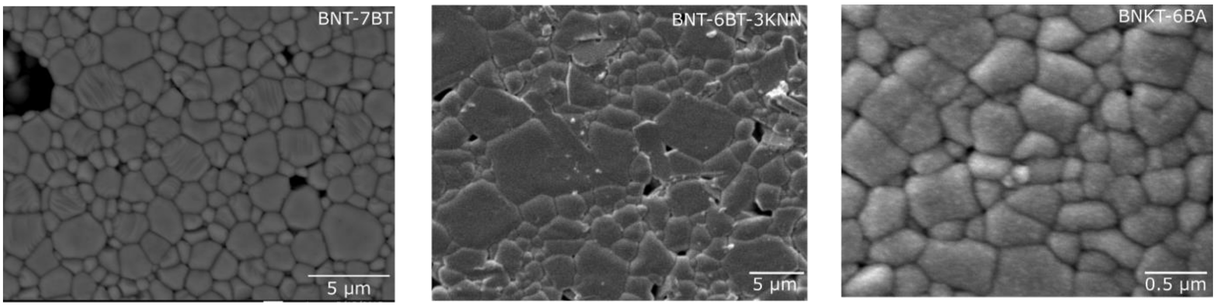

Figure 5.6: SEM micrographs of pure end members, BNT-7BT obtained with a beam of 15kV, BNT-6BT-3KNN obtained at 6000x, with a beam of 15kV, BNKT-6BA obtained with a beam of 15kV. (Note the change of scale in BNKT-6BA).

Representative SEM images of the freely sintered end members are shown in Figure 5.6. In Figure 5.7, representative SEM images of the granular microstructure in the 2-2 composites can be observed at the top, middle and bottom of the sample, where the top and bottom are the matrix phase and the middle is the seed phase. From Figure 5.6, the average grain size of the freely sintered BNT-7BT seed is determined to be 1.65 µm. The grain size of the central seed region in the BNKT-BA/BNT-BT 2-2 composite is well below this value, no matter the seed percentage. In contrast, the average grain size of freely sintered BNKT-6BA is 0.4 µm, from which a far smaller deviation can be observed in the 2-2 composite. Details of the determination of grain and pore size are provided in the Experimental Methodology.

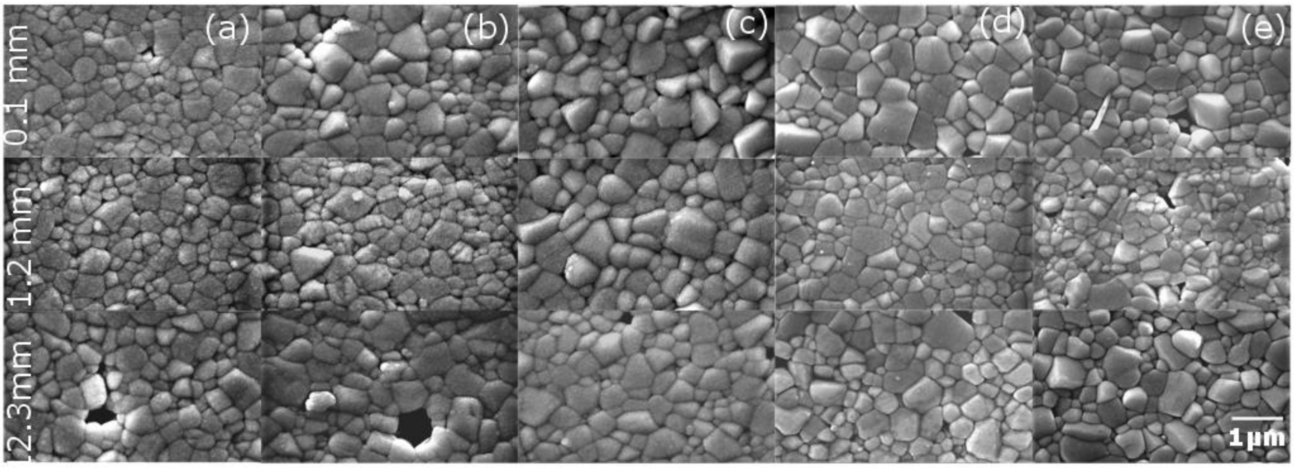

Figure 5.7: Representative SEM images of grain sizes across BNKT-6BA/BNT-7BT 2-2 composites at 0.1mm, 1.2mm, and 2.3mm from the top of the sample (a)10% seed (b) 20% seed (c) 30% seed (d) 40% seed (e) 50% seed

A more quantitative analysis of the microstructure is presented in Figure 5.8. An increase in the pore size and reduction in the grain size is apparent in the inner seed layer of each composition. When considering the internal stresses due to the difference in shrinkage rate from 900-1100 °C, the seed is expected to experience tension in this temperature regime, while the matrix experiences compression. The average grain size at the center of the seed region size decreases from 0.33 µm in the 10% sample to 0.31 µm with 30% seed. In the 40 and 50% seed composites, the interface region is close to 0.32 µm, similar to the grain size at lower seed contents. However, the average grain size in the seed region is found to decrease to 0.27 and 0.26 µm, respectively. Decreasing grain size in the seed region implies an increase in compressive stress, or a reduction in tensile stress, with increasing seed content. The latter corresponds to predictions based on the Chartier model shown in Figure 5.3.

In the matrix phase, the 30% composite has the highest grain size, 0.45 µm, whereas the 40% and 50% compositions have smaller grain sizes in the matrix phase (0.35 µm). This data also corresponds to the predictions shown in Figure 5.3, where the matrix phase experiences an increasing compressive stress with increasing seed content.

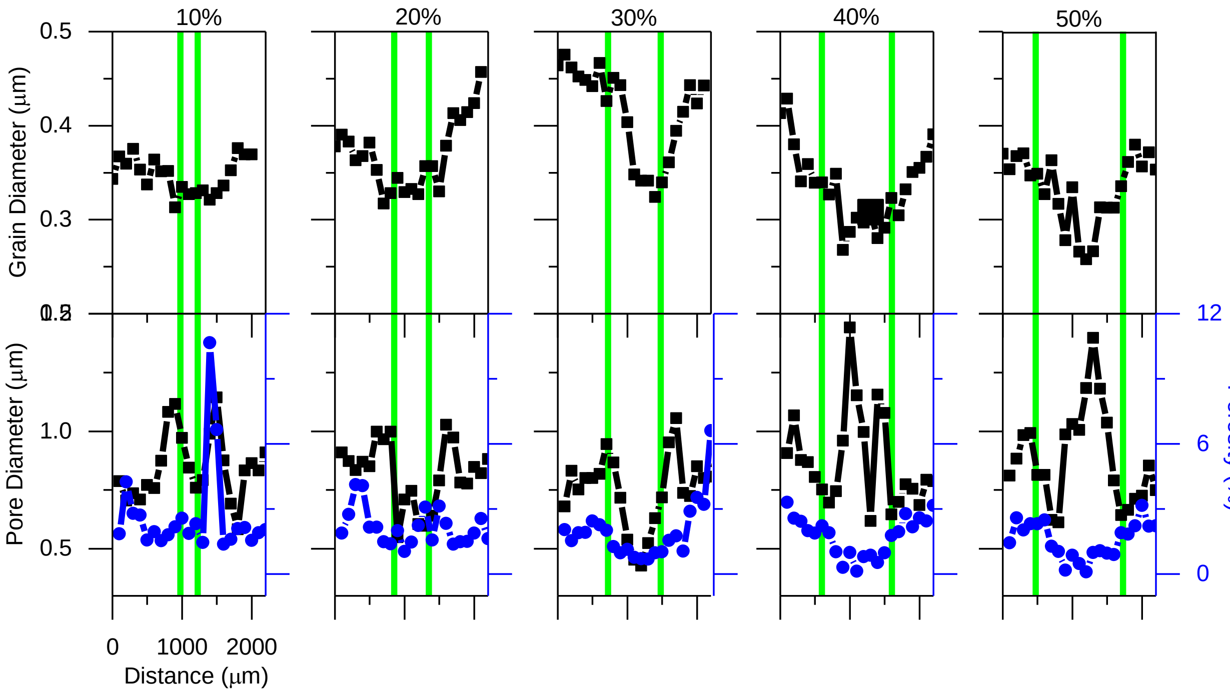

Figure 5.8: Quantitative Analysis of Microstructure in BNKT-6BA/BNT-7BT 2-2 Composites through Grain Size and Porosity

It is also noteworthy that in the 50% 2-2 composite, the grain size in the seed region has a sharp peak of 0.33 µm, and the remaining region of the seed has a much smaller grain size of approximately 0.1–0.2 µm. A similar phenomenon, albeit not as sharp, can be observed in the 40% 2-2 composite, where the seed region has a maximum grain size of 0.3 µm peaking in the center, with lower grain size of 0.15 µm on either side of 0.3 µm region. This indicates that the influence of co-sintering is not uniform through each layer.

Across each sample, a large number of small pores (< 0.1 µm) were found in the matrix region, and a smaller number of very large pores were found in the seed region. In the 10% composite, a peak in the pore size can be observed at approximately 1400 µm across the sample, with a corresponding dip in the porosity in that region. The porosity of the seed region decreases with increasing seed content from 10% to 50%. This may also be connected to the fact that tensile stresses reduce with increasing seed content. The pore size of the seed region also decreases with increasing seed content from 10 to 30% seed, which is also easily correlated to the reduced tensile stress. However, at 40 and 50% seed, the pore size of the seed region increases substantially.

The influence of the interdiffusion shown in Chapter 4 cannot be neglected in the discussion of microstructure. It was shown previously that a high concetration of Al and K was localized to the pores in the 0-3 composites. With this in mind, it is possible that increasing layer thickness influences the kinetics of diffusion. The reduction of pore number in the

10-30% composites can also be a consequence of increased diffusion between seed and matrix, because the interdiffusion range covers the complete seed region. At higher seed contents, the seed region is thicker and therefore larger than the total interdiffusion zone. As a result, pores are filled by diffusing species from the matrix region at only at the seed/matrix region interface. However, at the center of the seed region, the pores are not filled and undergo tension from sintering stresses, thereby expanding.

Previous investigations using techniques such as hot forging have shown a reduction in grain size when a compressive stress is applied during sintering [5]. On the other hand, constrained sintering studies have shown an elongation of pores and grains, which was attributed to tensile stresses [195]. Therefore, the grain size appears to depend on several factors, including internal stresses, but a more complete picture of the mechanisms of grain growth must include the kinetics of this process, namely diffusion. Because of the concentration gradient between the seed and matrix layers, interdiffusion of Al and K may also affect the grain growth. It must be stated that the Chartier model assumes uniform distribution of in-plane biaxial stresses, whereas in reality constrained sintering results in inhomogeneous stress states across each layer [44]. The inhomogeneous grain size of the seed layer may be a consequence of the inhomogeneous concentration of Al and K in the seed region, as well as inhomogeneous stress states. Previous work has shown that the grain size and porosity of multilayers are strongly influenced by stresses arising from constrained sintering at the interface [151].

The influence of grain size has been observed very often in ferroelectrics [209], [210]. This size influence has been attributed to the influence of grain boundaries on domain wall motion under applied fields, where they act as pinning centers [65], [66]. The effect of reduced grain size improving the ferroelectric response was observed in BNT-6BT when comparing the polarization response with a grain size between 1 and 2.5 μm, where it was found that the highest remanent polarization was in the smallest grain size samples [212]. Therefore the influence of internal stress on microstructure can be used as a parameter for the tailoring of microstructure towards the optimization of electromechanical behavior.

5.3.3. Residual Stresses Due to Differences of CTE in Sintered Bodies

The determination of the residual stress state in the final sintered samples requires an understanding of the thermal contraction during cooling of already densified samples. For this purpose, the shrinkage from the sintering temperature to room temperature must be determined, as shown in Figure 5.9, and used to evaluate the CTE over that temperature range, shown in Figure 5.10. Each matrix material is shown in comparison to the seed material to facilitate discussion. This data is obtained from freely sintered constituents and is then used to determine the internal residual stress due to the differences in CTE.

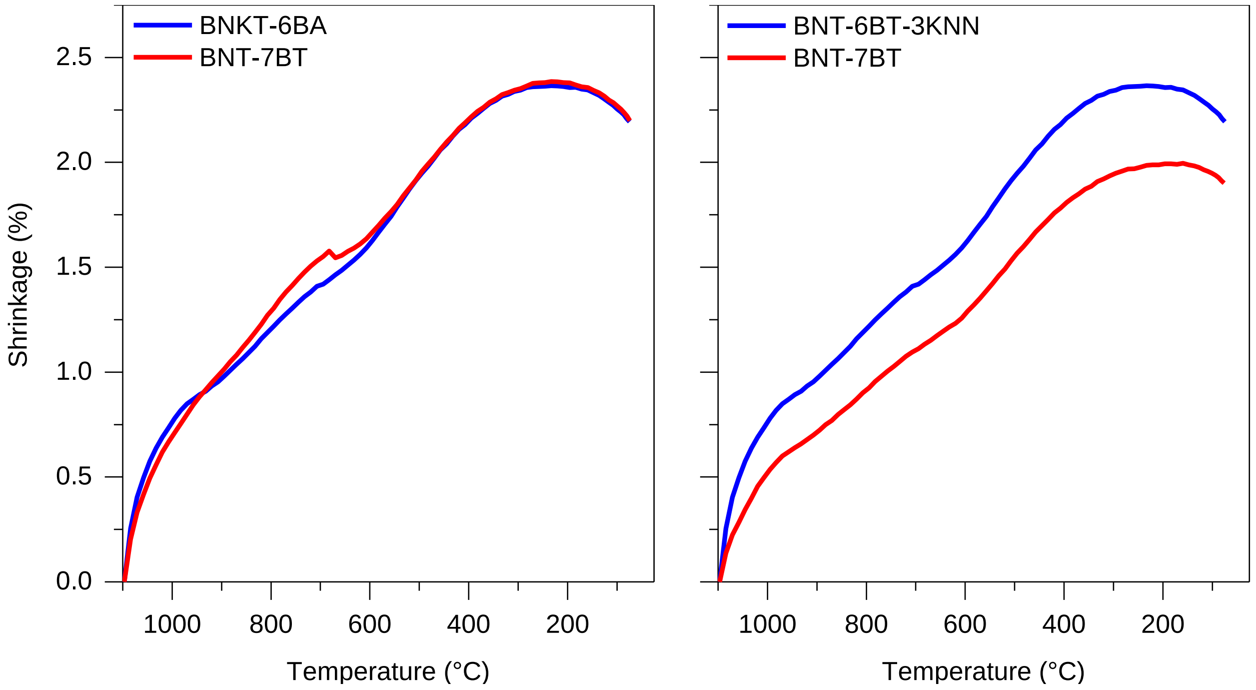

Figure 5.9: Shrinkage as a function of temperature for BNT-7BT, BNKT-6BA and BNT-BT-3KNN, with BNT-7BT shown in both panels to facilitate comparison with the matrix material

It can be observed that the difference in shrinkage between BNT-BT-KNN and BNT-7BT is several orders of magnitude higher than in the difference in shrinkage between BNKT-6BA and BNT-7BT. There is also a maximum at 300 °C, meaning that an expansion occurs in the temperature range from 25 °C to 300 °C, instead of a contraction, during cooling. This may be attributed to a temperature-dependent phase transition from a cubic to a lower symmetry tetragonal and rhombohedral phase, as has been frequently observed in BNT-based relaxors [39], [213], [214].

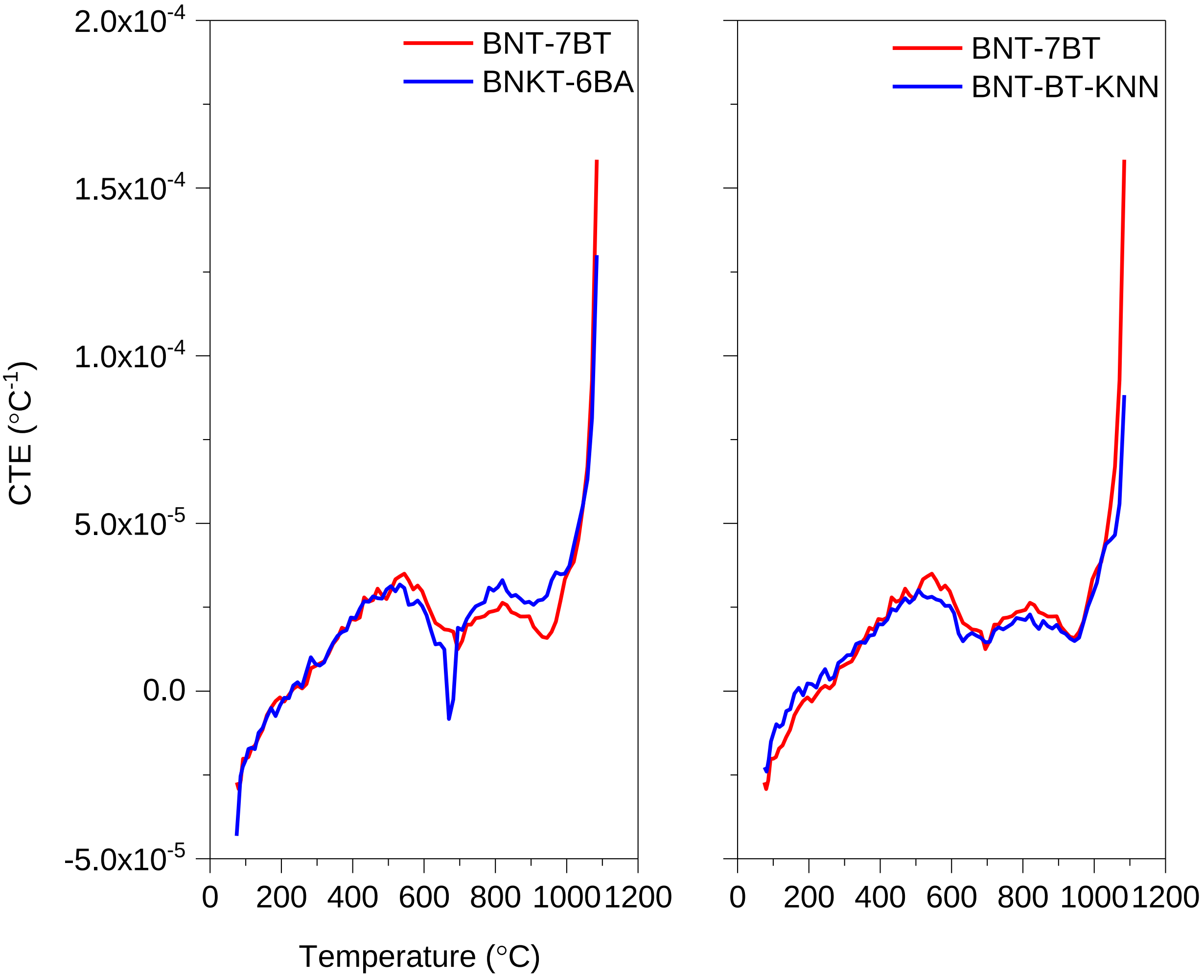

Figure 5.10: CTE as a function of temperature in BNT-7BT, BNKT-6BA and BNT-BT-3KNN, with BNT-7BT shown in both panels to facilitate comparison with the matrix material, obtained from sintered samples heated to 1100 °C and then cooled. Only the cooling curve is shown.

Using the Chartier model, the internal stresses in a 2-2 composite resulting from the difference in CTE can be determined. The results of this calculation are shown in Figure 5.11. At higher temperatures (T >500 °C), the BNT-7BT layer is in compression while the matrix BNKT-6BA and BNT-BT-KNN layers are in tension, a reversal of the stress states during sintering. However, from 470 °C to 25 °C, BNT-BT is under tension and BNT-BT-KNN is under compression. Because annealing is performed at 400 °C, the stress state predicted in this temperature range is likely to have a strong influence on the electromechanical response of composites.

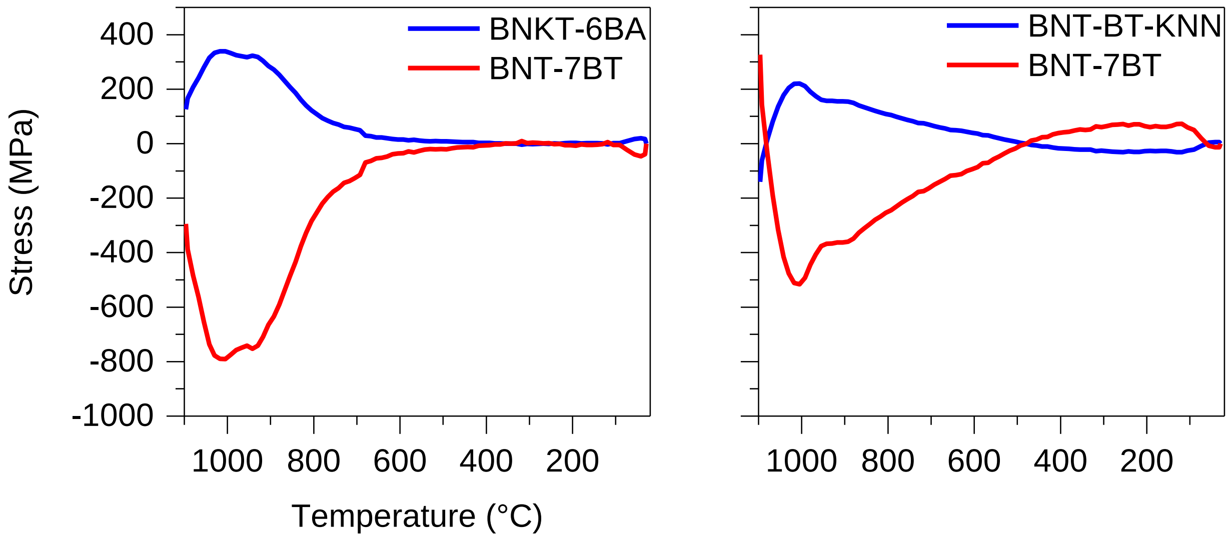

Figure 5.11: Final stress state upon cooling from sintering temperature to room temperature in 2-2 composites of BNT-7BT/BNKT-6BA and BNT-7BT/BNT-BT-3KNN as a function of temperature, at a seed content of 30%

The difference in shrinkage results in an internal stress at room temperature that cannot be eliminated by annealing, as shown by the nonzero stress state in either layer of the composite in Figure 5.12. This provides evidence of the lack of equivalence between ER matrix materials in a composite, despite their similar electromechanical behavior. In a 2-2 composite with BNKT-6BA, BNT-7BT is in compression, whereas in a composite with BNT-BT-KNN, it is in tension. Increasing seed content in the BNKT-6BA composite results in increased tensile stresses in the matrix and reduced compressive stresses in the seed. The structural data shown in Chapter 4 pointed to an increase in the lattice parameter of the matrix BNKT-BA region, indicative of tensile stresses, which corroborates the prediction of the Chartier model shown in Figure 5.11.

On the other hand, in the BNT-BT-KNN composite, increasing the seed content reduces the tensile stresses in the seed layer and increases the compressive stresses in the matrix layer. This correlates to the structural data determined by micro-XRD in this composite system, (see Figure 4.4 and Figure 4.8), in which the lattice parameters of the seed region increased relative to the freely sintered constituent, indicative of a tensile stress, whereas the lattice parameters of the matrix region decreased, indicative of a compressive stress.

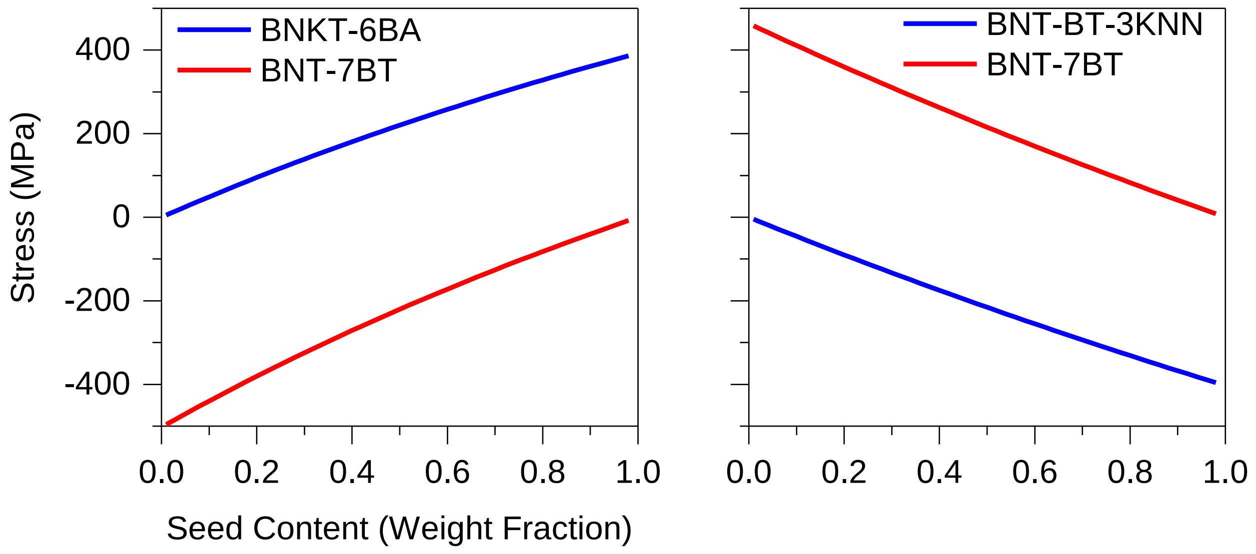

Figure 5.12: Final stress state upon cooling from sintering temperature to room temperature in 2-2 composites of BNT-7BT/BNKT-6BA and BNT-7BT/BNT-BT-3KNN as a function of seed content

5.3.4. Crack Propagation in 2-2 Composites as Evidence of Residual Stress States

To confirm the presence of residual stress, indentation methods are a useful method due to the influence of these stresses on crack propagation [215]. In ferroelectric ceramics, this influence is complicated by the fact that the internal stress generated by crack propagation can, upon exceeding the coercive stress, induce domain switching [216]. When such domain reorientation inhibits crack propagation, it is termed ferroelastic toughening [217]. The mechanism by which this toughening occurs is based on the fact that the process zone of a crack exerts a tensile stress sufficient to induce domain reorientation [218]. When the initial domain orientation is parallel to the crack, the mechanical stress at the crack process zone induces domain reorientation perpendicular to the crack. This reorientation results in compressive closure stress, which decreases the crack propagation [219]. On the other hand, when the domains along the crack are initially perpendicular to the crack, the tensile stresses from the crack process zone can not reorient the domains. Therefore, under Vickers indentation, the direction of longest crack propagation is indicative of domains oriented perpendicular to the crack.

In the case of relaxor materials, domains can only be formed by stresses above the coercive stress. The internal stresses due to difference in CTE shown in Figure 5.12 will result in domains perpendicular to the crack in the x-direction. The crack propagation parallel to the interface is therefore expected to be shorter than the cracks perpendicular to the interface, as shown schematically in Figure 5.13 (b).

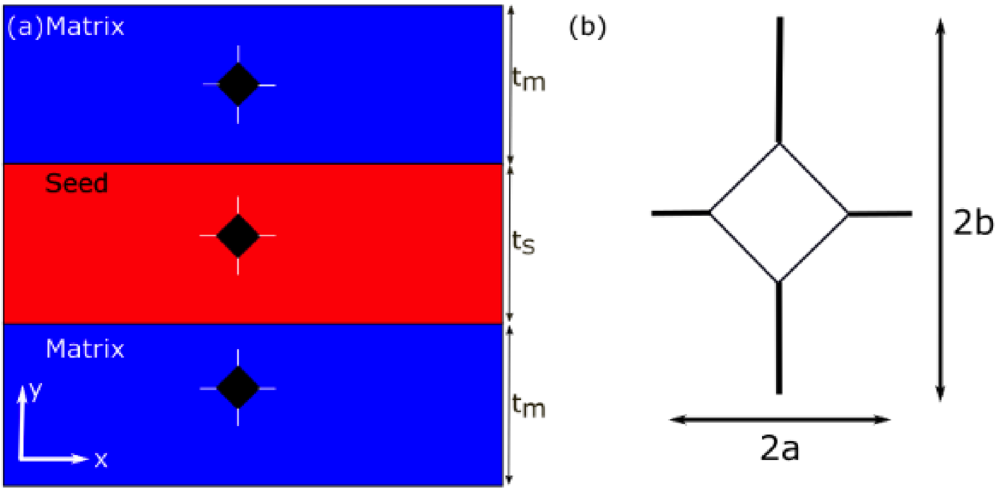

Figure 5.13: Schematic of Vickers indentation (a) in 2-2 composite (b) crack length parallel and perpendicular to interface between seed and matrix

Vickers indentation was used to verify the stress state of each layer of the co-sintered multilayer. Figure 5.13 (a) shows a schematic of the 2-2 composite, with the approximate position of the indents and a coordinate system to guide the analysis of crack propagation. The 2b length is aligned perpendicular to the interface (y-axis), whereas the 2a length is parallel to the interface (x-axis). During testing, three indents were applied in each layer, with a minimum spacing of 700 µm to avoid interactions between indents. Cracks emanating from the indent are approximately an order of magnitude shorter than the overall layer thickness, ensuring that the crack propagation did not extend into the next layer. Vickers indentation experiments were also performed on bulk unpoled BNT-7BT and BNKT-6BA end members.

In Figure 5.14, the crack propagation from a Vickers indent in freely sintered BNKT-6BA, BNT-7BT and the respective layer of the 2-2 composite are shown. Table 5 summarizes the numerical values determined from Figure 5.14 - Figure 5.15. In the bulk end members, shown in the bottom row of Figure 5.14, the crack propagation is isotropic, meaning that the 2a and 2b crack lengths are approximately equal, *i.e.*, a/b ≈ 1 for both samples. In the multilayer composite structure, however, a significant crack anisotropy is observed. In the BNKT-6BA layers, 2b is nearly 32 % longer than 2a. In contrast, the anisotropy is reversed in the BNT-7BT layer, with a horizontal crack length (2a) that is 59 % longer than the vertical direction (2b). This resulted in an a/b ratio of 0.68 in the BNKT-6BA layer and 2.45 in the BNT-7BT layer. The difference in anisotropy indicates a difference in stress states between the two layers, namely the BNKT-6BA layer is in tension, whereas the BNT-7BT layer is in compression.

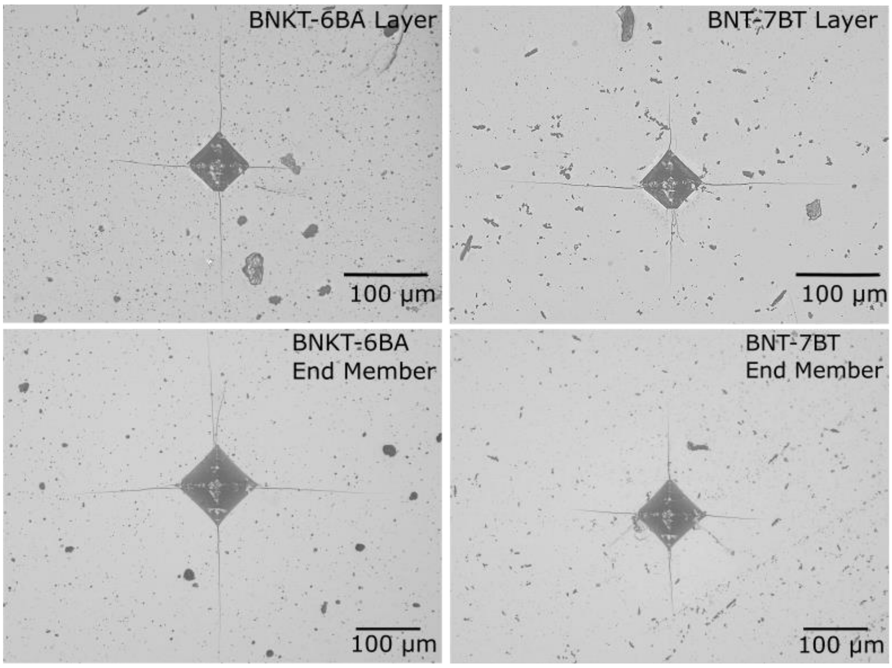

Figure 5.14: Light microscope images of Vickers indents in 2-2 composites and pure end members for comparison in the BNKT-6BA/BNT-7BT composite system

In Figure 5.15, a light microscope image of the Vickers indent and associated cracks on the compressed BNT-7BT sample are shown, where it can be observed that the cracks parallel to the direction of compressive stress (2b) are longer than the cracks perpendicular to it (2a). The crack anisotropy *a*/*b* in mechanically compressed BNT-7BT is 0.76. This behavior is comparable to the crack propagation observed in the BNT-7BT region of the 2-2 composite, where compressive stress is parallel to the interface, and the crack propagation is also extended parallel to the interface in comparison to the cracks perpendicular to the interface, and the stress direction. It was shown by Schader *et al.* that the coercive stress of BNT-6BT is –335 MPa, meaning that an external applied stress resulted in a mechanically induced transition to long-range ferroelectric order [76]. This means that domains can coalesce from polar nanoregions found in relaxors as a result of the application of mechanical stress. These domains will be perpendicular to the direction of applied stress, *i.e.*, oriented in the x-direction. As a result, crack propagation will induce 90° switching of the domains, resulting in compressive stress along the crack wake, which limits its propagation. This can be observed in the shorter length of the 2a cracks vs. the 2b cracks in Figure 5.15, resulting in an *a/b* ration of 0.76.

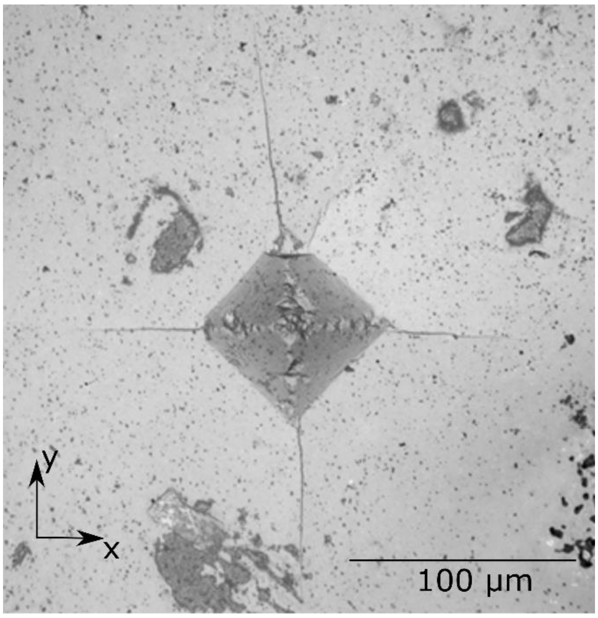

Figure 5.15: Light microscope image of a Vickers indent in BNT-7BT compressed ex-situ along the y-direction to -400 MPa

It is important to note, however, that the stresses in the multilayer structure are residual, while the externally applied stress is removed and the indentation experiment was performed *ex situ*. Another important difference is the direction of stress: in a 2-2 composite, residual stresses are in-plane and biaxial, whereas an external applied pressure induces a uniaxial stress. The a/b ratio in compressed BNT-7BT is 0.76. Keeping in mind that the direction of the stresses in compressed BNT-7BT is perpendicular to that of the BNT-7BT layer in the composite, the ratios can be compared by taking the inverse of the compressed sample, which is 1.32. The anisotropy of the BNT-7BT layer in the composite is therefore significantly larger than the compressed sample, despite the fact that the crack lengths are smaller.

Table 5: Crack propagation in constituents and 2-2 composites of BNKT-BA/BNT-7BT and BNT-BT-KNN/BNT-7BT

Material	*2a (µm)*	*2b (µm)*	*a/b Ratio*
BNKT-6BA	*33.9*	*34.5*	*0.98*
BNT-7BT	*26.6*	*27.3*	*0.97*
BNKT-6BA Layer	*55.2*	*81.1*	*0.68*
BNT-7BT Layer (6BA)	*102.7*	*42.0*	*2.45*
BNT-7BT Mechanically Compressed	*173.0*	*228.8*	*0.76*

The data above shows that mechanical stress arising from differences in CTE and sintering is an important factor in the behavior of ferroelectric composites. This factor must be considered when optimizing the composition, synthesis, and use of composites because it is known to influence electromechanical properties, [198], [220] including inducing stress-induced structural phase transitions in single-crystal and polycrystalline ferroelectrics [219], [197].

5.4. Influences of Mechanical Stress

The presence of internal stresses has been described and ascertained from the investigations described above. In this section, the influence of these stresses on the material properties of the end members will be discussed. It is well known that mechanical stress can act on a number of length scales, thereby influencing the crystal structure, mechanical properties such as hardness and elastic modulus, and the dielectric and ferroelectric response. All of these parameters were examined under compressive stress, for both the seed and matrix materials. In several cases, only one matrix material is examined, because of the availability of samples of the correct aspect ratio for mechanical testing.

5.4.1. Influence of Mechanical Stress on Crystal Structure

In situ stress-dependent XRD of pure BNT-7BT and BNT-7BT-1KNN were performed with the assistance of Dr. Manuel Hinterstein and Dr. Neamul Khansur at ID15 of ESRF. Details of this measurement can be found in the Experimental Methodology section. These results were published in [219], and the figures below are taken directly from that publication.

Figure 5.16 shows the stress-induced structural changes in the two constituents of the BNT-BT-KNN/BNT-7BT system through *in situ* diffraction experiments and the macroscopic stress-strain behavior. Although the KNN content is not the same as that used in the 2-2 composite system, a similar ergodicity in its strain response is observed and, therefore, can be considered analogous to the matrix material in the rest of the work. A stress-induced phase transformation is clearly visible for both compositions. In the BNT-7BT system, variation in (200_{pc}) and (222_{pc}) reflections as a function of compressive stress demonstrates a transformation from a pseudocubic to a mixed tetragonal-rhombohedral state. The diffraction patterns collected after mechanically unloading to σ_{rem} is indistinguishable from that of the σ_{max}. Therefore, the induced phase transformation in this composition can be termed irreversible. A similarly irreversible transition from a pseudocubic to tetragonal symmetry was observed in BNT-7BT under an applied electric field [68].

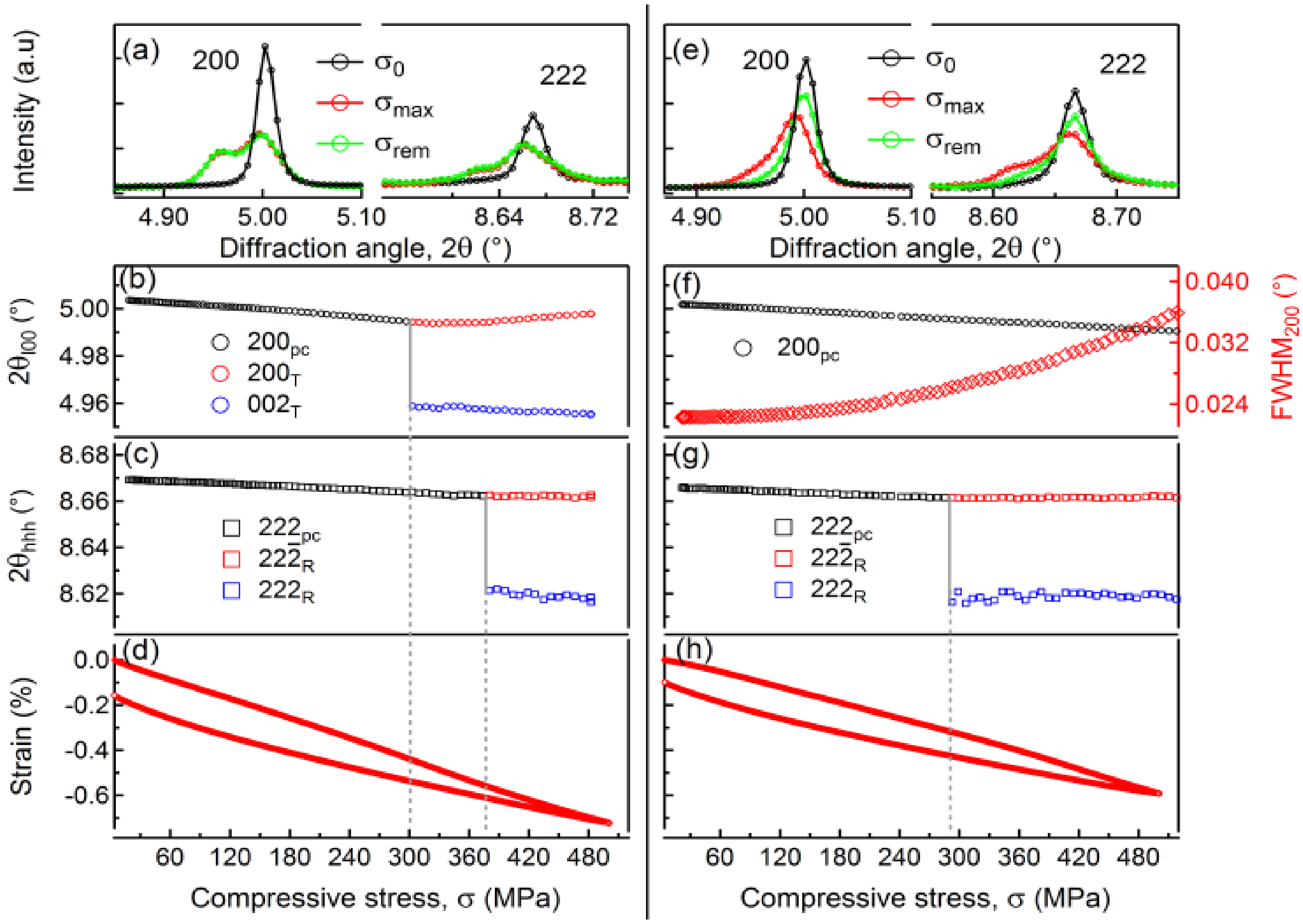

Figure 5.16: Stress-induced structural changes in nonergodic BNT-7BT (a-c) and ergodic BNT-6BT-1KNN (f-h) relaxor. Diffraction data represent the scattering vector angle perpendicular to the stress field vector. Macroscopic stress-strain loop for BNT-7BT and BNT-BT-KNN are shown in (d) and (h) respectively, from [219]

The effect of mechanical stress on BNT-BT-KNN also shows a change in crystal structure. However, these changes were reversible, as evidenced by the fact that the diffraction patterns at $\sigma_{rem} \approx \sigma_0$. The change in ($200_{pc}$) and ($222_{pc}$) peak position and ($200_{pc}$) peak width ($FWHM_{200}$) indicate that the ergodic NBT-6BT-1KNN transformed from pseudocubic to mixed phase with lower symmetries. This is consistent with previous *in situ* diffraction measurements on related compositions under electric field, in which a reversible electric-field-induced phase transformation from pseudocubic to distorted rhombohedral phase were shown [222]. The electric-field-induced and stress-induced structural transformations for both nonergodic and ergodic relaxors are analogous. Similarly, structural investigations in lead-free BNT-6BT under applied mechanical stress have shown that, above a critical stress value, a structural phase transition is induced, and below the critical stress value a change in the lattice parameters can be observed [76], [197].

While the long-range structure is pseudocubic in the initial state, the relaxor-like nature of the as-processed NBT-7BT and NBT-6BT-1KNN signifies that the material contains disorder at the atomic or nanometer length scale, which may be in the form of octahedral tilt disorder as well as cation occupational and displacement disorder. Therefore, the nature of the electric-field and/or stress-induced phase transformation in these materials has been perceived as an establishment of long-range ordering of the short-range lower symmetries and simultaneous development of the corresponding lattice distortion with applied external field. Within a composite structure, internal stresses will affect the crystalline phase and long-range order of the end members. In the presence of a constant residual stress arising from sintering interactions and differences in CTE, both the ergodic relaxor matrix and nonergodic relaxor seed will have altered crystal structures, a change in the corresponding long-range order and, as a consequence, an alteration of their electromechanical response.

The irreversible peak splitting of the (200) peak and broadening of the (222) peak in BNT-7BT can be compared to the diffraction patterns of the 2-2 composites shown in Chapter 4. Under compressive stress, the (200) reflection shifts to lower angles and a broadening as evidenced by an increase in the FWHM can be observed. Similarly, in the 10% composite matrix region, a shift to lower angles was observed, which resulted in an increase in the *c* and *a* lattice parameters. The diffraction patterns and lattice parameters calculated thereof in the 20% composite were not uniform: the left matrix region had a smaller lattice parameter than the freely sintered sample, whereas the right matrix region had a higher lattice parameter than the freely sintered sample. One divergence is apparent between the freely sintered BNT-BT-KNN and the matrix regions of the composite: a pronounced peak splitting was observed in both the (111) and (200) reflections in the composites, whereas only (222) peak splitting was observed in compressed BNT-BT-KNN. Comparing the diffraction patterns of BNT-7BT under compression and the seed regions of the 10 and 20% composite, more divergences become apparent. In the freely sintered BNT-BT, peak splitting of both the (200) and (222) reflections takes place under sufficient stress, but no splitting of the (111) reflection can be observed in the 20% composite. On the other hand, in the 10% composite there is a pronounced peak splitting of the (111) reflection similar to the compressed BNT-7BT. The (200) peak of compressed BNT-BT-KNN shifts to lower angles under compressive stress, without splitting. This was not observed in the composite system, where instead an increased (200) peak splitting was observed in the matrix regions, as was shown in Figure 4.10. A summary of the comparison is given in Table 6.

Table 6: Comparison of the diffraction patterns of freely sintered BNT-7BT and BNT-BT-KNN under compression and that component in the 2-2 composite

	Compressive Stress	*10% 2-2 composite*	*20% 2-2 composite*
Seed (BNT-7BT)	*Shift of (200) peak to lower angles* *Increase of (200) FWHM* *(222) peak splitting at -300 MPa*	*Reduced lattice constant* *Splitting of (111) and (200) peaks*	*Inhomogeneous lattice constant* *Splitting of (111) reflection*
Matrix ***(BNT-BT-KNN)***	*(200) peak splitting at -300 MPa* *(222) peak splitting at -360 MPa* *Shift of (222) peak to lower angles*	*Reduced lattice constant* *Increase of (200) FWHM*	*Single (111) reflection* *Splitting/ increase of FWHM of (200) reflection*

5.4.2. Influence of Stress on Mechanical Properties in Bulk End Members

As shown in Figure 5.12, in the 2-2 composite of BNKT-BA/BNT-7BT, the BNT-7BT layer experiences residual compressive stresses. In order to determine the effect of compressive stress on BNT-7BT, the elastic modulus as a function of stress was investigated with partial unloading experiments. During testing the compressive stress was reduced by 10% from the current stress level to measure the instantaneous elastic modulus. In Figure 5.17, a partial unloading experiment is shown and compared to measurement during linear loading/unloading; partial unloading did not adversely affect macroscopic ferroelastic behavior. The bottom of Figure 5.17 depicts the measured elastic moduli at room temperature as a function of stress. During compressive stress loading, there was an increase in the apparent macroscopic elastic modulus, similar to observations for PZT [46]. In contrast to PZT, however, BNT-7BT is expected to undergo a relaxor-ferroelectric transition during mechanical loading [76], whereby stress induces a long-range ferroelectric order with a preferential domain orientation perpendicular to the applied uniaxial compressive stress. Upon unloading, the elastic modulus decreases but retains a higher value in the remanent state than in the initially virgin state. The nonergodic nature of BNT-7BT results in a higher volume fraction of domains aligned perpendicular to the applied stress direction.

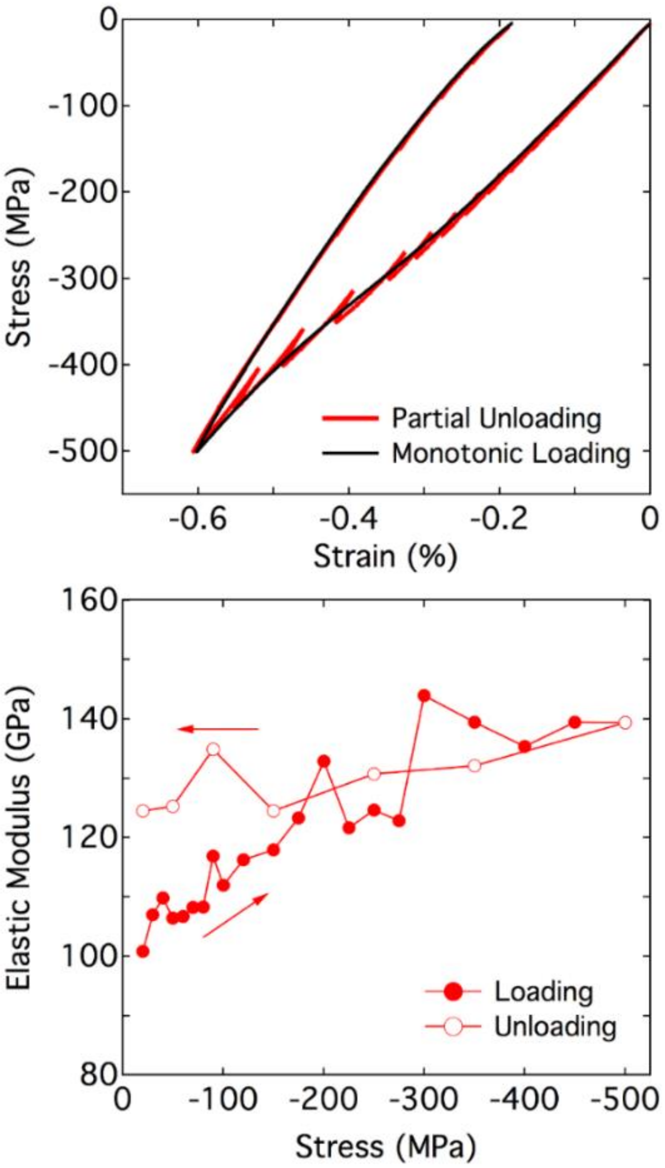

Figure 5.17: Stress-strain curve of BNT-7BT with partial loading in order to determine elastic modulus as a function of stress, shown in bottom panel, from [223]

5.4.3. Local Mechanical Properties of 2-2 Composites Investigated by Nanoindentation

Using nanoindentation, the local mechanical properties were characterized through the thickness of the ceramic/ceramic composite, enabling a comparison to the elastic modulus of compressed BNT-7BT shown in Figure 5.17. The determined values for elastic modulus and hardness are shown with the chemical composition and grain size at the same position in Figure 5.18 to facilitate analysis. Resonant frequency damping analysis (RFDA) determined values of BNT-7BT have been reported at approximately 110 GPa [202], whereas in this work, nanoindentation-based determination of the elastic modulus is 180 GPa for BNT-7BT and 160 MPa for BNKT-6BA. The lower RFDA derived values may be due to this measurement technique incorporating pores, thereby lowering the overall elastic modulus value, whereas the value given by nanoindentation is closer to the “ideal” phase pure, 100% dense material [224].

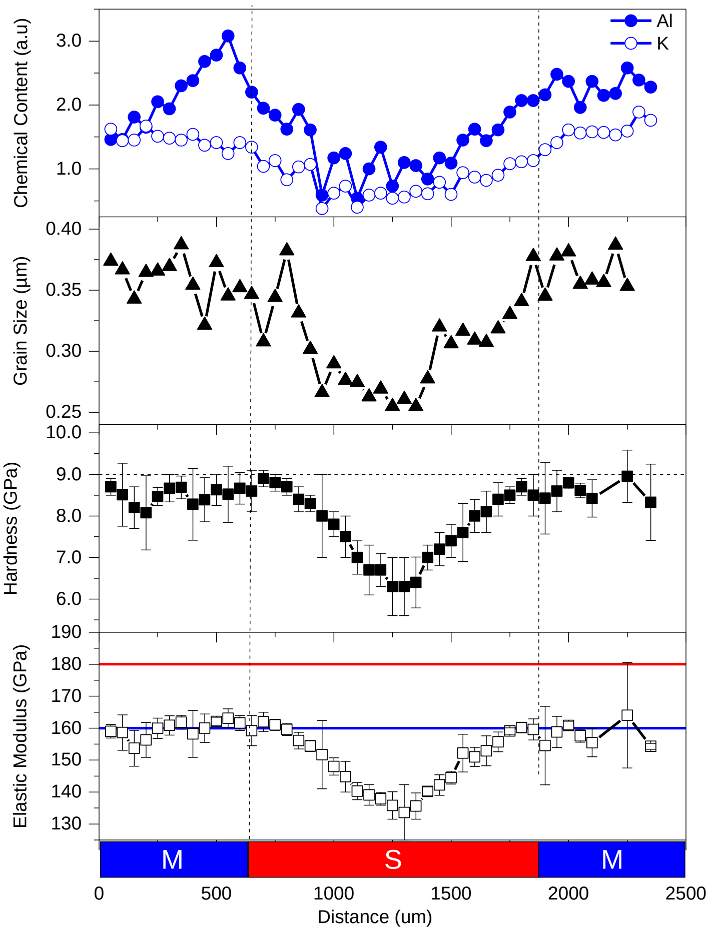

Figure 5.18: Elastic modulus and hardness as a function of position in a 2-2 composite of BNKT-6BA/50% BNT-7BT, with the red line and blue indicating the elastic modulus of BNT-7BT and BNKT-BA respectively in a freely sintered disc. [223]

In the matrix BNKT-BA region, both the elastic modulus and hardness determined by nanoindentation corresponds well to the bulk values. In contrast, the elastic modulus and hardness of BNT-7BT within the layered structure fall well below that of the bulk material. As shown in Figure 5.18, the hardness and elastic modulus is lower in the seed region (center) than the top and bottom matrix layers. The values of the elastic modulus in the seed region range from 160 GPa at the seed/matrix interface to 130 GPa at the center of the seed region. These values correspond closely to those determined in BNT-BT under compression. However, as shown in Figure 5.17, under increased compressive stress, the elastic modulus was shown to increase from the initial partial unloading step, but in the composite, the elastic modulus value of BNT-7BT is lower than the pure end member.

Residual stress influences the behavior of the applied indentation force. In a laminate, the residual stress is biaxial away from the surface. At the cross-section surface, due to the lack of tractions perpendicular to the surface, the stress state should be uniaxial, in-plane, and perpendicular to the indentation direction. Because hardness is measured in terms of the measurement depth as a function of stress, a material with tensile stress will be less resistant to the indentation force, resulting in a greater measurement depth and lower hardness value. On the other hand, compressive stress will result in greater resistance to the indentation force, corresponding to a lower measurement depth and a higher hardness value [225]. In addition, applied stress has been shown to change the macroscopic elastic modulus of ferroelastic materials due to the anisotropic elastic properties [46], [226], [227]. For example, ferroelastic switching during compressive stress loading results in an increase in the volume fraction of domains oriented perpendicular to the applied stress, which increases the apparent elastic modulus. As was determined in Figure 5.12, the residual stresses in the BNT-7BT layer due to differences in CTE range from -300 to -400 MPa, depending on seed content. Previous ferroelastic measurements on BNT-7BT have revealed a coercive stress of approximately –315 MPa, which corresponds well to values of other BNT-BT compositions [219]. Through the inclusion of destabilizing compounds, such as $BiAlO_3$ [110], or $(K_{0.5}Na_{0.5})NbO_3$ [173], which increase the ergodic nature of BNT-based materials, there is a subsequent increase in the coercive stress. There are currently no available studies on the ferroelastic response of BNKT-BA, but published data on another ergodic relaxor, BNT-6BT-*x*KNN, shows an increase in the coercive stress from –369 MPa for 0KNN to –421 MPa and >–500 MPa for 1KNN and 2KNN, respectively [219]. From this it can be assumed that the coercive stress of BNKT-6BA is higher than BNT-7BT, meaning that the BNKT-6BA layer will undergo the stress-induced relaxor-ferroelectric transition at a higher stress [76]. In the virgin state, both materials will remain pseudocubic when determining the average crystallographic symmetry and their elastic responses will be isotropic. Under the application of a stress above the critical value, a stress-induced relaxor-ferroelectric transition will result in the formation of ferroelectric long-range order, analogous to the electrical case [177]. Due to the formation of a domain structure, it is expected that the anisotropic elastic properties of the non-cubic phase will affect the observed elastic modulus and hardness. This indicates that the stress in the BNT-7BT layer is in the vicinity of the coercive stress (–315 MPa), which has resulted in the formation of a long-range ferroelectric order and the reduction of the elastic modulus and hardness. In contrast, the matrix layer, which experiences lower stresses (below 200 MPa), will remain in the relaxor state, without a domain structure that influences indentation depth. The elastic modulus is determined perpendicular to the internal residual stress during nanoindentation, and it is, therefore, expected that the elastic modulus will decrease because of an increase in the volume fraction of domains parallel to the measurement direction. Similar results were observed by Fett *et al.*, who showed that orientation of domains plays an important role in the measured elastic modulus [226]. In that work, unpoled PZT samples with a random domain orientation had a higher elastic modulus than electrically poled samples.

A gradient in the values for elastic modulus and hardness can be observed across 500 µm. The spread of the hardness is highest at 900 µm, 1550 µm, and in the center at 1300 µm. It has been observed that the stress state in laminates is inhomogeneous, resulting in an inhomogeneous measurement of hardness across laminate layers of the same composition. However, inhomogeneity in the present investigation may also be attributed to interdiffusion, which results in compositional inhomogeneity as well as an inhomogeneous stress distribution through the thickness of the layer. EDS analysis was performed next to the first indent at each row parallel to the interface, thereby ensuring that the composition and mechanical properties are from the same position relative to the interface. From Figure 5.18, it is clear that the drop in the hardness does not occur at the same position as the drop in K and Al content. The slope of the gradient in hardness is also higher than the slope in gradient of elemental content.

Micromechanical properties appear to correlate more strongly with grain size than with chemical composition. A reduction in the hardness correlates in position to a reduction in grain size. This corresponds to previous work on hardness as a function of grain size in ceramic materials, dating back to 1978, when Sargent and Page showed that, contrary to the effect observed in metals, the microhardness increased with increasing grain size in polycrystalline MgO ceramics, and explained it to be due to the similar size of the grain and indentation [228]. The grain size is strongly affected by the presence of sintering stresses due to differences in shrinkage rate between BNKT-6BA and BNT-7BT, as shown in Figure 5.8. BNT-7BT was found to have lower shrinkage at the sintering temperature than the matrix, resulting in biaxial tensile stresses on the seed region. Despite the fact that in many other materials, a lower grain size is associated with a higher hardness [11], [229], it appears that in this system, the influence of internal stress plays a stronger role in the change in mechanical properties.

5.5. Internal Stresses in 2-2 Composites due to Piezoelectric Interactions

Internal stresses in the 2-2 composite structure can also occur during the application of an electric field, due to the difference in transverse piezoelectric coefficients between the two end members. To determine the lateral and transverse piezoelectric coefficients in the pure end members, the digital image correlation (DIC) method was employed during application of an electric field. These measurements were performed in collaboration with Dr. Di Chen and Professor Mark Kamlah at the Karlsruhe Institute of Technology. A detailed description of this method can be found in the Experimental Methodology section.

The validation of this method for determination of strain was performed through a simultaneous measurement of mechanical displacement by linear variable displacement transducers. A comparison between the LVDT determined strain and the DIC determined strain is shown in Figure 5.19.

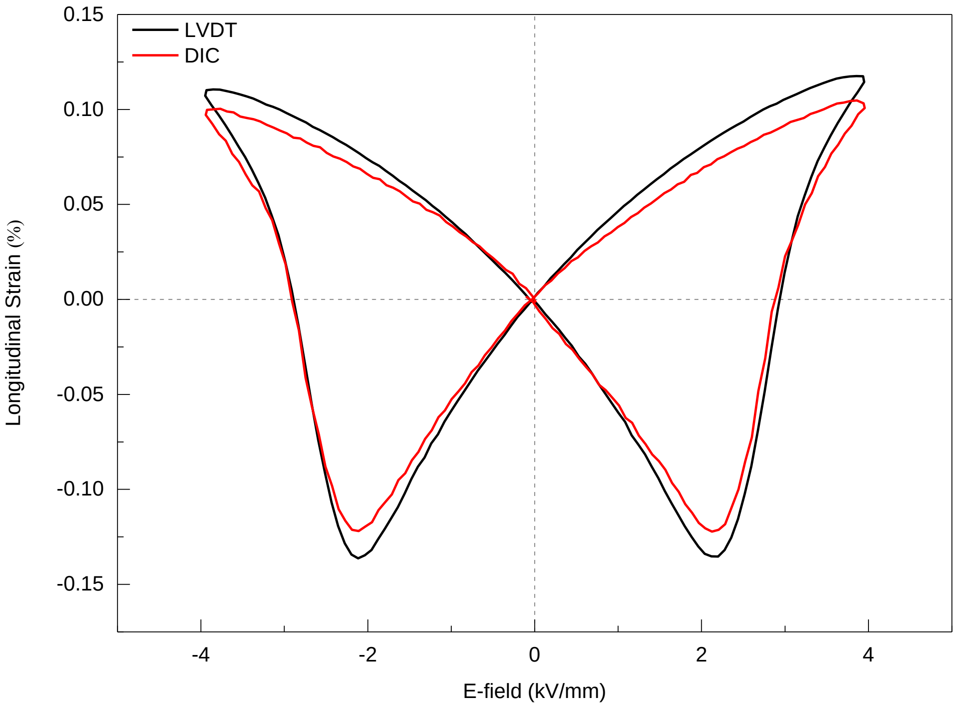

Figure 5.19: Comparison between electric-field-induced strain determined by LVDT (red) and DIC (black) in BNT-7BT

The strain determined through the DIC method is shown in Figure 5.20 for both the longitudinal and transverse directions. This enables a calculation of the volume change, shown in black. The volume of the pure end members as a function of electric field is the sum of the longitudinal strain and two times the transverse strain, with the assumption of transverse isotropy [77]. The sample volume contracts with applied field in both BNT-BT-KNN and BNT-BT. The initial volume change in BNT-7BT far exceeds that of BNT-BT-3KNN at 2 kV/mm, the coercive field of BNT-7BT. The volume change as a function of electric field observed in this work corresponds to previous measurements by Jo *et al.* [77].

Stress as a function of electric field in the matrix and seed layers was determined using a modified Chartier model:

$$\sigma_S(E) = \frac{Y_S Y_M(\varepsilon_S(E) - \varepsilon_M(E))}{(1-v)} \frac{\frac{h_s}{h_M}}{2Y_S\frac{h_s}{h_M} + Y_M} \tag{5.3}$$

$$\sigma_M(E) = -2\frac{h_s}{h_M}\sigma_S \tag{5.4}$$

where ε_S and ε_M values are the transverse strain values measured at the instantaneous value of the applied field E, and all other variables correspond to those found in Equations 5.1 and 5.2, enabling an approximation of the stress state throughout a bipolar loading cycle

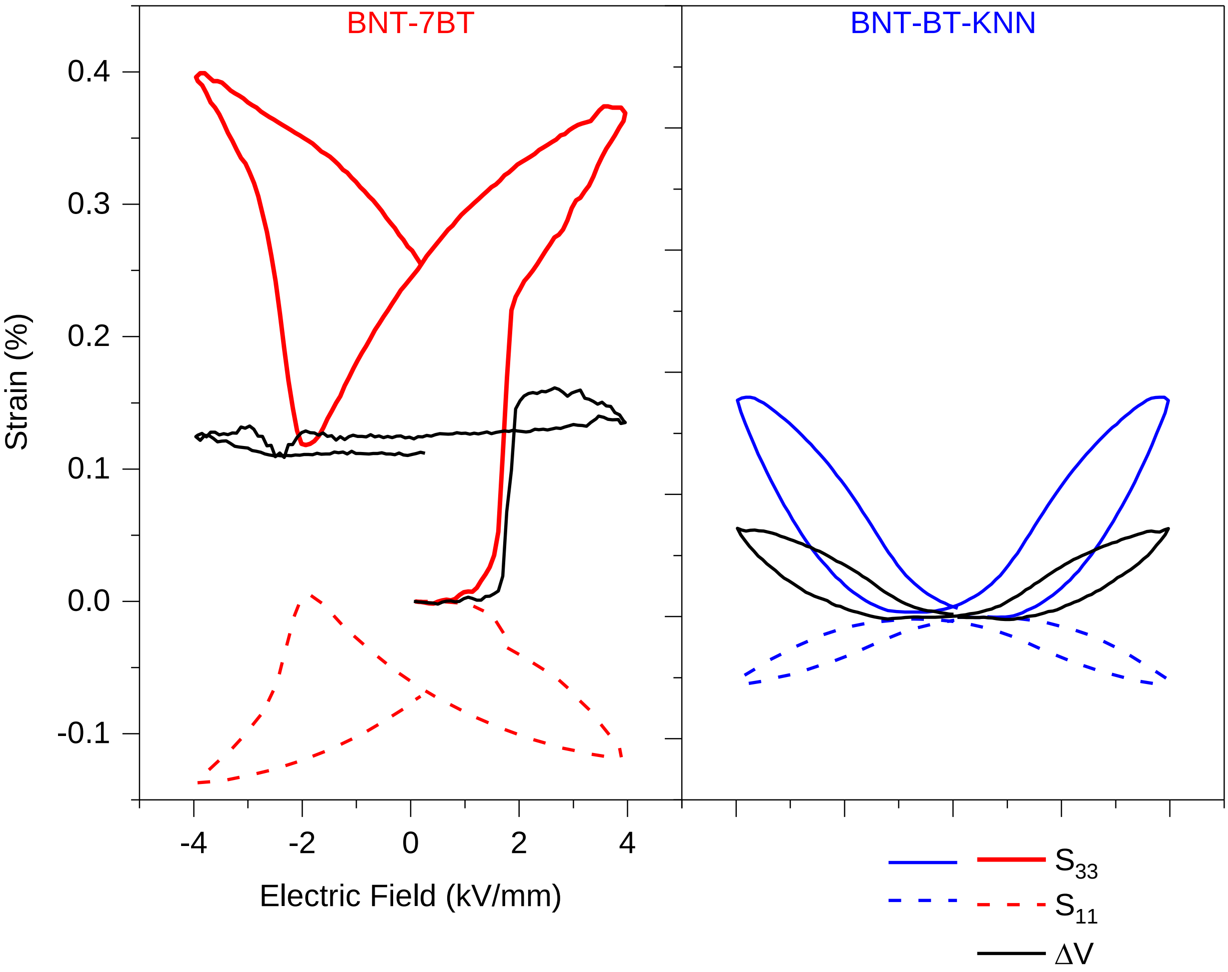

Figure 5.20: Longitudinal and transverse strain, shown in solid and dashed lines respectively in pure end members BNT-BT and BNT-BT-KNN, and volume change shown in black, all in % strain

The electromechanical properties of BNT-7BT and BNT- BT-KNN as determined by the DIC method are shown in Table 7. The difference in remanent strain values of the two end members will also result in residual stresses after application of an electric field. Using Equations 5.3 and 5.4, the stress states in the matrix and seed can be determined. The residual stresses, at 41 MPa for the seed layer and -10 MPa for the matrix layer, are well below the coercive stresses sufficient to induce domain formation. However, the stresses generated due to differences in d_{31}^* during electric field cycling are likely to exceed these values.

Table 7: Electromechanical Properties Determined by DIC Method, determined at a field of 4 kV/mm, with a frequency of 10 mHz

	Ec (kV/mm)	d_{33}^{*}(pm/V)	d_{31}^{*} (pm/V)	Sremanent (%)	$\sigma_{residual}$ (MPa)
BNT-BT-KNN	0.5	44.25	13.1	0.07	41
BNT-BT	1.8	92	293	0.22	-10

The determined stress as a function of electric field in each component of the composite is shown in Figure 5.21. The stress under positive electric field as a function of seed content, at 1, 2, 3, and 4 kV/mm, is shown in Figure 5.21 (a). A sharp jump in the stress state occurs from 1 to 2 kV/mm. Under initial loading by a positive field, the matrix layer undergoes compression, while the seed layer experiences tension. These stresses can also not be ignored during poling, as application of an electric field on 2-2 composites will result in internal stresses in the poled body. Because of the large scale of tensile stress at values of 2 kV/mm and higher, care must be taken to avoid delamination during poling and cycling by large fields. In this work, delamination occurred consistently in samples loaded with bipolar cycles, likely as a result of the stresses generated from the difference in d_{31}^{*} at high fields.

In Figure 5.21 (b), stress over a single bipolar cycle is shown. Over most of the loading cycle, the seed layer is in tension and the matrix layer is in compression. However, during unloading of the negative field, from -2.25 kV/mm to -1.6 kV/mm, the matrix is in compression and the seed is in tension. The final stress state after one bipolar cycle is determined to be 90 MPa in the seed layer and -40 MPa in the matrix layer. These stresses are likely to influence the polarization and strain response to an applied electric field. Because the in-plane stresses will result in domains aligned parallel to the applied electric field, it is expected that the compressive stress in the matrix layer will enhance its strain and polarization response to an applied electric field.

The addition of stress during applied electric field will also contribute to and affect the electromechanical behavior of the two components differently. As was shown in Figure 5.21, during application of an electric field, both components of the composite will exhibit a stress in addition to the residual stress from processing.

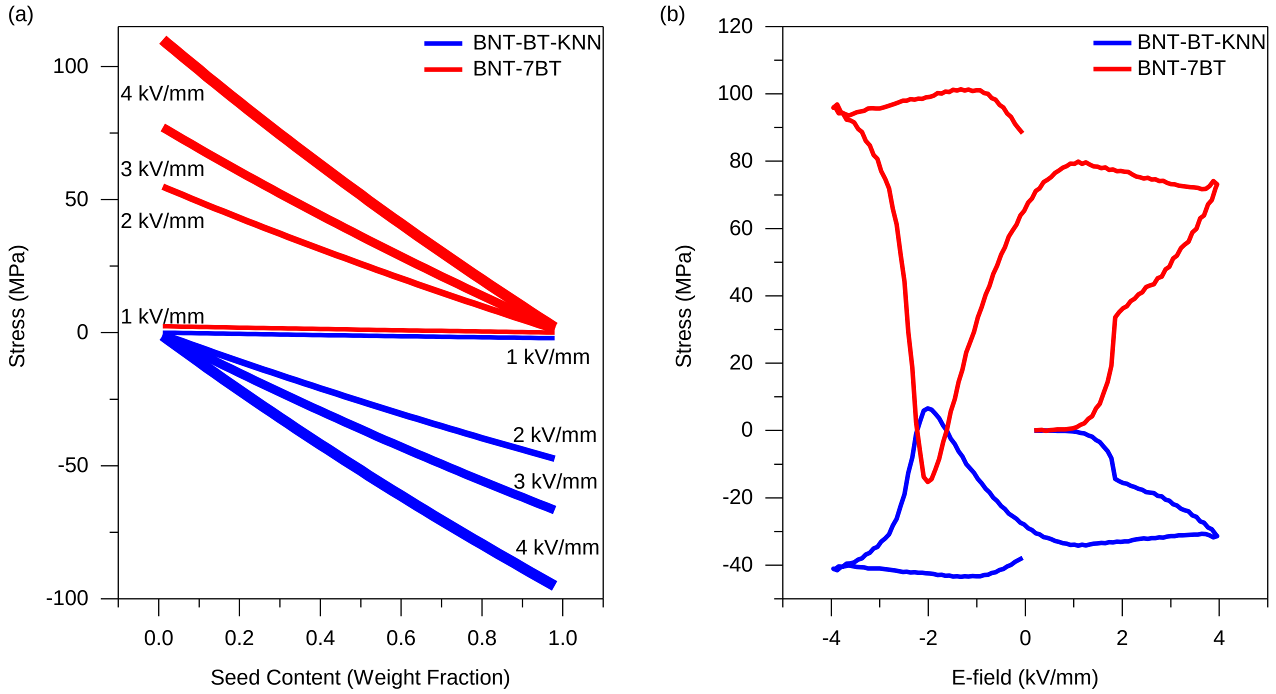

Figure 5.21: Stress due to difference in transvese strain in the BNT-7BT and BNT-BT-KNN layers of the 2-2 composite (a) as a function of seed content, under fields of 1, 2 and 4 kV/mm, (b) stress as a function of applied electric field in a 2-2 composite of 30% seed

5.5.1. Influence of Mechanical Stress on Dielectric and Ferroelectric Response of Pure Constituents

Because of the large stresses determined to be present in the 2-2 composite structure, both as a consequence of difference of CTE and transverse strain response to an applied electric field, it is important to investigate the effect of stress on dielectric and ferroelectric behavior of the pure constituents. The dielectric behavior of ferroelectrics and relaxors has been shown to be strongly influenced by the application of an external mechanical field, dating to investigations on $BaTiO_3$ [230]. For instance, the dielectric response has been shown to be affected by applied mechanical stress, *e.g.*, the application of hydrostatic stress on Rochelle salt has been shown to reduce its transition temperature [231]. A similar influence of hydrostatic stress on the phase transition temperature was observed in $BaTiO_3$ [232], $Ba_{0.75}Sr_{0.25}TiO_3$ [233] and $PbTiO_3$ [234]. It is important to note, however, that the influence of hydrostatic stresses may differ from that of in-plane biaxial stresses as found in the 2-2 composites of this work.

In Figure 5.22 the influence of stress on permittivity is shown at room temperature in BNT-7BT and BNT-6BT-3KNN. An inflection point in the permittivity can be observed in BNT-7BT at -30 MPa. Compressive stress clearly decreases the permittivity values for both systems, but the permittivity of BNT-7BT has a large hysteresis, whereas the BNT-BT-KNN system does not. The effect of mechanical stress on the dielectric response was investigated in detail in the BNT-BT system by Schader *et al.*, who showed that as a consequence of a mechanically induced relaxor-to-ferroelectric transition, the permittivity decreased [76]. The origin of this decrease was attributed to the increased resistance to motion of PNRs due to the uniaxial compression and the increasing correlation between the PNRs, which results in a decreased response to a small electric field. A similar nonlinearity to the one at -30 MPa in this work was observed, however, at a slightly higher compressive stress of -51 MPa in BNT-6BT.

The influence of mechanical stress on dielectric properties strongly depends on microstructure. For instance, a significant difference in the dependence of permittivity on stress was observed in BT upon changing its grain size. Fine-grained BT showed an increase in the permittivity with increasing stress, whereas coarse-grained BT showed a decrease under identical conditions [235]. This difference was explained by the fact that fine-grained ceramics more closely resemble a single domain structure, whereas the coarse-grained material contains multiple domains walls. In light of such findings, the complexity of the influence of sintering stresses must be considered. In this work, we show that the composite structure has a significant effect on the grain size of its constituents. The influence of residual stress on the composite dielectric is likely coupled to the influence of internal sintering stresses during processing.

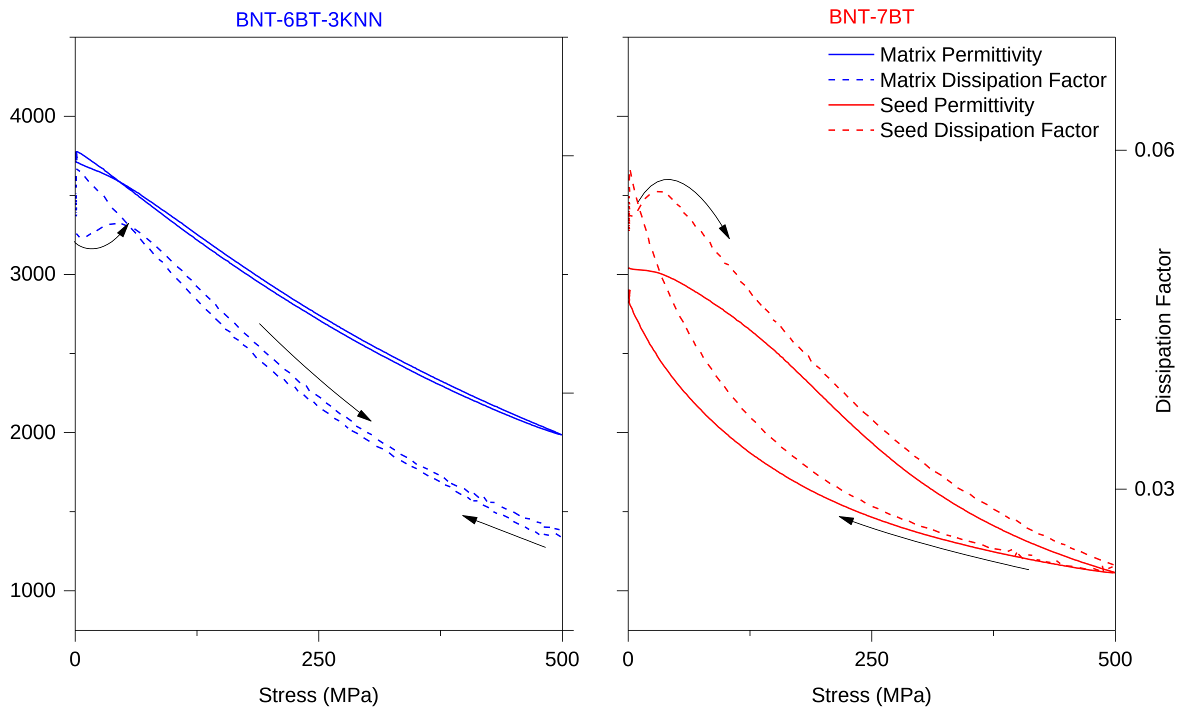

Figure 5.22: Dielectric permittivity and loss as a function of compressive stress at 25 °C in BNT-7BT and BNT-6BT-3KNN, solid line showing permittivity and dashed line showing dissipation factor

Ferroelectric behavior is well-known to be affected by mechanical stress. In light of the evidence of internal stress both before and during electric field loading, the polarization response of the freely sintered end members was evaluated under compression. It can be observed that the remanent polarization decreases with increasing pressure in BNT-7BT and BNKT-6BA. For all three tested materials, increasing stress results in a reduced maximum polarization as well. The effects of stress on the remanent polarization, maximum polarization, and coercive field are shown in Figure 5.24. The coercive field is not strongly affected by mechanical stress, but the remanent polarization and maximum polarization both decrease with increasing compressive stress. The decrease in maximum polarization has an inflection point at -30 MPa in BNT-7BT, which parallels the inflection point of permittivity under stress in Figure 5.22. A similar inflection point was observed by Dittmer *et al.* in BNT-6BT, but at a temperature of 100 °C. However at lower temperatures, the inflection point occurred at stresses ranging from -90 to -120 MPa [198]. Because BNT-7BT is on the tetragonal side of the MPB in the BNT-BT binary solid-state solution, as compared to BNT-6BT, it appears that the addition of BT to this system results in an increased response to mechanical stress. The additional amount of BT has been shown to reduce its elastic modulus [236]. Therefore, the fact that at room temperature, lower stresses are required to depole BNT-7BT as compared to BNT-6BT may be related to increased domain mobility.

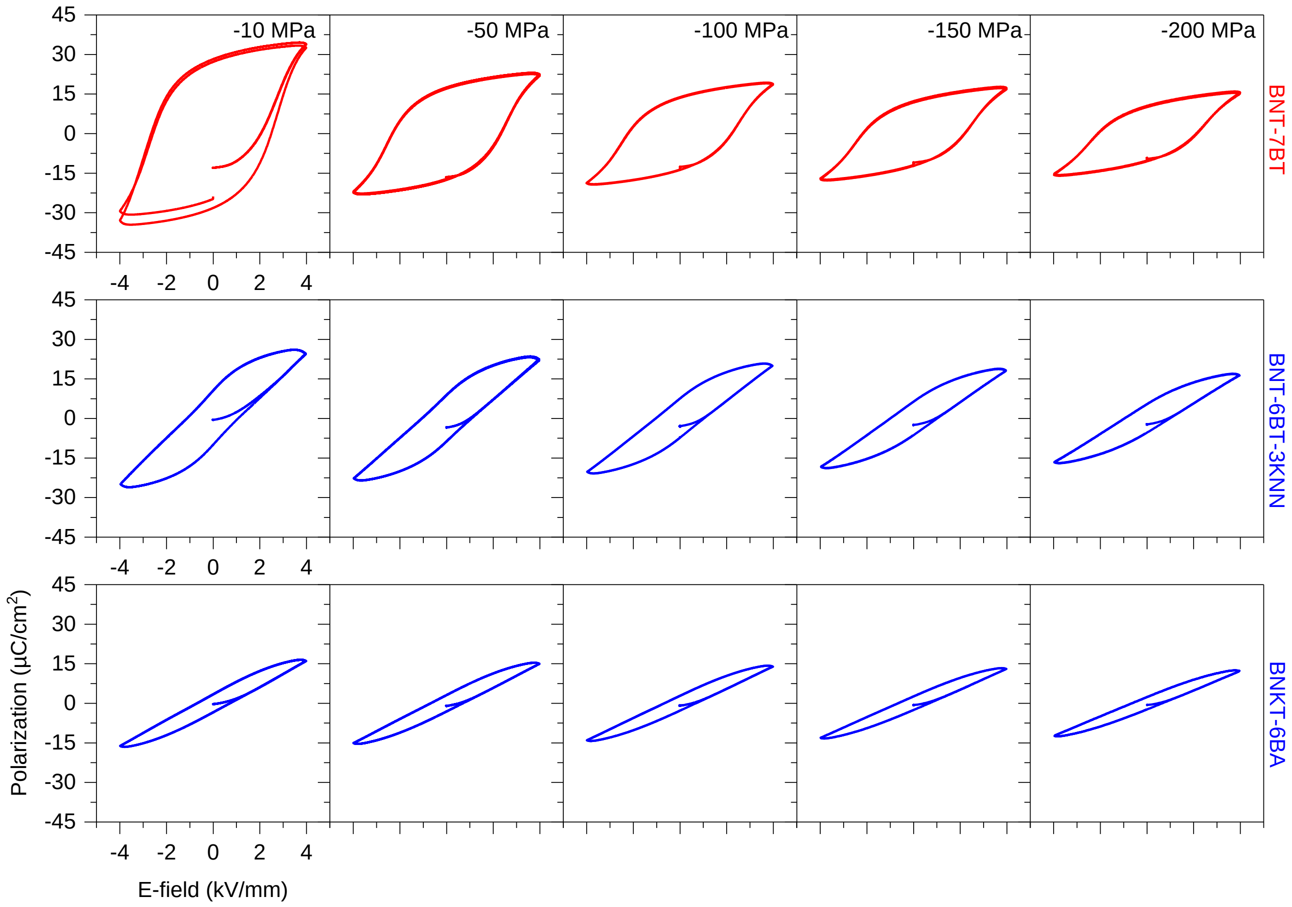

Figure 5.23: Polarization as a function of applied electric field, at room temperature, under constant uniaxial compressive stresses of -10 to -200 MPa in BNT-7BT, BNT-6BT-3KNN and BNKT-6BA

Such an inflection point appears in BNT-BT-KNN as well, but at a much higher stress of -300 MPa. Further investigations over the range of -250 to -350 MPa are required to precisely determine the stress value at which the inflection point occurs. It is also interesting to note that the remanent polarization increases slightly at -300 MPa in BNT-BT-KNN, from 3.5 μC/cm^2 at -30 MPa to 4.1 μC/cm^2 at -300 MPa. It is further notable that the two ER matrix materials, BNKT-6BA and BNT-BT-KNN, appear to be largely stress insensitive, which may be beneficial for integration into devices in which clamping of components occurs.

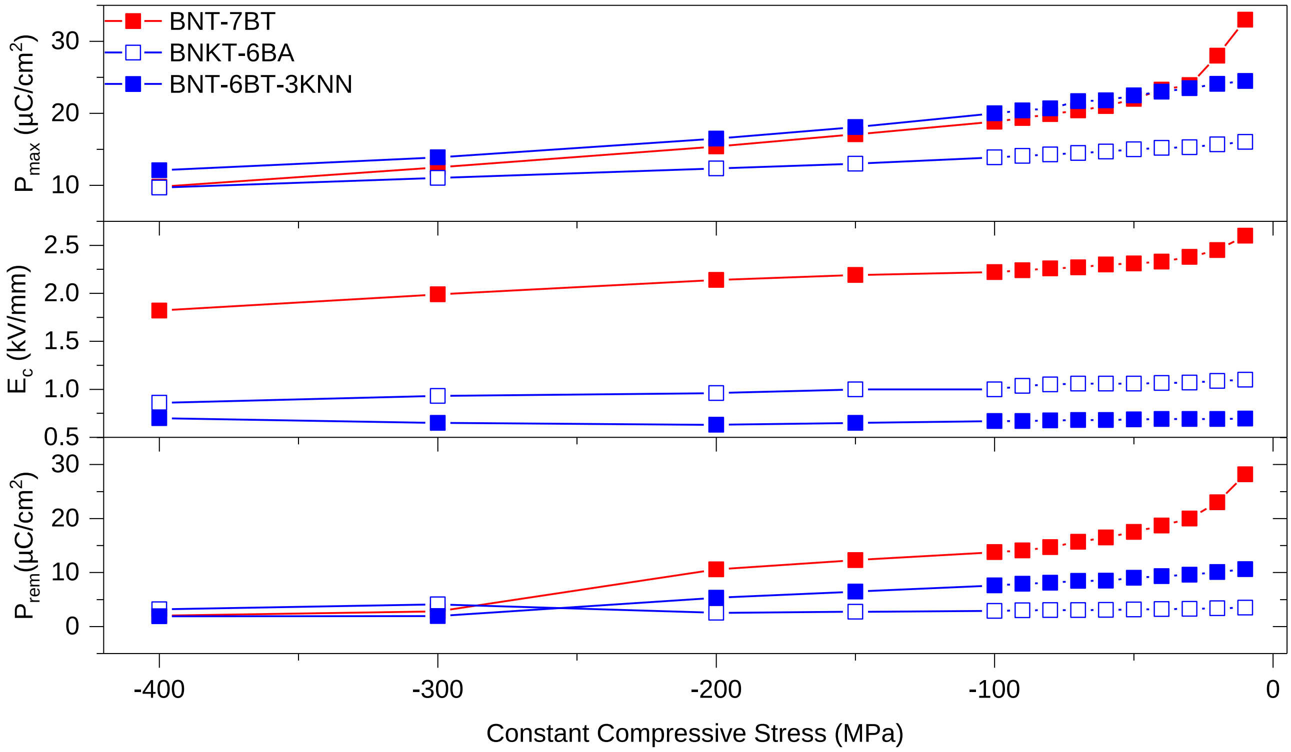

Figure 5.24: P_{max}, P_{rem}, and E_c as a function of compressive stress in BNT-7BT, BNKT-6BA and BNT-6BT-3KNN.

As shown in Figure 1.16, mechanical stress in a ferroelectric results in domain orientation perpendicular to the stress. A compressive in-plane biaxial stress, therefore, will result in domains perpendicular to the seed-matrix interface. The electrodes for the 2-2 composite samples in this work are applied parallel to the interface, meaning that an applied electric field will be parallel to the orientation of domains aligned by internal stress. Therefore, a compressive stress should result in a lower coercive field, as the internal stress will facilitate domain orientation. This has previously been observed in PZT, where the application of a radial stress was shown to reduce the poling field by 40% [237]. However, the remanent polarization is reduced with the application of uniaxial compressive stress. Because the initial state of the ceramic is mechanically textured, (*i.e.*, some domains have been formed that are parallel in direction to the applied electric field), the difference between the initial state and the remanent state is lower than that of unstressed samples. Therefore, the remanent polarization is lower. Previous work in BZT-BCT has observed a similar reduction in remanent polarization with compressive stress and was explained by a decreasing domain wall density. An electric field induces domain formation parallel to the applied field, and a compressive mechanical stress induces domain formation and alignment perpendicular to the mechanical stress. When these two fields are applied simultaneously in the same direction, there is a competitive interaction between them. This means that a reduced polarization state is likely relative to an unstressed sample under electric field. Therefore, the final maximum polarization state of a sample under both compressive mechanical stress and an applied electric field is reduced relative to the maximum polarization of an unstressed sample. Similar reductions in remanent and maximum polarization was observed in soft PZT [220], in which it was shown that stresses above the coercive field effectively depolarize the material and prevent non-180° domain switching. A polarization response was still observed due to 180° domain switching, which was not restricted by mechanical stress.

Based on the above results, a compressive stress on either the seed or the matrix phase of the composite will result in a reduced remanent polarization. In Figure 5.21, of Section 5.5, it was determined that during the application of an electric field, the matrix undergoes in-plane compression as the field increases. However, in 2-2 composites, the internal stresses are perpendicular to the applied electric field and measured strain and polarization, whereas for the direct measurement of the effect of stress on the dielectric and ferroelectric behavior, it is only possible to apply a stress parallel to the direction of the applied electric field. Previous work has shown that biaxial compressive stresses increase the remanent polarization in the field direction, when the applied electric field is perpendicular to the stress [237].

5.6. Summary

The sintering shrinkage and coefficients of thermal expansion for BNT-BT-KNN, BNKT-BA and BNT-BT were measured as a function of temperature, enabling a determination of residual stress in the 2-2 composites. An optimized sintering temperature was proposed based on these results, with the goal of reducing residual stresses. Residual stresses due to differences in CTE were determined and compared to evidence of residual stresses from anisotropic crack propagation under Vickers indentation. The anisotropy was attributed to the formation of domains as a mechanism of stress-relaxation, which resulted in anisotropic ferroelastic toughening responses in the composite. Local strain evaluation during application of an electric field through DIC enabled the determination of both d_{33}^* and d_{31}^* in BNT-BT and BNT-BT-KNN as a function of electric field, which showed that the absolute value of the stress during application of an electric field is in the MPa range.

As this chapter shows, the mechanisms of interaction between seed and matrix in lead-free ferroelectric composites is quite complex. Although residual stresses due to differences in shrinkage and thermal expansion are equivalent in terms of direction, upon application of an electric field, the internal stresses reverse direction. Throughout the production and use of the composite, new stresses arise that influence its final ferroelectric and piezoelectric behavior. These stresses can be tailored to optimize the mechanical and electromechanical properties of composites by tailoring the composition, sintering temperature and other available parameters to the desired internal stress state. In the final chapter of this work, the dielectric and electromechanical response of the composite systems will be presented and evaluated in light of the mechanical and structural interactions presented in Chapters 4 and 5.

6. Dielectric, Ferroelectric and Ferroelastic Behavior of Lead-Free Composite Systems

6.1. Introduction

Ceramic/ceramic composite systems have shown an improvement in the piezoelectric and ferroelectric response to applied electric fields, yielding promising electromechanical behavior for actuator applications. As discussed in the introduction, previous work has investigated polarization and strain coupling as mechanisms of interaction that result in nonlinear increases of electromechanical properties with increasing seed content [2], [132], [147], [150]. However, the interaction between seed and matrix during sintering was neglected in those studies.

To better understand the effect of the composite structure, the electromechanical and ferroelectric response of several composite systems were evaluated under applied electrical and mechanical fields. As discussed in Chapter 4, determination of diffusion between the seed and matrix phases proved challenging due to the close chemical composition between the two end members of the BNT-BT-3KNN/BNT-BT system. Therefore, a model systems comprising ergodic relaxor BNKT-6BA as the matrix, and BNT-7BT as the seed, was also prepared. In this chapter, the dielectric, ferroelectric, and electromechanical properties of 2-2 BNT-BT-3KNN/BNT-BT composites as well as 0-3 and 2-2 BNKT-6BA/BNT-7BT composites are described. In Section 6.2 the small signal dielectric response of these material systems is discussed, while in Section 6.3 the large signal ferroelectric and piezoelectric response is presented. Finally, the role of mechanical stress in 0-3 BNT-BT-3KNN/BNT-BT composites are compared to the response to large signal applied electric fields. These results are discussed in light of the evidence of changes in crystal structure and composition shown in Chapter 4, and the presence of residual stresses described in Chapter 5.

6.2. Temperature and Frequency Dependent Small Signal Dielectric Behavior of Lead-Free Ceramic/Ceramic Composites

To investigate the dielectric behavior, the temperature-dependent permittivity of lead-free BNT-based relaxors was examined. As was discussed in the introduction, the dielectric permittivity in relaxors is strongly frequency dependent. For relaxors that undergo a field-induced transition to a ferroelectric state, the permittivity is further affected by the application of an external electric field, resulting in a poled ceramic. Upon heating, a poled relaxor undergoes a temperature-dependent state change from poled ferroelectric to unpoled relaxor. A sharp change in permittivity can be observed at T_d and is indicative of a temperature-dependent state change [72], [238]. BNT has a T_d of 187 °C [160], and the addition of BT lowers the T_d to 106 °C [165]. Previous work with 0-3 BNT-BT-KNN/BNT-BT composites showed no observable phase transition temperature compared to the sharp transition at a T_d of 130 °C observed in BNT-7BT [169]. The dielectric behavior of poled composites enables an understanding of the influence of the seed on the ergodic nature of the composite, by determining whether there is an observable T_d. The frequency dependent permittivity reveals the mechanisms governing the interaction between seed and matrix phases, as it probes the dipole-dipole interactions. Sharp changes in permittivity are also generally associated with temperature-dependent phase transitions in the crystal structure, as in the case of BT. However, a sharp transition at T_d has also been observed in BNT-BT ceramics without an accompanying change in crystal structure, but rather a reduction in polar order [239]. The temperature at which depoling occurs is strongly composition dependent as well [240]. The T_B of BNT-6BT and BNT-BT-3KNN was previously determined by Zhang *et al.* to be 676 °C and 655 °C respectively [241], well above the temperatures reported here due to the instability of silver electrodes above 600 °C. Therefore, the discussion will be limited to T_m and T_d when possible.

6.2.1. Dielectric Behavior of BNT-based Relaxors as a Function of Temperature and Frequency

Figure 6.1 shows the temperature-dependent dielectric permittivity of the ER matrices BNT-6BT-3KNN and BNKT-6BA and the NR seed BNT-7BT. A comparison between the poled and unpoled state can be made, as well as an observation of the influence of temperature. Analysis of the small signal behavior is based on the following parameters: T_m, the difference between the poled and unpoled states below T_m, the permittivity at temperatures above T_m, the temperature of onset of frequency dispersion, and, for composites, the difference between the permittivity values at room temperature and the predicted values from the rule of mixtures approximation.

In ergodic relaxors, a poling treatment has no observable effect on permittivity, which is to be expected. Of the two ergodic relaxors discussed in this chapter, BNT-BT-3KNN shows the smallest difference in permittivity between the poled and unpoled state. The room temperature permittivity of BNT-BT-3KNN is slightly lower than that of BNKT-6BA. BNKT-6BA has a visible difference in the permittivity of the poled and unpoled state, particularly above 200 °C, where the poled state exceeds the unpoled state by approximately 100 units. The temperature at which the maximum permittivity can be observed also varies between the two ergodic relaxors, with BNKT-6BA having the highest temperature at maximum permittivity of 300 °C, while in BNT-6BT-3KNN this occurs at 250 °C.

The dielectric permittivity of BNT-7BT, the polar seed material, is shown at the bottom of Figure 6.4. It can be seen that below the $T_{F\text{-}R}$ of 110 °C the unpoled state has a much higher permittivity than the poled state. There is no frequency dispersion in the poled state, as compared to the unpoled state. This difference can be attributed to the relatively higher mobility of PNRs in the unpoled state, whereas in the poled state PNRs are fixed due to strongly oriented domains [242], resulting from a field-induced transition from a relaxor to a ferroelectric state. The poled state comprises a collection of aligned domains, which can, therefore, be described as a ferroelectric state. Upon heating past $T_{F\text{-}R}$, the long-range order is disrupted due to the increase in kinetic energy of the system, and the dielectric response of the material returns to a mechanism based on the greater mobility of PNRs in response to a small signal electric field. This increase in mobility persists until T_B [23], [243], at which point the system is no longer contains PNRs and, therefore, a lower dipole orientation will occur in response to small signal electric fields [37], [244].

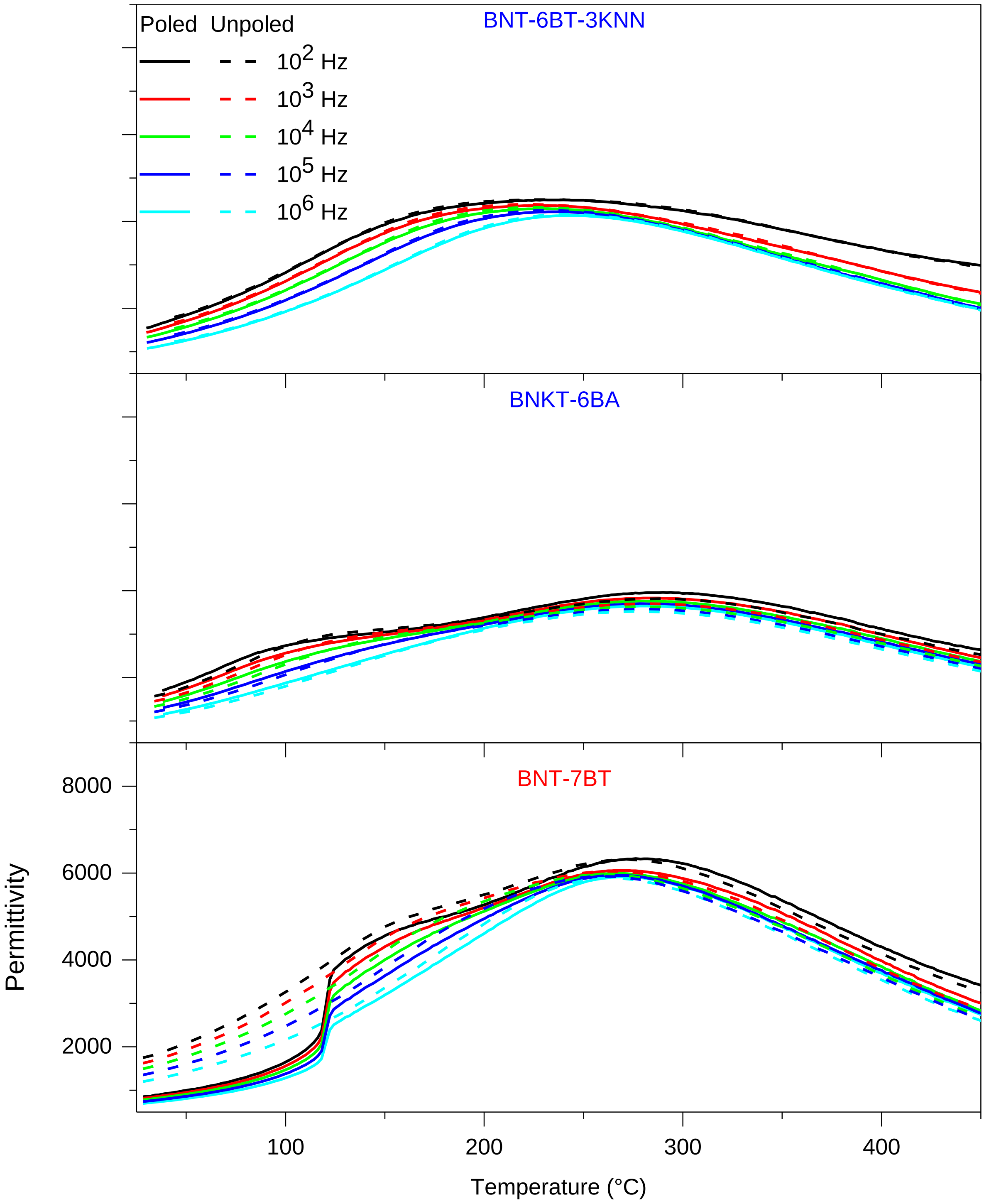

Figure 6.1: Dielectric permittivity of BNT-6BT-3KNN and BNKT-6BA as a function of frequency and temperature, from room temperature to 450 °C

In the unpoled state, BNT-7BT has a mixture of rhombohedral and tetragonal symmetries, resulting in a pseudocubic XRD pattern. As discussed in Chapter 4, upon application of a field, a peak splitting has been observed that indicates a transition to a predominantly rhombohedral phase. There is still some controversy as to the effect of temperature on BNT-BT. Recent work by Vögler *et al.* examined the influence of temperature and composition on the presence of

PNRs in BNT-BT by tracking the elastic modulus as a function of temperature in poled and unpoled samples [245]. That investigation revealed the existence of PNRs above the depolarization temperature, which has been attributed to the presence of rhombohedral PNRs as well as remaining ferroelectric domains. There was also a temperature range above T_d in which the presence of domains could still be observed. The presence of PNRs, according to Vögler *et al.*, persists up to a T_B of 700 °C. In general, below T_B, dipoles in the disordered regions of the material are more correlated and therefore form PNRs. Between T_B and the Vogel-Fulcher temperature, (in that work, the temperature at which the poled and unpoled sample correspond in elastic modulus), the relaxor is in an ergodic state with a spatial and temporal average of zero in the orientation of the PNRs. Further decrease of the temperature results in increased correlation of PNRs as well as reduced mobility, which renders the material in a nonergodic state.

6.2.2. Small Signal Dielectric Behavior of BNT-BT-KNN/BNT-BT Composites as a Function of Temperature and Frequency

The first system to be discussed is the BNT-BT-KNN/BNT-7BT composite system, the dielectric behavior of which is shown in Figure 6.2. In the 0-3 composites, the difference between poled and unpoled states is weak, compared to the difference in pure BNT-7BT. The 0-3 composite of 10% seed content has a more pronounced shoulder than in the unpoled state. In the 20% composite, no difference between the poled and unpoled states can be observed, whereas in the 30% composite, the unpoled state has a more smeared shoulder than the poled state. In the 2-2 composites, larger differences between the poled and unpoled states can be observed. The permittivity of unpoled samples is higher than in the poled state at all frequencies in the 10 % 2-2 system. The difference between the poled and unpoled states can be observed at room temperature, where the poled sample has a permittivity value 350 units higher than the unpoled sample. With increasing temperature, the difference in permittivity increases between poled and unpoled states, reaching 600 units at T_m.

In the 2-2 composite of 20% seed content, an anomaly occurs at in the temperature range of 320 °C -410 °C at 10 kHz, where a large difference in permittivity can be observed between the poled and unpoled state. This is in contrast to the T_d of the seed material BNT-7BT, which occurs well below this temperature, at 117 °C. For this composite, the unpoled state has a higher permittivity than the poled state at all other temperatures. In the 30% 2-2 composites, the permittivity of the unpoled state is higher than the poled state, and a smeared shoulder in the permittivity curve can be observed in the unpoled state. Smeared transitions are generally attributed to the presence of PNRs of different sizes and chemical inhomogeneities [246].

The temperature of maximum permittivity, as determined at 10^4 Hz, increases with increasing seed content from 256 °C in the 0-3 composite of 10% seed content to 259 °C in the 20% composite, and 278 °C in the 30% composite. Groh *et al.* also showed that increasing the BNT-7BT content results in a larger difference between the dielectric permittivity of the poled and unpoled composite [147]. This was used as evidence of the retention of a polar phase in the composite. Just as in Groh's work, the 30% 0-3 composite does not show an increase in permittivity at high temperatures.

Further analysis was performed through comparison of experimental values to rule of mixtures predictions. This comparison is enumerated in detail in Table 8. The maximum permittivity in the 0-3 composites exceeds the values predicted by the rule of mixtures by 112 in the 10% composite, but the deviation of approximately 30 from predicted values is much lower in the 20% and 30% composites. The 2-2 composites are slightly closer to the approximation, and their deviation from the prediction is not uniform, with the 10% composite having a much lower value, deviating from predictions by -678.

These differences may be caused by a number of factors, including differences in stress state and diffusion paths during co-sintering. As was shown in Chapter 5, differences in sintering trajectory have a significant influence on microstructure. High tensile stresses in the seed region were predicted during co-sintering, as shown in Figure 5.3. Significantly, the highest tensile stresses occur in the 10% seed composite, which is also the seed content at which the largest deviation from predicted values is observed. Sintering stresses were shown to result in increased pore size in Figure 5.5.

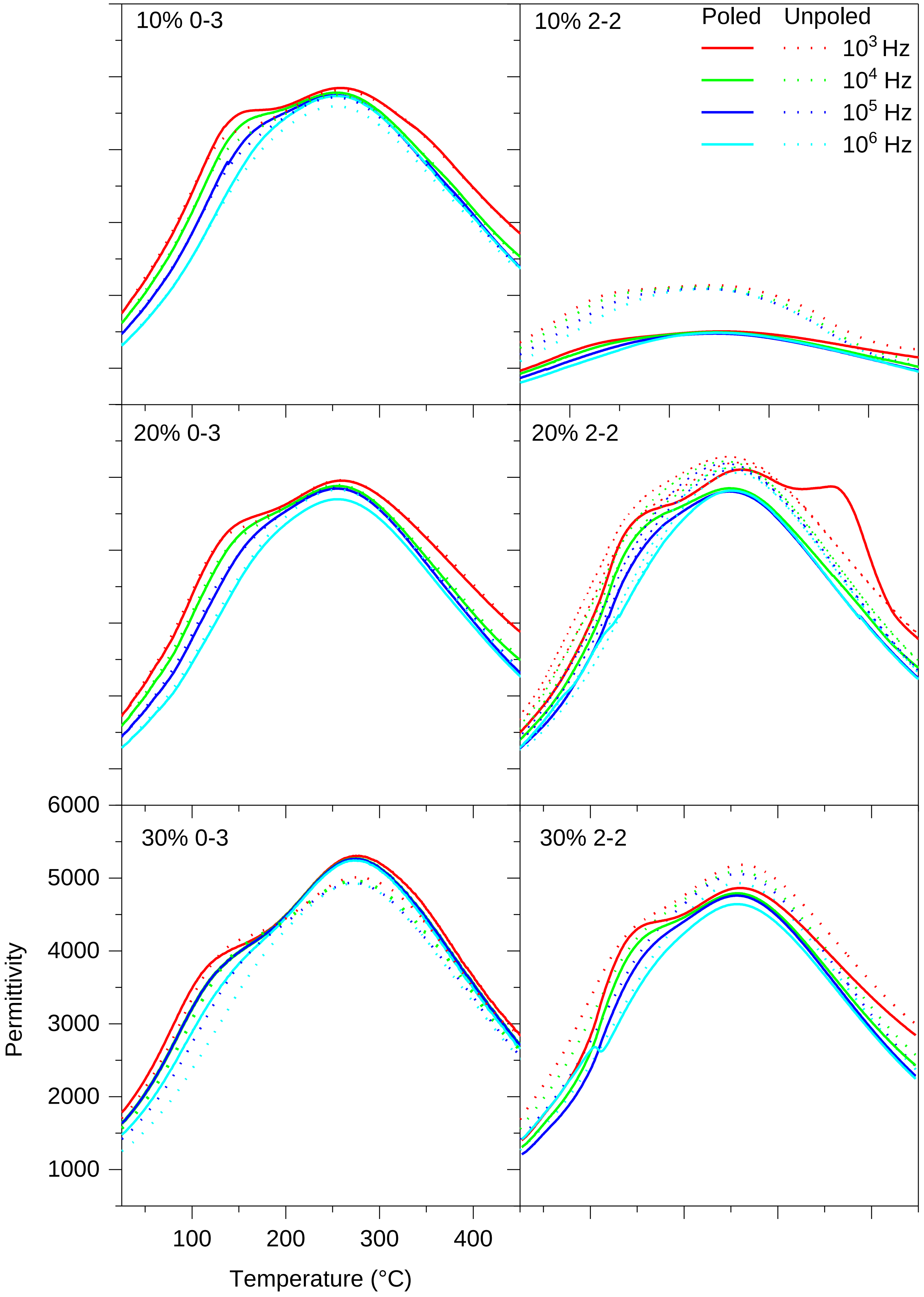

Figure 6.2: Temperature and frequency dependent permittivity of BNT-BT-KNN/BNT-7BT Composites

Previous work on constrained thick films of BNT-BT and BNT-BT-KNN under tensile stress have shown a reduced dielectric permittivity relative to bulk ceramics sintered under the same conditions, as well as a reduced T_{F-R} [247]. This was attributed to the higher porosity found in the thick films relative to bulk ceramics. Residual stresse due to differences in CTE are likely to further influence the bulk dielectric behavior of 2-2 composites. In this work, it was shown that residual stresses in the 10% composite are approximately -100 MPa in the matrix layer and 400 MPa in the seed material. Increasing seed content results in increasing compressive stress in the matrix and decreasing tensile stresses in the seed, (see Figure 5.12). It was further shown that under compressive stress, the permittivity of both BNT-BT-KNN and BNT-7BT reduce, even under stresses below the coercive stress (Figure 5.22). As was shown in Figure 5.21, the application of an electric field generates a tensile stress in the seed layer of approximately 50 MPa. The tensile stress in the seed layer due to difference in CTE is 420 MPa, and the tensile stress under an applied field of 2 kV/mm is 50 MPa. Therefore, the total stress in the poled sample is 470 MPa on the seed layer, whereas the unpoled sample has only the stress from CTE. It is possible that the higher tensile stresses in the BNT-7BT layer resulted in an reduced dielectric permittivity, but a complete understanding of this phenomenon is not yet clear. At higher seed contents, the tensile stress both as a consequence of differences in CTE and d_{31}^{*} are lower relative to the 10% composite. This may explain the lower difference between poled and unpoled 2-2 composite permittivity values at higher seed contents. In addition, the 20 and 30% seed content 2-2 composites have significantly higher permittivity values as compared to the 10% 2-2 composites, likely due to the lower stresses from CTE differences in these compositions.

Table 8: BNT-BT-KNN/BNT-BT composite system permittivity at room temperature, 10^3 Hz in the unpoled state compared to predicted values of rule of mixtures values

	10% Seed Content	*20% Seed Content*	*30% Seed Content*
Prediction	*1630*	*1689*	*1748*
0-3	*1742*	*1718*	*1780*
Deviation from prediction	*+112*	*+29*	*+32*
2-2	*953*	*1736*	*1684*
Deviation from prediction	*-678*	*+47*	*-64*

Although it was not possible to directly determine the influence of tensile stress on the materials used in this study, it has been shown that tensile stresses also reduce the permittivity of BKT-based dielectrics [201]. On the other hand, under tensile stress, thin films of PMN-PT have an increased dielectric permittivity at room temperature, whereas under compressive stress the dielectric permittivity is below that of the bulk, unstressed material [248]. The same investigation showed an increase in the small signal piezoelectric coefficient under tension. As shown in Figure 5.12, the maximum tensile stress in the BNT-7BT seed region occurs at 10% seed content. Therefore, the strong deviation from predicted values in the 10% may be more strongly attributed to the tensile stresses, which approach 400 MPa in the seed region, than the compressive stresses in the matrix region.

Porosity and grain size may also result in differences between the 0-3 and the 2-2 composites in terms of ferroelectric properties. The large gradient in pore size across the 2-2 composition differs greatly from the 0-3 composites in which pore distribution is homogeneous. The pores can be treated as a third phase with low permittivity, resulting in charge accumulation at the interface between a pore and the ferroelectric material and a localized large electric field at that interface, a phenomenon that has been described in porous dielectrics as well [249]. Previous studies by Topolov *et al*. of a composite system comprising single-crystal rods in a porous polymer matrix have shown that porosity plays a significant role in the anisotropy of the ferroelectric response as well as the maximum strain [250]. Interestingly, both porosity and pore aspect ratio were determined to nonlinearly affect the maximum strain. The model proposed by Topolov *et al.* predicts that the electromechanical response of porous materials with small aspect ratios is much higher than that of large aspect ratios. The influence of pores on ferroelectric response has also been investigated by R. Khachaturyan *et al.*, who determined through finite-element simulations that electric field distributions in PZT are independent of pore-size, but highly sensitive to the shape and orientation of pores [251].

Grain size is a further microstructural parameter worthy of consideration in the formation of ferroelectric ceramics, as it has been shown to dramatically influence the electromechanical response of bulk ceramics, having been well established to affect the dielectric properties of BT and PZT [252], [211], [253]. Frey *et al.* demonstrated that grain boundary interfaces during sintering changed the lattice parameters of BT, with an accompanying change in dielectric response. The association between dielectric permittivity and grain size was explained by modeling grains as capacitors in series, where the grain boundary and bulk have different dielectric constants, resulting in a change in the total dielectric response as the ratio of grain bulk to boundary volume decreased with decreasing grain size [9]. A strong dependence of the permittivity on grain size was shown in $BaTiO_3$ [211].

A further consideration is the possible formation of a KNN-rich orthorhombic phase at the seed/matrix interface, as discussed in Chapter 4. The dielectric permittivity of KNN is significantly lower than BNT-7BT, with room temperature values recorded at 500 – 700 units [254]. Its presence in the composite would, therefore, be expected to lower the total dielectric permittivity. However, because of its ferroelectric nature, it may also serve as a secondary polar seed region in the composite, which aligns the surrounding nonpolar matrix. Further investigation of the presence and influence of this phase in composites is required in order to fully understand its role in the dielectric response.

6.2.3. Small Signal Dielectric Behavior of BNKT-6BA/BNT-BT Composites as a Function of Temperature and Frequency

As discussed in Chapter 4, the model system comprised of BNKT-6BA as the matrix was produced and evaluated in order to facilitate the investigation of effects of interdiffusion on composites. The dielectric behavior as a function of temperature and frequency in 0-3 and 2-2 composites of this composition are shown in Figure 6.3.

Although the samples of this system underwent the same poling conditions as those of the BNT-BT-KNN system, they do not appear to be poled. A comparison of permittivity values in the poled and unpoled states reveals a very limited effect of poling on the dielectric response of both 0-3 and 2-2 composites, indicating an increased ergodicity in this system as compared to the BNT-BT-KNN/BNT-BT composites. Differences in the dielectric response of the two composite structures can also be observed. The permittivity of the 2-2 composites with 40 and 50 % seed content is higher than the 0-3 composites of the same composition.

T_m lies between 260 and 280 °C for all 0-3 and 2-2 composites. In the 0-3 composites of 10, 20 and 30% seed content, this temperature is 270 °C, and in the same compositions with a 2-2 structure this temperature is 262 °C. A slight increase of the T_m occurs in the composites of 40% seed content of both 0-3 and 2-2 structure, with a value of 274 and 268 °C respectively, whereas in the 2-2 composite of 50% seed content, a reduction of T_m to 252 °C occurs. The narrow temperature window for the maximum permittivity demonstrates that T_m is relatively stable with seed content and composite structure, and does not diverge from the T_m of the pure constituents BNKT-6BA and BNT-7BT.

Above T_m, the frequency dispersion has significantly reduced. This is in stark contrast to the BNT-BT-KNN system, in which at temperatures greater than T_m the permittivity values measured at 10^4 Hz are between 100 and 1000 units higher than the values at 10^5 Hz. This points to an absence of space-charge polarization contributions to the dielectric response of BNKT-BA composites. Because space-charge polarization generally occurs at sharp chemical interfaces or inhomogeneities [255], as well as sharp differences in resistivity [253], a more diffuse chemical interface is likely in this composite system. A much clearer onset of frequency dispersion can be observed in the BNKT-BA composite system than in the previously discussed BNT-BT-KNN composites, due to the low degree of frequency dispersion at higher temperatures.

In the absence of an applied field, there are two mechanisms of interaction between the composite constituents: chemical and mechanical. In terms of chemical interactions, B-site cation disorder has been shown to play a role in the observation of frequency dispersion as demonstrated by Dkhil *et al.* [256]. In this system, Al is a B-site cation in BNKT-BA that may migrate into the B-site of BNT-7BT, as shown in Chapter 4. Such an aliovalent B-site occupancy would result in a destabilization of long-range order. This should result in a lower permittivity. This also implies that the long-range order is less stable with temperature, and the transition temperature will reduce.

In Table 9, the permittivity values at room temperature, 10^3 Hz in the unpoled state are compared to predicted values from the rule of mixtures. The 10 and 20% 0-3 composites are below predicted values by 70 units, whereas the 30, 40 and 50% 0-3 composites are all at least 200 units below the predicted values. A much larger deviation from rule of mixtures is observed in the 2-2 composites of 10 and 20% seed content.

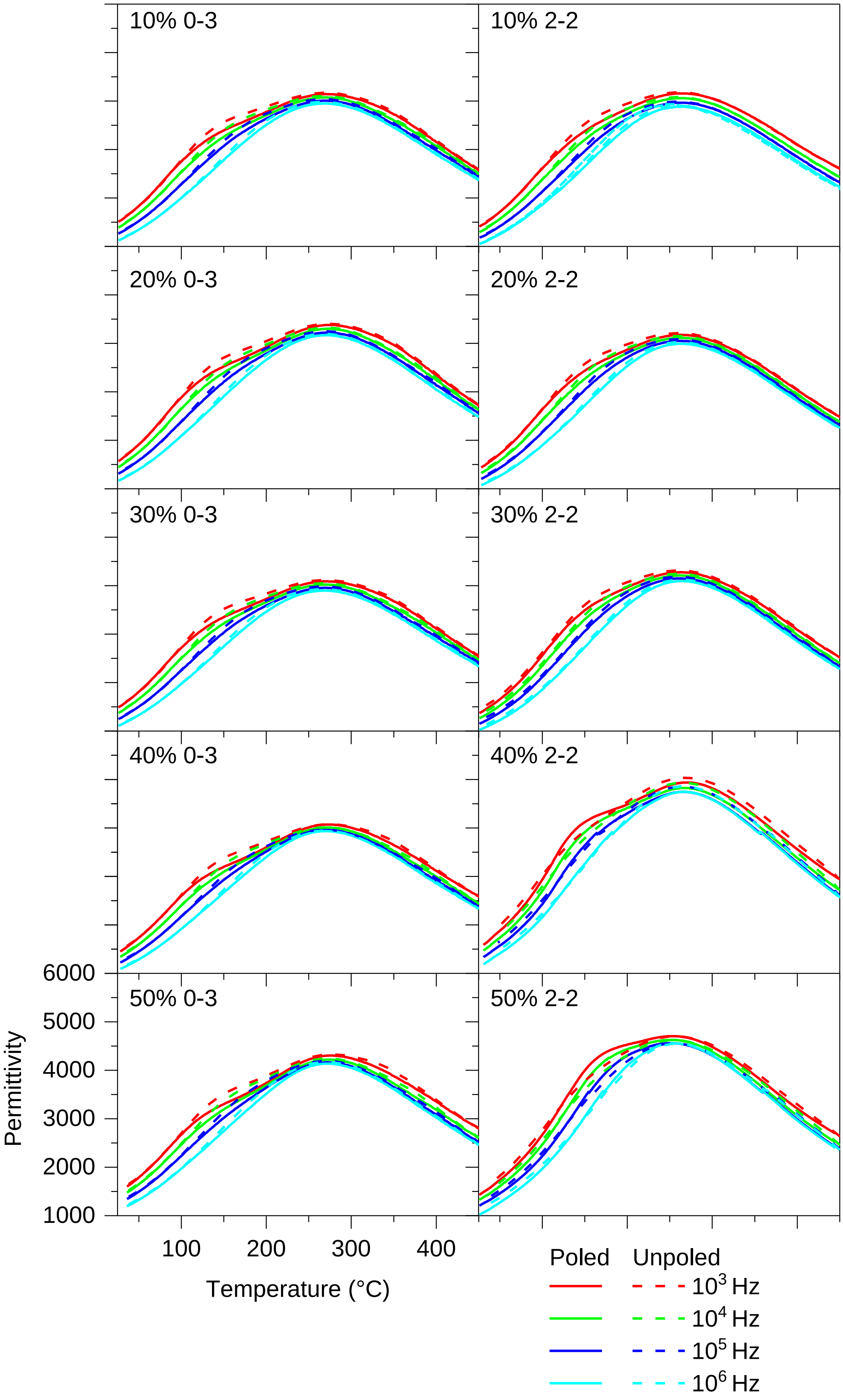

Figure 6.3: Temperature and frequency dependent permittivity of BNKT-BA/BNT-7BT composites

Table 9: BNKT-6BA composite system permittivity at room temperature, 10^3 Hz in the unpoled state compared to predicted values of rule of mixtures values calculated from Equation 1.1

	10%	20%	30%	40%	50%
Prediction	1583	1647	1711	1775	1839
0-3	1507	1568	1488	1454	1600
Deviation	-74	-79	-223	-321	-229
2-2	1409	1438	1370	1585	1502
Deviation	-174	-212	-331	-190	-337

The first cause for deviation from rule of mixtures predictions to be discussed is the chemical interaction between seed and matrix during sintering. It was shown by Ullah *et al.* that the addition of Al to BNT-BT reduced both T_d and the dielectric permittivity at T_m [110]. However, that composition showed an increase in the dielectric constant at room temperature with the addition of Al. Therefore, the addition of K to BNT-BT is likely to also play a role in the deviations from predicted permittivity values. In ternary solid state solutions of BNT, BKT and BA, the addition of BKT has resulted in an increase in dielectric response [257]. However, a corresponding decrease in grain size was also associated with increasing BKT content. Such a change in microstructure is often associated with increased dielectric permittivity values [211].

As discussed in the previous section, changes to microstructure from co-sintering stresses may also contribute to deviations from the rule of mixtures predicted values. Increased porosity and/or pore size will reduce the dielectric permittivity. Evidence of large pores formed in the seed layer was shown in Figure 5.7 and is likely to play a role in the lower values of the dielectric permittivity as compared to rule of mixtures predictions.

The room temperature dielectric constant of 0-3 and 2-2 composites was also evaluated in the BNKT-BA/BNKT system by Jeong *et al.* [150], who showed that the 2-2 composite has a higher room temperature dielectric constant than the 0-3 composite system. In this work, only the composite with 40% seed content had a higher maximum permittivity in the 2-2 composites. This difference may be in part due to the difference in A-site cations in the BNKT-6BA/BNT-7BT system, where Ba^{2+} is an aliovalent substitution for K^+. The differences in CTE and sintering stresses also vary significantly between the two systems.

6.3. Large Signal Ferroelectric Behavior of Lead-free Ceramic/Ceramic Composites

In this section, the electromechanical behavior of the composite systems is discussed in terms of its response to large signal applied electric fields relevant to actuator applications. Actuators are generally activated by applied electric fields, which generate a ferroelectric response. In relaxor ferroelectrics, this electromechanical response from the virgin state is the result of a growth of PNRs, and an accompanying increased correlation length between PNRs. Upon further application of an electric field, PNRs evolve into aligned domains that orient along the direction of the applied field. This is the so-called relaxor-to-ferroelectric transition, which is accompanied by a large strain. In nonergodic relaxors this transition is partially irreversible as a result of the long-range chemical order, whereas in an ergodic relaxor with reduced chemical order the removal of the field results in a return to the original disordered state prior to the application of the field. The piezoelectric and ferroelectric response to an applied field of 6 kV/mm, 1 Hz at room temperature of the two ergodic relaxors, BNT-6BT-3KNN and BNKT-6BA, used in this work are shown in Figure 6.4. The ergodicity of these materials is apparent from their low remanent strain. However, these two ER materials have several drawbacks to their application as actuators, namely the high hysteresis of the strain response [258], resulting in undesirable self-heating [128], [259], the high coercive fields required to achieve the ferroelectric long-range order that results in a high strain response, and the low (relative to PZT) response to applied fields of 2 kV/mm, which is the driving field used in PZT, therefore requiring the use of high voltages to achieve desired strain responses.

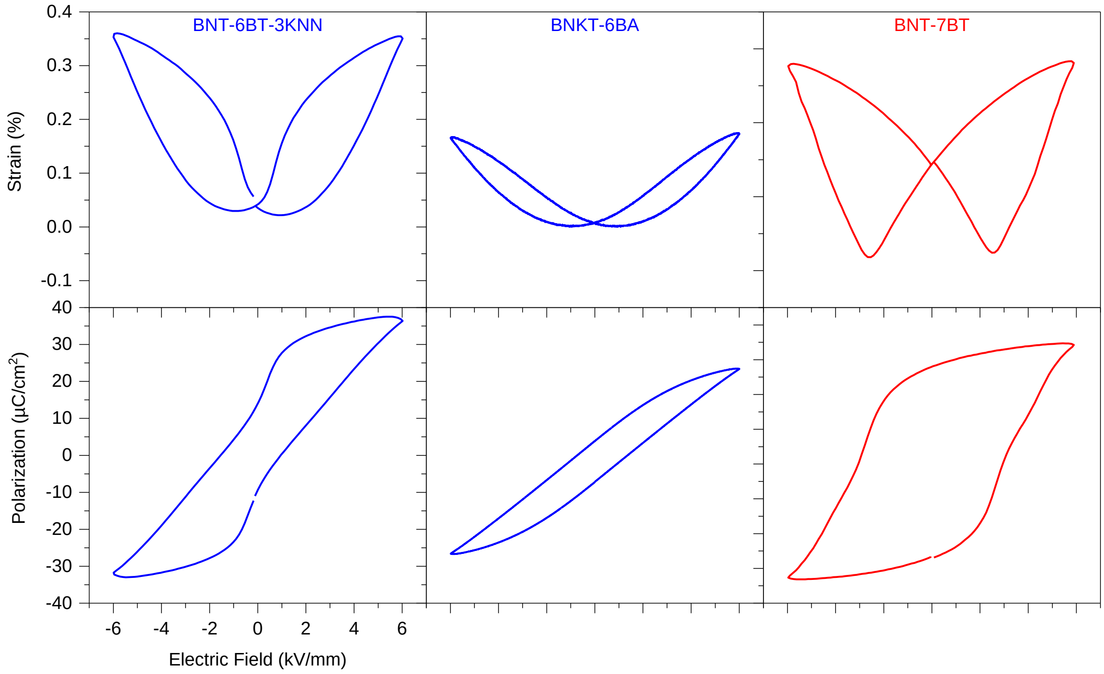

Figure 6.4: Large signal ferroelectric and piezoelectric response of BNT-based ERs (BNT-6BT-3KNN and BNKT-6BA) and NR BNT-7BT used as matrix and seed respectively, in this work, measured at 1 Hz, 25 °C.

In order to eliminate these hurdles to the implementation of lead-free relaxors as actuators, the addition of a polar seed material was undertaken by previous authors. The piezoelectric and ferroelectric behavior of BNT-7BT used as the polar seed is shown in Figure 6.4. The field at which poling occurs is 2 kV/mm and a coercive field of 2.3 kV/mm can be observed, as well as a high remanent strain and polarization indicative of a retained polar order desirable in a polar seed. As can be seen in Figure 6.4, the remanence is due to an irreversible transition from a relaxor to a ferroelectric under an applied electric field.

6.3.1. Large Signal Ferroelectric and Piezoelectric Response of BNT-6BT-3KNN/BNT-7BT 0-3 and 2-2 Composites

To elucidate the mechanisms of enhancement observed in composites, 2-2 and 0-3 composites of BNT-6BT-3KNN/BNT-7BT were produced and measured under identical conditions. Figure 6.5 provides a comparison of the response to an applied electric field of 4 kV/mm at maximum between 0-3 and 2-2 composites of BNT-6BT-3KNN and BNT-7BT.

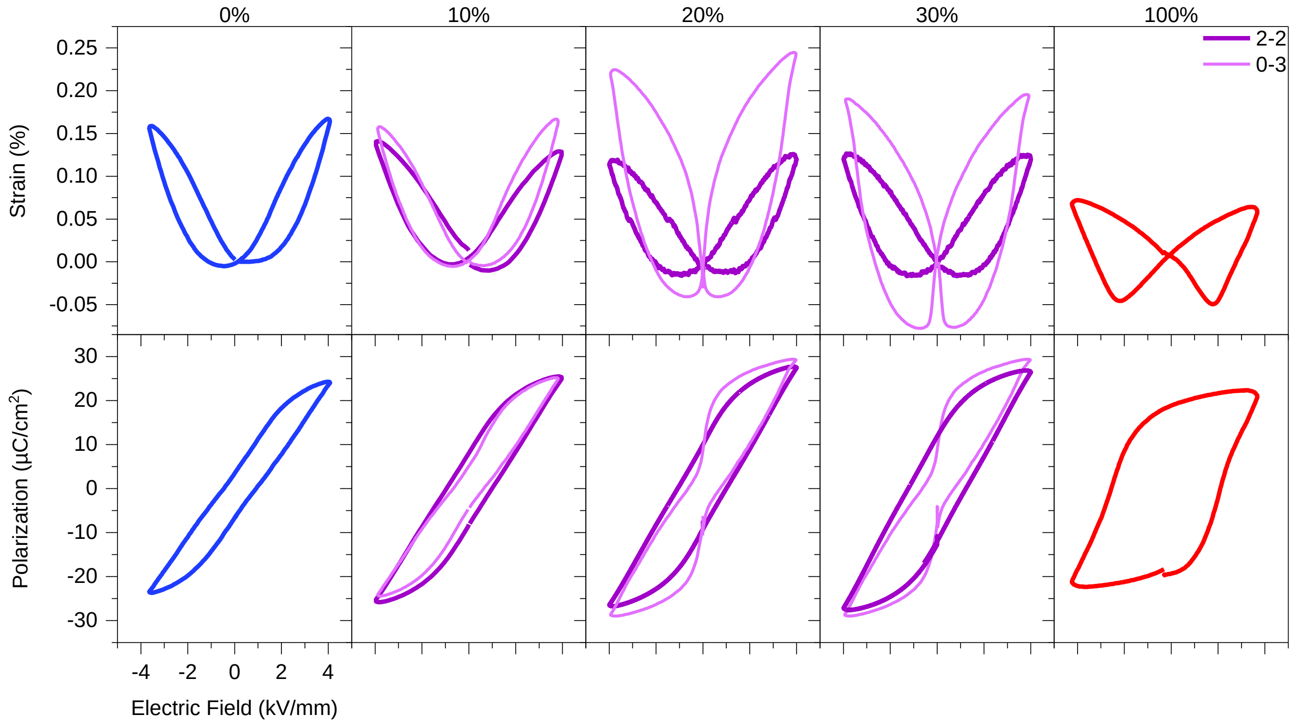

Figure 6.5: BNT-6BT-3KNN/BNT-7BT 2-2 composites large signal ferroelectric and piezoelectric virgin behavior, 50 mHz, 2nd cycle

A large difference in electromechanical response between the 2-2 and 0-3 composites can be observed. At 4 kV/mm and 50 mHz, the maximum strain in this study was attained with 20% 0-3 composites. A negative strain can also be observed in the 30% 0-3 composite, exceeding that of the pure BNT-7BT. The polarization loops of the 0-3 composites have a clear pinching, as compared to those of the 2-2 structure, and this feature becomes more prominent with increasing seed content. Pinched polarization loops are indicative of polar defects that prevent domain wall switching [260], as well as a disruption of the long-range order [261], [262], and are associated with a transition from the ergodic relaxor to the ferroelectric state. As this feature is more apparent in 0-3 composites, it appears that they retain the ergodic state of the matrix more than 2-2 composites.

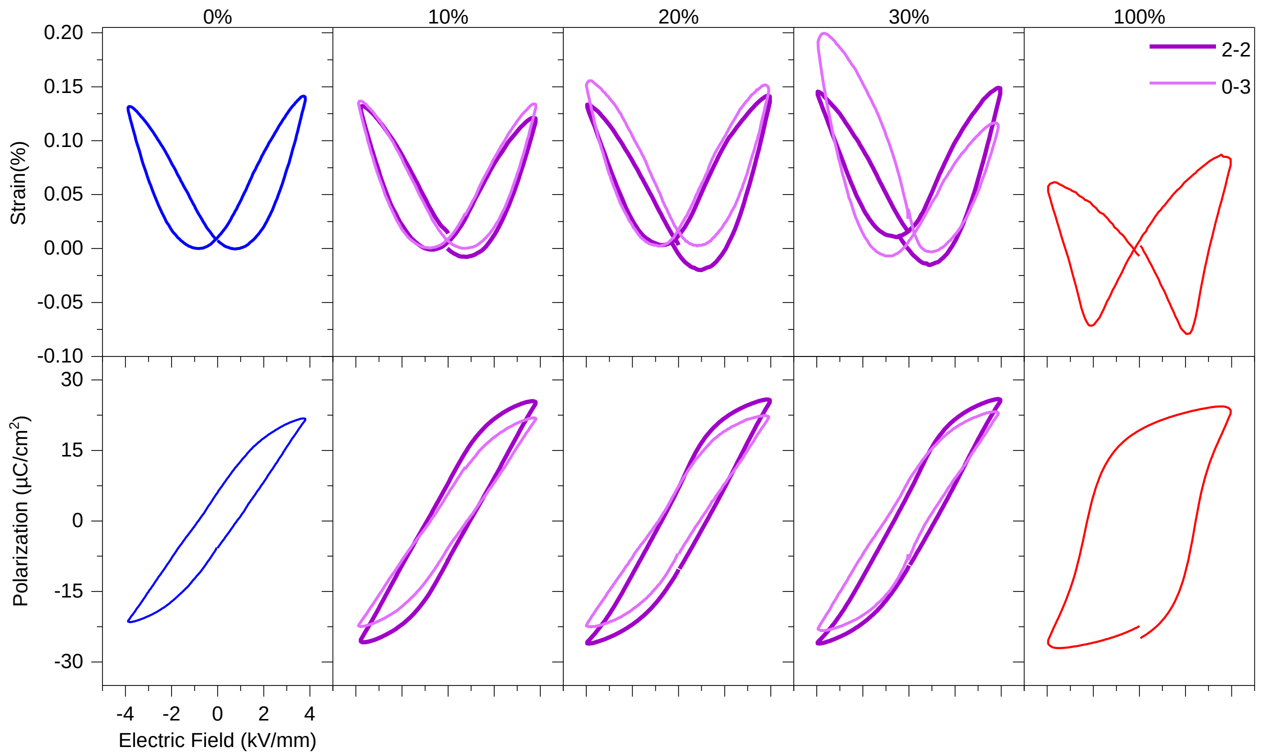

Figure 6.6: BNT-6BT-3KNN/BNT-7BT 2-2 and 0-3 composites large signal ferroelectric and piezoelectric behavior at 4 kV/mm maximum electric field, 1 Hz, 2nd cycle

When measured at 1 Hz, as shown in Figure 6.6, an asymmetry can be observed in the strain response of the 2-2 composites, as well as the 0-3 composite of 30% seed content. It appears that the application of an electric field at a higher frequency may be the origin of the asymmetry: it is possible that a large internal electric field arises that must be compensated, thereby reducing the strain response in one direction. This large internal field, when faced with a slow loading rate as found in external fields of low frequency, is overcome. Under low frequencies, new domains may act on neighboring domains that arose from internal stresses.However, under a higher frequency, the external field loading rate is too rapid to allow for complete reversal and alignment of domains along the direction of the external applied field. The internal field may be due to a difference in the conductivities of the two components of the composite, the effect of which is more pronounced in 2-2 composites due to a larger surface area along which charges can accumulated, as opposed to 0-3 composites in which the seed distribution is more homogeneous. Higher frequencies would, therefore, not be able to redistribute the charges at the interface. No such asymmetry was reported in this composition in previous work on 0-3 BNT-BT-KNN/BNT-BT composites by Groh *et al.*[147]. The internal field appears to be aligned parallel to the positive applied field in 2-2 composites, resulting in a reduced response to a positive field as the domains are already aligned in that direction. No such asymmetry is observed in the pure matrix material, although a slight asymmetry can be seen in the pure seed material. Therefore, it appears that the generation of an internal field is the result of the 2-2 composite structure.

Asymmetries in the strain response have been observed in fatigue testing of piezoelectric materials, with an increased asymmetry arising with higher fatigue cycling [263]. This has been attributed to point defects that cluster during cycling, which include cracks and pores, resulting in a charge accumulation that generates internal bias fields [264]. Asymmetry has also been observed in hard PZT, and is generally attributed to the presence of polar defects which result in an internal bias field [265]. Evidence of internal fields resulting in asymmetric ferroelectric responses was also observed in PZT doped with Al, Mn and Fe [266].

It is possible that the composite structure itself results in accumulation or clustering of point defects that gives rise to the asymmetries observed in this work, rather than the clustering of point defects during cycling. One possible source for an internal field is the residual stresses arising from differences in thermal expansion during annealing, as shown in Figure 5.12. Such stresses, as discussed in Chapter 5, result in domain orientation parallel to the applied electric field. An applied electric field on such a stressed sample will induce domain rotation. It was also shown that in-plane biaxial stresses arise during application of an electric field in 2-2 composites due to the difference in transverse strain of the two end members. These stresses also orient domains parallel to the applied field, which gives rise to an enhanced strain response. In other work, negative strain has been ascribed to the presence of a long-range ferroelectric order which disappears with increasing temperature as the T_{F-R} is approached [177]. Based on this, it appears that a positive field is able to induce a long-range ferroelectric order, whereas a negative field does not.

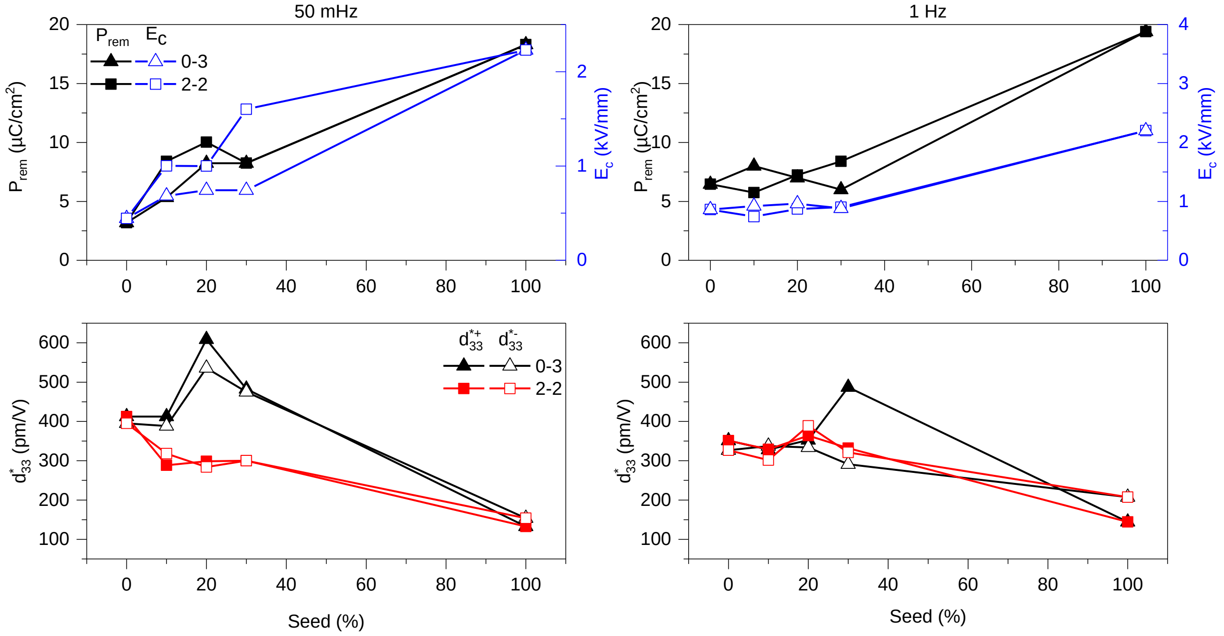

Figure 6.7: d_{33}^*, remanent polarization and coercive field as a function of composition in BNT-BT-KNN/BNT-7BT composites, shown for frequencies of 1 Hz and 50 mHz. d_{33}^* is shown under positive and negative fields to highlight the asymmetry of the bipolar strain response

An evaluation of the figures of merit of the large signal response are shown in Figure 6.7. At 50 mHz, the coercive field increases with increasing seed content in the 2-2 composites. In the 0-3 composites there is an increase from the matrix (0.45 kV/mm) to 10% seed content (1 kV/mm), above which there is no difference in coercive field. At a frequency of 1 Hz, the coercive field remains stable with seed content in the 2-2 composite. In the 0-3 composite, the addition of seed does not change the coercive field at 1 Hz.

With increasing seed content, an increase in the remanent polarization is observed at 50 mHz. This increase is higher in the 0-3 than in the 2-2 composite, at both 10 and 20% seed content. A maximum in the remanent polarization can be observed in the 0-3 composite of 20% seed content. At 30% seed content, the remanent polarization of both the 2-2 and 0-3 composites are identical, at a value of 9 µC/cm^2. The remanent polarization at 1 Hz has a nonlinear response to increasing seed content, with an increase relative to the pure matrix observed in the 10% 0-3 composite, and a decrease in the 2-2 composite of the same seed content. At 20% seed, the remanent polarization of the 0-3 and 2-2 composites nearly overlap, and at 30% seed the 2-2 composite has a higher value than the 0-3. The differences are very small relative to the difference in remanent polarization between the seed and matrix. If the composites were to follow the rule of mixtures predictions, an increase in remanence should be observed with increasing seed content. This is, however, clearly not the case.

A nonlinear relationship can also be observed between the seed content and the d_{33}^*. Because of the asymmetry observed in this system, this value is shown as determined from the application of a positive and negative field, where the positive d_{33}^* is shown with a filled symbol and the negative d_{33}^* is shown with an open symbol. The difference between the values under positive and negative fields is a reflection of the asymmetry. At 50 mHz, the largest asymmetry occurs in the 0-3 composite of 20% seed content, whereas in the 2-2 composites a higher degree of symmetry can be observed. In general, an increase in the d_{33}^* value can be observed in the 0-3 composites at 50 mHz with increasing seed content, despite the fact that this value is lower both in the seed (191 pm/V) and matrix (400 pm/V), the only exception being the 10% 0-3 composite, which falls to 319 pm/V. Under 1 Hz, the largest asymmetry occurs in the 0-3 composite with 30% seed content. Comparing the 0-3 and 2-2 composites, at 20% seed, there is an overlap in their d_{33}^* values, similar to the overlap of the remanent polarization values. At 30% seed, the 0-3 composite d_{33}^* exceeds the 2-2 composite by nearly 20 pm/V.

In the 2-2 composites, a lower frequency (50 mHz) applied field results in an observable drop in the d_{33}^*. The difference in internal stress states between 0-3 and 2-2 composites may play a role in this behavior. In addition, the larger surface area around which charge accumulation can occur in 2-2 composites affects the conductivity and build-up of internal fields. Considering the asymmetry observed both here and in the referenced work, the presence of an internal field may affect the response at different frequencies. The asymmetry in the 30% 0-3 composite was present at 1 Hz, pointing to a large-scale charge accumulation in the composite. However, these values are still well below the d_{33}^{*} of lead-based ferroelectrics, which ranges from 600 to 800 pm/V [58].

Groh *et al.* had investigated the frequency dependent large signal behavior of BNT-BT-KNN/BNT-7BT 0-3 composites and shown that a reduced frequency resulted in an increased d_{33}^{*}. In that work, the composition at which the highest strain was observed also shifted with higher frequencies, from 20% seed at 500 mHz, to 30% seed at 50 Hz [169]. This shift was explained by Groh *et al.* as follows: PNRs are exposed to an applied field for less time at higher frequencies, giving them less time to grow and develop long-range ferroelectric order. Therefore, at higher frequencies, a larger quantity of seed material is required to lower the poling field and induce switching of the matrix phase. In this work, at lower frequencies the highest strain is observed in the 20% 0-3 composite, and at higher frequencies the strain response is increased at both 20 and 30% seed.

6.3.2. Influence of Temperature on Large Signal Ferroelectric and Piezoelectric Response of BNT-BT-KNN/BNT-7BT 2-2 Composites

Because BNT-BT-KNN composites have a d_{33}^{*} value that renders them competitive with PZT, a more detailed investigation of their large signal response was performed as a function of temperature. As 0-3 composites were already investigated for their temperature-dependent ferroelectric behavior by Groh *et al*. [169], a comparison between 0-3 and 2-2 composites can be made. All measurements for the figures below were performed using a maximum electric field of 4 kV/mm, 1 Hz bipolar cycles. Measurements were limited to this applied field in order to prevent electrical breakdown of 2-2 samples due to internal stresses at higher fields.

Figure 6.8 depicts the ferroelectric response of BNT-7BT, while Figure 6.9 shows the same for BNT-6BT-3KNN. These data are provided as reference for the behavior of the composites. In BNT-7BT, with increasing temperature, the polarization loop narrows, indicating a reduced coercive field, and the maximum polarization increases. The negative strain decreases with increasing temperature, and by 130 °C the strain response is similar to that of an ergodic relaxor, resulting in a higher total usable strain. The T_d of BNT is 106 °C [240]. In this work, T_d occurs at 124 °C. A pinching of the polarization loop can be observed at 110 °C, which becomes more pronounced at 130 °C. This is indicative of a field-induced RE-FE transition, which is reversible at this temperature. Its reversibility is the result of the reduction of the correlation length of PNRs with increasing temperature. The same change in polarization loops as a function of temperature, namely the increasingly pinched shape, has also been demonstrated in BNT-6BT by Xu *et al.* [72]. The RE-FE transition was predicted by Raman spectroscopy as a function of temperature in BNT-6BT by Wylie-van-Eerd *et al.* [267], who observed no discontinuity in structure in this temperature range, and, therefore, proposed that there is a loss of long-range ferroelectric order and a reduction of the correlation length of order parameters, resulting in a nonpolar response to applied electric fields. A reduction in the coercive field, remanent polarization and maximum polarization, with increased temperature in BNT-6BT was also observed by Zhang *et al.* [268]. *In situ* XRD investigations of BNT-BT showed that with increasing temperature a reduced (200) peak splitting occurs, which in BNT-5BT results in a single (200) peak a 167 °C indicative of a cubic phase [269]. In the same study, increased BT content resulted in a higher transition temperature. Therefore, the highest temperature recorded here is still below the phase transition temperature of this seed and a hysteresis should still be observed. This hysteresis is a double-loop due to the reversible field-induced FE state above the $T_{F\text{-}R.}$

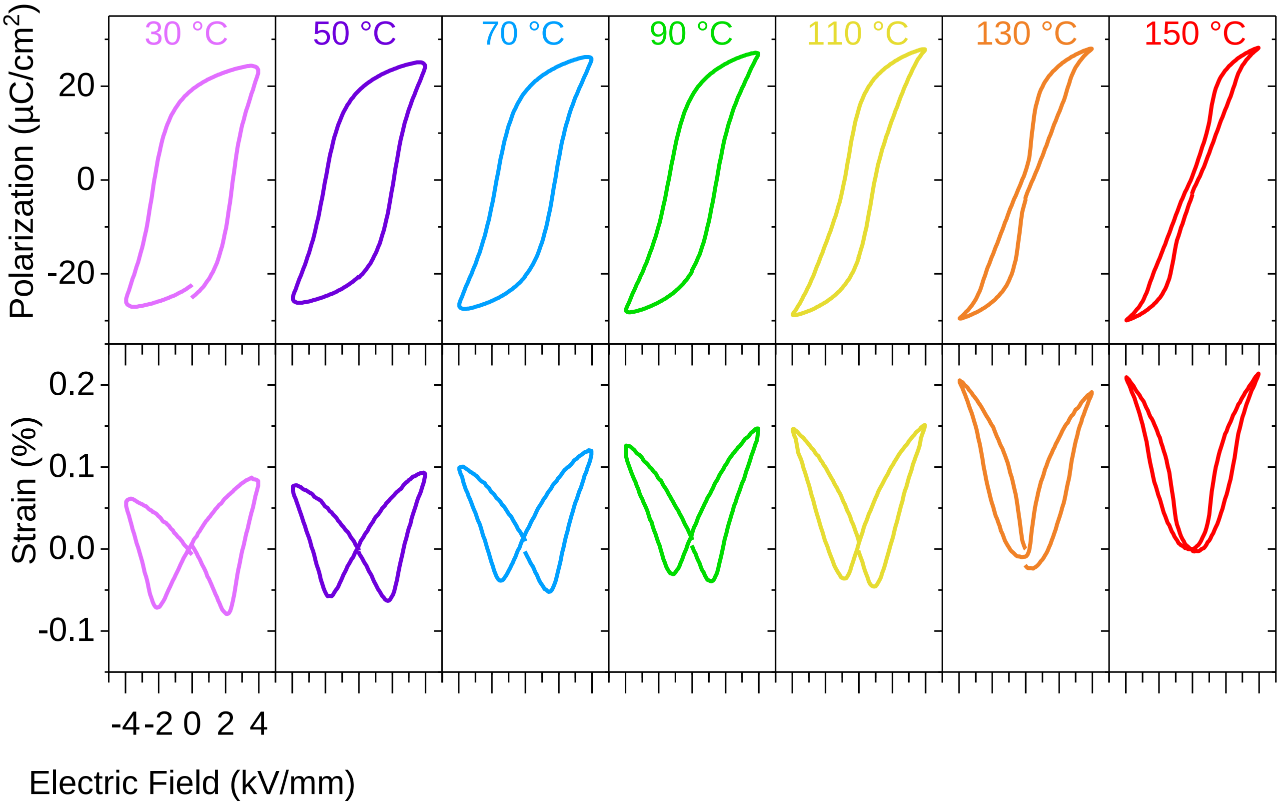

Figure 6.8: BNT-7BT temperature-dependent ferroelectric response, 30 °C to 150 °C, under applied fields of 4 kV/mm, 1 Hz, showing the 2nd strain and polarization loops

BNT-BT-KNN (Figure 6.9) shows a reduction in the maximum polarization with increasing temperature, as well as a reduction in the coercive field. This is in line with temperature-dependent ferroelectric behavior of BNT-6BT-2KNN and BNT-6BT-1KNN characterized by Jo *et al.* [270]. The width of the polarization loops decreases, also pointing to a reduced coercive field with increasing temperature. Similarly, the strain response to applied field at this temperature is nearly quadratic, characteristic of electrostriction, with slimmer hysteresis loops. Increasing temperature results in a drop in the maximum strain in BNT-BT-KNN, limiting its so-called “giant strain” [173] behavior to temperatures below 80 °C.

This temperature limitation has significant implications for the usability of this material system, due to the broad temperature ranges to which actuators are exposed [128]. In terms of large signal ferroelectric behavior, the maximum unipolar strain of BNT-6BT-3KNN was shown to reduce with increasing temperature, accompanied by a narrowing of the hysteresis loop, in support of the data presented in this work [271].

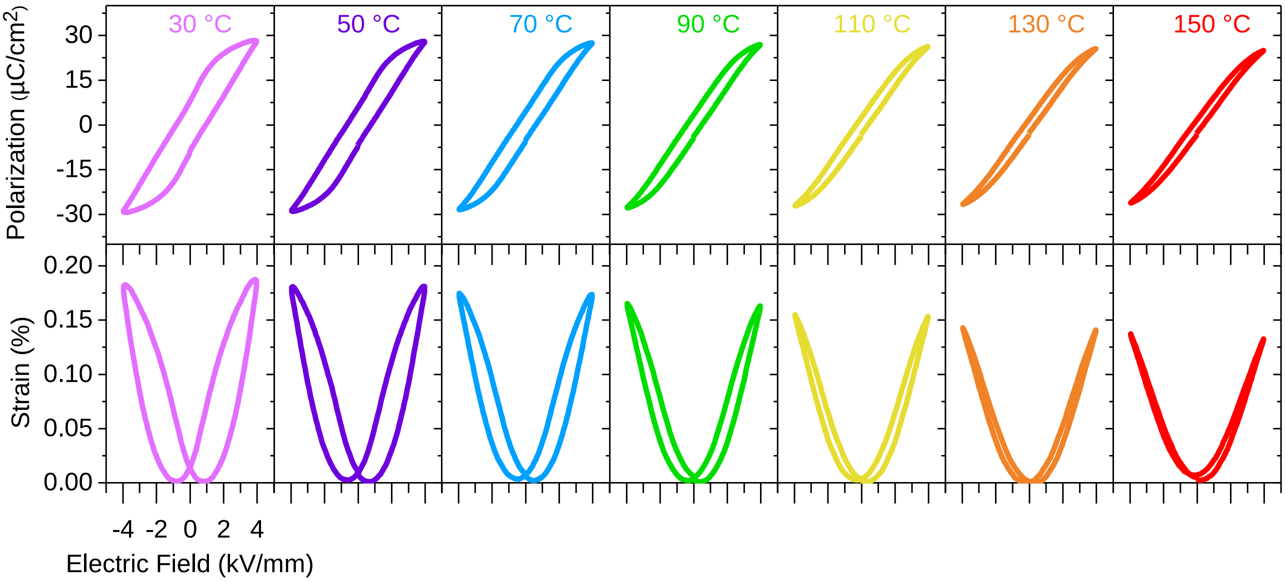

Figure 6.9: BNT-6BT-3KNN temperature-dependent ferroelectric response, from 30 °C to 150 °C, under applied fields of 4 kV/mm, 1 Hz, showing the 2nd strain and polarization loops

The temperature dependent large signal ferroelectric response of 2-2 composites of BNT-BT-KNN/BNT-BT are shown in Figure 6.10. The 10% composite response displays an increased conductivity with increasing temperature, which begins at 120 °C. As a consequence, the polarization loops have an arched shape defined by an increase in polarization when reducing the applied field from E_{max} [48]. From 30 °C to 90 °C the polarization loops narrow in width, indicating a decrease in the coercive field. Above 90 °C, the loops begin to widen, indicating an increased coercive field. In this temperature range, an increase in conductivity can also be observed in the polarization loops. No conductivity contributions can be observed in the polarization loops of the pure constituents, as shown in Figure 6.8 and Figure 6.9, indicating that this conductivity is likely a consequence of the composite structure. Two possible explanations for conductivity can be speculated, the first being that a new, conductive composition is formed at the interface of the two end members; the second possible explanation is that as a consequence of internal stresses, microcracks and increased porosity arise, resulting in a conductive path between electrodes during the painting and burning in of silver paste as electrodes.

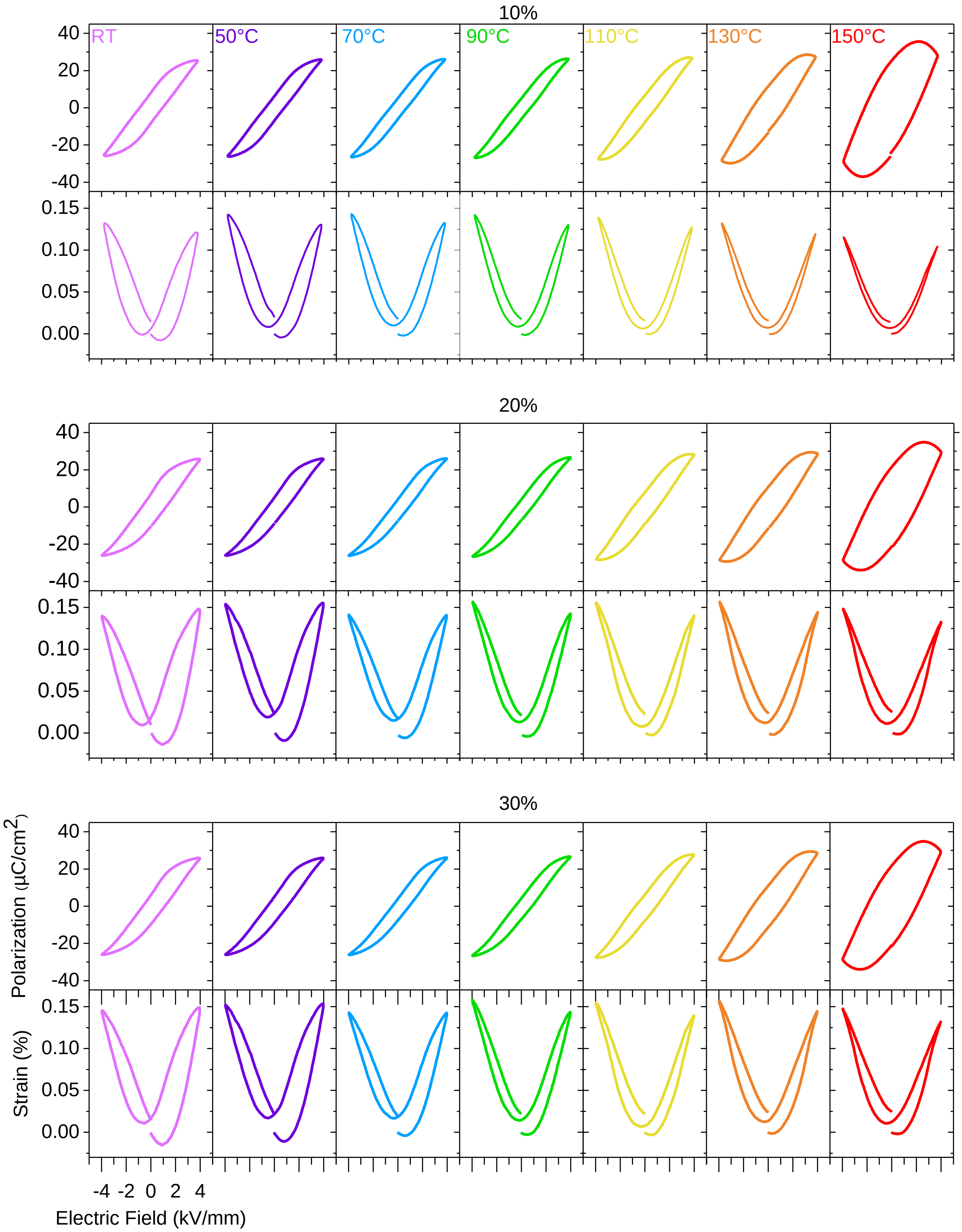

Figure 6.10: BNT-BT-KNN/BNT-BT 2-2 10%, 20%, 30% composite temperature-dependent ferroelectric response from 30 °C to 150 °C, under applied fields of 4 kV/mm, 1 Hz, showing 2nd loops

With 20% seed content, it can be observed that the polarization loop narrows at 70 °C, as a result of reduced E_c, and remains narrow up to 110 °C. At this temperature, and going up to 150 °C, polarization loops characteristic of conductive ferroelectrics appear, as was pointed out previously in the discussion of the 10% composites. The maximum polarization remains at approximately 25 μC/cm^2 from 30 °C to 90 °C. At higher temperatures, the maximum polarization increases more rapidly with increasing temperature, maximizing at 30 μC/cm^2 at 150 °C.

In the 2-2 composite with 30% seed content, the maximum polarization is stable with temperature up to 100 °C and begins to increase at 110 °C. A polarization loop characteristic of leakage can be observed at 120 °C, with the leakage current becoming more pronounced with increasing temperature up to 150 °C. The coercive field reduces with increasing temperature, as indicated by a narrowing of the polarization loop, up to 100 °C, beyond which it begins to widen again.

The maximum strain of the 10% 2-2 composite increases slightly with increasing temperature up to 110 °C, and then begins to reduce at higher temperatures between 130 °C and 150° C. At 150 °C the hysteresis of the strain response is almost gone, which can be ascribed to an increased crystalline symmetry in the material and an electrostrictive response to applied field, rather than a ferroelectric alignment of domains resulting in an enhanced strain response. The hysteresis begins to decrease at 90 °C. In contrast to BNT-BT-KNN, there is a marked stability in the maximum strain from 30 °C to 130 °C in the composites, thereby increasing the temperature range under which this material could be utilized as an actuator.

The strain response of the 20% 2-2 composite maximizes at 50 °C. The asymmetry of the strain response does not become apparent until 90 °C, which may imply that the formation an internal field that causes this asymmetry occurs at a higher temperature in the 20% composition than the 10% composition. The remanent strain is reduced with increasing temperature, and the negative strain is almost completely absent from 90 °C on.

In the 30% 2-2 composite, the maximum, negative and remanent strain are nearly identical at 30 °C and 50 °C. At 70 °C a drop in the maximum strain can be observed. At 90 °C the maximum strain increases slightly and an asymmetry arises in the maximum strain value. This asymmetry persists up to 150 °C. Between 90 °C and 130 °C, the maximum strain remains stable again, as does the remanent strain. A minor asymmetry was observed in the 30% 0-3 composites by Groh *et al.* at 75 °C, but was not apparent at higher temperatures [169].

There is a drawback to the 2-2 composite temperature stability, in that the maximum strain achieved by this composite structure, which never exceeds 0.12%, is below that of the pure matrix strain at 130 °C, which has a value of 0.14%. A stabilization of the d_{33}^* as a function of temperature was also observed in 0-3 composites with 30% seed by Groh *et al.* [169]. An asymmetry can be observed in the maximum strain under positive and negative field at all temperatures, which may be indicative of an internal field aligning domains preferentially, as was shown at room temperature in this system in Figure 6.6.

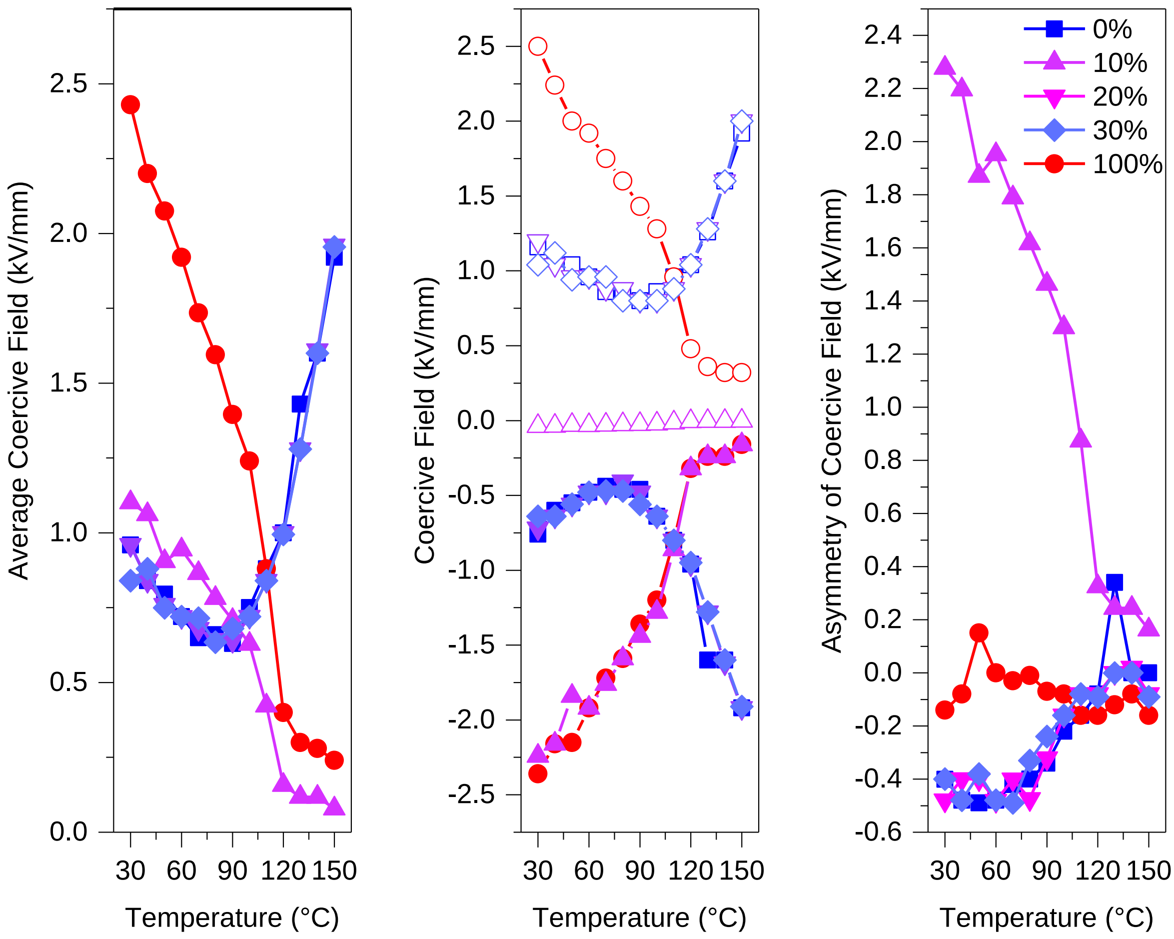

Figure 6.11: Coercive field analysis of 2-2 BNT-BT-KNN/BNT-7BT composites at different seed contents, showing the average coercive field and the asymmetry in the coercive field as a function of temperature, with the positive coercive field shown using empty symbols and negative coercive field shown using filled symbols

In Figure 6.11, the coercive field is presented as a function of seed content and temperature. For all samples, the coercive field tends to decrease with increasing temperature up to 90 °C. The pure seed material coercive field decreases with temperature nearly linearly up to 120 °C, as do the pure matrix material and 30% composite. The coercive field of the 10% 2-2 composite also decreases with increasing temperature, in line with temperature-dependent measurements of 0-3 composites that show a reduction in the coercive field no matter the seed content [169], but the behavior of the 20 and 30% seed 2-2 composites does not correspond to 0-3 composite behavior of the same composition. In the 20 and 30% composites, the coercive field increases with increasing temperature. These composites also have a larger asymmetry in the coercive field, indicating an internal bias field.

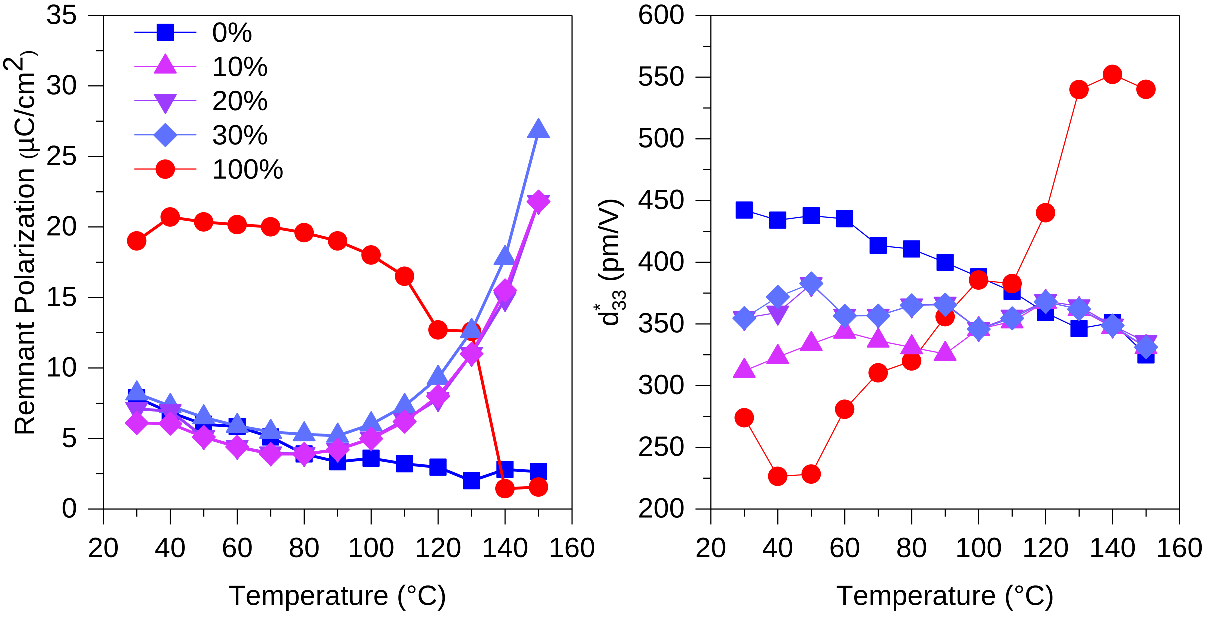

Figure 6.12: Remanent polarization and large signal piezoelectric coefficient of 2-2 BNT-BT-KNN/BNT-7BT composites as a function of temperature at different seed contents, from 0% (pure BNT-BT-KNN), to 100% (pure BNT-7BT)

As shown in Figure 6.12, the remanent polarization of the composites remains close to that of the pure matrix at temperatures between 30 °C and 100 °C and then increases at temperatures above 100 °C. At 130 °C, the depoling temperature of BNT-7BT, all of the composites have the same remanent polarization as the pure seed, and above that temperature their remanence exceeds that of both the pure matrix and seed. Once again, this behavior does not correspond to the temperature-dependent remanent polarization observed previously in 0-3 composites, in which it was shown that the remanent polarization reduces with temperature [169]. This difference is likely due to the conductivity observed in 2-2 composites.

The large drop in remanent polarization in the composites relative to the pure seed may in part be attributed to the presence of internal stresses. It was shown in Figure 5.12 that the matrix material had residual compressive stresses of approximately -100 MPa. It was further shown in Figure 5.24 that such compressive stresses can reduce the remanent polarization by up to 50%. On the other hand, the seed material experienced tensile stresses. Previous work in BNT-BKT ceramics have shown that tensile stresses in thick films resulted in a reduced remanent polarization [201]. It is, therefore, likely that the residual stresses in the 2-2 composites play a role in its ferroelectric response.

The d^*_{33} at 30 °C is highest in the pure matrix material, and this superiority continues up to 110 °C. A steady drop in the d^*_{33} can be observed with increasing temperature. However, the seed material shows a drop in d^*_{33} from 30 °C to 40 °C, remains stable at 50 °C and then begins to climb, reaching a maximum at 130 °C. It is clear that of the five compositions investigated, pure BNT-7BT has the highest d^*_{33} value at temperatures between 120 °C and 150 °C. It appears that the addition of BNT-7BT to BNT-BT-KNN as a 2-2 composite results in a temperature stable d_{33}^{*}, as evidenced by the small difference in d_{33}^{*} in the composites in the temperature range of 30 °C to 150 °C. The effect of seed content is also noticeable. The 10% composite shows the lowest d_{33}^{*} between 30 °C and 120 °C and decreases in value above 120 °C, from 312 pm/V to 300 pm/V at 130 °C. It drops 20 pm/V at 140 °C and 150 °C. The 20 and 30% composites have nearly the same d_{33}^{*} values of approximately 350 pm/V over the whole measured temperature range. This was not the case in 0-3 composites, measured by Groh *et al.*, which showed a range of 350 to 450 pm/V when measured at 4kV/mm, 500 mHz in the 20% and 30% composites [169]. As a result of the conductivity apparent in 2-2 composites, the electromechanical performance is less suitable for actuators than 0-3 composites.

6.3.3. Local Electromechanical Behavior of BNT-BT-KNN/BNT-7BT 2-2 Composites

Digital image correlation enables strain tracking of individual regions of the 2-2 composite. This technique was described in detail in the Experimental Methods chapter and was used in Chapter 5 to determine the transverse strain of the individual end members. The local strain in a 2-2 BNT-BT-KNN/BNT-7BT is depicted in Figure 6.13 under bipolar loading of 4 kV/mm. There is a clear interface between the seed and matrix regions in terms of the degree of strain in each region. In particular, a difference between the middle region and the top and bottom regions can be observed, after application of both a positive and negative field. A negative strain, indicating compression, can be observed in the matrix region, whereas a positive strain, indicating tension, can be observed in the seed region. These strain directions correspond to the directions of the stresses predicted from the difference in transverse strain of the pure end members, (see Figure 5.21). The center of the seed region has a strain of 0.2%, whereas the interface between the seed and matrix regions has a strain of 0.1%, with a small region where a gradient can be observed.

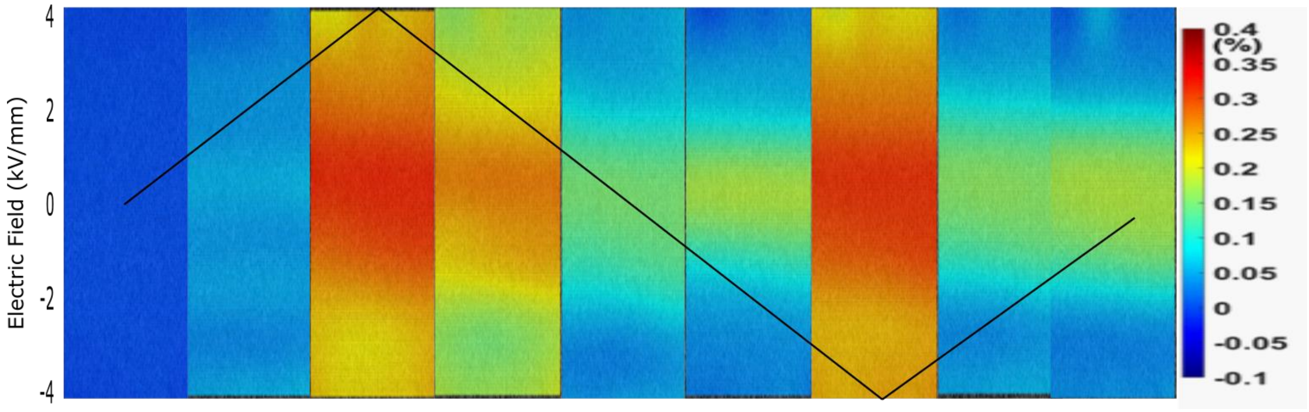

Figure 6.13: Strain maps of BNT-BT-KNN/BNT-7BT 2-2 composites under applied electric field of 4 kV/mm, 10 mHz, with the black line across the panel corresponding to the applied triangular waveform of the electric field, whose values in % strain are indicated on the axis to the right. Obtained through DIC

by Dr. Di Chen of the Karlsruhe Institute of Technology, with the entire sample of 2.5 mm height represented in each panel

An average of the strain for the regions of matrix and seed can be determined as a function of applied electric field using this technique, the result of which is shown in Figure 6.14. In addition, a larger remanence can be observed in the matrix layer of the composite than in the pure end member. A slight asymmetry in the maximum strain of the bottom matrix layer is apparent, which parallels the observations of asymmetry in the total strain of the 2-2 composites shown in Figure 6.5.

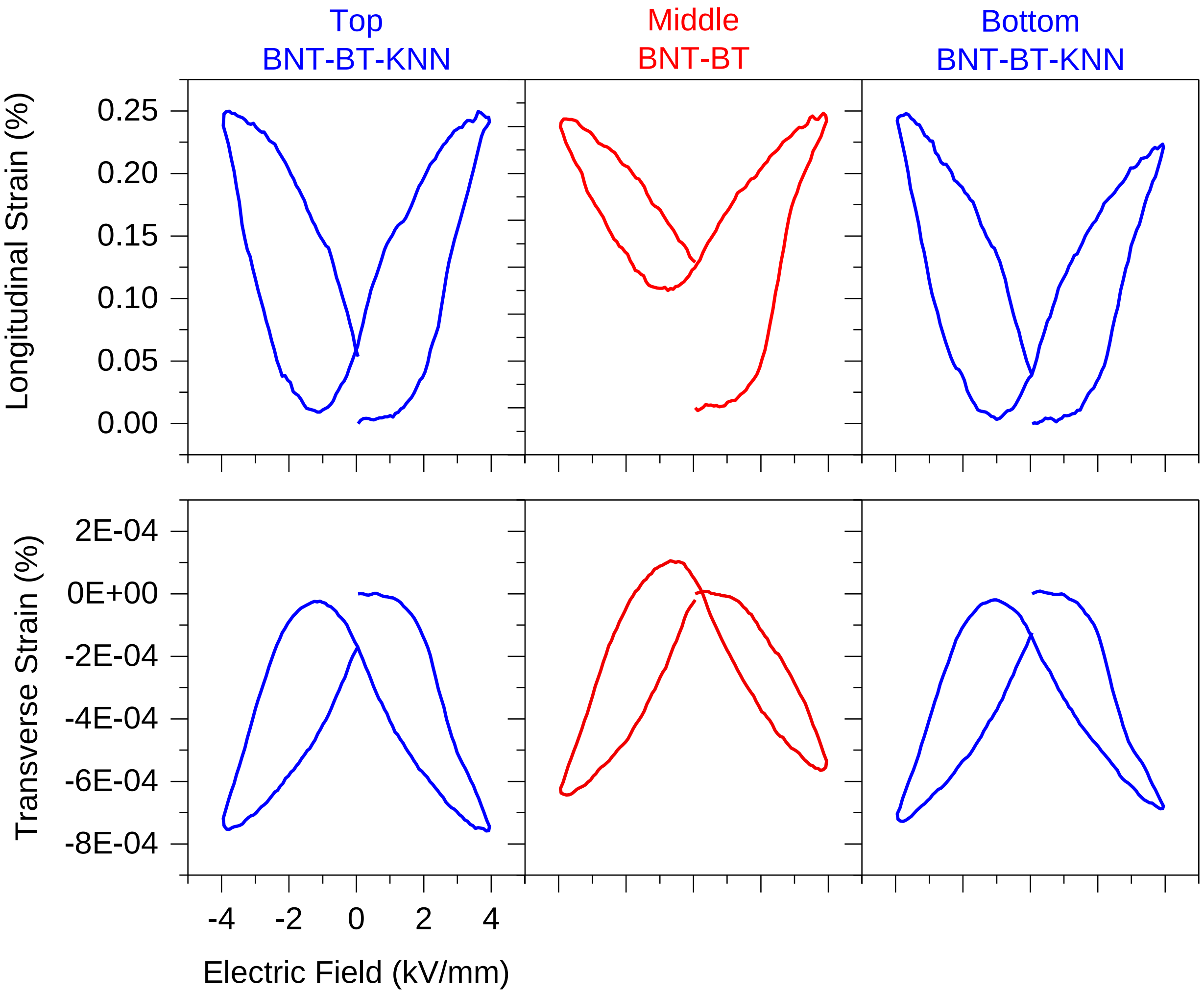

Figure 6.14: Longitudinal and transverse strain in 2-2 BNT-BT-KNN/BNT-7BT composite by region, 1st cycle under 4kV/mm, 10 mHz frequency bipolar loading

A comparison between the remanent strain of the free constituents and the components of the 2-2 composite is made in Table 10. The remanent strain of the matrix and seed regions reduces in the 2-2 composite relative to the freely sintered end members. This may be due to a clamping effect arising from the internal stresses in the 2-2 composites. The d_{33}^{*} value of the matrix layer increases slightly from 442 pm/V in the freely sintered state to 468 pm/V in the composite.

On the other hand, the d_{33}^{*} value of BNT-7BT decreases in the composite structure. As shown in Figure 5.21, and Figure 5.12 during application of an electric field, and as a consequence of differences in CTE, the seed material is in tension, while the matrix material is in compression. It appears that such stresses result in an enhanced strain response in the matrix component, and a reduced strain response in the seed component. As previously discussed, stresses perpendicular to the direction of applied electric field result in domains oriented parallel to the field, thereby enhancing the bulk strain response of the matrix layer. The tensile stresses in the seed material, on the other hand, reduce its strain response. Previous work measuring the influence of tensile stress on the polarization response of PZT showed that such stresses result in a depolarization of the ceramic [272]. A similar mechanism, which prevents complete polarization of the seed material due to tensile stresses, may be the source of the reduced strain response in the seed layer.

Table 10: Strain Response of components of 2-2 composite determined by DIC and compared to pure constituents at 10 mHz, 4 kV/mm

	ε_r (%)	d_{33}^{*} (pm/V)
BNT-BT-KNN (freely sintered)	*0.07*	*442*
BNT-6BT-3KNN (2-2 layer)	*0.06 (top)* *0.04 (bottom)*	*468*
BNT-7BT (freely sintered)	*0.22*	*293*
BNT-7BT (2-2 layer)	*0.15*	*50*

6.3.4. Large Signal Ferroelectric and Piezoelectric Response of BNKT-6BA/BNT-7BT 0-3 and 2-2 Composites

As was mentioned in the prior discussion, the BNKT-BA/BNT-7BT system serves as a model of an ER/NR composite, used to facilitate investigations of chemical interaction. In order to establish its utility as an experimental model, a demonstration of enhanced electromechanical properties was undertaken through measurements of its strain and polarization response to large signal electrical fields.

The presented measurements were performed with a maximum applied field of 4kV/mm and a frequency of 1 Hz (Figure 6.15). At this field, the polarization response of the 0-3 and 2-2 structures overlap almost perfectly, indicating a very similar bulk electrical response. The maximum strain of the composite exceeds that of the matrix. At 50% the 0-3 composite has a higher strain than the 2-2 composite, at 20% and 40% seed the strain response is identical and at 10% and 30% the strain response of the 2-2 composite is higher than the 0-3 composite. An overlap in the polarization loops of the 0-3 and 2-2 composites is apparent.

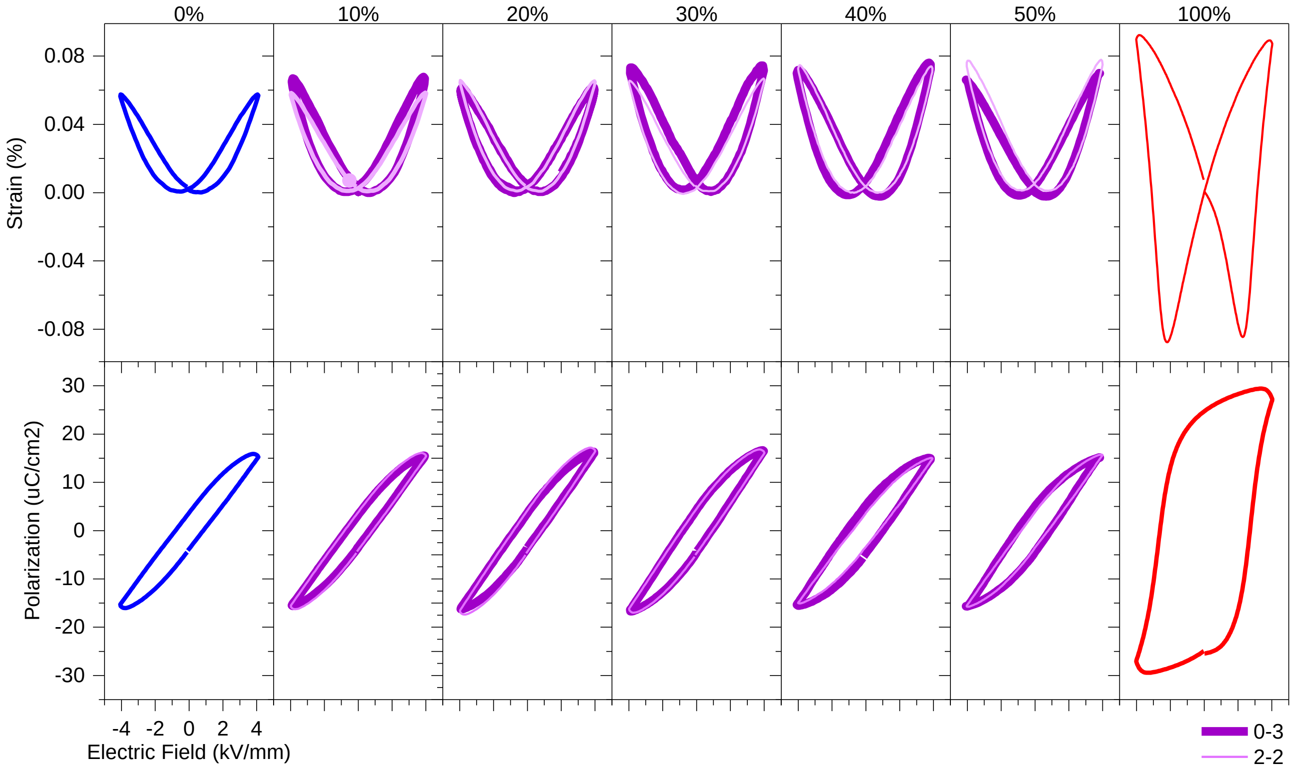

Figure 6.15: BNKT-6BA/BNT-7BT composites large signal polarization and strain loops at 4kV/mm, 1 Hz

The polarization and strain loops of BNKT-6BA/BNT-7BT composites to a maximum applied field of 6 kV/mm at 1 Hz are shown in Figure 6.16 for 2-2 and 0-3 composites as a function of seed content. The matrix (BNKT-6BA) and the seed material (BNT-7BT) are also shown, in blue and red, respectively. It can be clearly seen that the 2-2 and 0-3 composites show a nearly constant maximum polarization of 42 μ C/cm^2 as a function of seed content up until 50%. The 30 %, 40% and 50% composites of both 0-3 and 2-2 structures have a higher maximum strain than the starting matrix and seed materials. The 10 and 20% composites show a very similar strain and polarization response for both the 0-3 and 2-2 structure. At higher seed percentages, the 2-2 structure has a slightly higher strain response of approximately 0.02% relative to the 0-3 structure.

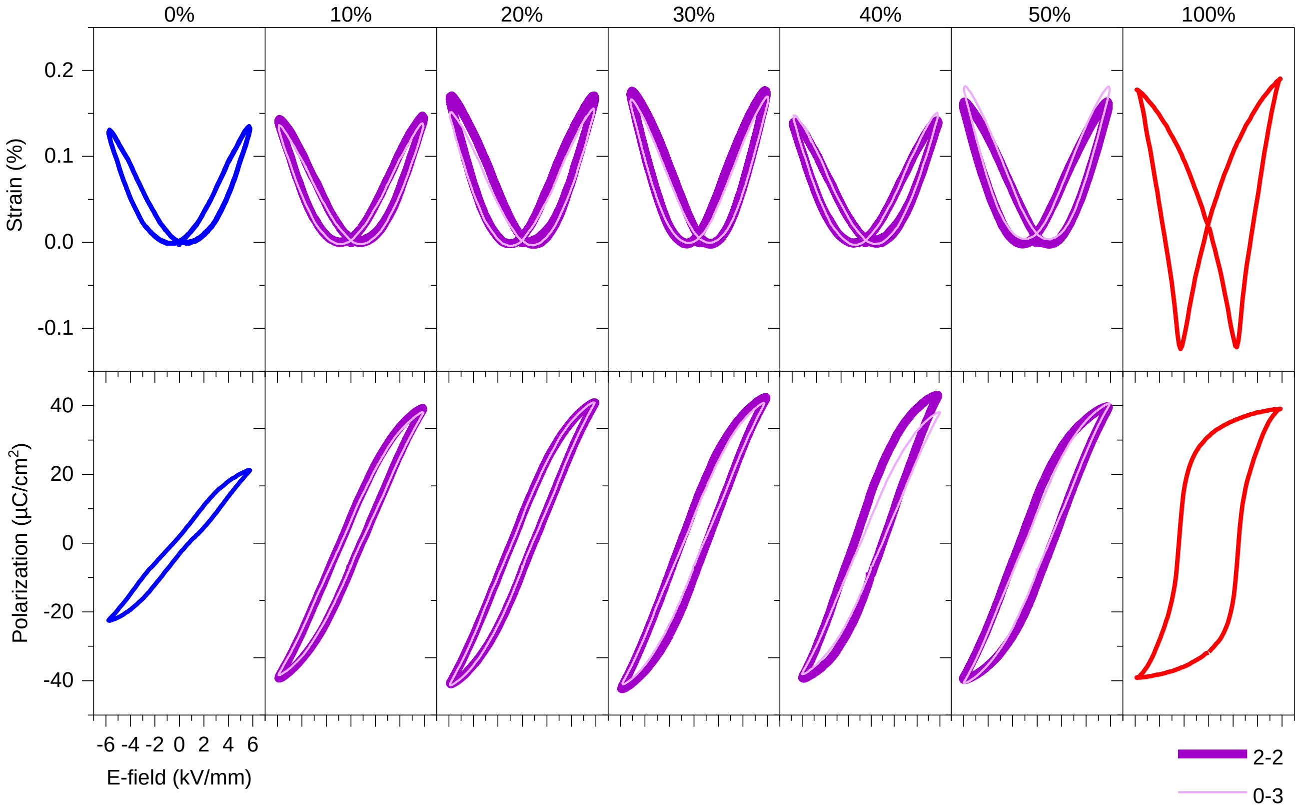

Figure 6.16: BNKT-6BA/BNT-7BT composites large signal strain and polarization loops at 6kV/mm, 1 Hz

Another parameter of note is the negative strain, or more specifically, lack thereof in these composites. The negative strain, therefore, does not follow a rule of mixtures upon addition of the BNT-7BT seed. The same is true of the remanent strain, which remains below 0.01% for all composites. The maximum polarization does not increase with increasing seed content either, as has been previously observed in BNT-BT-KNN/BNT-7BT composites [1].

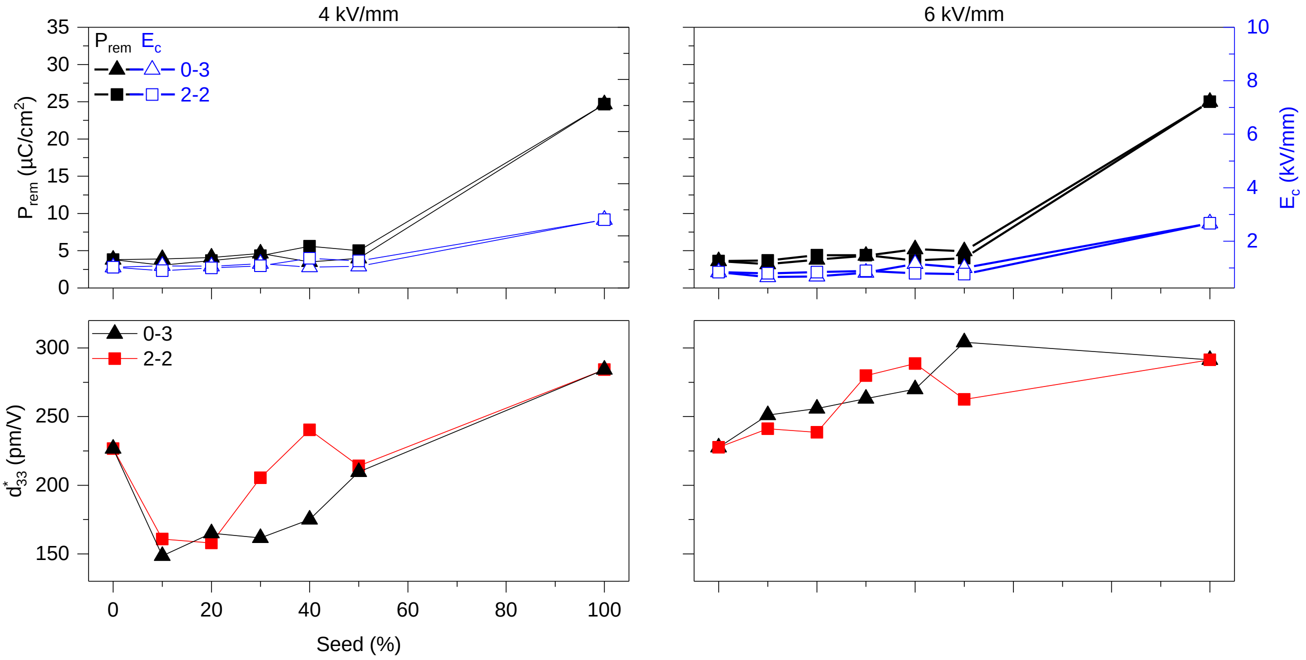

Figure 6.17: d^*_{33}, remanent polarization and coercive field as a function of seed content and composition, at 4 and 6 kV/mm maximum electric field for BNKT-6BA/BNT-7BT composites

In Figure 6.17, an analysis of the characteristic parameters of the large signal response are compared as a function of seed content, for both 4 kV/mm and 6 kV/mm. For seed contents of 10 and 20%, the d^*_{33} decreases in both the 0-3 and 2-2 composites. With 30 and 40% seed content, the 2-2 composite shows a much larger d^*_{33} than the 0-3 composites, and the d^*_{33} overlaps for the 0-3 and 2-2 composites at 50% seed content. Under fields of 6 kV/mm, there is an enhanced d^*_{33} relative to the pure matrix material for all compositions and structures. At seed contents of 10, 20 and 50%, the 0-3 composite has higher d^*_{33} values, whereas at 30 and 40% seed, the d^*_{33} value is highest in the 2-2 composites. It should be noted that the maximum strain of the pure matrix material is lower than 0.2% that previously reported by Lee *et al*. [7]. This is most likely due to a shorter sintering time of 2 h as opposed to 4 h, which in this study was tailored to optimize co-sintering with BNT-7BT. While all ceramics produced in this work had a density of at least 95%, a reduced sintering time would also affect the chemical homogeneity within grains, as well as grain size. Interestingly, a simple rule of mixtures approach would suggest that there should be little enhancement in the unipolar strain of the composite structure due to similar maximum strain values of the end members. In addition, the stability of the d^*_{33} values in the 2-2 composites with varying seed content also indicates that the enhancement observed is not necessarily due to the presence of the polar seed, but an interaction between the seed and matrix materials that is identical in all four compositions, independent of seed content. Figure 4.14 showed that the diffusivity of Al is stable in the 30, 40 and 50% 2-2 composites, paralleling the uniform d^*_{33} for these three compositions. It is possible that this observed plateau in the diffusivity indicates a saturation above approximately 30% seed. Therefore, chemical diffusivity may play a significant role in the electromechanical behavior of the 2-2 composites, in addition to the exact value of the seed content.

The remanent polarization remains stable no matter the seed content, and significant increase can be observed from 50 to 100% seed. This is indicative of an ergodic nature in the composites, be they 0-3 or 2-2 in structure, and aligns with the negligible negative strain observed in this system as well. The coercive field does not vary with increasing applied field, and the value remains independent from seed content. 2-2 and 0-3 composites have nearly identical coercive fields, which is expected from the strong overlap of the polarization loops shown in Figure 6.15 and Figure 6.16. As shown in Figure 6.17, the coercive field is not strongly affected by the composite structure. d_{33}^{*} as a function of seed varies greatly between the 4 and 6 kV/mm responses. An enhancement of this value is only observed at 4 kV/mm in the 40% seed. At 6 kV/mm, however, an enhancement can be observed relative to the pure matrix for all composites. This is likely because measurements performed at 4 kV/mm did not reach the poling field of the system, limiting the strain response to piezoelectric strain and electrostriction, whereas at 6 kV/mm, the field is high enough to induce a ferroelectric state followed by domain switching, thereby increasing the contribution to the total strain from purely piezoelectric to the additional strains of domain alignment and switching.

The EDS analysis shown in Chapter 4 may help to explain the large and small signal electromechanical response. In the 2-2 composite, the millimeter length scale of diffusion of Al was shown to result in the formation of at least two new solid solutions in the matrix: (i) an Al-depleted matrix phase (BNKT-BA), which is known to have high d_{33} values [2], and (ii) a Ba-doped BNKT-BA phase. BNKT-1.5BA and BNKT have been used as seed material in composite systems, where BNKT-6BA is the matrix and is shown to significantly reduce the poling field and increase the strain response [150]. Such a system can be described as a functionally graded ceramic [273], which has been observed by Zhang *et al.* both in lead-based [274] and lead-free [275] laminate piezoceramics. However, in the 0-3 composites the diffusion path is much shorter, due to the seed particle size. Therefore the final chemical composition is expected to have a more homogeneous distribution of Al throughout the sample, differing from that of the 2-2 composite.

In the heterogeneous case of 2-2 composites, Al depletion in the matrix phase would result in the formation of (100-x)BNKT-xBA, where $x < 3$ mol% results in a non-ergodic relaxor with high remanent polarization [110]. This would imply the formation of new polar constituents that behave like a new “seed,” inducing polarization in the surrounding ergodic matrix. BNKT-0.05BA as a seed in a BNKT-BA matrix was previously described by Lee *et al*. [7] and Jeong *et al*. [150]. Differing from the aforementioned works, in the present study a seed with $BaTiO_3$ was used and the presence of Ba was observed in the matrix layer, which was not in the original matrix member.

Additional evidence of the influence of Al^{3+} doping on BNT-BT can be found in the work of Chen *et al.* [276], in which an increase in ferroelectric behavior, based on higher negative strain and remanent polarization, relative to pure BNT-6BT, was observed. They argue that this is due to an increase in oxygen vacancies that contribute to the formation of defects that act as pinning centers, resulting in a decrease in domain wall motion. Therefore, an Al-rich BNT-BT seed phase may result in a higher remanent polarization than a pure BNT-BT middle seed layer alone. However, recent work by Bai *et al*. investigating the addition of BA into BNT-BT has shown that with 2 mol% BA, the remanent strain under applied field is almost zero, with a maximum strain of 0.35% [277]. Above and below 2% mol BA, the maximum strain falls to values closer to 0.2%. Interestingly, the composition with 2 mol% BA, found to have a maximum unipolar strain by Bai *et al*., approximately corresponds to the amount found in the interdiffusion zone between the seed and matrix in the present study.

The presence of Ba in the interface region was also demonstrated and, therefore, the effect of Ba on the original matrix material, BNKT-6BA, must also be examined. Studies on a BNKT-BA material with 6 at% Ba have been performed by Fu *et al*. [278]. In a composition with 6 at% Ba and <4 at% Al, high remanence was observed. This composition is close to that observed at the interdiffusion region in the present work, thereby implying that the interdiffusion resulting from the 2-2 composite structure results in an expanded polar phase in the 2-2 composite, comprised of the BNT-7BT seed and Ba-doped BNKT-BA. In addition, the influence of compressive stress on the electromechanical response of BNT-BT was shown to reduce the remanent polarization. Therefore the presence of compressive stresses in this layer of the 2-2 composite will also likely drive down the total remanent polarization of the composite.

6.3.5. Influence of Sintering Time on Bulk Electromechanical Response in BNKT-BA/BNT-7BT 2-2 composites

The influence of sintering time on the electromechanical properties was investigated, based on evidence of increased interdiffusion as a consequence of longer sintering times, as shown in Figure 4.22. It is therefore hypothesized that increased interdiffusion contributes to the electromechanical strain, resulting in an increased maximum strain in response to an applied electric field. The results of this investigation are shown in Figure 6.18. The maximum strain clearly increases with increasing sintering time from 0.032% at 2 h to 0.039% at 6 h and 0.052% at 24 h.

However, this is accompanied by an increase in negative strain, reducing the total usable strain for actuator applications. The coercive field does not have a linear relationship with sintering time, as it increases from 2.13 kV/mm when sintered for 2 h to 2.26 when sintered for 6 h, followed by a drop to 2.17 when sintered for 12 h. The 24 h sintered sample showed a large increase in the coercive field as compared to the 2 h sample, to 2.4 kV/mm. The maximum and remanent polarization follow the same trend as the strain, showing an increase in value with increasing sintering time.

As shown in Figure 4.22, increased sintering time resulted in increased interdiffusion of Al and K from the matrix to the seed, and of Ba from the seed to the matrix. At 24 h, the chemical composition across the 2-2 composites was essentially homogeneous. For the matrix material, a K content below 15% has been shown to have a higher remanent and maximum polarization than the same material with K contents of 20-25% [109]. Therefore, diffusion of K out of the matrix and into the seed would result in a reduced K content in the matrix and a resultant increase in the polarization response as well as a reduced ergodicity of this response. The strain response would also be similarly affected by the loss of K, as the same work showed that the negative strain of BNKT-BA with 15 and 20% K has a negative strain between 0.1 and 0.15%, whereas higher K contents of 20 and 25% result in a negative strain of 0.05 and 0%, respectively. Therefore diffusion of K out of the matrix is expected to also increase the negative strain.

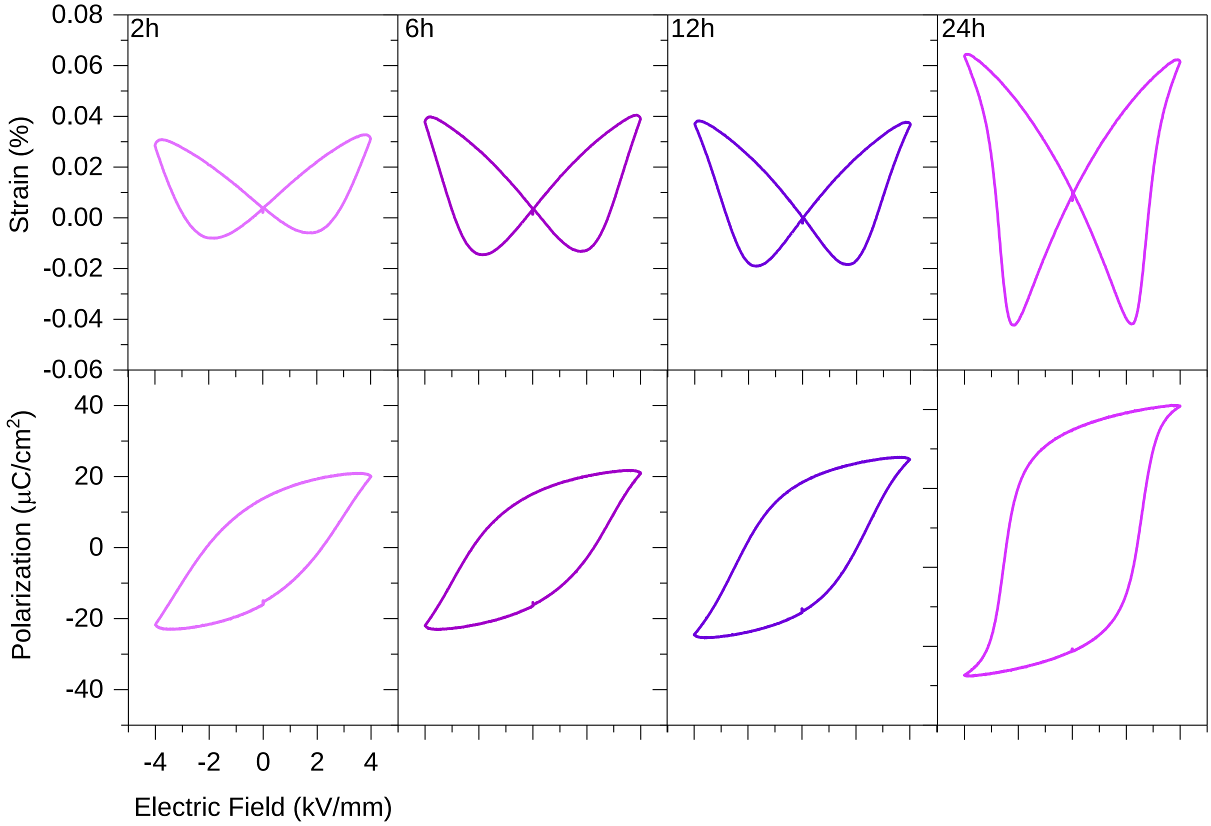

Figure 6.18: Strain and polarization loops in response to applied electric field of 4 kV/mm, 50 mHz for 2-2 BNKT-6BA/BNT-7BT composite of 40% BNT-7BT content sintered for 2 h, 6 h, 12 h, and 24 h

In the work of Ullah *et al.* the maximum strain increased with increasing K content, because of the increased ergodicity of the material. In this work, a lower K content in the matrix did not reduce the maximum strain. Instead, an increase in the maximum strain is shown in Figure 6.19 in the 2-2 composite. This increase in strain may be due to the changed chemical composition of the seed layer, as well as the influence of Ba diffusing into the matrix layer, which was not investigated in Ullah *et al.*'s work.

There is also a reduced concentration of Al in the matrix layer with increasing sintering time. The influence of Al content on the electromechanical response of BNKT-BA was investigated by Ullah et al. [108]. Increasing Al content from 0 to 7.5% resulted in a reduced coercive field, remanent polarization and maximum polarization. Therefore, a reduced Al content in the matrix phase as a consequence of diffusion into the seed would increase the maximum polarization and remanent polarization, as can be observed in Figure 6.19. The negative and maximum strain were shown to also be strongly dependent on Al content, with a complete disappearance of the former at an Al content of 5%, as compared to a negative strain of 0.15% with an Al content of 2.5%. It can therefore be expected that a reduced Al content in the matrix would result in an increase of the negative strain, corresponding to the behavior shown in Figure 6.19 of an increasing negative strain with increasing sintering time.

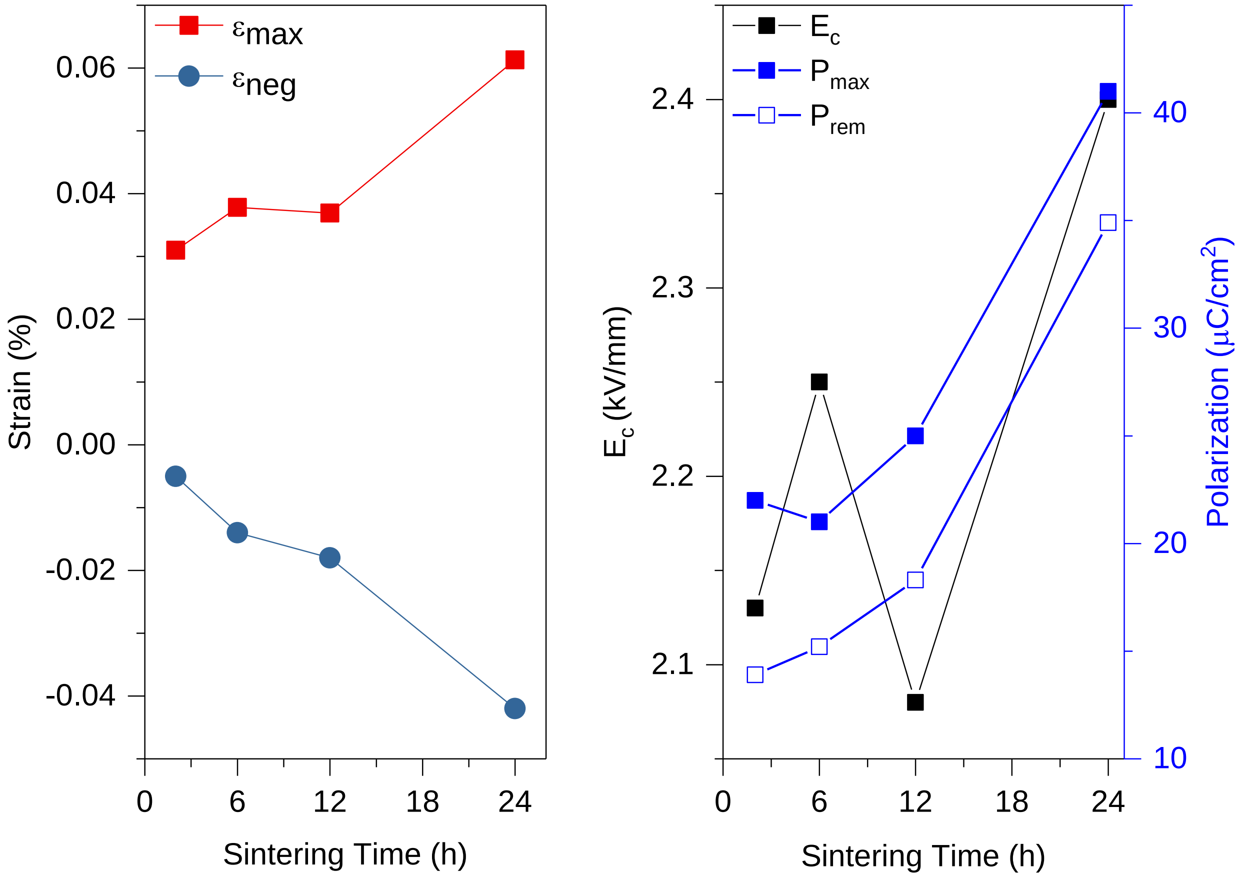

Figure 6.19: Effect of sintering time on strain and polarization in BNKT-BA/BNT-7BT 2-2 composite of 40% BNT-7BT

A similar influence of sintering time on composites was observed by Lee *et al.* in the 0-3 composite system of BNKT-6BA/BNT [149]. In that work, it was shown that Al and K diffuse into the BNT phase. The maximum polarization increased with increasing sintering time, but the remanent polarization reduced from 4h sintering to 36 h sintering, and an increase was only observed at 56 h sintering. The strain response reduced slightly from 4 to 12 h, and increased at 36 h.

For these three sintering times the strain response could be described as ergodic, however at 48h sintering time, the strain response had a large remanence in the bipolar loop and a very narrow hysteresis and maximum strain in the unipolar loop. The enhancement observed up to 36 h was attributed to the larger grain size of the BNT seed. However, an increased sintering time resulted in greater interdiffusion of Al and K into the BNT seed, reducing its ferroelectric behavior.

6.4. Large Signal Ferroelastic Stress-Strain Behavior in Lead-free Composites

A stress-induced transition to a ferroelastic state analogous to the electric field-induced transition to a ferroelectric state has been observed both in lead-based [279] and lead-free [197] relaxors. It is also known to effect the electromechanical response of ferroelectrics [280]–[283]. Therefore, the ferroelastic behavior of BNT-6BT-3KNN, BNT-7BT and 0-3 composites thereof were examined at uniaxial stresses up to -500 MPa. All measurements shown in this section are virgin curves. 2-2 composites were not included in this study due the high likelihood of mechanical failure in this composite structure as a result of existing internal stresses. A correlation between ferroelastic and ferroelectric behavior was expected, due to the ability of compressive stresses to induce a ferroelectric state through domain formation in BNT-6BT as observed by Schader *et al.* [76]. Such a correlation between the ferroelastic and ferroelectric behavior has also been observed in lead-based systems such as PZT [284].

Each composition will first be discussed independently in terms of the influence of temperature on its stress-strain curve. This will be followed by a comparison of characteristic parameters, *i.e.,* maximum strain, hysteresis, remanent strain and back-switching, between all compositions, including pure constituents. Room temperature measurements of the pure matrix and seed components are shown in Figure 6.20. The remanent strain of BNT-7BT is much higher than that of BNT-6BT-3KNN, parallel to the remanence in response to an applied electric field. The maximum strain achieved by compressing BNT-7BT is -0.78% as compared to -0.46% for BNT-6BT-3KNN, showing a much higher strain response in the seed. This may be due to the fact that -500 MPa is below the coercive stress of BNT-6BT-3KNN, as evidenced by the absence of an inflection point in its loading curve, whereas the coercive stress of BNT-7BT is approximately -320 MPa at room temperature. Below the coercive stress, generally termed the onset stress [76], [197], [285], [286], the alignment of PNRs by an applied field is initiated, which contributes to the total strain in addition to the linear elastic deformation, thereby resulting in a nonlinear stress-strain curve as can be observed in Figure 6.20.

6.4.1. Ferroelastic Behavior of Pure Constituents BNT-6BT-3KNN and BNT-7BT

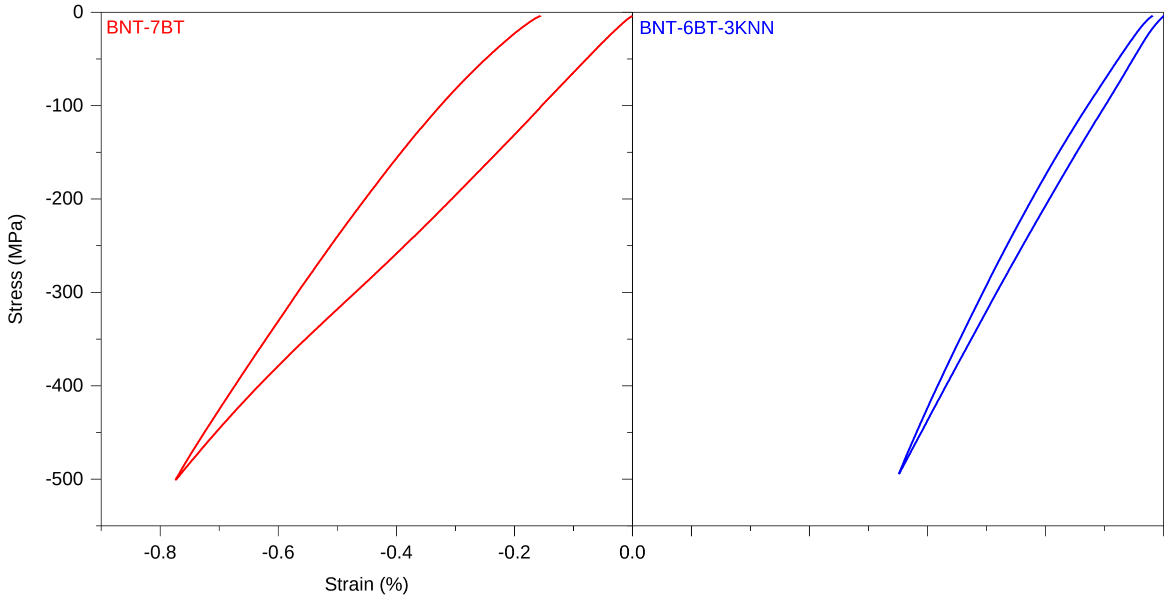

Figure 6.20: Ferroelastic behavior of BNT-7BT and BNT-6BT-3KNN at room temperature, -500 MPa maximum uniaxial stress, 5 MPa/s loading rate, virgin loops, one cycle

The temperature-dependent behavior of the matrix BNT-6BT-3KNN and seed BNT-7BT, as well as 0-3 composites thereof, were evaluated for ferroelastic behavior in a temperature range of -40 °C and 130 °C, corresponding to the operating temperatures of piezoceramic actuators in automotive applications [287]. The addition of 3KNN to BNT-BT appears to push the material towards an ergodic phase chemically.

The ferroelastic behavior of BNT-7BT as a function of temperature is shown in Figure 6.21. With increasing temperature, the remanent strain reduces, resulting in a fully closed, double-loop like, hysteresis at 110 °C. At 130 °C, no hysteresis is visible. This temperature corresponds to the depoling temperature at which the electrical response is ergodic, shown in Figure 6.8. At 130 °C, the maximum strain drops to -0.5% from the room temperature strain of -0.9 %. A similar reduction in maximum strain with temperature was observed in BNT-6BT by Webber *et al.* [197] and was attributed to the reduction of spontaneous strain in the unit cell with increasing temperature. At temperatures below room temperature, a relatively high coercive field can be observed from the inflection point of the stress-strain response. The maximum strain increases with increasing temperature from -40 °C to 130 °C. However, structural investigations of BNT-BT at low temperature by Ma *et al.* have not revealed any changes in crystal structure [288]. Therefore, this difference cannot be attribute to a temperature-dependent phase transition. The lower strain may result from the lower contribution of mechanically induced domain formation, *i.e.* a mechanically induced RE-FE transition. Because domain formation is more difficult at low temperatures, and the coercive stress is higher, stress-induced domain formation and switching contributes less to the total strain of the sample at low temperatures [289].

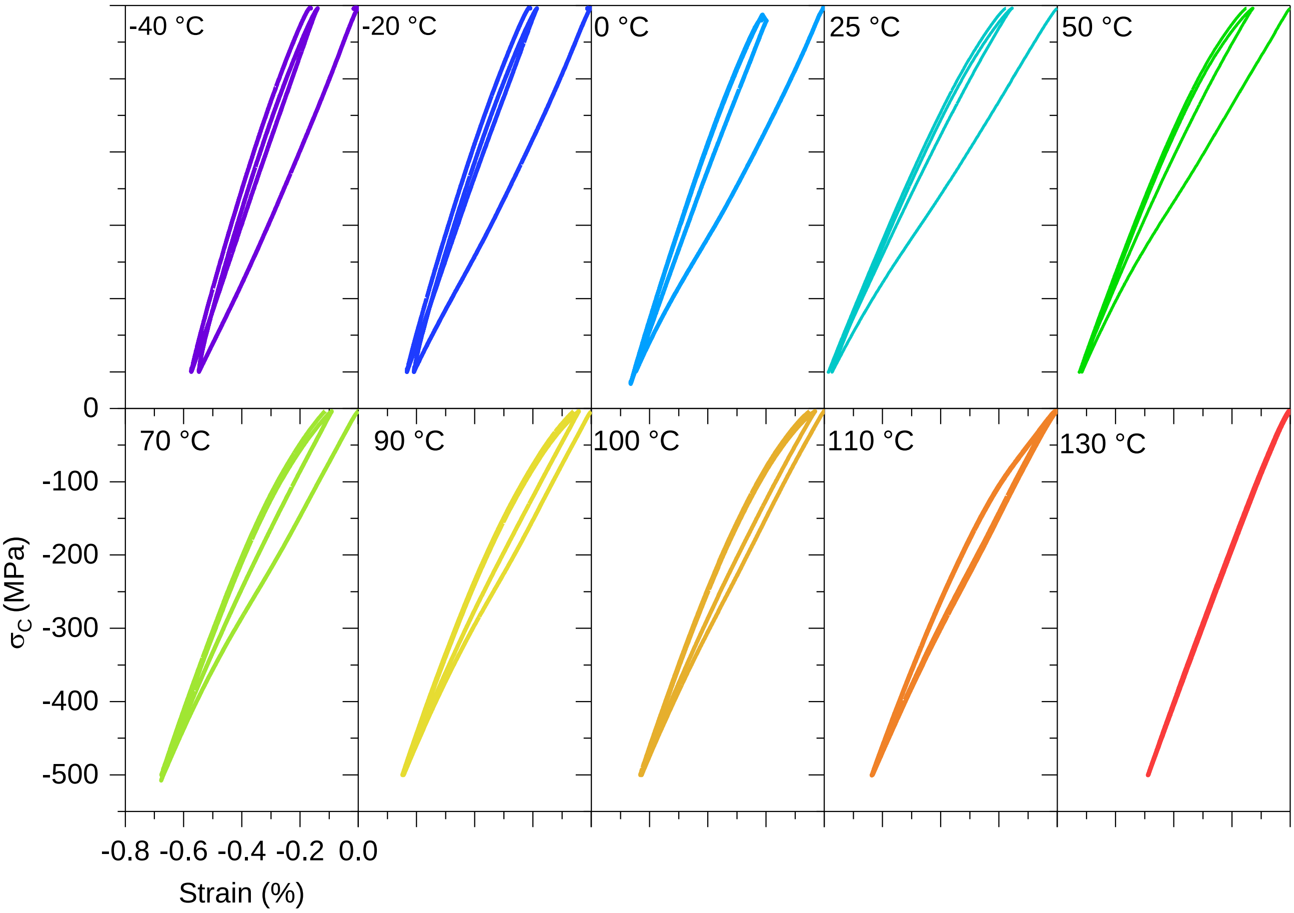

Figure 6.21: Ferroelastic behavior of BNT-7BT from -40 °C to 130 °C, under a compressive stress of 500 MPa applied at 5 MPa/S, 1st and 2nd cycle

As shown in Figure 6.22, in BNT-6BT-3KNN, at low temperatures, a remanence could be observed, as well as a hysteresis of the loops. With increasing temperature, the remanence is reduced, completely disappearing at 50 °C. The hysteresis also notably reduced with increasing temperature, and a complete absence of hysteresis arises at 50 °C. Increasing the temperature to 50, 70 and 90 °C resulted in an increased maximum strain of approximately 0.5%, as well as a decrease in the area of the hysteresis and an apparent increase in the linearity of the stress-strain curve, indicating a reduced contribution of domain switching to the total strain as the temperature increases. The corresponding reduction in hysteresis with temperature further corroborates the source of reduced linearity as a reduced degree of switching. Although the transition to the ferroelastic state is incomplete, some domain formation occurs, which in BNT-7BT as a nonergodic relaxor, is irreversible. The long-range order induced by mechanical stress can therefore be observed as a remanent strain in BNT-7BT, whereas in BNT-BT-KNN, removal of the field results in a reversible return to the original sample dimensions; therefore, no remanent strain is observed. In further contrast to BNT-7BT, very little back-switching in the pure matrix material occurs.

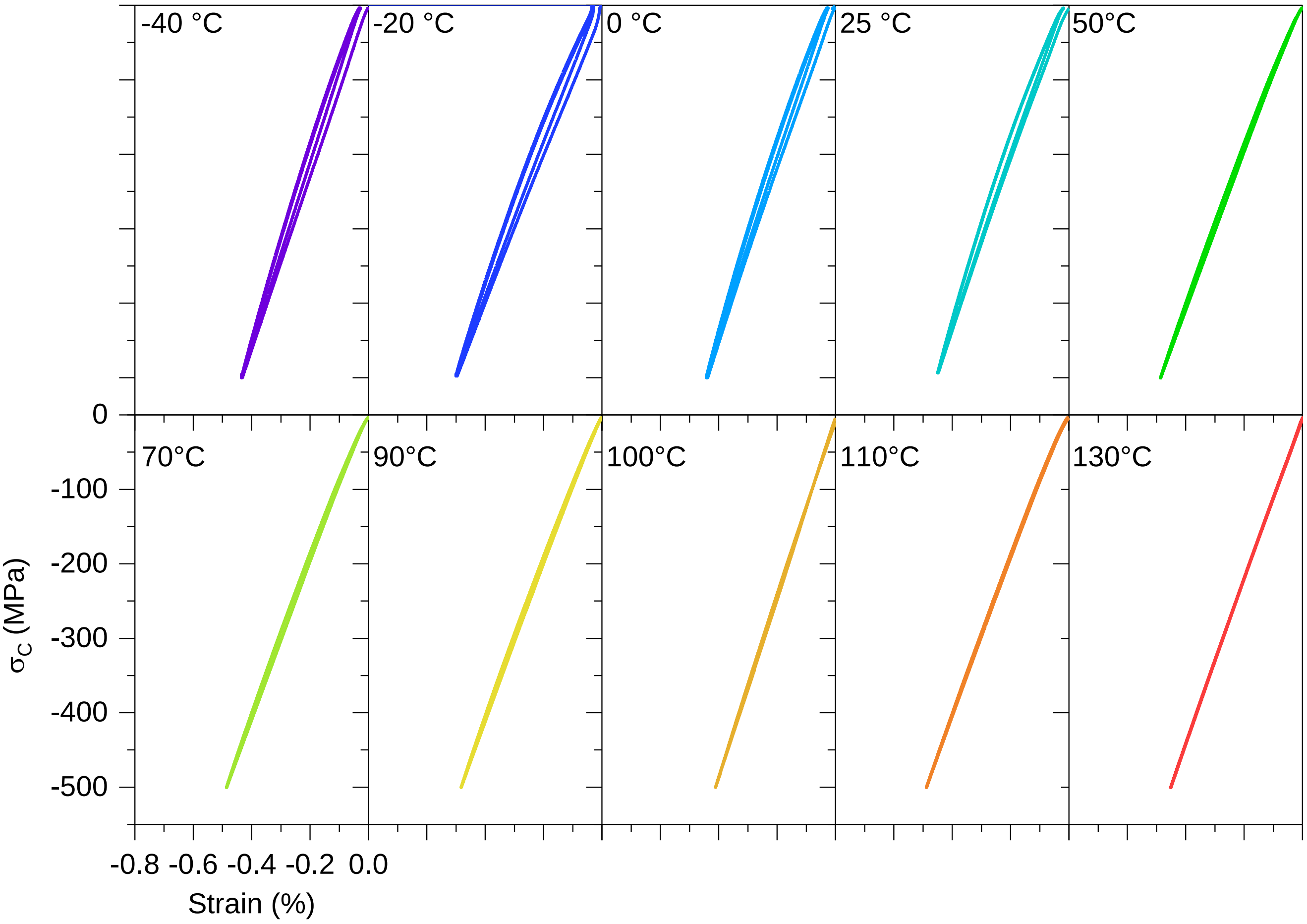

Figure 6.22: Ferroelastic behavior of BNT-6BT-3KNN from -40 °C to 130 °C, under a compressive stress of 500 MPa applied at 5 MPa/S, 1st and 2nd cycle

6.4.2. Ferroelastic Behavior of 0-3 BNT-BT-KNN/BNT-7BT Composites

Having discussed the temperature-dependent ferroelastic response of the pure constituents, an examination of the same phenomenon in 0-3 composites is now warranted.

Figure 6.23 depicts the stress-strain response of the 0-3 BNT-6BT-3KNN/BNT-7BT composites over a temperature range of -40 °C to 110 °C. The maximum strain increases with increasing temperature for all composites in the temperature range of -40 to 50 °C, above which it reduces with increasing temperature. For all composites, the hysteresis decreases with increasing temperature, and by 110 °C there is a complete lack of hysteresis. In the 10% composite, at low temperature a pronounced remanence and hysteresis can be observed, both of which decrease with increasing temperature. Remanent strain can only be observed at -40 and -20 °C, above which it completely disappears. The lack of remanence indicates a reduced long-range order with increasing temperature, whereas the disappearance of hysteresis implies that the

PNRs are no longer aligned by an external field due to higher mobility with at higher temperatures. Not surprisingly, similar to the pure matrix material, a coercive stress, *i.e.*, an inflection point of the stress-strain curve, is not attained at room temperature. However, a clear nonlinearity at 25 °C can be observed in all composites, which becomes more pronounced at 50 °C. Above 50 °C, the strain response becomes increasingly linear in all composites. An increase in back-switching can be observed at 50 °C, as evidenced by the inflection during removal of the applied field. This phenomenon becomes less apparent at temperatures above 50 °C.

Investigations of temperature-dependent ferroelectric properties in 0-3 composites by Groh et al. showed a nonlinear drop in negative and remanent strain of 30% and 50% composites from 50 °C to 70 °C [169]. This nonlinearity does not occur in the remanent polarization. No nonlinearities were apparent in 0-3 composites in the dielectric response [147]. In the pure matrix material, a reduction of the hysteresis occurs at 50 °C. Zhang *et al.* observed a freezing temperature of BNT-BT-3KNN at 48 °C [98]. At this temperature, a transition from a non-ergodic to an ergodic response occurs, i.e., the long-range order of PNRs is disrupted by thermal destabilization. The nonlinearities observed at 50 °C may be associated with this transition.

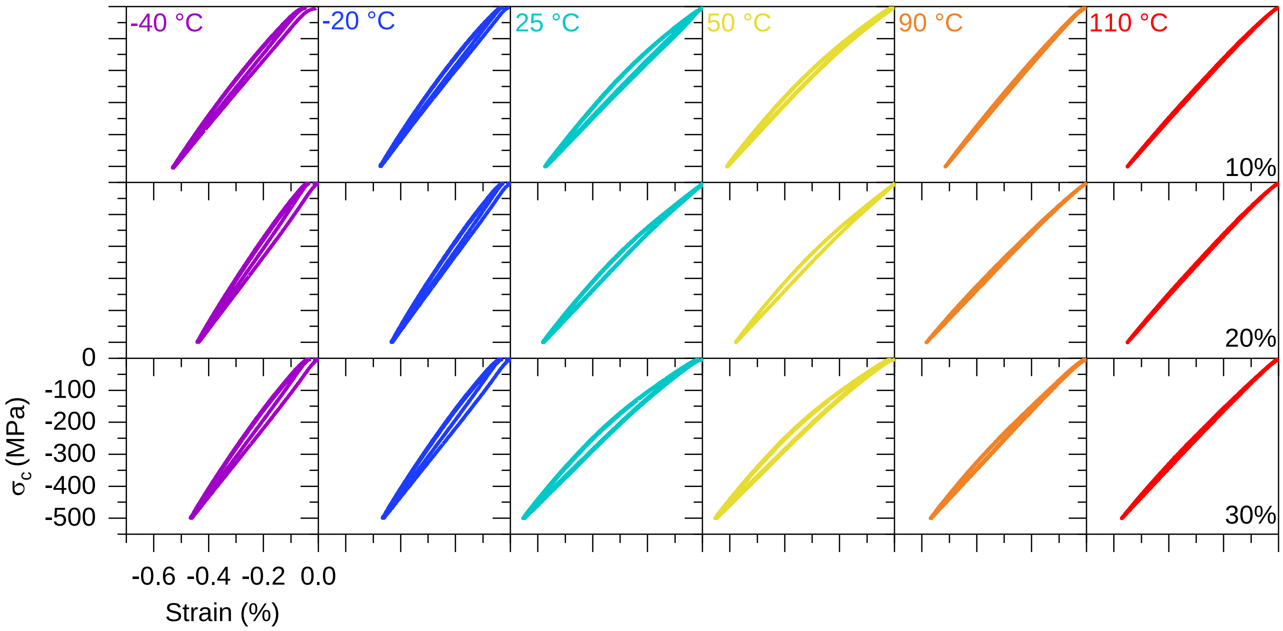

Figure 6.23: Ferroelastic response of BNT-6BT-3KNN/BNT-7BT 0-3 composites of 10, 20 and 30% seed content, as a function of temperature

Measurements were also performed at -150 °C to test the limits of the ferroelastic stress-strain response at low temperatures, the results of which are depicted in Figure 6.24. The maximum strain decreased to approximately -0.4% for the 0 and 10% compositions. The addition of 20% seed resulted in an enhanced strain response of -0.45%. An increase in back-switching with temperature can be seen in this composition as well. It has been previously predicted that an ergodic - nonergodic transition would occur in BNT-6BT-3KNN at low temperatures. These measurements of ferroelastic behavior do not provide evidence of such a transition, as the remanent strain remains very low even at low temperatures. This may be because the coercive stress of BNT-BT-KNN is not attained, as it is above the fracture stress of this material. Although a change in crystal structure from pseudocubic to rhombohedral was observed through *in-situ* XRD measurements at -290 MPa (see Figure 5.16), a transition from relaxor to ferroelastic behavior has not been observed at this pressure. This corresponds to investigations where the addition of KNN to BNT-7BT increased the coercive field [173]. The stress-strain curve of pure BNT-7BT narrows significantly at -150 °C relative to its response at -40 °C shown in Figure 6.21. It is likely that the reduced hysteresis and remanent strain is the result of an increased coercive field at this low temperature. The maximum strain is highest in the 20 and 30% composites and exceeds that of both the pure matrix and seed by 0.04%.

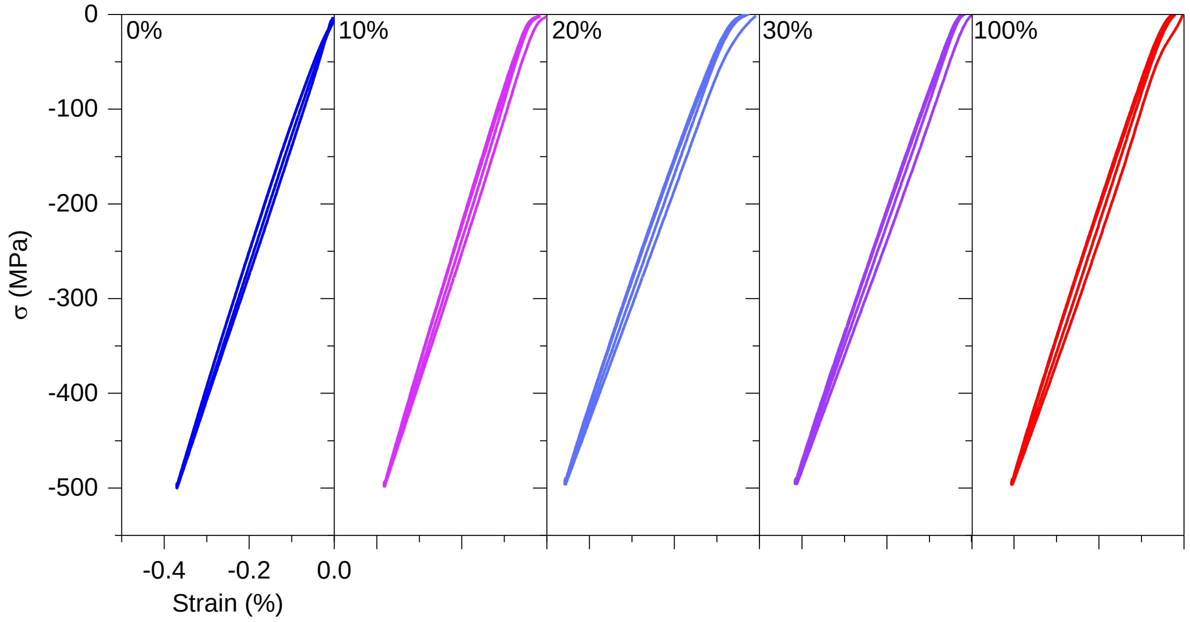

Figure 6.24: Ferroelastic Response of BNT-6BT-3KNN/BNT-7BT 0-3 composites with different seed contents at -150 °C under an applied mechanical stress of -500 MPa, 1st and 2nd loop

A comparison of the characteristic parameters of ferroelastic stress-strain curves of all compositions of BNT-6BT-3KNN/BNT-7BT 0-3 composites is shown inFigure 6.23. Maximum strain, remanent strain, hysteresis, and back-switching are compared for all compositions over the temperature range of -150 °C to 130 °C. Just as in the ferroelectric case, an increase in the maximum strain can be observed in the composites relative to the pure matrix material at all temperatures other than -20 °C. The discrepancy at this temperature may be due to measurement error and resultant data scattering. At room temperature, the 30% composite has the same maximum strain as the pure seed, despite the fact that its remanent strain is very low (below -0.05%). At 130 °C, the maximum strain of all composites exceeds that of BNT-7BT. The remanent strain of the composites does not change significantly with seed content at room temperature, never exceeding 0.05%, despite the fact that the remanence of the pure seed material is significantly higher, *i.e.*, 0.12% at room temperature.

The remanent strain of the seed reduces below and above 0 °C. At room temperature, the remanent strain of the composites with 10 and 20% seed falls below that of the pure matrix, a surprising result considering the high remanence of the seed at that temperature. The lower remanence observed in these composites does not correspond to the remanent strain as a function of composition in response to applied electric fields, which was discussed in 6.3.1. It is possible that a reduced remanent strain may be caused by the composite structure, either through mechanical or chemical interactions. For instance, the internal stresses arising from differences in sintering trajectories may be released during application of a uniaxial stress. As the stress is applied, deformation also occurs perpendicular to the uniaxial stress as a consequence of the Poisson's ratio effect, which is a tensile stress opposing the direction of the applied stress. The tensile stress would result in release of compressive internal stresses generated during processing, accompanied by tensile strains. The combination of compressive strains and tensile strains results in a net reduction in total strain, therefore resulting in a reduction in remanent strain. Chemical interactions through diffusion may also result in an increased ergodicity as a consequence of decreased long-range order in the perovskite structure. However, as previously discussed, evidence of such chemical interactions in 0-3 composites of BNT-BT-KNN/BNT-BT has been difficult to obtain.

Comparing the remanence in response to an electric field shown in Figure 6.8 and mechanical field shown in Figure 6.21 as a function of temperature, it is apparent that they follow a very similar pattern, with a linear decrease between room temperature and 100 °C, followed by a nonlinear drop at 110 °C, the $T_{F\text{-}R}$ of BNT-7BT,. The inflection point for remanence observed at the $T_{F\text{-}R}$ in response to mechanical stress provides another indication that an applied mechanical field results in a domain orientation that is disrupted by increasing temperature.

The same comparison can be made for the composites, starting from highest seed content. The 30% composite has a maximum remanent strain at room temperature and reduces with both increasing and lowering temperature, in response to mechanical stress. Groh *et al.*'s work shows a precipitous decrease of maximum strain from -0.5% at room temperature to 0.05% at 50 °C, from which it further lowers to 0 % between 75 °C and 150 °C. In the 30% composite, between room temperature and 50 °C a much smaller drop in remanent strain occurs in response to mechanical stress, from -0.04 % to -0.025 %. This reduction continues at 70 °C, where a remanent strain of nearly 0% can be observed, and this value is stable at 90 and 100 °C. An increase in the remanent strain can be observed, however, at 110 °C and 130 °C. No such increase occurs in response to electric field according to Groh *et al.*'s work. It should be noted that the differences between the remanent strain at 50 °C and 100 °C approach the limit of measurement accuracy in this system. The stability of remanent strain as a function of temperature in the 10 and 20% composites in response to mechanical fields strongly parallels that of the response to electric field shown in Groh *et al.*'s work. The remanent strain does not increase linearly with added seed in the composite and, therefore, does not appear to follow the rule of mixtures approximations.

The hysteresis in the composites is more easily justified by the rule of mixtures explanation than the remanent strain, as it can clearly be seen that the 30% composite has highest hysteresis at all temperatures. Hysteresis is indicative of large inelastic nonlinearities, such as the formation of domains by mechanical stress, which results in a larger volume change than a purely linear elastic stress-strain response [41]. At low temperatures, the hysteresis of all the compositions is nearly identical. The pure seed experiences the highest increase in hysteresis with increasing temperature up to 0 °C.

Above 0 °C the hysteresis reduces linearly with increasing temperature up to 110 °C, the T_{F-R}, at which point a nonlinear drop in the hysteresis can be observed because of the onset of a nonergodic/ergodic relaxor transition with temperature. All of the other compositions also show an increase in hysteresis with increasing temperature, which plateaus at room temperature and then begins to reduce with increasing temperature. In the case of 30% seed, a sharp maximum can be observed in the hysteresis at room temperature. A similar reduction in the width of the hysteresis loops was observed by Groh *et al.* in 0-3 composites under applied electric field with increasing temperature [169], showing further analogues between the mechanical and electrical response of composites.

Back-switching is stable as a function of temperature in BNT-7BT at between -40 °C and 50 °C. Above this temperature, back-switching increases continuously up to 130 °C. In BNT-6BT-3KNN, the level of back-switching increases from -40 °C to 50 °C, begins to reduce at 70 °C, and then increases at 90 °C, followed by a precipitous drop at 100 °C. A reduction in back-switching at this temperature occurs in the 10 and 20% composite, albeit less precipitously. However, no such reduction in back-switching was observed in the 30% composite. At 100 °C, the back-switching of the 30% composite exceeds that of the pure seed material, again defying rule of mixtures predictions. At 130 °C, the back-switching in all the composites exceeds that of both the pure constituents, which have negligible back-switching. Because back-switching is indicative of internal stresses that oppose the applied field, the increasing in back-switching in the 30% seed material points to an elevated internal mechanical field, particularly at higher temperatures. This internal stress may in part be the result of differences in CTE between the two components of the composite, resulting in an increased back-switching with increased seed content and temperature.

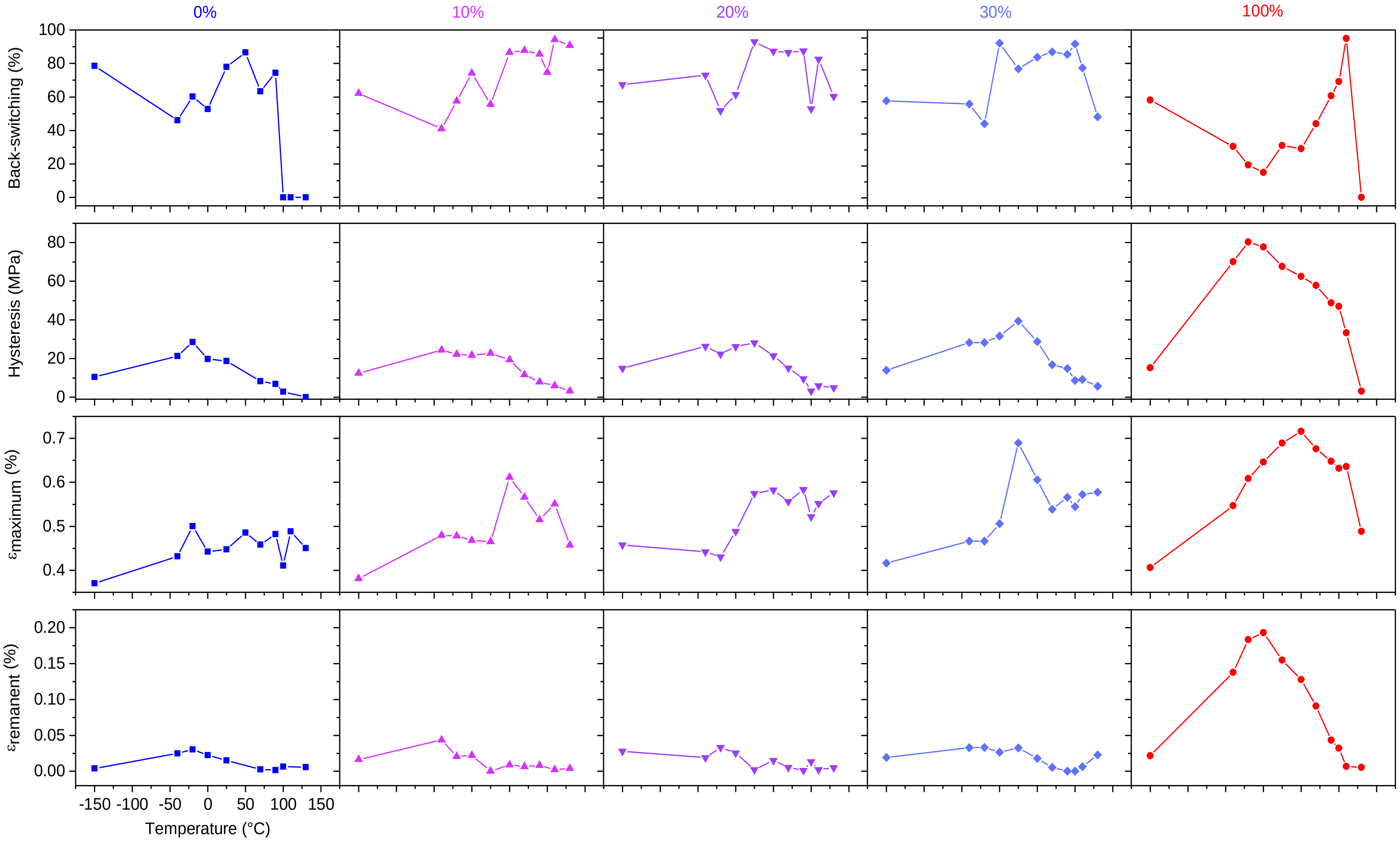

Figure 6.25: Back-switching, hysteresis, maximum strain and residual strain as a function of temperature for BNT-6BT-3KNN,BNT-7BT and 0-3 composites thereof

6.5. Summary

In this chapter, the bulk electromechanical response of BNT-6BT-3KNN/BNT-7BT and BNKT-6BA/BNT-7BT composites was presented. The dielectric response of three composite systems was shown. A comparison between the 0-3 and 2-2 composite structures for all of these systems was presented. In the BNT-6BT-3KNN/BNT-7BT composite system, a large difference in the permittivity of the poled and unpoled states was apparent in 2-2 composites, whereas 0-3 composites demonstrated a behavior more similar to an ergodic relaxor. For composites with BNKT-BA as the ER matrix phase, the poled and unpoled states had very similar dielectric behavior as a function of temperature, indicating an ergodicity in this system.

Large signal ferroelectric measurements at room temperature were presented for all three composite systems investigated. A large difference in the 2-2 and 0-3 composites was shown for BNT-6BT-3KNN/BNT-7BT system in both the polarization and strain response, with a more pronounced pinching of polarization loops in 0-3 composites as well as a higher strain response. The frequency dependence of the room temperature ferroelectric response was evaluated in BNT-6BT-3KNN/BNT-7BT composites, comparing the response at 1 Hz and 50 mHz. An enhancement of the properties was observed in 0-3 composites but not in 2-2 composites. At 1 Hz, an enhancement was observed in both composite structures. The temperature dependence of ferroelectric response of 2-2 BNT-6BT-3KNN/BNT-7BT composites was evaluated at 4 kV/mm, 1 Hz applied field. A stabilization of the strain response with increasing temperature was observed, an important parameter for actuator applications where self-heating can affect the piezoelectric response of stack actuators.

BNKT-6BA/BNT-7BT 0-3 and 2-2 composites overlapped in their polarization response, but a much higher strain response was observed in 2-2 composites. The maximum electric field dependence of the room temperature ferroelectric response was shown for BNKT-6BA/BNT-7BT composites. The strain response was highly dependent on applied voltage. An improvement of the ferroelectric properties was only observed at 6 kV/mm applied fields, because this field exceeded the coercive field, enabling domain formation and switching contributions to the total strain response.

The mechanical response to applied compressive stress was evaluated for 0-3 BNT-6BT-3KNN/BNT-7BT composites as a function of temperature. Composites showed greater thermal stability than the pure constituents in terms of hysteresis and maximum strain, but in general a reduction in the hysteresis and remanence was observed with increasing temperature. These results are in many ways analogous to the response of the same system to applied electric field and temperature in the work of Groh *et al.*, providing important insight into the parallels of ferroelastic and ferroelectric behavior of lead-free relaxor composite systems.

The ultimate goal of investigations of lead-free ferroelectrics is the replacement of lead-based materials. The composite systems presented in this work demonstrate promising steps towards improving lead-free systems, namely through reduction of hysteresis as well as increasing the operating temperature range up to 130 °C under applied electric fields. These results provide insight into ways to optimize lead-free materials for actuator applications by changing the stress state and chemical composition of composites through sintering trajectories.

7. Appendix: Composites of BNT-25ST/BNT-7BT

A presentation of a "null hypothesis" of interdiffusion between the BNT-ST/BNT-7BT 2-2 composite system is shown as an example of a material system in which a very low degree of interdiffusion occurs. Such a system is expected to correspond more closely to models that assume no chemical interaction between seed and matrix in composites, *e.g.*, the rule of mixtures model, polarization and strain coupling models, and the Brugemann inclusion model, all of which were presented in the introduction. The influence of co-sintering on interdiffusion was examined lastly in a 2-2 composite of BNT-25ST and BNT-7BT. For this investigation, a bilayer composed of one layer of BNT-7BT and one layer of BNT-25ST was used.

7.1. EDS SEM in BNT-ST/BNT-7BT (2-2)

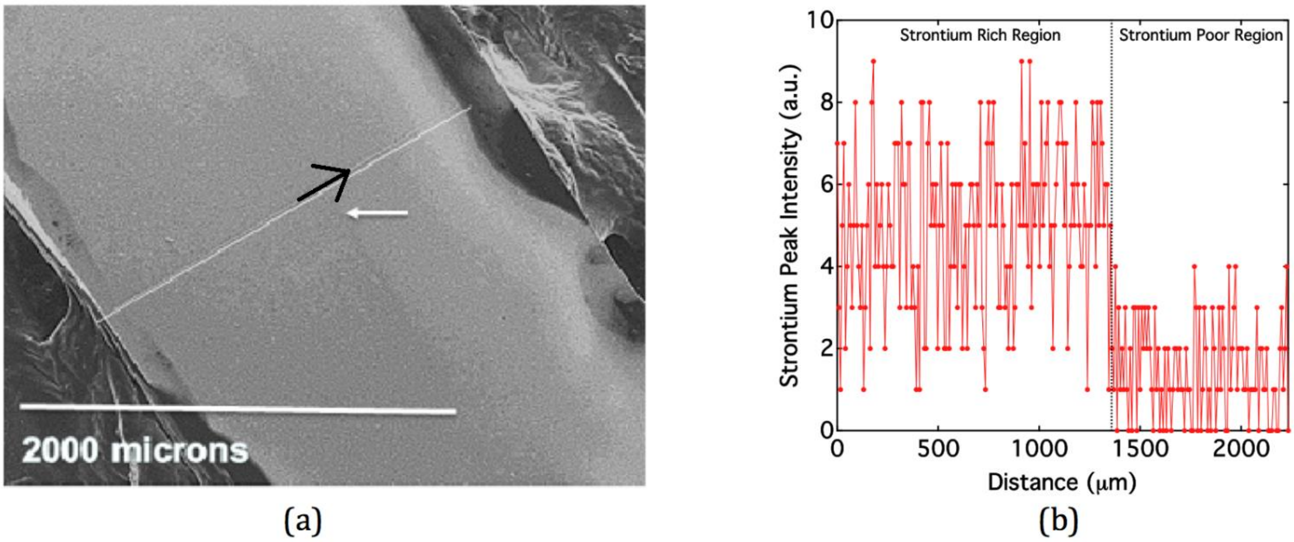

Figure 7.1: An SEM image of the cross-section of the bilayer composite (a), where the white line indicates the EDS scanning axis and the arrow shows the BNT-25ST/BNT-7BT interface (b) the EDS scanning results for strontium content as a function of distance through the thickness direction, from [290]

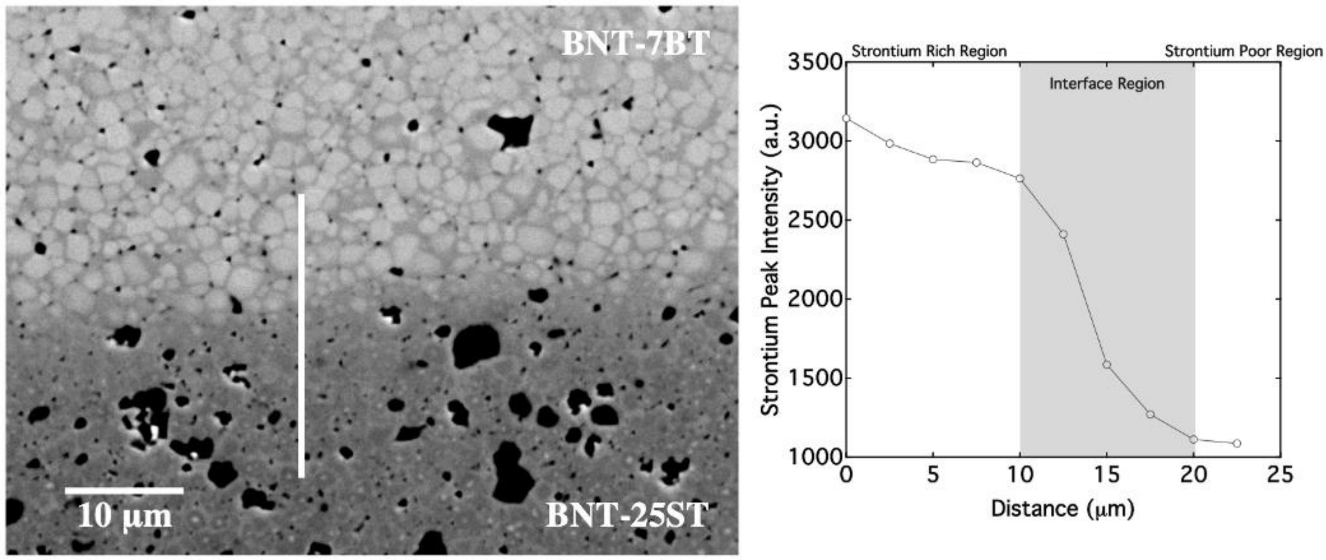

(a) (b)

Figure 7.2: Electron backscatter image of the interface region in the BNT-7BT/BNT-25ST bilayer on the left and on the right, a determination of strontium content at 10 points along the scanning line (white line) showing the compositional variation at the interface, from [290].

In this system, interdiffusion was predicted to be limited, due to the large size of the strontium ion [83]. Figure 7.1 (a) depicts the full width of the sample, with a white arrow pointing at the interface region at 1200 µm. A large-scale analysis of composition across the sample is shown in Figure 7.1 (b), in which a sharp drop in the strontium content at the center of the sample can be observed. As shown in Figure 7.2, the interdiffusion range of strontium is quite narrow compared to the rest of the composite systems discussed in this work, with an interface region of only 10 µm.

7.2. Raman investigations of BNT-25ST/BNT-7BT 2-2 composites

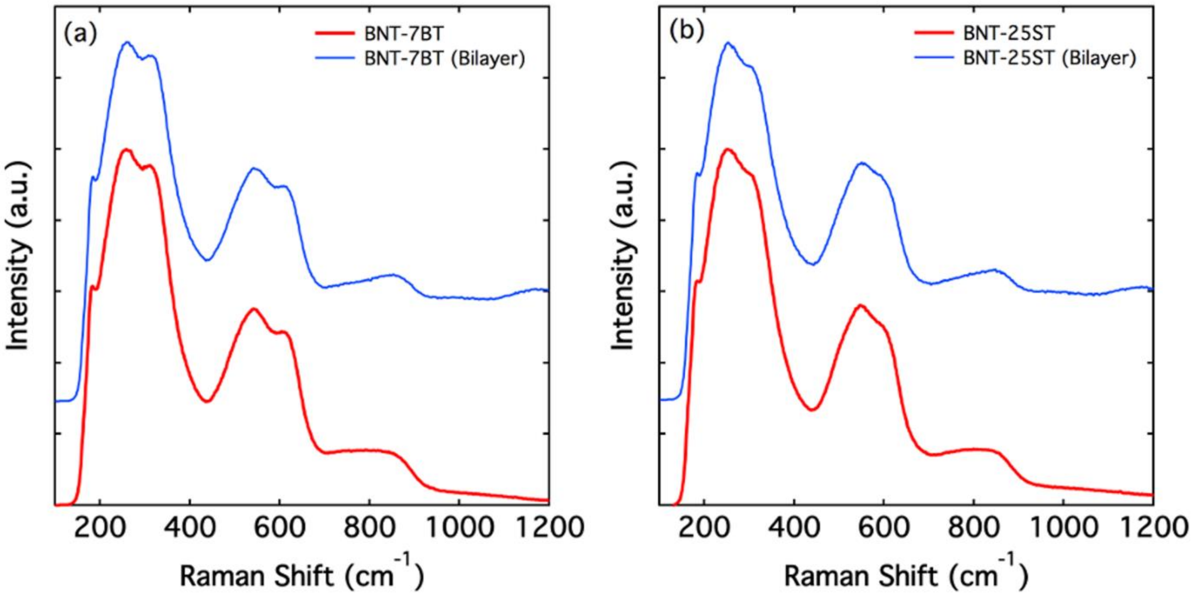

Figure 7.3: Raman spectroscopy comparison of BNT-7BT and BNT-25ST, both freely sintered and in a 2-2 composite, from [290]

Further examination by Raman spectroscopy was performed on each component of the composite and compared to the spectra obtained from the freely sintered constituent, as shown in Figure 7.3. The spectrum for BNT-7BT corresponds very well with the spectrum from the strontium-poor region of the bilayer composite, shown in Figure 7.3(a). This is particularly apparent by the splitting of the A_1 mode involving the Ti-O bond at approximately 270 cm^{-1} and the BO_6 modes centered at ~550 cm^{-1}, which has been shown by Foronda *et al.* to increase with the concentration of BT [165]. Similarly, the spectrum for as-sintered BNT-25ST corresponds well in terms of the positions of the peaks with the portion of the bilayer with higher strontium content. These results also agree with previous investigations on the room temperature Raman spectra for various compositions of BNT-ST [291]. It was shown that with increasing ST content a peak broadening, (that eventually appears as overlapping peaks, occurs at ~256 cm^{-1}), while a shoulder occurred at ~560 cm^{-1}, consistent with the findings of this work. The similarity between end members and the respective composite component points to limited changed in crystal structure a consequence of co-sintering.

7.3. Small Signal Dielectric Behavior of BNT-25ST/BNT-7BT composites as a Function of Temperature and Frequency

All dielectric and electromechanical measurements and samples used for the study thereof were part of an Advanced Research Lab performed by Hakimeh Wakily, under the direct supervision of the author.

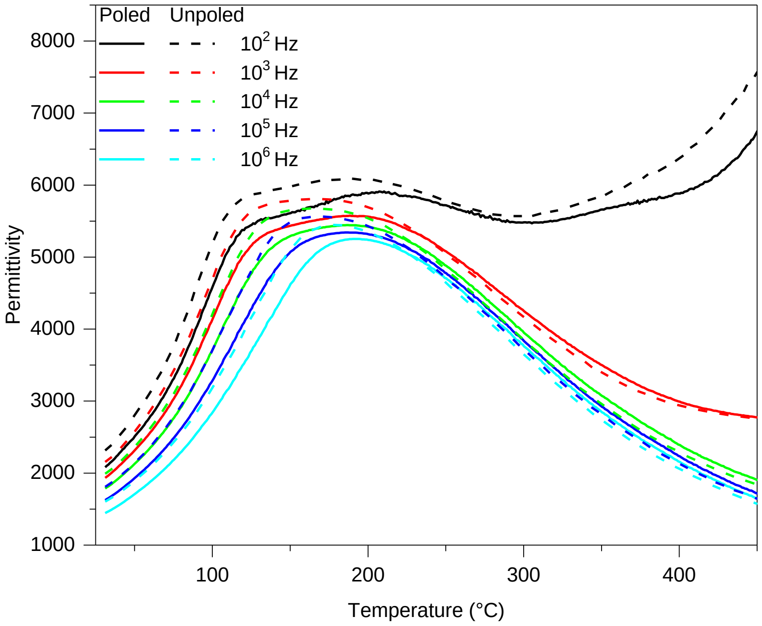

Figure 7.4: BNT-ST Permittivity as a function of temperature, modified from [290].

In BNT-25ST. the difference between the poled and unpoled permittivity decreases above 200 °C. Previous investigations of poled BNT-25ST have revealed an anomaly in the dielectric loss at 5 °C [292], indicative of a transition between the ferroelectric and relaxor state. A change in the latent heat, which is indicative of a phase transition was also observed in the field-induced ferroelectric phase at all temperatures. As previously discussed, PNRs often persist above this transition temperature, which may explain the broader temperature range at which a difference in the permittivity between the poled and unpoled states is observed in this work. BNT-25ST retains high frequency dispersion beyond $T_{m,}$ similar to observations made in PMN, which were explained by surface charge effects [293]. Such surface charges may be due to the core-shell structure of BNT-ST, in which the majority of Sr can be found in the shell as a consequence of the low diffusability of Sr during calcination[294], resulting in an inhomogeneous charge distribution in individual grains [105].

The dielectric response of 0-3 and 2-2 composites is shown in Figure 7.5. The difference between the permittivity values of the poled and unpoled states at room temperature in 0-3 ceramics is on the order of 158 units in 10%. In the composites of 20% and 30% seed content the difference between the poled and unpoled samples is nearly 0, and in the 50% seed 0-3 composite the difference increases to 545 units. In 2-2 composites, the difference between the permittivity of the poled and unpoled state at room temperature is between 160 and 180 units, depending on frequency. In the 2-2 composites of 20% seed content, the difference between poled and unpoled states at room temperature increases to 400 units at 1 kHz, and remains at this value in the 30 and 50% seed 2-2 composites. The unpoled 2-2 composites have a higher maximum permittivity than the 0-3 for compositions at 10, 20 and 30% seed, with 5607 and 5952 at 10% 0-3 and 2-2 respectively, 5592 and 5983 at 20% 0-3 and 2-2 respectively, and 6092 and 6252 at 30% 0-3 and 2-2 respectively. Increasing seed content increases the maximum permittivity in both the 0-3 and 2-2 composites. The 50% seed composition has a higher maximum permittivity in the 0-3 composite than the 2-2, because the permittivity of the 2-2 composite shows a decrease at 50% seed, whereas the 0-3 composite continues to increase.

In the 30 and 50% composite 2-2 composites, there is a drop in the 1 MHz permittivity curve of the poled sample at approximately 110 °C, the depolarization temperature of BNT-7BT. At the same temperature, there is a sharp change in the slope of the permittivity curve at all frequencies. Schader *et al.* showed that increased mechanical stress resulted in a sharper drop in permittivity in BNT-BT at 77 °C [76]. The presence of internal stresses due to differences in CTE and sintering shrinkage is highly likely in this composite system, and appears to result in a compressive stress in the seed as opposite a tensile stress as in the BNT-BT-KNN and BNKT-BA composites. There is a further difference in stress states in the 0-3 and 2-2 composites: the planar isotropic conditions of 2-2 composites would result in biaxial tensile and compressive stresses whereas in the 0-3 composites, hydrostatic stresses are expected. This difference in stress state may be why the aforementioned drop in permittivity is observed only in 2-2 composites.

At temperatures above T_m, a large frequency dispersion between the dielectric response at 1 kHz and 10 kHz can be observed in all 2-2 composites, corresponding to the same behavior in pure BNT-ST. This behavior may also be attributed to the space charge polarization resulting from an inhomogeneous distribution of strontium in BNT-ST due to its core-shell structure. The 2-2 composites have a larger interface surface area than the 0-3 composites, resulting in a more pronounced dielectric response that is characteristic of the pure matrix.

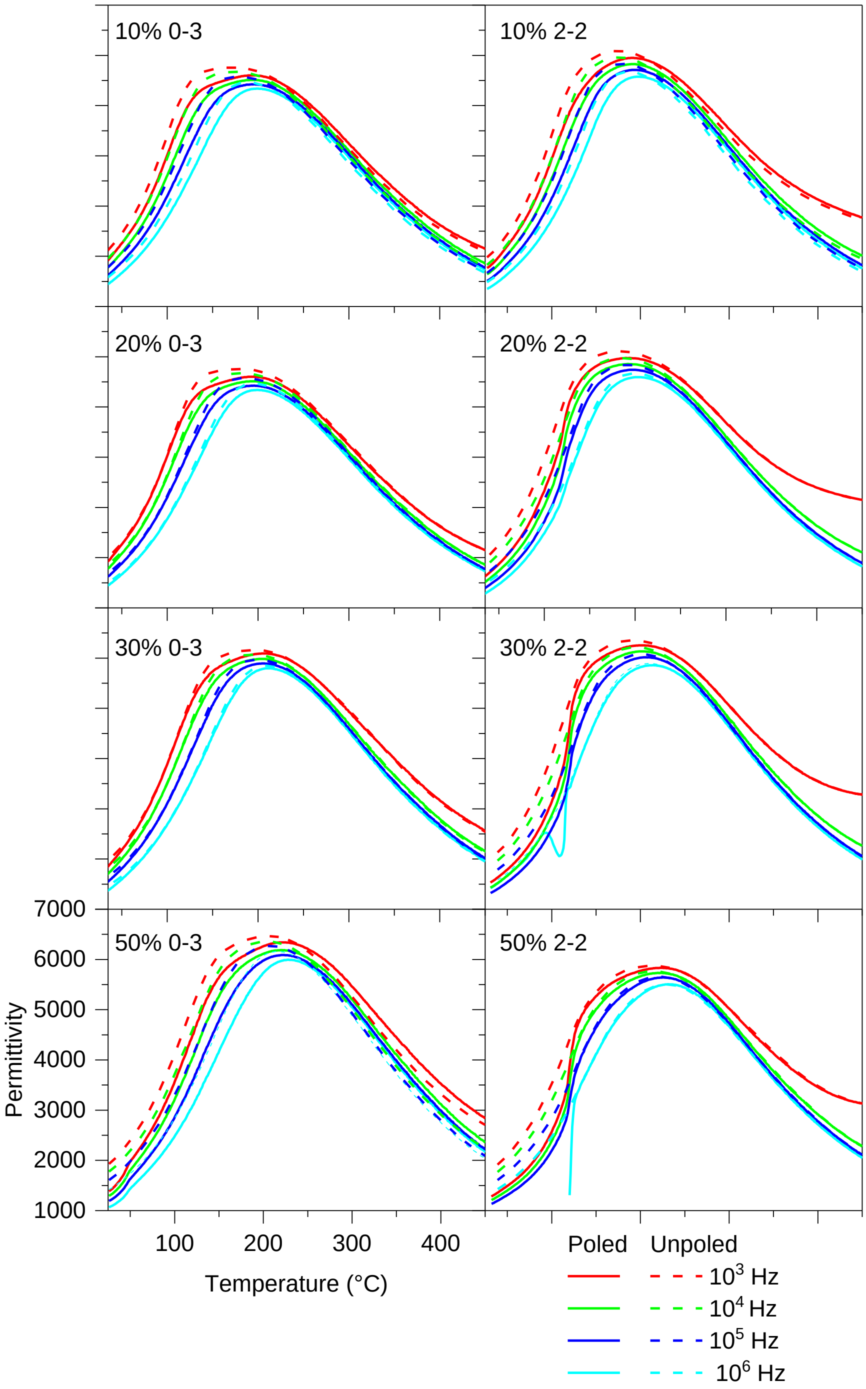

Figure 7.5: BNT-25ST/BNT-7BT composite permittivity as a function of temperature and frequency from room temperature – 450 °C for poled and unpoled samples

At the interface, the addition of Ba to BNT-ST, which has an ionic radius of 1.75 Å as compared to 1.55 Å of Sr [83], would result in an increased Goldschmidt tolerance factor. Previous work has shown that an increasing amount of Sr added to BNT results in a reduction of the T_m [295], which was attributed to a weakening of the translation symmetry of dipoles and a reduction in the size of PNRs. Therefore, an increase in the tolerance factor from that of pure BNT-25ST could result in an increased stabilization of the long-range order, as the substitution of Pt as an A-site cation in BNT has revealed in the same work by Lee *et al.* [295]. It is also possible that internal stresses immobilize the PNRs, and that these stresses increase with increasing seed content. Schader *et al.* showed that it is possible to induce a poled state in BNT-6BT through the application of compressive stress and that the sharpness of the dielectric anomaly at $T_{F\text{-}R}$ is sharper with higher applied mechanical stress [76]. Because such stresses are more prevalent in the planar isotropic conditions of 2-2 composites than in the hydrostatic stresses of micron scale inclusions in the 0-3 composite, the 2-2 composite structure has a higher stress-induced stabilization of PNRs.

Table 11: BNT-25ST composite system permittivity at room temperature, 1 kHz in the unpoled state compared to predicted values of rule of mixtures values calculated from Equation 1.1

	10%	*20%*	*30%*	*50%*
Prediction	*2116*	*1905*	*1694*	*1272*
0-3	*2096*	*1938*	*1913*	*1930*
Deviation	*-20*	*33*	*219*	*658*
2-2	*1828*	*2058*	*2130*	*1960*
Deviation	*-288*	*153*	*436*	*688*

The permittivity values at room temperature in the unpoled state for 1 kHz are shown in Table 11 and compared to predicted values calculated using the rule of mixtures with Equation 1.1. In both structures, the composite of 10% seed has a permittivity value below the prediction, but the difference is much higher in the 2-2 composite. The 20% composites have a higher value than the prediction, but once again the difference is much higher in the 2-2 composite. The uncertainty of the permittivity values is 3%, above the deviation of the 0-3 composites, therefore it can be said that the 0-3 composite experimental values fall within the predicted values, which is indicative of the retention of the polar seed and nonpolar matrix phase properties in the 10 and 20% 0-3 composite structure. The 30 and 50% seed content composites differ from the predicted value by 219 and 658 respectively in the 0-3 structure, and 436 and 688 in the 2-2 structure. This larger deviation in all of the 2-2 composites and the 30 and 50% 0-3 composites is indicative of a change in the dielectric properties of the seed and matrix in the composite structure. Co-sintering was also shown to influence grain size, and that may increase the dielectric permittivity values, as previously discussed. Further investigations of sintering stresses and microstructure in this composite system are required before a conclusion on the cause of changes in dielectric permittivity can be made.

7.4. Large Signal Ferroelectric and Piezoelectric Response of BNT-25ST/BNT-7BT 0-3 and 2-2 Composites

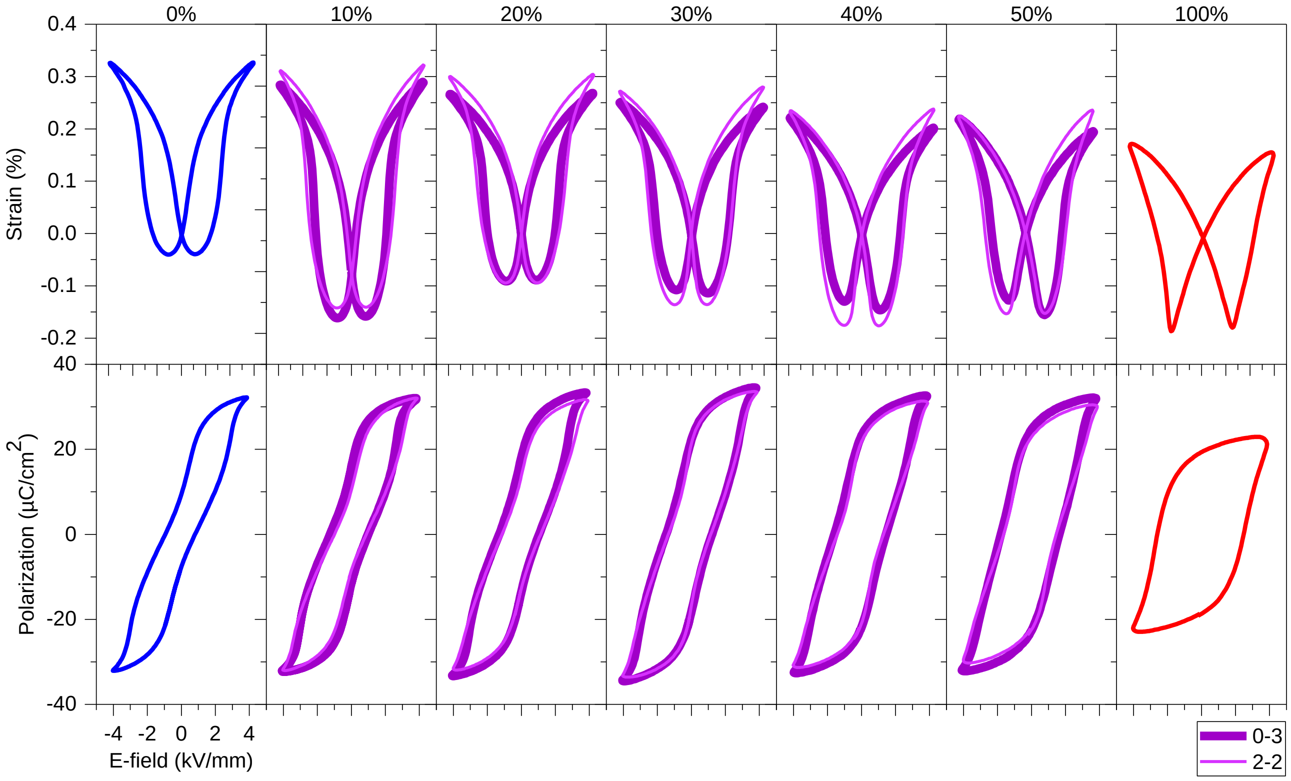

Figure 7.6: room temperature bipolar strain and polarization hysteresis curves for 0-3 and 2-2 composites as a function of constituent content, performed at a frequency of 1 Hz and a maximum electric field 4 kV/mm. BNT-25ST is the matrix material and BNT-7BT is the seed.

As discussed previously, composites with BNT-25ST as the matrix phase were also used as a model system because of the large difference in composition between seed and matrix. Figure 7.6 shows the large signal ferroelectric response of composites comprising BNT-25ST as the ergodic relaxor matrix and BNT-7BT as the nonergodic relaxor/ferroelectric seed. In comparison to the BNKT-6BA/BNT-7BT composites, this material system shows a high negative strain and remanent polarization, with no apparent increase in the maximum strain with increasing seed content. A pinching of the polarization loops occurs in the pure matrix and 10, 20, and 30% seed content composites, but at higher seed contents this feature is no longer present.

BNT-ST/BNT-7BT composites did not show any enhancement in the maximum strain relative to the pure constituents, and instead showed an increase in negative strain with increasing seed content. They also displayed an increased remanent polarization, exceeding that of the pure seed material.

Figure 7.7 depicts the characteristic parameters of the large signal ferroelectric response for BNT-25ST/BNT-7BT composites. The remanent polarization can be seen to increase with increasing seed constant, exceeding that of the pure seed material at 30, 40 and 50% seed. The 2-2 and 0-3 composites differ in remanent polarization at 10 and 20% seed of 7 and 5 μC/cm^2 respectively. At 30 and 40% seed, the difference between the 0-3 and 2-2 composites is below 1 μC/cm^2. At 50% seed the 2-2 composite exceeds that of the 0-3 composite by 4 μC/cm^2, attaining a value of 26 μC/cm^2 as compared to 19 μC/cm^2 in the pure seed. The coercive field appears to increase linearly with seed content in both the 0-3 and 2-2 composites.

As a consequence of the increase in negative strain with increasing BNT-7BT content, the total usable strain also reduced, which is easily interpreted as a reduction in the large signal piezoelectric coefficient. This reduction is nonlinear, with an inflection point between 30 and 40%, indicating that the relationship between piezoelectric coefficient and seed content is not a simple rule of mixtures relationship.

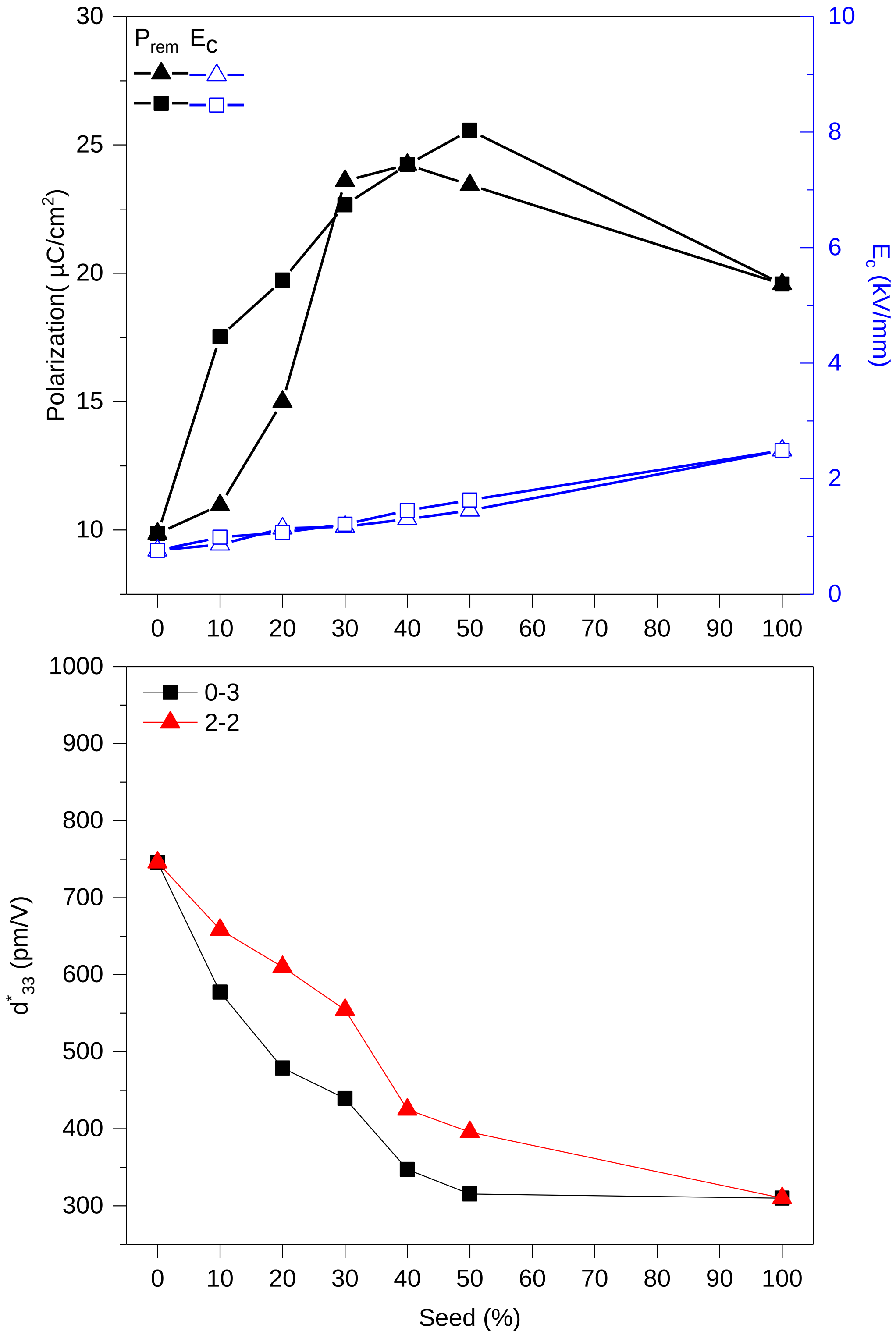

Figure 7.7: piezoelectric coefficient, remanent polarization and coercive field as a function of seed content and composition, at 4 kV/mm maximum field for BNT-25ST/BNT-7BT composites

Bibliography

[1] C. Groh, D. J. Franzbach, W. Jo, K. G. Webber, J. Kling, L. A. Schmitt, H.-J. Kleebe, S.-J. Jeong, J.-S. Lee, and J. Rödel, *Adv. Funct. Mater.*, pp. 356–362, Sep. 2013.

[2] D. S. Lee, S. J. Jeong, M. S. Kim, and J. H. Koh, *J. Appl. Phys.*, vol. 112, no. 12, p. 124109, 2012.

[3] M. Tillman, J. A. Yeomans, and R. A. Dorey, *Ceram. Int.*, vol. 40, no. 7, pp. 9715–9721, Aug. 2014.

[4] L. C. De Jonghe, M. N. Rahaman, and C. H. Hsueh, *Acta Metall.*, vol. 34, no. 7, pp. 1467–1471, Jul. 1986.

[5] R. Zuo, E. Aulbach, and J. Rödel, *Acta Mater.*, vol. 51, no. 15, pp. 4563–4574, 2003.

[6] X. Cui, J. Zhou, B. Li, and Z. Tong, *Mater. Manuf. Process.*, vol. 22, pp. 251–255, 2007.

[7] D. S. Lee, D. H. Lim, M. S. Kim, K. H. Kim, and S. J. Jeong, *Appl. Phys. Lett.*, vol. 99, no. 6, p. 062906, 2011.

[8] M. N. N. Rahaman, *Ceramics Processing and Sintering*, 2nd ed. New York: CRC Press, 2003.

[9] M. H. Frey, Z. Xu, P. Han, and D. A. Payne, *Ferroelectrics*, vol. 206, no. 1, pp. 337–353, Feb. 1998.

[10] H.-L. Li, Q. Liu, J.-J. Zhou, K. Wang, J.-F. Li, H. Liu, and J.-Z. Fang, *J. Eur. Ceram. Soc.*, vol. 36, no. 11, pp. 2849–2853, 2016.

[11] R. Chaim and M. Hefetz, *J. Mater. Sci.*, vol. 39, no. 9, pp. 3057–3061, May 2004.

[12] A. Moulson and J. Herbert, *Reports Prog. Phys.*, 2003.

[13] S. A. Runge, *Reiseführer Odenwald mit Bergstraße, Darmstadt, Heidelberg*, 2nd ed. 2016.

[14] C. Kittel, *Solid State Physics*, 8th ed. John Wiley & Sons, Ltd, 2004.

[15] G. Juarez-Martinez, A. Chiolerio, and P. Allia, “Maxwell–Wagner Effect,” in *Encyclopedia of Nanotechnology*, Dordrecht: Springer Netherlands, 2012, pp. 1276–1285.

[16] R. Waser, U. Böttger, and S. Tiedke, *Polar Oxides: Properties, Characterization, and Imaging*. 2005.

[17] J. C. Burfoot and G. W. Taylor, *Polar Dielectrics and Their Applications*. Los Angeles: University of California Press, 1979.

[18] M. Johnsson and P. Lemmens, “Crystallography and Chemistry of Perovskites,” in *Handbook of Magnetism and Advanced Magnetic Materials*, 2007.

[19] R. A. Cowley, S. N. Gvasaliya, S. G. Lushnikov, B. Roessli, and G. M. Rotaru, *Adv. Phys.*, vol. 60, no. 2, pp. 229–327, Apr. 2011.

[20] J. Curie and P. Curie, *J. Phys. Theor. Appl.*, vol. 1, no. 1, pp. 245–251, 1882.

[21] M. Kamlah, *Continuum Mechanics and Thermodynamics*, vol. 13, no. 4. pp. 219–268, 2001.

[22] J. Valasek, *Phys. Rev.*, vol. 17, no. 4, pp. 475–481, Apr. 1921.

[23] G. A. Samara, *J. Phys. Condens. Matter*, vol. 15, no. 9, pp. R367–R411, Mar. 2003.

[24] C. Galassi, “Advances in Processing of Bulk Ferroelectric Materials,” in *Multifunctional Polycrystalline Ferroelectric Materials: Processing and Properties*, J. Ricote, Ed. Springer Science & Business Media, 2011, pp. 1–37.

[25] Y. Hiruma, H. Nagata, and T. Takenaka, *J. Appl. Phys.*, vol. 104, no. 12, p. 124106, 2008.

[26] I. Levin, I. Reaney, E.-M. Anton, W. Jo, J. Rödel, J. Pokorny, L. Schmitt, H.-J. Kleebe, M. Hinterstein, and J. Jones, *Phys. Rev. B*, vol. 87, no. 2, p. 024113, Jan. 2013.

[27] H. Ouchi, K. Nagano, and S. Hayakawa, *J. Am. Ceram. Soc.*, vol. 48, no. 12, pp. 630–635, Dec. 1965.

[28] Z. G. Ye, *Key Eng. Mater.*, vol. 155–156, pp. 81–122, 1998.

[29] I. K. Jeong, T. Darling, J. Lee, T. Proffen, R. Heffner, J. Park, K. Hong, W. Dmowski, and T. Egami, *Phys. Rev. Lett.*, vol. 94, no. 14, p. 147602, Apr. 2005.

[30] M. Davies, E. Aksel, and J. L. Jones, *J. Am. Ceram. Soc.*, vol. 94, no. 5, pp. 1314–1316, May 2011.

[31] G. Burns and F. H. Dacol, *Solid State Commun.*, vol. 48, no. 10, pp. 853–856, Dec. 1983.

[32] G. Burns and B. A. Scott, *Solid State Commun.*, vol. 13, no. 3, pp. 423–426, 1973.

[33] G. . Smolenskii and A. I. Agranovskaya, *Solid State Phys.*, vol. 1, pp. 1562–1572, 1959.

[34] W. Kleemann, *J. Mater. Sci.*, vol. 41, no. 1, pp. 129–136, Jan. 2006.

[35] V. Y. Shur, *Phase Transitions*, vol. 65, no. 1–4, pp. 49–72, Jul. 1998.

[36] K. Binder and A. P. Young, *Rev. Mod. Phys.*, vol. 58, no. 4, pp. 801–976, Oct. 1986.

[37] A. A. Bokov and Z. G. Ye, *J. Mater. Sci.*, vol. 41, no. 1, pp. 31–52, Jan. 2006.

[38] J. Zang, M. Li, D. C. Sinclair, T. Frömling, W. Jo, J. Rödel, T. Frömling, W. Jo, J. Rödel, T. Frömling, W. Jo, and J. Rödel, *J. Am. Ceram. Soc.*, vol. 97, no. 5, pp. 1523–1529, May 2014.

[39] J. Kling, W. Jo, R. Dittmer, S. Schaab, and H. J. Kleebe, *J. Am. Ceram. Soc.*, vol. 96, no. 10, pp. 3312–3324, Jul. 2013.

[40] V. K. Wadhawan, *Bull. Mater. Sci.*, vol. 6, no. 4, pp. 733–753, 1984.

[41] E. K. H. Salje, *Annu. Rev. Mater. Res.*, vol. 42, no. 1, pp. 265–283, Aug. 2012.

[42] K. Aizu, *Jpn. J. Appl. Phys.*, vol. 8, no. 12, pp. 1424–1434, Dec. 1969.

[43] V. K. Wadhawan, *Bull. Mater. Sci.*, vol. 6, no. 4, pp. 733–753, Sep. 1984.

[44] T. Adachi, T. Sekino, T. Nakayama, T. Kusunose, and K. Niihara, *Mater. Lett.*, vol. 57, no. 20, pp. 3057–3062, 2003.

[45] E. Salje and G. Hoppmann, *Mater. Res. Bull.*, vol. 11, no. 12, pp. 1545–1549, Dec. 1976.

[46] K. G. Webber, E. Aulbach, T. Key, M. Marsilius, T. Granzow, and J. Rödel, *Acta Mater.*, vol. 57, no. 15, pp. 4614–4623, Sep. 2009.

[47] J. E. Daniels, G. Picht, S. Kimber, and K. G. Webber, *Appl. Phys. Lett.*, vol. 103, no. 12, 2013.

[48] B. Jaffe, “Piezoelectric Transducers Using Lead Titanate and Lead Zirconate,” 2708244, 1955.

[49] T. R. Shrout and S. J. Zhang, *J. Electroceramics*, vol. 19, no. 1, pp. 113–126, Feb. 2007.

[50] S. Wada, S. Suzuki, T. Noma, T. Suzuki, M. Osada, M. Kakihana, S. E. Park, L. E. Cross, and T. R. Shrout, *Jpn. J. Appl. Phys.*, vol. 38, no. 9, pp. 5505–5511, 1999.

[51] S. Roberts, “Ceramic Dielectrics and Method of Making,” 2541833, 1954.

[52] G. H. Haertling, *J. Am. Ceram. Soc.*, vol. 82, no. 4, pp. 797–818, 1999.

[53] Z. Kutnjak, J. Petzelt, and R. Blinc, *Nature*, vol. 441, no. 7096, pp. 956–9, Jun. 2006.

[54] D. Viehland, S. J. Jang, L. E. Cross, and M. Wuttig, *J. Appl. Phys.*, vol. 68, no. 6, p. 2916, 1990.

[55] *“Eu-Directive 2011/65/Eu: Restriction of the Use of Certain Hazardous Substances in Electrical and Electronic Equipment (RoHS)"*, no. April. Off. J. Eur. Union, 2010, pp. 88–110.

[56] J. Wu, D. Xiao, and J. Zhu, *Chem. Rev.*, vol. 115, no. 7, pp. 2559–2595, Apr. 2015.

[57] P. K. Panda, *J. Mater. Sci.*, vol. 44, no. 19, pp. 5049–5062, Jul. 2009.

[58] J. Rödel, K. G. Webber, R. Dittmer, W. Jo, M. Kimura, and D. Damjanovic, *J. Eur. Ceram. Soc.*, vol. 35, no. 6, pp. 1659–1681, Jun. 2015.

[59] W. Jo, R. Dittmer, M. Acosta, J. Zang, C. Groh, E. Sapper, K. Wang, and J. Rödel, *J. Electroceramics*, vol. 29, no. 1, pp. 71–93, May 2012.

[60] E. Wainer and N. R. Thielke, “Dielectric Materials and Method of Making the Same,” 2277733, 1942.

[61] A. B. Ржанов, *Успехи физических наук*, vol. 38, no. 4, pp. 461–489, 1949.

[62] H. D. Megaw, *Proc. Phys. Soc.*, vol. 58, no. 2, pp. 133–152, Mar. 1946.

[63] B. N. Rao, A. Senyshyn, L. Olivi, V. Sathe, and R. Ranjan, *J. Eur. Ceram. Soc.*, vol. 36, no. 8, pp. 1961–1972, 2016.

[64] V. Dorcet, G. Trolliard, and P. Boullay, *Chem. Mater.*, vol. 20, no. 15, pp. 5061–5073, Aug. 2008.

[65] T. Takenaka, K. Maruyama, and K. Sakata, *Jpn. J. Appl. Phys.*, vol. 30, no. 9B, pp. 2236–2239, 1991.

[66] T. Takenaka and H. Nagata, *Key Eng. Mater.*, vol. 157–158, pp. 57–64, 1999.

[67] C. Ma, H. Guo, S. P. Beckman, and X. Tan, *Phys. Rev. Lett.*, vol. 109, no. 10, p. 107602, Sep. 2012.

[68] J. E. Daniels, W. Jo, J. Rödel, and J. L. Jones, *Appl. Phys. Lett.*, vol. 95, no. 3, p. 032904, Jul. 2009.

[69] C. Ma, X. Tan, E. Dul’kin, and M. Roth, *J. Appl. Phys.*, vol. 108, no. 10, p. 104105, 2010.

[70] Y. J. Dai, J. S. Pan, and X. W. Zhang, *Key Eng. Mater.*, vol. 336–338, pp. 206–209, 2007.

[71] D. Lin, Z. Li, F. Li, Z. Xu, and X. Yao, *J. Alloys Compd.*, vol. 489, no. 1, pp. 115–118, Jan. 2010.

[72] C. Xu, D. Lin, and K. W. Kwok, *Solid State Sci.*, vol. 10, no. 7, pp. 934–940, Jul. 2008.

[73] D. Zhou and M. Kamlah, *J. Appl. Phys.*, vol. 98, no. 10, p. 104107, Nov. 2005.

[74] Q. D. Liu and J. E. Huber, *J. Eur. Ceram. Soc.*, vol. 26, no. 13, pp. 2799–2806, 2006.

[75] J. E. Daniels, W. Jo, J. Rödel, and J. L. Jones, *Appl. Phys. Lett.*, vol. 95, no. 3, p. 032904, 2009.

[76] F. H. Schader, Z. Wang, M. Hinterstein, J. E. Daniels, and K. G. Webber, *Phys. Rev. B*, vol. 93, no. 13, p. 054304, Apr. 2016.

[77] W. Jo and J. Rödel, *Appl. Phys. Lett.*, vol. 99, no. 4, p. 042901, 2011.

[78] J. E. Daniels, W. Jo, J. Rödel, V. Honkimäki, and J. L. Jones, *Acta Mater.*, vol. 58, no. 6, pp. 2103–2111, Apr. 2010.

[79] C. Ma, “Transmission electron microscopy investigation of the microstructural mechanisms for the piezoelectricity in lead-free perovskite ceramics,” 2012.

[80] P. B. Groszewicz, M. Gröting, H. Breitzke, W. Jo, K. Albe, G. Buntkowsky, and J. Rödel, *Sci. Rep.*, vol. 6, p. 31739, Aug. 2016.

[81] O. Elkachai, M. Manier, J. . P. Mercurio, O. Elkechai, M. Manier, and J. . P. Mercurio, *Phys. Status Solidi Appl. Mater. Sci.*, vol. 157, no. 499, pp. 499–506, 1996.

[82] C. F. Buhrer, *J. Chem. Phys.*, vol. 36, no. 3, p. 798, 1962.

[83] R. D. Shannon, *Acta Crystallogr. Sect. A*, vol. 32, no. 1, p. 751, 1976.

[84] W. Zhao, H. P. Zhou, Y. K. Yan, and D. Liu, *Key Eng. Mater.*, vol. 368–372, pp. 1908–1910, 2008.

[85] N. H. Khansur, R. Benton, T. H. Dinh, J. S. Lee, J. L. Jones, and J. E. Daniels, *J. Appl. Phys.*, vol. 119, no. 23, 2016.

[86] C. Luo, Y. Wang, W. Ge, J. Li, D. Viehland, O. Delaire, X. Li, and H. Luo, *J. Appl. Phys.*, vol. 119, no. 17, 2016.

[87] G. Trolliard and V. Dorcet, *Chem. Mater.*, vol. 20, no. 15, pp. 5074–5082, Aug. 2008.

[88] C. Luo, Y. Wang, W. Ge, J. Li, D. Viehland, O. Delaire, X. Li, and H. Luo, *J. Appl. Phys.*, vol. 119, no. 17, p. 174102, May 2016.

[89] F. Tsai, V. Khiznichenko, and J. M. Cowley, *Ultramicroscopy*, vol. 45, pp. 55–63, 1992.

[90] L. Egerton and D. M. Dillon, *J. Am. Ceram. Soc.*, vol. 42, no. 9, pp. 438–442, 1959.

[91] G. Shirane, R. Newnham, and R. Pepinsky, *Phys. Rev.*, vol. 96, no. 3, pp. 581–588, 1954.

[92] J. Tellier, B. Malic, B. Dkhil, D. Jenko, J. Cilensek, and M. Kosec, *Solid State Sci.*, vol. 11, no. 2, pp. 320–324, Feb. 2009.

[93] L. Egerton and D. M. Dillon, *J. Am. Ceram. Soc.*, vol. 42, no. 50702022, pp. 439–442, 1959.

[94] K. Wang and J. F. Li, *J. Adv. Ceram.*, vol. 1, no. 1, pp. 24–37, Mar. 2012.

[95] L. Liu, M. Knapp, H. Ehrenberg, L. Fang, H. Fan, L. A. Schmitt, H. Fuess, M. Hoelzel, H. Dammak, M. P. Thi, and M. Hinterstein, *J. Eur. Ceram. Soc.*, 2016.

[96] T. N. Yasuyoshi Saito, Hisaaki Takao, Toshihiko Tani, Tatsuhiko Nonoyama, Kazumasa Takatori, Takahiko Homma and M. Nakamu, *Phys. Status Solidi B*, vol. 432, no. November, pp. 84–87, 2004.

[97] S. Zhang, Tao, A. B. Kounga, E. Aulbach, H. Ehrenberg, and J. Rödel, *Appl. Phys. Lett.*, vol. 91, no. 11, p. 112906, 2007.

[98] J. Zang, M. Li, D. C. Sinclair, W. Jo, and J. Rödel, *J. Am. Ceram. Soc.*, vol. 97, no. 5, pp. 1523–1529, May 2014.

[99] S. T. Zhang, A. B. Kounga, W. Jo, C. Jamin, K. Seifert, T. Granzow, J. Rödel, and D. Damjanovic, *Adv. Mater.*, vol. 21, p. NA-NA, Aug. 2009.

[100] L. A. Schmitt and H.-J. Kleebe, *Funct. Mater. Lett.*, vol. 03, no. 01, pp. 55–58, Mar. 2010.

[101] J. Kling, X. Tan, W. Jo, H.-J. Kleebe, H. Fuess, and J. Rödel, *J. Am. Ceram. Soc.*, vol. 93, no. 9, pp. 2452–2455, Apr. 2010.

[102] K. Sakata and Y. Masuda, *Ferroelectrics*, vol. 7, no. 1, pp. 347–349, Jan. 1974.

[103] Y. Hiruma, Y. Imai, Y. Watanabe, H. Nagata, and T. Takenaka, *Appl. Phys. Lett.*, vol. 92, no. 26, p. 262904, Jul. 2008.

[104] M. Acosta, W. Jo, and J. Rödel, *J. Am. Ceram. Soc.*, vol. 97, no. 6, pp. 1937–1943, Jun. 2014.

[105] M. Acosta, L. A. Schmitt, L. Molina-Luna, M. C. Scherrer, M. Brilz, K. G. Webber, M. Deluca, H. J. Kleebe, J. Rödel, and W. Donner, *J. Am. Ceram. Soc.*, vol. 98, no. 11, pp. 3405–3422, Nov. 2015.

[106] W. Krauss, D. Schütz, F. A. Mautner, A. Feteira, and K. Reichmann, *J. Eur. Ceram. Soc.*, vol. 30, no. 8, pp. 1827–1832, Jun. 2010.

[107] J. Zylberberg, A. A. Belik, E. Takayama-Muromachi, and Z. G. Ye, *Chem. Mater.*, vol. 19, no. 26, pp. 6385–6390, Dec. 2007.

[108] A. Ullah, C. W. Ahn, A. Hussain, I. W. Kim, H.-I. Hwang, and N.-K. Cho, *Solid State Commun.*, vol. 150, no. 25, pp. 1145–1149, 2010.

[109] A. Ullah, C. W. Ahn, A. Hussain, S. Y. Lee, J. S. Kim, and I. W. Kim, *J. Alloys Compd.*, vol. 509, no. 6, pp. 3148–3154, Feb. 2011.

[110] A. Ullah, C. W. Ahn, A. Hussain, and I. W. Kim, *J. Electroceramics*, vol. 30, no. 1–2, pp. 82–86, Apr. 2012.

[111] D. Damjanovic, "Chapter 4: Hysteresis in Piezoelectric and Ferroelectric Materials," in *The Science of Hysteresis*, Elsevier, 2006, pp. 337–465.

[112] T. Dinh, C. H. Yoon, J. K. Kang, Y. H. Hong, and J. S. Lee, *Ferroelectrics*, vol. 487, no. 1, pp. 142–148, Dec. 2015.

[113] R. E. Newnham, *Ferroelectrics*, vol. 68, no. 1, pp. 1–32, Jan. 1986.

[114] A. W. Tavernor, H. P. S. Li, and R. Stevens, *J. Eur. Ceram. Soc.*, vol. 19, no. 10, pp. 1859–1863, 1999.

[115] F. D. Minatto, P. Milak, A. De Noni, D. Hotza, and O. R. K. Montedo, *Adv. Appl. Ceram.*, vol. 114, no. 3, pp. 127–138, 2015.

[116] G. N. Howatt, R. G. Breckenridge, and J. M. Brownlow, *J. Am. Ceram. Soc.*, vol. 30, no. 8, pp. 237–242, Aug. 1947.

[117] R. E. Newnham, *Annu. Rev. Mater. Sci.*, vol. 16, no. 1, pp. 47–68, Jan. 1986.

[118] J. Ryu, A. V. Carazo, K. Uchino, and H. E. Kim, *J. Electroceramics*, vol. 7, no. 1, pp. 17–24, 2001.

[119] D. A. G. Bruggeman, *Ann. Phys.*, vol. 416, no. 7, pp. 636–664, 1935.

[120] M. Wang and N. Pan, *Mater. Sci. Eng. R Reports*, vol. 63, no. 1, pp. 1–30, 2008.

[121] A. Davidson and M. Tinkham, *Phys. Rev. B*, vol. 13, no. 8, pp. 3261–3267, 1976.

[122] R. Nath, S. Zhong, S. P. Alpay, B. D. Huey, and M. W. Cole, *Appl. Phys. Lett.*, vol. 92, p. 012916, 2008.

[123] Z. G. Ban, S. Alpay, and J. Mantese, *Phys. Rev. B*, vol. 67, no. 18, p. 184104, May 2003.

[124] R. Nath, S. Zhong, S. P. Alpay, B. D. Huey, and M. W. Cole, .

[125] J. H. Haeni, P. Irvin, W. Chang, R. Uecker, P. Reiche, Y. L. Li, S. Choudhury, W. Tian, M. E. Hawley, B. Craigo, A. K. Tagantsev, X. Q. Pan, S. K. Streiffer, L. Q. Chen, S. W. Kirchoefer, J. Levy, and D. G. Schlom, *Nature*, vol. 430, no. 7001, pp. 758–761, Aug. 2004.

[126] Y. S. Kim, D. J. Kim, T. H. Kim, T. W. Noh, J. S. Choi, B. H. Park, and J.-G. Yoon, *Appl. Phys. Lett.*, vol. 91, no. 4, p. 042908, Jul. 2007.

[127] C. B. Eom, R. J. Cava, R. M. Fleming, J. M. Phillips, R. B. vanDover, J. H. Marshall, J. W. P. Hsu, J. J. Krajewski, W. F. Peck, V. Gopalan, L.-Q. Chen, D. G. Schlom, and C. B. Eom, *Science (80-.).*, vol. 258, no. 5089, pp. 1766–1769, Dec. 1992.

[128] M. S. Senousy, R. K. N. D. Rajapakse, D. Mumford, and M. S. Gadala, *Smart Mater. Struct.*, vol. 18, no. 4, pp. 045008–045019, Apr. 2009.

[129] S. R. Winzer, N. Shankar, and A. P. Ritter, *J. Am. Ceram. Soc.*, vol. 72, no. 12, pp. 2246–2257, Dec. 1989.

[130] T. R. Shrout, W. A. Schulze, and J. V. Biggers, *Ferroelectrics*, vol. 34, no. 1, pp. 105–111, Feb. 1981.

[131] N. H. Khansur, C. Groh, W. Jo, C. Reinhard, J. A. Kimpton, K. G. Webber, and J. E. Daniels, *J. Appl. Phys.*, vol. 115, no. 12, p. 124108, Mar. 2014.

[132] H. Zhang, C. Groh, Q. Zhang, W. Jo, K. G. Webber, and J. Rödel, *Adv. Electron. Mater.*, vol. 1, no. 6, pp. 1500018–1500027, Apr. 2015.

[133] D. Gobeljic, V. V Shvartsman, A. Belianinov, B. Okatan, S. Jesse, S. V Kalinin, C. Groh, J. Rödel, and D. C. Lupascu, *Nanoscale Res. Lett.*, 2015.

[134] F. C. Sun, M. T. Kesim, Y. Espinal, and S. P. Alpay, *J. Mater. Sci.*, vol. 51, no. 1, pp. 499–505, Jul. 2015.

[135] A. Grigoriev, C. Yang, M. Meisami Azad, O. Causey, D. A. Walko, D. S. Tinberg, and S. Trolier-McKinstry, *Phys. Rev. B*, vol. 91, no. 10, p. 104106, Mar. 2015.

[136] D. E. Dausch, E. Furman, F. Wang, and G. H. Haertling, *Ferroelectrics*, vol. 177, no. 1, pp. 237–253, Mar. 1996.

[137] D. E. Dausch, E. Furman, F. Wang, and G. H. Haertling, *Ferroelectrics*, vol. 177, no. 1, pp. 221–236, Mar. 1996.

[138] D. Damjanovic, M. Demartin Maeder, P. Duran Martin, C. Voisard, and N. Setter, *J. Appl. Phys.*, vol. 90, no. 11, p. 5708, 2001.

[139] D. A. Saravanos and P. R. Heyliger, *J. Intell. Mater. Syst. Struct.*, vol. 6, no. 3, pp. 350–363, May 1995.

[140] R. K. Bordia and R. Raj, *J. Am. Ceram. Soc.*, vol. 68, no. 6, pp. 287–292, Jun. 1985.

[141] T. Chartier, D. Merle, and J. L. Besson, *J. Eur. Ceram. Soc.*, vol. 15, no. 2, pp. 101–107, Jan. 1995.

[142] R. Gao, X. Chu, Y. Huan, Z. Zhong, X. Wang, and L. Li, *J. Eur. Ceram. Soc.*, vol. 35, no. 1, pp. 389–392, 2015.

[143] Z. L. Gui, Y. L. Wang, and L. T. Li, *Ceram. Int.*, vol. 30, no. 7, pp. 1275–1278, 2004.

[144] N. Iwagami, H. Nagata, I. Sakaguchi, and T. Takenaka, *J. Ceram. Soc. Japan*, vol. 124, no. 6, pp. 644–647, 2016.

[145] J. I. E. Xu, *J. Mater. Sci.*, vol. 33, pp. 1023–1030, 1998.

[146] D. Gobeljic, V. V Shvartsman, A. Belianinov, B. Okatan, S. Jesse, S. V Kalinin, C. Groh, J. Rödel, and D. C. Lupascu, *Nanoscale*, vol. 8, pp. 2168–2176, Jan. 2016.

[147] C. Groh, W. Jo, and J. Rödel, *J. Am. Ceram. Soc.*, vol. 97, no. 5, pp. 1465–1470, Jan. 2014.

[148] G. Y. Kim, K. D. Sung, Y. Rhyim, S. Y. Yoon, M. S. Kim, S. J. Jeong, K. H. Kim, J. Ryu, S. D. Kim, and S. Y. Choi, *Nanoscale*, Nov. 2015.

[149] D. S. Lee, S. J. Jeong, M. S. Kim, and K. H. Kim, *Jpn. J. Appl. Phys.*, vol. 52, p. 021801, 2013.

[150] S.-J. Jeong, M.-S. Kim, S.-M. Jang, I.-S. Kim, S. Mohsin, and J.-S. Song, *J. Alloys Compd.*, vol. 646, pp. 1058–1067, Oct. 2015.

[151] D. J. Green, O. Guillon, and J. Rödel, *J. Eur. Ceram. Soc.*, vol. 28, no. 7, pp. 1451–1466, Jan. 2008.

[152] J. Lu, H. H. Hng, X. Song, T. Zhang, and J. Ma, *J. Am. Ceram. Soc.*, vol. 94, no. 5, pp. 1528–1535, May 2011.

[153] X. Rong, J. Chen, J.-T. Li, J. Zhuang, and X.-J. Ning, *J. Appl. Phys*, vol. 54, 2015.

[154] C.-E. Cheng, F. Dinelli, C.-T. Yu, H.-W. Shih, Z. Pei, C.-S. Chang, and F. S.-S. Chien, *Jpn. J. Appl. Phys*, vol. 54, p. 122301, 2015.

[155] L. Amaral, C. Jamin, A. M. R. Senos, P. M. Vilarinho, and O. Guillon, *J. Eur. Ceram. Soc.*, vol. 33, no. 10, pp. 1801–1808, Sep. 2013.

[156] D. Kuscer, F. Levassort, M. Lethiecq, A.-P. Abellard, and M. Kosec, *J. Am. Ceram. Soc.*, vol. 95, pp. 892–900, Nov. 2012.

[157] N. Wongdamnern, D. Maurya, Y. Zhou, M. Sanghadasa, R. Yimnirun, and S. Priya, *Mater. Res. Express*, vol. 1, no. 1, p. 016305, Mar. 2014.

[158] Y. Hiruma, H. Nagata, and T. Takenaka, *J. Appl. Phys.*, vol. 105, no. 8, p. 084112, 2009.

[159] Smolenskii G. A., Isupov V. A., Agranovskaya A. I., and Kranik N. N., *Sov. Phys. - Solid State*, vol. 2, no. 11, 1961.

[160] Y. Hiruma, H. Nagata, and T. Takenaka, *J. Appl. Phys.*, vol. 105, no. 8, pp. 0–8, 2009.

[161] A. Sasaki, T. Chiba, Y. Mamiya, and E. Otsuki, *Jpn. J. Appl. Phys.*, vol. 38, p. 5564, 1999.

[162] K. Yoshii, Y. Hiruma, H. Nagata, and T. Takenaka, *Jpn. J. Appl. Phys.*, vol. 45, no. 5B, pp. 4493–4496, May 2006.

[163] Y.-R. Zhang, J.-F. Li, B.-P. Zhang, and C.-E. Peng, *J. Appl. Phys.*, vol. 103, no. 7, p. 074109, Apr. 2008.

[164] T. Takenaka, K. Maruyama, and K. Sakata, *Jpn. J. Appl. Phys.*, vol. 30, no. Part 1, No. 9B, pp. 2236–2239, Sep. 1991.

[165] H. Foronda, M. Deluca, E. Aksel, J. S. Forrester, and J. L. Jones, *Mater. Lett.*, vol. 115, pp. 132–135, Jan. 2014.

[166] S. T. Zhang, A. B. Kounga, E. Aulbach, H. Ehrenberg, and J. Rödel, *Appl. Phys. Lett.*, vol. 91, no. 11, p. 112906, 2007.

[167] S.-J. Jeong, D.-S. Lee, M.-S. Kim, S.-M. Jang, I.-S. Kim, S. Mohsin, and J.-S. Song, *J. Electroceramics*, vol. 33, pp. 230–238, Jul. 2014.

[168] M. Acosta, W. Jo, and J. Rödel, *J. Am. Ceram. Soc.*, vol. 97, no. 6, pp. 1937–1943, 2014.

[169] C. Groh, W. Jo, and J. Rödel, *J. Appl. Phys.*, vol. 115, no. 23, p. 234107, Jun. 2014.

[170] D. Chen, “Experimental Investigation of Strain Distributions and Polarization in Lead-based and Lead-free Ferroelectrics,” Karlsruhe Institute of Technology, 2017.

[171] F. H. Schader, “Mechanical Stability of the Electromechanical Properties and Phase Transitions in Lead-Containing and Lead-Free Ferroelectrics,” Technical University of Darmstadt, 2016.

[172] L. A. Schmitt, M. Hinterstein, H.-J. Kleebe, and H. Fuess, *Journal of Applied Crystallography*. 01-Aug-2010.

[173] S. T. Zhang, A. B. Kounga, E. Aulbach, T. Granzow, W. Jo, H.-J. Kleebe, and J. Rödel, *J. Appl. Phys.*, vol. 103, no. 3, p. 034107, Feb. 2008.

[174] V. Hauk and B. Scholtes, *Structural and Residual Stress Analysis by Nondestructive Methods*. Elsevier, 1997.

[175] O. G. D’yachenko, S. Y. Istomin, A. M. Abakumov, and E. V. Antipov, *Inorg. Mater.*, vol. 36, no. 3, pp. 247–259, 2000.

[176] F. Gao, X. Dong, C. Mao, F. Cao, and G. Wang, *J. Am. Ceram. Soc.*, vol. 94, no. 12, pp. 4162–4164, Dec. 2011.

[177] L. A. Schmitt, J. Kling, M. Hinterstein, M. Hoelzel, W. Jo, H.-J. Kleebe, and H. Fuess, *J. Mater. Sci.*, vol. 46, no. 12, pp. 4368–4376, Mar. 2011.

[178] R. W. Balluffi, S. Allen, and W. C. Carter, *Kinetics of Materials*. Hoboken, New Jersey: John Wiley & Sons, Inc., 2005.

[179] A. Kushima and B. Yildiz, *J. Mater. Chem.*, vol. 20, no. 23, p. 4809, 2010.

[180] A. Atkinson and T. M. G. M. Ramos, *Solid State Ionics*, vol. 129, no. 1–4, pp. 259–269, Apr. 2000.

[181] P. B. Groszewicz, H. Breitzke, R. Dittmer, E. Sapper, W. Jo, G. Buntkowsky, and J. Rödel, *Phys. Rev. B*, vol. 90, no. 22, p. 220104, Dec. 2014.

[182] I. Abrahams, A. J. Bush, G. E. Hawkes, and T. Nunes, *J. Solid State Chem.*, vol. 147, no. 2, pp. 631–636, 1999.

[183] J. F. Stebbins, S. K. Lee, and J. V. Oglesby, *Am. Mineral.*, vol. 84, no. 5–6, pp. 983–986, 1999.

[184] P. B. Groszewicz, H. Breitzke, W. Jo, J. Rödel, and G. Buntkowsky, *J. Appl. Phys.*, vol. 121, no. 11, p. 114104, Mar. 2017.

[185] C. Tealdi, C. Ferrara, L. Malavasi, P. Mustarelli, C. Ritter, A. Spinella, D. Massiot, P. Florian, Z. Gan, and G. Hoatson, *J. Mater. Chem.*, vol. 22, no. 21, p. 10488, May 2012.

[186] A. J. Woo, *Bull. Korean Chem. Soc.*, vol. 20, no. 10, pp. 1205–1208, 1999.

[187] A. A. Belik, T. Wuernisha, T. Kamiyama, K. Mori, M. Male, T. Nagai, Y. Matsui, and E. Takayama-Muromachi, *Chem. Mater.*, vol. 18, no. 1, pp. 133–139, 2006.

[188] J.-S. Park, C.-J. Jeon, Y.-H. Jeong, J.-S. Yun, and J.-H. Cho, *Mater. Lett.*, vol. 167, pp. 218–221, 2016.

[189] S. Kawashima, M. Nishida, I. Ueda, and H. Ouchi, *J. Am. Ceram. Soc.*, vol. 66, no. 6, pp. 421–423, 1983.

[190] Z. Zhao, V. Buscaglia, M. Viviani, M. T. Buscaglia, L. Mitoseriu, A. Testino, M. Nygren, M. Johnsson, and P. Nanni, *Phys. Rev. B - Condens. Matter Mater. Phys.*, vol. 70, no. 2, 2004.

[191] K. Uchino, E. Sadanaga, T. Hirose, S. W. Kwon, and D. H. Yoon, *J. Am. Ceram. Soc.*, vol. 72, no. August, pp. 1555–58, Aug. 1989.

[192] M. H. Frey and D. A. Payne, *Phys. Rev. B*, vol. 54, no. 5, pp. 3158–3168, 1996.

[193] H. Chen, B. Shen, J. Xu, L. Kong, and J. Zhai, *J. Am. Ceram. Soc.*, vol. 95, no. 11, pp. 3514–3518, 2012.

[194] R. Bermejo, Y. Torres, A. J. Sánchez-Herencia, C. Baudín, M. Anglada, and L. Llanes, *Acta Mater.*, vol. 54, no. 18, pp. 4745–4757, 2006.

[195] L. Amaral, C. Jamin, A. M. R. Senos, P. M. Vilarinho, and O. Guillon, *J. Am. Ceram. Soc.*, vol. 95, no. 12, pp. 3781–3787, Dec. 2012.

[196] P. M. Vilarinho, A. Mahajan, I. Sterianou, and I. M. Reaney, *J. Eur. Ceram. Soc.*, vol. 32, no. 16, pp. 4319–4326, Dec. 2012.

[197] K. G. Webber, Y. Zhang, W. Jo, J. E. Daniels, and J. Rödel, *J. Appl. Phys.*, vol. 108, no. 1, p. 014101, 2010.

[198] R. Dittmer, K. G. Webber, E. Aulbach, W. Jo, X. Tan, and J. Rödel, *Acta Mater.*, vol. 61, no. 4, pp. 1350–1358, Feb. 2013.

[199] T. Ohno, H. Yanagida, K. Maekawa, T. Arai, N. Sakamoto, N. Wakiya, H. Suzuki, S. Satoh, and T. Matsuda, *Thin Solid Films*, vol. 585, pp. 91–94, 2015.

[200] B. Ma, S. Liu, S. Tong, M. Narayanan, and U. (Balu) Balachandran, *J. Appl. Phys.*, vol. 112, no. 11, p. 114117, Dec. 2012.

[201] P. Fan, Y. Zhang, J. Huang, W. Hu, D. Huang, Z. Liu, B. Xie, X. Li, J. Xiao, and H. Zhang, *Ceram. Int.*, vol. 42, no. 2, pp. 2534–2541, 2016.

[202] R. Dittmer, W. Jo, K. G. Webber, J. L. Jones, and J. Rödel, *J. Appl. Phys.*, vol. 115, no. 8, p. 084108, Feb. 2014.

[203] J.-H. Cho, Y.-H. Jeong, J.-H. Nam, J.-S. Yun, and Y.-J. Park, *Jpn. J. Appl. Phys.*, vol. 52, no. 10R, p. 101501, Oct. 2013.

[204] R. Bordia, R. Zuo, O. Guillon, S. Salamone, and J. Rödel, *Acta Mater.*, vol. 54, no. 1, pp. 111–118, Jan. 2006.

[205] C. Jamin, T. Rasp, T. Kraft, and O. Guillon, *J. Eur. Ceram. Soc.*, vol. 33, no. 15–16, pp. 3221–3230, Dec. 2013.

[206] A. Atkinson, J.-S. Kim, R. Rudkin, S. Taub, and X. Wang, *J. Am. Ceram. Soc.*, vol. 94, no. 3, pp. 717–724, Mar. 2011.

[207] L. Amaral, P. M. Vilarinho, and A. M. R. Senos, *Mater. Chem. Phys.*, vol. 149–150, pp. 445–452, Jan. 2015.

[208] B. W. Sheldon, J. D. Nicholas, and S. Mandowara, *J. Am. Ceram. Soc.*, vol. 94, no. 1, pp. 209–216, Jan. 2011.

[209] C. Lichtensteiger, M. Dawber, and J. Triscone, *Phys. Ferroelectr. A Mod. Perspect. Top. Appl. Phys.*, vol. 105, pp. 305–337, 2007.

[210] G. Arlt, D. Hennings, and G. de With, *J. Appl. Phys.*, vol. 58, no. 4, p. 1619, 1985.

[211] G. Arlt, *Ferroelectrics*, vol. 104, no. 1, pp. 217–227, Apr. 1990.

[212] M.-S. Yoon, N. H. Khansur, B.-K. Choi, Y.-G. Lee, and S.-C. Ur, *Ceram. Int.*, vol. 35, no. 8, pp. 3027–3036, Dec. 2009.

[213] W. Jo, S. Schaab, E. Sapper, L. A. Schmitt, H. J. Kleebe, A. J. Bell, and J. Rödel, *J. Appl. Phys.*, vol. 110, no. 7, 2011.

[214] Y. Hiruma, K. Yoshii, H. Nagata, and T. Takenaka, *Ferroelectrics*, vol. 346, no. 1, pp. 114–119, Mar. 2007.

[215] S. Carlsson and P.-L. Larsson, *Acta Mater.*, vol. 49, no. 12, pp. 2179–2191, 2001.

[216] F. Fang and W. Yang, *Mater. Lett.*, vol. 46, no. 2, pp. 131–135, 2000.

[217] B. S. Li, J. S. Cherng, K. J. Bowman, and I. W. Chen, *J. Amer. Ceram. Soc.*, vol. 71, no. July, pp. C362–C364, Oct. 1988.

[218] G. A. Schneider, *Annu. Rev. Mater. Res.*, vol. 37, no. 1, pp. 491–538, Aug. 2007.

[219] K. G. Webber, M. Vögler, N. Khansur, B. Kaeswurm, J. Daniels, and F. Schader, *Smart Mater. Struct.*, Jan. 2017.

[220] S. Pi and C. S. Lynch, *Acta Mater.*, vol. 44, no. 10, pp. 4137–48, 1996.

[221] M. Davis, D. Damjanovic, and N. Setter, *Phys. Rev. B*, vol. 73, no. 1, p. 014115, Jan. 2006.

[222] M. Hinterstein, M. Knapp, M. Hölzel, W. Jo, A. Cervellino, H. Ehrenberg, and H. Fuess, *J. Appl. Crystallogr.*, vol. 43, no. 6, pp. 1314–1321, Oct. 2010.

[223] A. Ayrikyan, O. Prach, N. H. Khansur, S. Keller, S. Yasui, M. Itoh, O. Sakata, K. Durst, and K. G. Webber, *Acta Mater.*, vol. 148, pp. 432–441, 2018.

[224] D. P. H. Hasselman, *J. Am. Ceram. Soc.*, vol. 45, no. 9, pp. 452–453, Sep. 1962.

[225] Y. Zhang, M. Allahkarami, and J. C. Hanan, *J. Mech. Behav. Biomed. Mater.*, vol. 6, pp. 120–127, 2012.

[226] T. Fett, D. Munz, and G. Thun, *Ferroelectrics*, vol. 274, no. 1, pp. 67–81, Jan. 2002.

[227] D. Zhou, R. Wang, and M. Kamlah, *J. Eur. Ceram. Soc.*, vol. 30, no. 12, pp. 2603–2615, Sep. 2010.

[228] P. M. Sargent and T. F. Page, *Proc. Br. Ceram. Soc.*, vol. 26, pp. 209–224, 1978.

[229] A. Krell and P. Blank, *J. Am. Ceram. Soc.*, vol. 78, no. 4, pp. 1118–1120, 1995.

[230] G. G. Leonidova and T. R. Volk, *Sov. Phys. - Solid State*, vol. 7, no. 11, pp. 2694–2696, 1966.

[231] D. Bancroft, *Phys. Rev.*, vol. 53, no. 7, pp. 587–590, Apr. 1938.

[232] T. Ishidate, S. Abe, H. Takahashi, and N. Môri, *Phys. Rev. Lett.*, vol. 78, no. 12, pp. 2397–2400, Mar. 1997.

[233] G. Shirane and K. Sato, *J. Phys. Soc. Japan*, vol. 6, no. 1, pp. 20–26, Jan. 1951.

[234] G. A. Samara, *Phys. Rev.*, vol. 151, no. 2, pp. 378–386, Nov. 1966.

[235] W. R. Buessem, L. E. Cross, and A. K. Goswami, *J. Am. Ceram. Soc.*, vol. 49, no. 1, pp. 36–39, 1966.

[236] M. Vögler, N. Novak, F. H. Schader, and J. Rödel, *Phys. Rev. B*, vol. 95, no. 2, p. 024104, Jan. 2017.

[237] A. B. Kounga, E. Aulbach, T. Granzow, and J. Rödel, *Acta Mater.*, vol. 55, no. 2, pp. 675–680, 2007.

[238] O. Bidault, M. Licheron, E. Husson, and A. Morell, *J. Phys. Condens. Matter*, vol. 8017, 1996.

[239] G. Viola, H. Ning, X. Wei, M. Deluca, A. Adomkevicius, J. Khaliq, M. John Reece, and H. Yan, *J. Appl. Phys.*, vol. 114, no. 1, p. 014107, Jul. 2013.

[240] C. Xu, D. Lin, and K. W. Kwok, *Solid State Sci.*, vol. 10, no. 7, pp. 934–940, Jul. 2008.

[241] J. Zang, M. Li, D. C. Sinclair, T. Frömling, W. Jo, and J. Rödel, *J. Am. Ceram. Soc.*, vol. 27, no. 9, pp. 2825–2831, 2014.

[242] R. McQuade and M. R. Dolgos, *J. Solid State Chem.*, vol. 3, pp. 0–19, 2016.

[243] D. Damjanovic, “Hysteresis in Piezoelectric and Ferroelectric Materials,” in *The Science of Hysteresis*, vol. 3, I. Mayergoyz and G. Bertotti, Eds. Elsevier, 2005, pp. 337–465.

[244] R. Garg, B. N. Rao, A. Senyshyn, P. S. R. Krishna, and R. Ranjan, *Phys. Rev. B*, vol. 88, no. 1, p. 014103, Jul. 2013.

[245] M. Vögler, N. Novak, F. H. Schader, and J. Rödel, *Phys. Rev. B*, vol. 95, no. 2, p. 024104, Jan. 2017.

[246] S. B. Lang and H. L. W. Chan, *Frontiers in Ferroelectricity*. 2007.

[247] J. Zang, W. Jo, H. Zhang, and J. Rödel, *J. Eur. Ceram. Soc.*, vol. 34, no. 1, pp. 37–43, Jan. 2014.

[248] V. Nagarajan, S. P. Alpay, C. S. Ganpule, B. K. Nagaraj, S. Aggarwal, E. D. Williams, A. L. Roytburd, and R. Ramesh, *Appl. Phys. Lett.*, vol. 77, no. 3, p. 438, Jul. 2000.

[249] S. Kondrat, C. R. Pérez, V. Presser, Y. Gogotsi, and A. A. Kornyshev, *Energy Environ. Sci.*, vol. 5, no. 4, p. 6474, Mar. 2012.

[250] V. Y. Topolov, P. Bisegna, and C. R. Bowen, *Piezo-Active Composites: Orientation Effects and Anistropy*. Berlin, Heidelberg: Springer Berlin / Heidelberg, 2014.

[251] R. Khachaturyan, S. Zhukov, J. Schultheiß, C. Galassi, C. Reimuth, J. Koruza, H. von Seggern, and Y. A. Genenko, *J. Phys. D. Appl. Phys.*, vol. 50, no. 4, p. 045303, Feb. 2017.

[252] B. Jaffe, in *Ceramic Microstructures, Their Analysis, Significance and Production. Proceedings of the Third International Materials Symposium*, 1968, pp. 475–488.

[253] C. A. Randall, N. Kim, J. Kucera, W. Cao, and T. R. Shrout, *J. Am. Ceram. Soc.*, vol. 81, no. 3, pp. 677–88, 1998.

[254] J. Ryu, J.-J. Choi, B.-D. Hahn, D.-S. Park, W.-H. Yoon, and K.-H. Kim, *Appl. Phys. Lett.*, vol. 90, no. 15, p. 152901, 2007.

[255] D. Damjanovic, *Rep. Prog. Phys*, vol. 1267, 1998.

[256] B. Dkhil, P. Gemeiner, A. Al-Barakaty, L. Bellaiche, E. Dul’kin, E. Mojaev, and M. Roth, *Phys. Rev. B*, vol. 80, no. 6, p. 064103, Aug. 2009.

[257] D. A. Fernandez-Benavides, A. I. Gutierrez-Perez, A. M. Benitez-Castro, M. T. Ayala-Ayala, B. Moreno-Murguia, and J. Muñoz-Saldaña, *Materials (Basel).*, vol. 11, no. 3, p. 361, 2018.

[258] J. Zheng, S. Takahashi, S. Yoshikawa, K. Uchino, and J. W. C. Vries, *J. Am. Ceram. Soc.*, vol. 79, no. 12, pp. 3193–3198, Dec. 1996.

[259] M. S. Senousy, F. X. Li, D. Mumford, M. Gadala, and R. K. N. D. Rajapakse, *J. Intell. Mater. Syst. Struct.*, vol. 20, no. 4, pp. 387–399, Sep. 2008.

[260] M. Morozov, “Softening and Hardening Transitions in Ferroelectric Pb(Zr,Ti)O 3 Ceramics,” Ecole Polytechnique Federal de Lausanne, 2005.

[261] A. Ullah, S. Y. Lee, H. J. Lee, I. W. Kim, C. W. Ahn, H.-I. Hwang, A. Hussain, and J. S. Lee, *J. Korean Phys. Soc.*, vol. 57, no. 4, pp. 1102–1105, 2010.

[262] M. I. Morozov and D. Damjanovic, *J. Appl. Phys.*, vol. 104, no. 3, 2008.

[263] Z. Luo, J. Glaum, T. Granzow, W. Jo, R. Dittmer, M. Hoffman, and J. Rödel, *J. Am. Ceram. Soc.*, vol. 94, no. 2, pp. 529–535, Feb. 2011.

[264] D. Lupascu and J. Rödel, *Adv. Eng. Mater.*, vol. 7, no. 10, pp. 882–898, 2005.

[265] L. Jin, F. Li, and S. Zhang, *J. Am. Ceram. Soc.*, vol. 97, no. 1, pp. 1–27, 2014.

[266] K. Carl and K. H. Hardtl, *Ferroelectrics*, vol. 17, no. 1, pp. 473–486, Jan. 1977.

[267] B. Wylie-van Eerd, D. Damjanovic, N. Klein, N. Setter, and J. Trodahl, *Phys. Rev. B*, vol. 82, no. 10, p. 104112, Sep. 2010.

[268] R. Dittmer, W. Jo, D. Damjanovic, and J. Rödel, *J. Appl. Phys.*, vol. 109, no. 3, pp. 3–8, 2011.

[269] K. Datta, P. A. Thomas, and K. Roleder, *Phys. Rev. B*, vol. 82, no. 22, p. 224105, 2010.

[270] W. Jo, T. Granzow, E. Aulbach, J. Rödel, and D. Damjanovic, *J. Appl. Phys.*, vol. 105, no. 9, p. 094102, 2009.

[271] S. T. Zhang, A. B. Kounga, E. Aulbach, W. Jo, T. Granzow, H. Ehrenberg, and J. Rödel, *J. Appl. Phys.*, vol. 103, no. 3, p. 034108, 2008.

[272] S. C. Hwang, C. S. Lynch, and R. M. McMeeking, *Acta Metall. Mater.*, vol. 43, no. 5, pp. 2073–2084, May 1995.

[273] A. Mortensen and S. Suresh, *Int. Mater. Rev.*, vol. 40, no. 6, pp. 239–265, Jul. 2013.

[274] H. Zhang, J.-F. Li, and B.-P. Zhang, *J. Am. Ceram. Soc.*, vol. 89, no. 4, pp. 1300–1307, Apr. 2006.

[275] H. Zhang, S. Yang, S. Yang, D. Kong, B.-P. Zhang, and Y. Zhang, *J. Eur. Ceram. Soc.*, vol. 31, no. 5, pp. 795–800, 2011.

[276] P.-Y. Chen, C.-C. Chou, C. Nan Chen, C.-S. Chen, and H. Chen, *Ceram. Int.*, vol. 39, pp. S129–S133, May 2013.

[277] W. Bai, D. Chen, Y. Huang, B. Shen, J. Zhai, and Z. Ji, *J. Alloys Compd.*, vol. 667, pp. 6–17, May 2016.

[278] P. Fu, Z. Xu, R. Chu, W. Li, X. Wu, and M. Zhao, *Mater. Chem. Phys.*, vol. 138, no. 1, pp. 140–145, Feb. 2013.

[279] P.-E. Janolin, B. Dkhil, M. Davis, D. Damjanovic, and N. Setter, *Appl. Phys. Lett.*, vol. 90, no. 15, p. 152907, Apr. 2007.

[280] J. Wang, B. Wylie-van Eerd, T. Sluka, C. Sandu, M. Cantoni, X.-K. Wei, A. Kvasov, L. J. McGilly, P. Gemeiner, B. Dkhil, A. Tagantsev, J. Trodahl, and N. Setter, *Nat. Mater.*, vol. 14, no. 10, pp. 985–90, 2015.

[281] D. Zhu and W. Ma, *Ceram. Int.*, vol. 40, no. 5, pp. 6647–6654, 2014.

[282] X. Tan and W. Jo, *J. Appl. Phys.*, vol. 106, p. 044107, 2009.

[283] J. A. Gallagher, T. Liu, and C. S. Lynch, *J. Appl. Phys.*, vol. 113, no. 8, p. 084103, Feb. 2013.

[284] A. B. Schäufele and K. H. Härdtl, *J. Am. Ceram. Soc.*, vol. 79, no. 10, pp. 2637–2640, Aug. 1996.

[285] K. G. Webber, M. Vögler, N. H. Khansur, B. Kaeswurm, J. E. Daniels, and F. H. Schader, *Smart Mater. Struct.*, vol. 26, no. 6, Jan. 2017.

[286] S. A. Klimin, A. B. Kuzmenko, M. A. Kashchenko, and M. N. Popova, *Phys. Rev. B*, vol. 93, no. 5, p. 054304, 2016.

[287] C. Schuh, T. Steinkopff, A. Wolff, and K. Lubitz, in *SPIE Smart Structures and Materials 2000: Active Materials: Behavior and Mechanics*, 2000, vol. 3992, pp. 165–175.

[288] C. Ma, H. Guo, and X. Tan, *Adv. Funct. Mater.*, vol. 23, no. 42, pp. 5261–5266, Nov. 2013.

[289] Y. Ehara, N. Novak, A. Ayrikyan, P. T. Geiger, and K. G. Webber, *J. Appl. Phys.*, vol. 120, no. 17, p. 174103.1-7, 2016.

[290] A. Ayrikyan, V. Rojas, L. Molina-Luna, M. Acosta, J. Koruza, and K. G. Webber, *IEEE Trans. Ultrason. Ferroelectr. Freq. Control*, vol. 62, no. 6, pp. 997–1006, Jun. 2015.

[291] D. Rout, K.-S. Moon, S.-J. L. Kang, and I. W. Kim, *J. Appl. Phys.*, vol. 108, no. 8, p. 084102, 2010.

[292] F. Weyland, M. Acosta, J. Koruza, P. Breckner, J. Rödel, and N. Novak, *Adv. Funct. Mater.*, vol. 26, no. 40, pp. 7326–7333, Sep. 2016.

[293] V. Bobnar, C. Filipič, A. Levstik, and Z. Kutnjak, *J. Appl. Phys.*, vol. 107, no. 8, p. 084104, 2010.

[294] J. Koruza, V. Rojas, L. Molina-Luna, U. Kunz, M. Duerrschnabel, H.-J. Kleebe, and M. Acosta, *J. Eur. Ceram. Soc.*, vol. 36, no. 4, pp. 1009–1016, Mar. 2016.

[295] J. K. Lee, K. S. Hong, C. K. Kim, and S. E. Park, *J. Appl. Phys.*, vol. 91, no. 7, pp. 4538–4542, Apr. 2002.

Curriculum Vitae

Personal Information

Last Name: Ayrikyan

First Name: Azatuhi

Date of Birth: May 25, 1984

Place of Birth: Moscow, Russia

Nationality: United States of America

Education

August 2013 – September 2018	Doctoral Candidate at TU Darmstadt, Materials Science, under supervision of Professor Kyle G. Webber, currently at the Friedrich Alexander University of Erlangen-Nuremberg
May 2011	Masters of Science, Boston University, Boston, Massachusetts, USA, Materials Science and Engineering
May 2006	Bachelor of Arts, Biological Sciences, 2006, Barnard College, Columbia University, New York, New York, USA

Teaching Supervision

May 2016 - January 2017	Supervisor of Masters thesis entitled “Lead-free Multilayer Composite Ferroelectrics” at Friedrich Alexander University
May 2016 – October 2016	Supervisor of Bachelors thesis entitled “Lead-free Multilayer Composite Piezoceramics” at Friedrich Alexander University
October 2015 – March 2015	Supervisor of Advanced Research Lab entitled “Electromechanical response of ferroelectric/relaxor trilayer based on BNKT-BA and BNT-BT” at TU Darmstadt
October 2015 – March 2015	Supervisor of Advanced Research Lab entitled “Electromechanical response of ferroelectric/relaxor 0-3 composites based on BNKT-BA and BNT-BT” at TU Darmstadt
June 2015 – November 2015	Supervisor of Advanced Research Lab entitled “Study on the Strain Enhancement Mechanisms of Ferroelectric BNT-7BT/Relaxor BNT-25ST Composites Using the Trilayer Structure Model” at TU Darmstadt
April – July 2014, 2015	Instructor for laboratory course “Ceramics Processing” in the Materials Science Department of TU Darmstadt
September – December 2012	Instructor for laboratory course “Introductory Physics” at Physics Department of Boston University

Refereed Publications

Ayrikyan, V. Rojas, L. Molina-Luna, M. Acosta, J. Koruza, K.G. Webber, Enhancing electromechanical properties of lead-free ferroelectrics with bilayer ceramic/ceramic composites,, IEEE Trans. Ultrason. Ferroelectr. Freq. Control. 62 (2015) 997–1006.

Ayrikyan, K.G. Weyland, Florian , Steiner, Sebastian, Duerrschnabe, Michael l, Luna, Leopoldo Molina-, Koruza, Jurij , Webber, Multilayer Lead-Free Piezoceramic Composites: Influence of Co-firing on Microstructure and Electromechanical Behavior, J. Am. Ceram. Soc. (2017): 3673-3683.

Y. Ehara, N. Novak, A. Ayrikyan, P.T. Geiger, K.G. Webber, Phase transformation induced by electric field and mechanical stress in Mn-doped $(Bi_{1/2}Na_{1/2})$TiO3-$(Bi_{1/2}K_{1/2})TiO_3$ ceramics, Journal of Applied Physics, 120 (17) (2016) 174103.1-7.

T. Frömling, S. Steiner, A. Ayrikyan, D. Bremecker, M. Dürrschnabel, L. Molina-Luna, H.-J. Kleebe, H. Hutter, K.G. Webber, M. Acosta, Designing properties of $(Na_{1/2}Bi_x)TiO_3$ -based materials through A-site non-stoichiometry, J. Mater. Chem. C. 6 (2018) 738–744

D. Chen, A. Ayrikyan, K.G. Webber, M. Kamlah, Time-dependent electromechanical response of $0.93(Na_{1/2}Bi_{1/2})TiO_3$-$0.07BaTiO_3$ lead-free piezoceramic under constant electric field, Journal of Applied Physics 121 (2017) 114106.

Ayrikyan, Azatuhi, et al. "Lead-Free Multilayer Piezoceramic Composites: Effect of Cosintering on Electromechanical Properties." IEEE Trans. Ultrason. Ferroelectr. Freq. Control 64.7 (2017): 1127-1134.

Ayrikyan, O. Prach, N.H. Khansur, S. Keller, S. Yasui, M. Itoh, O. Sakata, K. Durst, K.G. Webber, Investigation of residual stress in lead-free BNT-based ceramic/ceramic composites, Acta Mater. 148 (2018) 432–441

S. Wang, A. Ayrikyan, H. Zhang, K.G. Webber, B-X. Xu, Phase-Field Study of Electromechanical Coupling in Lead-Free Relaxor/Ferroelectric-Layered Composites, Adv. Electron. Mater. 2018, 1800710.

International Conference Presentations

“Tailoring Electromechanical Properties of Lead-free Ferroelectrics through Composite Structures” Oral Presentation UK Ferroelectrics Meeting, Teddington, UK, July 2015

“Lead-free Graded Functional Ceramics: Enhancement of Ferroelectric Properties through Tailored Structures” Oral Presentation, Materials Research Society Fall Meeting, Boston, Massachusetts, USA, December 2015

“In-Situ synchrotron measurements of stress-dependent ferroelastic behavior in BNT-based ferroelectrics” Oral Presentation IEEE ISAF, Darmstadt, Germany, August 2016

“Tailoring the Electromechanical Properties of Lead-Free Ferroelectrics with the Ceramic/Ceramic Composite Approach” Oral Presentation, IEEE ISAF, Darmstadt, Germany, August 2016

Page intentionally left blank

Erklärung

Ich versichere, dass ich die vorliegende Dissertation selbstständig und nur mit den angegebenen Quellen und Hilfsmitteln angefertigt habe. Die Arbeit hat in gleicher oder ähnlicher Form noch keiner Prüfungsbehörde vorgelegen.

Darmstadt, den ____________________________

Azatuhi Ayrikyan